NORTHWESTERN UNIVERSITY

Experimental and Theoretical Studies on Flexoelectricity

A DISSERTATION

SUBMITTED TO THE GRADUATE SCHOOL

IN PARTIAL FULFILLMENT OF THE REQUIREMENTS

for the degree

DOCTOR OF PHILOSOPHY

Field of Materials Science and Engineering

By

Christopher A. Mizzi

EVANSTON, ILLINOIS

June 2021

ABSTRACT

Experimental and Theoretical Studies on Flexoelectricity

Christopher A. Mizzi

This dissertation explores the fundamental science of flexoelectricity and its implications using a combined experimental and theoretical approach. I begin by introducing the flexoelectric effect and formalizing the basics of strain gradients, polarization, and flexoelectric coefficients. Next, I describe the development of a flexoelectric characterization system based upon three-point bending and demonstrate the tenets of measuring flexoelectric coefficients with experiments on single crystals of $SrTiO_3$. After deriving expressions for these measured flexoelectric coefficients for crystals of arbitrary symmetry and orientation in terms of flexoelectric tensor components, elastic constants, and geometric factors, I address anticlastic bending suppression effects in three-point bending and assess the use of Euler-Bernoulli beam theory.

Having established how to measure and interpret flexoelectric coefficients with three-point bending, I characterize the flexoelectric response of a range of commercially available single crystal oxides including $SrTiO_3$, $KTaO_3$, $LaAlO_3$, TiO_2, $YAlO_3$, and $DyScO_3$.

These measurements help address the issue of data deficiency in flexoelectricity by significantly increasing the number of systems in which flexoelectricity has been studied. They also indicate low dielectric constant materials have large flexocoupling voltages exceeding nominal expectations.

To explore the structural origins of these measured flexoelectric responses, I perform ab initio calculations of bulk flexoelectric coefficients. After benchmarking the bulk flexoelectric coefficients computed with an all-electron code and examining the impact of the exchange and correlation functional, I calculate the bulk flexoelectric coefficients of the (pseudo) cubic perovskites I characterized experimentally. I find the predicted flexoelectric coefficients differ in both size and magnitude from the measured values. To address this difference, I investigate the role of surfaces in flexoelectricity and demonstrate the importance of the strain derivative of the mean-inner potential to the total flexoelectric response of a finite sample. I then perform density functional theory calculations on many low energy surfaces to explore the role of surface chemistry, structure, and adsorbates on the strain derivative of the mean-inner potential. I also show how this flexoelectric contribution can be estimated from electron scattering factors. Ultimately, combining the mean-inner potential contribution to the total flexoelectric response with the first principles bulk flexoelectric coefficients yields good agreement with the $SrTiO_3$ and $KTaO_3$ measurements.

Moving beyond single crystals, I explore how the total flexoelectric response is impacted by defects. First, I show $LaAlO_3$ twin boundaries have flexoelectric coefficients $\sim$10 μC/m and dictate the flexoelectric response of twinned $LaAlO_3$ samples. Next, I demonstrate the flexoelectric response of Nb-doped $SrTiO_3$ is 10^3 times that of undoped

$SrTiO_3$. Lastly, I find MgO has an anomalously large flexoelectric response which greatly surpasses ab initio expectations. Collectively, these experiments demonstrate extrinsic contributions to flexoelectricity can often overshadow intrinsic contributions and dictate the total flexoelectric response.

Next, I explain why large charging occurs in the lanthanide scandates and its connection to large flexoelectric bending at the nanoscale. In doing so, I address the role of the 4f states in the bulk valence band of $GdScO_3$, $DyScO_3$, and $TbScO_3$ through a combination of photoelectron spectroscopy and ab initio simulations, and discuss determining a surface structure on the (110) surface of $DyScO_3$. I also provide some methods to overcome charging effects in X-ray photoelectron spectroscopy and electron energy loss spectroscopy.

Lastly, I argue triboelectricity is driven by contact deformation-induced band bending which arises through the flexoelectric effect. After developing a simplified flexoelectric model for triboelectricity based upon Hertzian contact, I generalize the model to incorporate band structure and treat contact deformation-induced band bending for two arbitrary materials in contact. I explore this model in some specific contact cases to demonstrate its connection to well-known charge transfer mechanisms and its ability to explain numerous experimental triboelectric observations which have been historically unexplained.

Acknowledgements

First, I would like to thank Professor Laurie Marks for his mentorship and guidance over the course of my PhD. He has taught me to identify interesting scientific problems and turn ideas into rigorous science. I appreciate his encouragement and support throughout my time at Northwestern, and I plan to heed his advice and continue to "follow the science". I also would like to thank the members of my dissertation committee: Professor Peter Voorhees, Professor Ken Poeppelmeier, and Professor James Rondinelli. Special thanks to Professor Peter Voorhees for his assistance during my postdoctoral search. I am also grateful to Professor Bill Halperin for serving on my qualifying exam committee.

I owe a debt of graduate to all members of the LDM group, past and present. Thanks to Emily H., Betty, Seyoung, Tassie, Lizzie, Ahmet, Xiao-Xang, Bruce, Emily G., Karl, and Hans for their research assistance, stimulating conversations, and making Catalysis B19 an amazing place to work. Thanks to Pratik for instigating my interest in flexoelectricity and being a great research companion. Thanks to Lawrence for helping me sort out any and all computer problems, and the invigorating conversations. Thanks to Alex helping me to understand tribology and for being a great cube-mate. Thanks to Ryan for frequent insightful discussions and musical interludes. Thanks to Zach for his collaboration on all things scandate and for always being a soundboard for ideas. Thanks to Tiffany for being a great lab partner in MSE 1140 Materials: The Future of Energy and

great groupmate nearly a decade later. Thanks to Evan for being an incredibly diligent undergrad researcher and helping me to grow as a mentor.

I would also like to thank specific collaborators for their help on aspects of work presented in this dissertation. The flexoelectric characterization system described in Chapters 2 and 3 benefitted from conversations with Dr. Pratik Koirala, and Evan Guo assisted with sample preparation and flexoelectric measurements included in Chapters 4 and 6. I found discussions with Professor Laurie Marks very helpful for the DFT calculations and analyses I performed in Chapters 4, 5, 6, and 8. In Chapter 7, DFT calculations were performed by Professor Laurie Marks, electron microscopy was done by Dr. Pratik Koirala, Dr. Ahmet Gulec, and Tiffany Ly, Zachary Mansley developed the X-ray photoelectron spectroscopy model, and Dr. Ryan Paull and Tiffany Ly supplied nanoparticles. I would also like to acknowledge Professor Laurie Marks for suggesting the possible connection between tribology, flexoelectricity, and triboelectricity, and Dr. Alex Lin for collaborating on the initial flexoelectric model for triboelectricity developed in Chapter 8. The work described in this dissertation was supported the U.S. Department of Energy, Office of Science, Basic Energy Sciences, under Award No. DE-FG02-01ER45945. I also would like to acknowledge financial support from the ICDD Ludo Frevel Crystallography Scholarship and the Searle Center's Graduate Teaching Fellows program.

Beyond research at Northwestern, I am grateful for the opportunities I have had in teaching and outreach. I thank the Searle Center whose programming has helped me grow as an educator and scholar, and I am indebted to Dr. Nancy Ruggeri, Kate Flom Derrick, and Professor Jon Emery for their assistance with my Graduate Teaching Fellow project. I especially thank Dr. Nancy Ruggeri for her help with my postdoctoral search

and dedication to bettering the Northwestern community. I would also like to thank Dr. Bruce Lindvall and the McCormick Graduate Leadership Council for providing me with an opportunity to be involved with the graduate student community. I particularly appreciate the countless hours Jaye, Curtis, Kirby, and I spent on the Engineering Grand Prix and SICC Saturdays, and the Fleetwood-Jourdain Center for hosting our events.

Most importantly, I extend infinite gratitude to my friends and family for their support over the years. I especially appreciate Rohit and Shane for being wonderful roommates and amazing friends, and want to give special thanks to Michaela, Rohit, Shane, Shreya, the Maxii, and Tiffany for the weekly video chats which have made the last year significantly better. To my parents and sisters: you are an inspiration and your love and support have enabled me to pursue my dreams. I cannot overstate how much I appreciate all you have done for me.

Last, but certainly not least, thank you Michaela for your boundless love and limitless encouragement. I cannot imagine a more perfect partner to have had on this journey and I look forward to the start of our Southwestern adventure.

List of abbreviations

AFM: atomic force microscopy.

AR-XPS: angle-resolved x-ray photoelectron spectroscopy.

BTO: $BaTiO_3$.

CB: conduction band.

DFPT: density functional perturbation theory.

DFT: density functional theory.

DL: double-layer.

DMA: dynamic mechanical analyzer.

DSO: $DyScO_3$.

EELS: electron-energy loss spectroscopy.

FEA: finite element analysis.

GGA: generalized gradient approximation.

GSO: $GdScO_3$.

KPM: Kelvin probe microscopy.

KTO: $KTaO_3$.

LAO: $LaAlO_3$.

LDA: local density approximation.

LIA: lock-in amplifier.

MAE: mean absolute errors.

MIP: mean-inner potential.

NGO: $NdGaO_3$.

pDOS: partial density of states.

PSD: phase-sensitive detector.

RBF: radial basis function.

REELS: reflection electron-energy loss spectroscopy.

RMSE: root mean square error.

SE: secondary electron.

SL: single-layer.

SNR: signal-to-noise ratio.

STO: $SrTiO_3$.

TB: twin boundary.

TED: transmission electron diffraction.

TEM: transmission electron microscopy.

TPB: three-point bending.

TSO: $TbScO_3$.

UPS: ultraviolet photoelectron spectroscopy.

VB: valence band.

VBM: valence band maximum.

XPS: x-ray photoelectron spectroscopy.

XRD: x-ray diffraction.

YAO: $YAlO_3$.

ZLP: zero loss peak.

Table of Contents

List of Tables

List of Figures

CHAPTER 1

Introduction

1.1. Motivation

Piezoelectricity was first reported by Jacques and Pierre Curie in 1880 [**1**]. Their experiments demonstrated that some crystals, including quartz and tourmaline, develop a polarization when compressed along certain crystallographic directions. Although their experimental apparatus was simple by today's standards, they were able to deduce from measurements that the existence of piezoelectricity was connected to underlying crystal symmetry.

> For a direction to have the properties of an electric axis in a crystal, it is necessary that this crystal lacks the same element of symmetry as that missing in an electric field pointed along this direction ...
>
> - J. Curie and P. Curie, *Journal de Physique theorique et appliquee* **1** (1882), 245251 [**2**]

Since the pioneering work of the Curie brothers, the piezoelectric effect has become something of a household name with applications in consumer electronics and musical instruments, among other areas [**3**]. In terms of the fundamental science, piezoelectricity is well-understood [**4**] and researchers are readily able to purchase equipment to measure piezoelectric coefficients and ab initio codes to compute piezoelectric coefficients using density functional theory (DFT) [**5**]. However, there is a fundamental limitation facing

piezoelectricity: piezoelectricity only exists in materials lacking inversion symmetry [**6**]. This unavoidable constraint significantly decreases the number of materials that exhibit bulk piezoelectricity [**3**]. Coupling this bottleneck with the fact that many of the best piezoelectric materials contain lead [**7**] generates a significant materials discovery challenge in the search for the next generation of electromechanical materials.

The question is then: are all non-piezoelectrics void of electromechanical functionality? To address this issue, it is useful to revisit the Curie brothers conclusion regarding symmetry and recast it as a more general statement:

$$\{Response\} = \{Material\} \times \{Stimulus\}. \tag{1.1}$$

As they correctly noted, an asymmetric response (i.e. polarization) was obtained by applying a symmetric stimulus (i.e. stress/strain) because piezoelectric materials have an intrinsic asymmetry (i.e. broken inversion symmetry). However, Eq. 1.1 suggests this is not the only route that produces an asymmetric response. An asymmetric response can also be obtained in a symmetric material (i.e. with inversion symmetry) if the stimulus is asymmetric [**8, 9**]. The simplest example of such a phenomenon is the dielectric response of an insulator: the application of an electric field (asymmetric stimulus) induces a polarization (asymmetric response) in all insulators, independent of their underlying symmetry [**8, 9**]. By extension, electromechanical functionality akin to piezoelectricity should be possible even in non-piezoelectric materials if the deformation is asymmetric. The lowest order electromechanical example of this is flexoelectricity, the coupling of polarization and strain gradient [**10, 11**]. Since a strain gradient is an asymmetric stimulus which

inherently breaks inversion symmetry, the flexoelectric effect exists in all materials. The differences between piezoelectricity and flexoelectricity are illustrated in Figure 1.1.

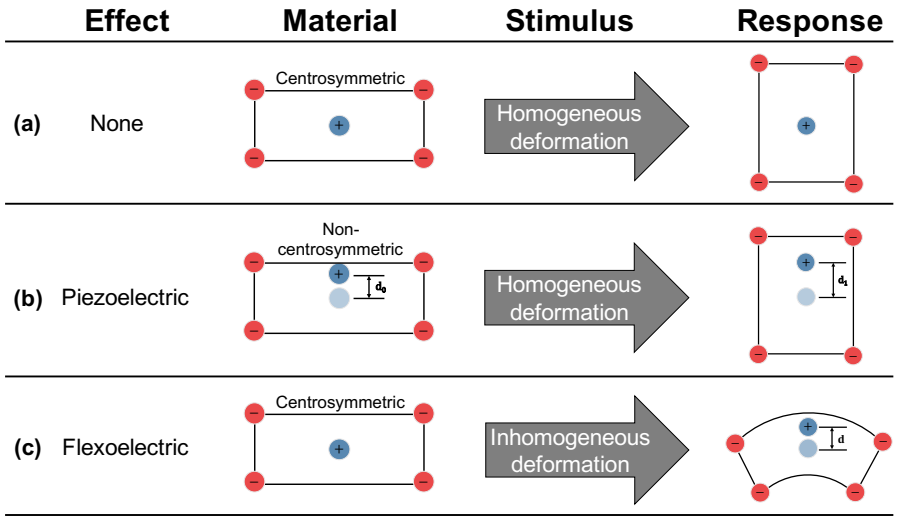

Figure 1.1. Either the material or the deformation must break inversion symmetry to induce a polarization from a mechanical deformation. (a) A centrosymmetric material is not polarized by a homogeneous mechanical deformation. (b) A non-centrosymmetric material is polarized by a homogeneous mechanical deformation. (c) A centrosymmetric material is polarized by an inhomogeneous deformation.

The past twenty years have seen a significant increase in the number of studies on flexoelectricity in crystalline solids, and much progress has been made since the first theoretical treatment by Mashkevich and Tolpygo in 1957 [**12**] and experimental observation by Bursian and Zaiikovski in 1968 [**13**]. The renewed interest in the flexoelectric effect can largely be attributed to the work by Ma and Cross which, at the turn of the century, established the importance of flexoelectricity in high dielectric constant ceramics [**14, 15, 16, 17, 18**]. Since then, flexoelectric couplings have been shown to profoundly impact mechanical [**19, 20**] and dielectric properties [**21, 22**], affect defect formation [**23**], and even participate in biological processes such as bone recovery [**24, 25**]. Much of this

interest is driven by the nanoscale importance of flexoelectricity: the intrinsic scaling of strain gradient with size leads to large strain gradients at small length scales, which can cause large flexoelectric responses even for materials with modest flexoelectric properties [**26, 27, 28, 29**]. For example, flexoelectric polarizations rivaling the spontaneous polarization of archetypal ferroelectrics have been measured in the vicinity of dislocations [**30**] and crack tips [**31**], and strain gradients associated with atomic force microscopy (AFM) tips are able to switch ferroelectric domains [**32, 33**].

Beyond this academic interest in the fundamental science of flexoelectricity, there have been demonstrations which indicate promising flexoelectric energy harvesting [**34, 35**], strain sensing [**36**], and actuation [**37**], and the connections between flexoelectricity, biology [**24, 25, 38, 39**], and triboelectricity [**40**] suggest that flexoelectricity could have significant medical and industrial relevance. To realize the potential these demonstrations hint at, it is necessary to advance the basic science of flexoelectricity to enable the tailoring, optimization, and engineering of flexoelectric properties.

1.2. Organization

This dissertation consists of 9 chapters. Chapter 2 provides an overview of flexoelectric characterization and introduces the system I have developed to measure flexoelectricity with three-point bending. Chapter 3 includes a rigorous treatment of the flexoelectric response of anisotropic crystals subjected to three-point bending as well as the experimental characterization of flexoelectric coefficients in several single crystal oxide systems. Chapter 4 provides first principles calculations of bulk flexoelectric coefficients in these same single crystal systems. Chapter 5 addresses the short-comings of the calculations

presented in Chapter 4 by considering the contribution of the mean-inner potential to flexoelectricity. Chapter 6 describes measurements of extrinsic contributions to flexoelectricity stemming from defects which lead to significant enhancements in the flexoelectric responses of $LaAlO_3$, $SrTiO_3$, and MgO crystals. Chapter 7 provides a description of my work on lanthanide scandates including the characterization of their bulk electronic structure, atomic and electronic surface structure, charging, and flexoelectric bending. Chapter 8 describes how deformation-induced band bending arising from flexoelectric couplings during contact drives triboelectricity. Chapter 9 suggests some areas for future research.

CHAPTER 2

Development of a Flexoelectric Characterization System

2.1. Introduction to Flexoelectric Characterization

The first experimental observation of the flexoelectric effect in crystalline solids occurred in 1968 with Bursian and Zaikovskii observing that $BaTiO_3$ (BTO) thin films tended to bend in the presence of an electric field [**13**]. However, it would be thirty-three years before the the experimental solid-state community revisited the flexoelectric effect. This reignition of interest in flexoelectricity was sparked by a series of experiments performed by Ma and Cross on high-dielectric constant ceramics [**14, 15, 16, 17, 18**]. These experiments provided the first experimental measurements of flexoelectric coefficients, the materials parameter describing the linear coupling between polarization and strain gradient, and also unequivocally demonstrated that many ceramics possessed flexoelectric coefficients that far surpassed simple theoretical predictions [**41**].

The seminal work by Ma and Cross triggered a substantial increase in the number of experimental studies on the flexoelectric effect in solids [**42, 43, 11, 10**], with a concomitant increase in the methods used to measure flexoelectric coefficients. Comprehensive comparisons of these methods can be found in reviews on the topic (e.g. [**43**]). Fundamentally, any flexoelectric characterization either follows a direct approach (electric response from mechanical stimulus) or converse approach (mechanical response from electrical stimulus) [**10**]. More formally, the direct flexoelectric effect describes the polarization (P) induced

by the application of a strain gradient ($\frac{d\epsilon}{dx}$)

$$P = \mu \frac{d\epsilon}{dx} \tag{2.1}$$

whereas the converse flexoelectric effect refers to the stress (σ) induced by a polarization gradient ($\frac{dP}{dx}$)

$$\sigma = \frac{\mu}{\chi} \frac{dP}{dx}. \tag{2.2}$$

Here, μ is flexoelectric coefficient and χ is dielectric susceptibility. Note, the direct and converse flexoelectric effects in Eq. 2.1 and 2.2 have been expressed in their scalar forms, the effects of other electromechanical couplings (e.g. piezoelectricity [**3**] and electrostriction [**44**]) have been neglected, and I have been somewhat cavalier with my treatment of electrostatic boundary conditions [**45, 46**]. These simplifications are meant to emphasize the fundamental physics behind flexoelectricity and will be maintained throughout the remainder of this chapter, where possible, to facilitate an understanding of the basic concepts of flexoelectric characterization before giving a rigorous description in Chapter 3.

Experimental investigations of flexoelectricity described in this dissertation will focus on the direct flexoelectric effect described by Eq. 2.1 since it is more experimentally tenable to apply strain gradients rather than polarization gradients. Throughout the remainder of Chapter 2, I will describe the development, implementation, and application of an apparatus to measure flexoelectricity using three-point bending (TPB). Section 2.2 provides an overview of my experimental approach, and is followed by an in-depth discussion of the three main aspects of these experiments: strain gradients (Section 2.3), polarization (Section 2.4), and flexoelectric coefficients (Section 2.5). In Section 2.6 I

validate and benchmark my apparatus using measurements performed on $SrTiO_3$ (STO) single crystals. The work in Chapter 2 benefitted from discussions with LDM group members, especially Dr. Pratik Koirala, Binghao (Evan) Guo, and Professor Laurence D. Marks.

2.2. Overview of Three-Point Bending Approach to Measuring Flexoelectricity

As mentioned above, experimental measurements of the direct flexoelectric effect require measuring the electric response of a sample subjected to a strain gradient. In choosing a method to apply strain gradients, it is important to consider some limitations. First, strains must be kept small to avoid spurious contributions from plastic deformation [**30**], fracture [**47, 31, 48**], and piezoelectricity [**49, 50, 51**]. Second, flexoelectric coefficients are ∼nC/m in centrosymmetric oxides [**52**] and ∼ μC/m in non-centrosymmetric oxides [**53**], indicating either large strain gradients (while maintaining small strains) must be used to generate sufficiently large electrical responses or small strain gradients must be used in conjunction with electric characterization capable of precisely measuring small electric responses.

One method of applying strain gradients that adheres to these constraints is TPB. A TPB geometry and the resulting strain gradient are illustrated in Figure 2.1. As demonstrated by Zubko et al. [**52**], dynamic mechanical analyzer (DMA)s in TPB configurations are well-suited for flexoelectric characterization because DMAs apply oscillatory strain gradients which induce oscillatory flexoelectric responses that can be measured precisely with a lock-in amplifier (LIA). Thus, the use of a DMA to bend samples provides

a means to overcome experimental challenges associated with measuring small currents while keeping strains small.

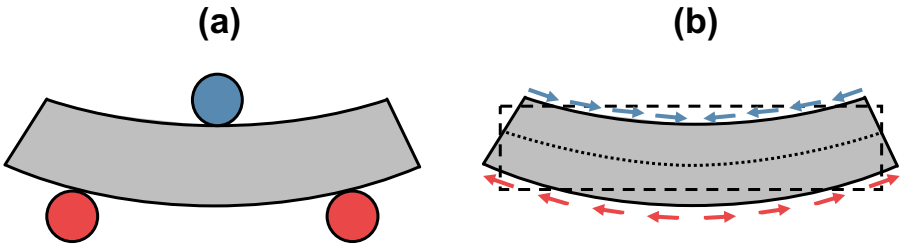

Figure 2.1. (a) Depiction of TPB. The sample (grey) sits on two supports (red) equidistant from the sample center. The sample is bent by a force applied at the sample center by the knife edge (blue). (b) Bending the sample in this manner places it in a state of inhomogeneous strain. The primary strain gradient is through the thickness of the sample: compared to the original shape (dashed, black), the deformed shape (grey) has one surface in a state of compression (arrows, blue) and the other in a state of tension (arrows, red). There is zero strain at the intermediate plane (dotted, black).

An overview of a typical flexoelectric experiment performed using a DMA in a TPB configuration is shown in Figure 2.2 for a centrosymmetric material. First, there is no polarization in the sample because there is no force applied to it. Next, a static force is applied to the sample center to maintain contact between the sample, knife edge, and supports during oscillatory motion. Then, an oscillatory force of a fixed magnitude (smaller than the static force to maintain contact) is applied to the sample which induces an oscillatory strain gradient. In Section 2.3 I describe how the magnitude of this strain gradient can be computed from the oscillatory force and sample geometry. As the oscillatory force (and strain gradient) increases and decreases, so does the polarization induced by flexoelectricity. In Section 2.4 I explain how the change in polarization caused by the oscillatory strain gradient is measured as a short-circuit current with a LIA. Thus, by

measuring the short-circuit current (proportional to polarization) at different oscillatory forces (proportional to strain gradient) it is possible to measure the flexoelectric coefficient of a sample using Eq. 2.1. In Section 2.5 I give a more rigorous interpretation of the flexoelectric coefficients measured in this manner, and discuss how their magnitude and sign are deduced from experimental measurables.

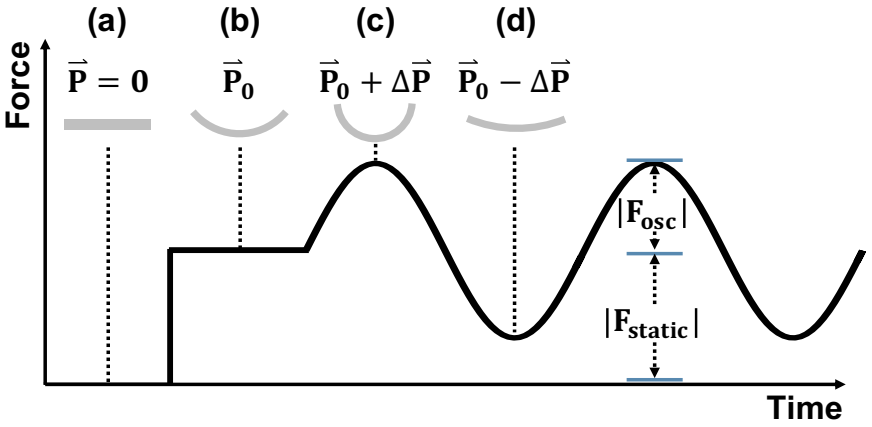

Figure 2.2. Summary of flexoelectric measurements using TPB (a) An initially unpolarized sample (grey) is subjected to (b) a static force F_{static} which induces a static polarization P_0. An oscillatory force F_{osc} (c) increases and (d) decreases P_0 by an amount ΔP. F_{osc} is proportional to the strain gradient and the short-circuit current is proportional to ΔP.

2.3. Application of Strain Gradients

2.3.1. Deformation in Materials

Solids subjected to external forces tend to deform [**54, 55, 56**]. If the solid returns to its original state once the forces are removed, the deformations are considered to be elastic. The work described here pertains to sufficiently small deformations such that they can always be considered elastic. Elastic deformations (u_i) constitute the differences in the

positions of points in a solid before (r_i) and after (r_i') the application of the external forces.

$$u_i = r_i' - r_i \tag{2.3}$$

When deformations are small and rigid body translations and rotations are disallowed, it is convenient to consider the extent of deformation relative to the original reference configuration known as strain. There are many other definitions of strain (e.g. Cauchy, Green, etc.) which apply in particular limits or under certain conditions [**57**], but, unless otherwise stated, all strains in this dissertation correspond to symmetrized strains of the form

$$\epsilon_{ij} = \begin{pmatrix} \frac{\partial u_1}{\partial x_1} & \frac{1}{2}(\frac{\partial u_1}{\partial x_2} + \frac{\partial u_2}{\partial x_1}) & \frac{1}{2}(\frac{\partial u_1}{\partial x_3} + \frac{\partial u_3}{\partial x_1}) \\ \frac{1}{2}(\frac{\partial u_1}{\partial x_2} + \frac{\partial u_2}{\partial x_1}) & \frac{\partial u_2}{\partial x_2} & \frac{1}{2}(\frac{\partial u_2}{\partial x_3} + \frac{\partial u_3}{\partial x_2}) \\ \frac{1}{2}(\frac{\partial u_1}{\partial x_3} + \frac{\partial u_3}{\partial x_1}) & \frac{1}{2}(\frac{\partial u_2}{\partial x_3} + \frac{\partial u_3}{\partial x_2}) & \frac{\partial u_3}{\partial x_3} \end{pmatrix}. \tag{2.4}$$

In this convention, the strain matrix is symmetric with ϵ_{ij}=ϵ_{ji}, derivatives are taken with respect to the unperturbed coordinate system, diagonal terms describe extension/compression, and off-diagonal terms describe shear. We will see in Chapter 4 that it is more convenient to work with unsymmetrized strain in some theoretical contexts [**58, 59**]. The unsymmetrized strain tensor is given by

$$\eta_{ij} = \begin{pmatrix} \frac{\partial u_1}{\partial x_1} & \frac{\partial u_1}{\partial x_2} & \frac{\partial u_1}{\partial x_3} \\ \frac{\partial u_2}{\partial x_1} & \frac{\partial u_2}{\partial x_2} & \frac{\partial u_2}{\partial x_3} \\ \frac{\partial u_3}{\partial x_1} & \frac{\partial u_3}{\partial x_2} & \frac{\partial u_3}{\partial x_3} \end{pmatrix}. \tag{2.5}$$

It is necessary to determine the gradient of Eq. 2.4 and 2.5 to treat flexoelectricity [**58, 59**]. Throughout this work, symmetrized strain gradients will be described with the notation

$$\epsilon_{ij,k} = \frac{d\epsilon_{ij}}{dx_k} \tag{2.6}$$

and unsymmetrized strain gradients are defined by

$$\eta_{i,jk} = \frac{d\eta_{ij}}{dx_k}. \tag{2.7}$$

According to definitions given in Eq. 2.4- 2.7, symmetrized strain gradients obey the symmetry $\epsilon_{ij,k}$=$\epsilon_{ji,k}$ and unsymmetrized strain gradients obey the symmetry $\eta_{i,jk}$=$\eta_{i,kj}$. Again, unless otherwise stated we will be using the symmetrized strain convention in this work. In this convention, longitudinal strain gradients are of the form $\epsilon_{ii,i}$, shear strain gradients are of the form $\epsilon_{ij,i}$, and transverse strain gradients are of the form $\epsilon_{ii,j}$.

Though the discussion of deformation, strain, and strain gradient has been general thus far, we now limit ourselves to one-dimensional quantities (i.e. $u(x)$, $\epsilon(x) = \frac{du}{dx}$, and $\epsilon_{,x} = \frac{d\epsilon}{dx} = \frac{d^2u}{dx^2}$ to focus on the nuances of the experimental apparatus throughout the remainder of Chapter 2. We return to a full three-dimensional treatment in Chapter 3.

2.3.2. Beam Bending

A sample in TPB rests on two supports separated by a distance L while a force is applied to the sample center by the "knife edge", as illustrated in Figure 2.3. Assuming the strain remains small throughout beam bending, the static displacement of a beam subjected to

this concentrated applied force is governed by

$$D\frac{d^4u}{dx^4} = 0 \tag{2.8}$$

where D is the flexural rigidity of the beam [**54, 56, 55**]. D is the product of Young's modulus, Y, and the second moment of area of the cross-section of the beam, I. To solve Eq. 2.8, known as the Euler-Bernoulli beam equation, the relevant boundary conditions for TPB are that the displacement and moment of the bent beam are zero at the edge of the beam (i.e. $u(x = 0) = 0$ and $D\frac{d^2u}{dx^2}(x = 0) = 0$) and the slope of the bent beam is zero at the beam center (i.e. $\frac{du}{dx}(x = L/2) = 0$). Additionally, there is a constant shear force in the beam induced by the set of concentrated loads in TPB which maintains static equilibrium (i.e. $\frac{d^3u}{dx^3} = -F/2, 0 \leq x \leq L/2$). Note, we only focus on solving Eq. 2.8 on one half of the beam because the solution on the other half can be acquired by symmetry. Eq. 2.8 with the appropriate boundary conditions yields the solution

$$u(x) = -\frac{F}{48D}(4x^3 - 3L^2x), \quad 0 \leq x \leq \frac{L}{2}. \tag{2.9}$$

This deformation corresponds to a strain given by

$$\epsilon(x) = \frac{du}{dx} = -\frac{F}{48D}(12x^2 - 3L^2), \quad 0 \leq x \leq \frac{L}{2} \tag{2.10}$$

and a strain gradient of

$$\frac{d\epsilon}{dx}(x) = \frac{d^2u}{dx^2} = -\frac{F}{2D}x, \quad 0 \leq x \leq \frac{L}{2}. \tag{2.11}$$

My measurements are carried out on beams with rectangular cross sections, so $I = \frac{bh^3}{12}$ where b is the beam width and h is the beam thickness [**56**]. Therefore, Eq. 2.11 can be specified for this work as

$$\frac{d\epsilon}{dx}(x) = -\frac{F}{Y}\frac{6}{bh^3}x, \quad 0 \leq x \leq \frac{L}{2} \tag{2.12}$$

or

$$\frac{d\epsilon}{dx}(x) = -\frac{24u_{L/2}}{L^3}x, \quad 0 \leq x \leq \frac{L}{2} \tag{2.13}$$

in terms of the center displacement $u_{L/2}$. More sophisticated treatments of beam bending, including the incorporation of anticlastic and anisotropic effects, are given in Chapter 3.

2.3.3. Dynamic Mechanical Analysis

DMA is a common method to characterize the complex elastic moduli of materials in the quasi-static regime (i.e. mHz to Hz) [**60, 61**]. Other techniques capable of investigating the frequency-dependence of elastic moduli operate at significantly higher frequencies (e.g. resonant ultrasound ∼kHz [**62**], ultrasound ∼MHz [**63**], and Brillouin scattering ∼GHz [**64**]), making DMAs a mainstay of the polymer [**65**] and domain wall [**60, 61**] communities. Though there are many possible geometries available for DMA experiments, such as compression, shear, tension, and bending, all DMA experiments follow the same basic principles. A DMA operates by applying an oscillatory mechanical stimulus (displacement or force) and measuring a complementary oscillatory mechanical response (force or

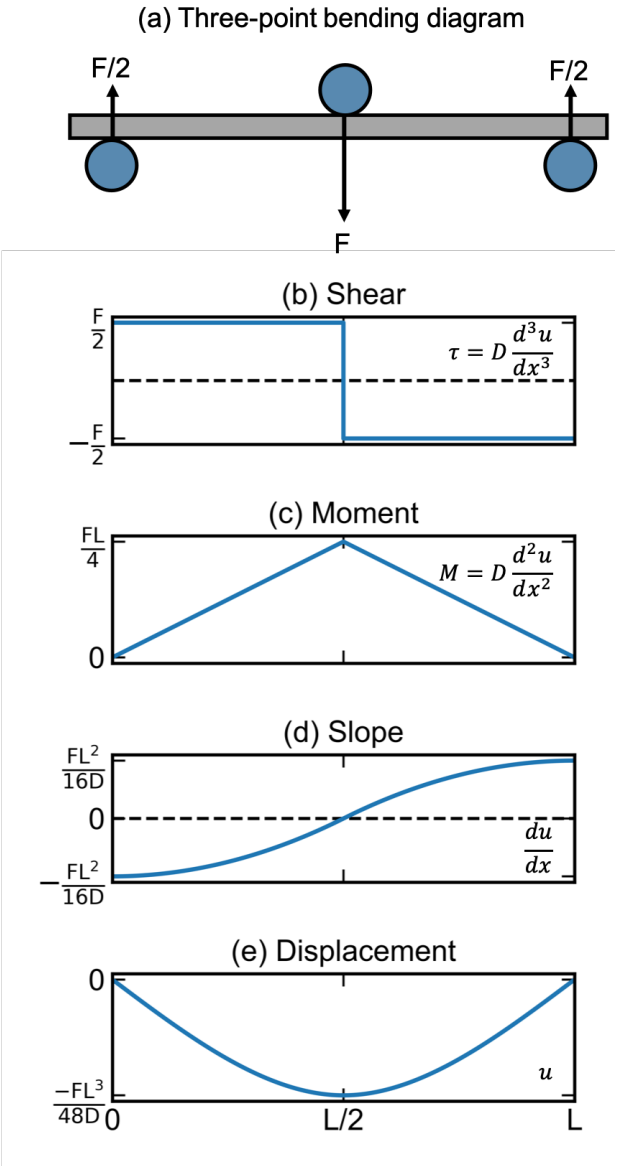

Figure 2.3. (a) Sketch of the concentrated loads present in TPB and the induced (b) shear, (c) moment, (d) strain, and (e) displacement. The relationship between the shear, moment, and strain with displacement is given in each plot. Note, the moment is proportional to the strain gradient.

displacement). The stimulus and response can be expressed as

$$f = f_S + f_D e^{i\omega t} \tag{2.14}$$

and

$$u = u_S + u_D e^{i(\omega t - \delta)} \tag{2.15}$$

where f and u denote the total force and displacement, f_S and u_S refer to static quantities used to maintain contact, f_D and u_D are dynamic quantities used to probe the complex elastic response at an oscillation frequency of ω, and δ is the phase difference between the stimulus and response [**66**].

For a particular test geometry (e.g. TPB) with known sample dimensions, it is possible to determine the complex sample compliance from the applied mechanical stimulus, measured response, and relative phase between the two. For TPB, the spring constant relating the dynamic displacement and force is given by

$$k = \frac{f_D}{u_D} e^{i\delta} = 4Yb \left(\frac{h}{L}\right)^3 \left(1 + \frac{3}{2}\left(\frac{h}{L}\right)^2 \frac{Y}{G}\right)^{-1} \tag{2.16}$$

where Y is the Youngs modulus along the length of the sample, b is the sample width, h is the sample thickness, L is the distance between the TPB supports, and G is the shear modulus [**60**]. In the limit of a thin sample, the G dependence is negligible and Eq. 2.16 can be rearranged as

$$Y = \frac{f_D}{u_D} \frac{L^3}{4bh^3} e^{i\delta}. \tag{2.17}$$

Samples used in my experiments typically have thicknesses h=0.5 mm and the three-point spacing is fixed to be L=8.4 mm, $\left(\frac{h}{L}\right)^2 \approx 4 \times 10^{-2}$, making the approximation used to obtain Eq. 2.17 quite good. For materials with minimal anelasticity, $\delta \approx 0$, Eq. 2.17 can

be combined with Euler-Bernoulli beam theory (Eq. 2.12 and 2.13) to give an expression for strain gradient in terms of measured quantities:

$$\frac{d\epsilon}{dx}(x) = \frac{24u_D}{L^3}x, \quad 0 \leq x \leq \frac{L}{2}. \tag{2.18}$$

2.4. Measuring Induced Polarization

2.4.1. Definition of Polarization

Polarization is an intensive quantity often considered as the solid-state analogue of dipole moment [**67, 68**]. When dealing with a finite set of point charges or a finite system with a continuous charge distribution, the dipole moment is a well-defined quantity. For point charges, the dipole moment $\mathbf{p}$ is a sum of the product of each point charge q_i and their position $\mathbf{r}_i$

$$\mathbf{p} = \sum_i q_i \mathbf{r}_i \tag{2.19}$$

and for continuous charge, it is defined as

$$\mathbf{p} = \int n(\mathbf{r})\mathbf{r}d\mathbf{r} \tag{2.20}$$

where $n(\mathbf{r})$ is the charge density and $\mathbf{r}$ is position [**68**]. Early theoretical descriptions of polarization sought to define it in terms of the dipole moment, namely as the dipole moment per unit volume.

$$\mathbf{P} = \frac{\mathbf{p}}{V} \tag{2.21}$$

However, such a treatment of polarization is undesirably ambiguous and fundamentally flawed [**67, 68, 69, 70, 71**]. As illustrated in Figure 2.4, the polarization in Eq. 2.21 has different values depending on the choice of unit cell [**68**]. This ultimately stems from the periodic nature of a crystalline charge density and is a fundamental limitation of any effort to define polarization as a function of charge density [**67, 68**].

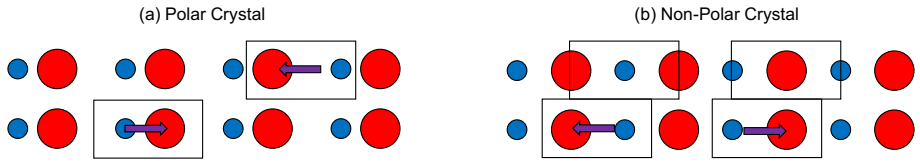

Figure 2.4. Ambiguity in the definition of polarization as the dipole moment per unit volume. (a) A demonstration of how the sign of the polarization can vary depending upon unit cell in a polar crystal. (b) Similar issues exist for non-polar crystals, where certain unit cells lead to a non-zero polarization.

A precise definition of polarization was only established in 1993 when Resta [**70**] and King-Smith and Vanderbilt [**69**] formulated a theory of polarization based upon adiabatic current flows. A quantum mechanical description of polarization obtained via this Berry-phase approach can obfuscate some of the more salient points relevant to these experiments, so this discussion is forgone until Chapter 4 when we consider the first principles theory of flexoelectricity. For the present conversation, the relevant conclusion from the modern theory of polarization is that only *changes* in polarization are well-defined and measurable quantities.

A classic example of how changes in polarization are measured is the Sawyer-Tower circuit [**68**] shown in Figure 2.5. This approach has long been used to characterize ferroelectricity and a similar approach is used here to measure flexoelectricity. As in the ferroelectric case, changes in the polarization of a sample are measured as alternating

current flow through an external circuit driven by the change in surface charge density on metal electrodes deposited on the sample. However, in a flexoelectric experiment, an oscillatory strain gradient is used to induce current flow instead of an electric field in the ferroelectric case.

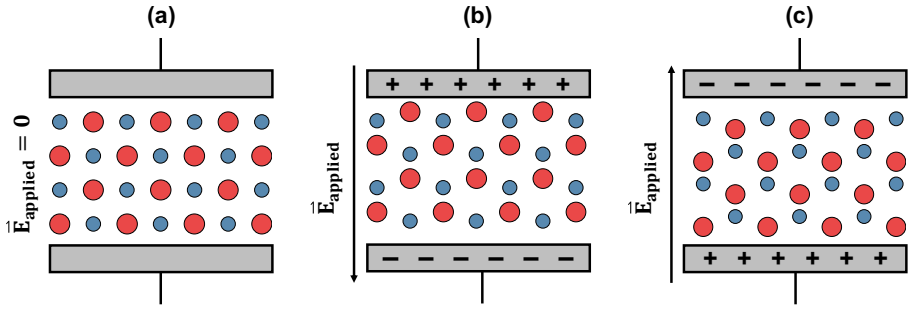

Figure 2.5. Typical ferroelectric polarization-reversal experiment. (a) An unpolarized ferroelectric material consisting of cations (blue) and anions (red) is (b) subjected to an applied electric field inducing a polarization across the sample. Surface charge densities in the metal electrodes (grey boxes) compensate for this polarization. (c) Reversing the direction of the applied electric field switches the direction of polarization and the sign of the surface charge densities on the metal electrodes. By alternating the direction of the applied electric field, the change in the surface charge density (proportional to sample polarization) causes a measurable current to flow through an external circuit.

2.4.2. Lock-In Amplifiers

Since the flexoelectric polarization induced by an oscillatory strain gradient yields an alternating current, LIA provide an accurate and precise way to measure flexoelectricity. A LIA is a device that provides a DC output proportional to an AC signal of interest [**72**]. A simplified circuit diagram for a typical LIA is shown in Figure 2.6. Its operation

relies upon a phase-sensitive detector (PSD) which multiplies a reference signal

$$I_{ref} = A\sin(\omega_A t) \tag{2.22}$$

and a signal of interest

$$I_{sig} = B\sin(\omega_B t + \delta) \tag{2.23}$$

yielding an oscillatory signal given by

$$I_{PSD} = I_{ref} I_{sig} = \frac{AB}{2}\left(\cos([\omega_A - \omega_B]t - \delta) - \cos([\omega_A + \omega_B]t + \delta)\right). \tag{2.24}$$

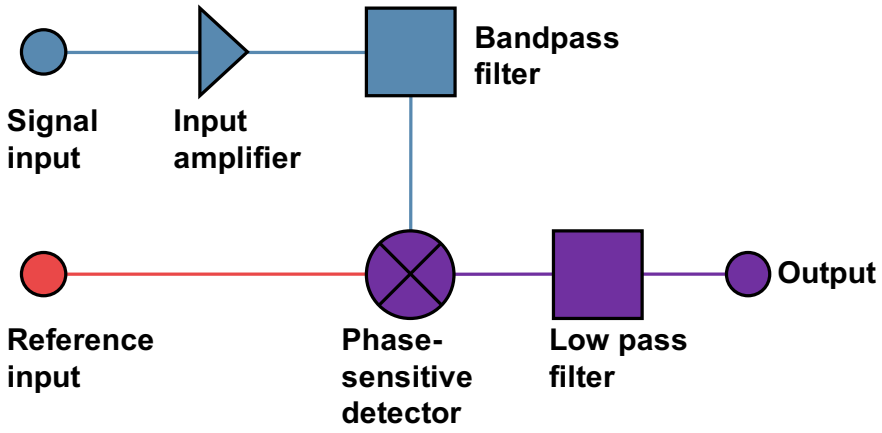

Figure 2.6. Circuit diagram of a basic LIA. An input signal (and any noise) are amplified to an optimal level for the PSD. A bandpass filter excludes most signal outside the desired frequency range. Simultaneously, a stable (and relatively noise-free) signal is provided to a reference channel. The PSD multiplies the signal and reference channels and a filter removes residual noise.

In general, the two input signals have different frequencies (ω_A, ω_B) and amplitudes (A,B), as well as a phase shift (δ). The time average of Eq. 2.24 is zero whenever $\omega_A \neq \omega_B$ and equal to $\frac{AB}{2}\cos(\delta)$ when $\omega_A = \omega_B$. Thus, by measuring I_{ref} and I_{sig} and computing their product, a LIA can isolate the components of an input signal at the same frequency of a reference signal, even if the input signal contains noise or contributions at other frequencies. Figure 2.7 includes an example of this multiplication process.

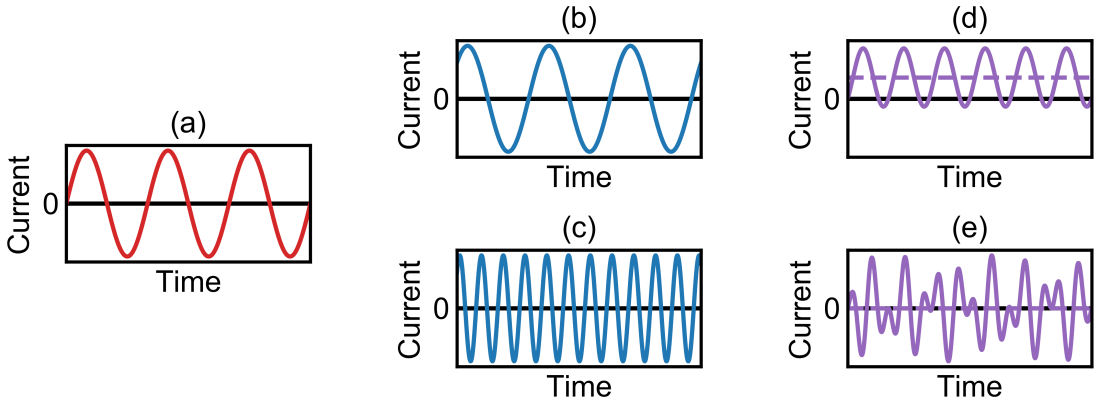

Figure 2.7. Example of LIA operation. When a reference signal (a) is multiplied by an input signal at the same frequency (b), the product is a signal with a non-zero time average (d). When a reference signal (a) is multiplied by an input signal at a different frequency (c), the product is a signal with a zero time average (e). In both (d) and (e) the time average is the dashed line.

2.5. Flexoelectric Coefficients

Having introduced the concepts of strain gradient and polarization, I now return to and motivate the constitutive flexoelectric effect equations, Eq. 2.1 and 2.2, using a phenomenological approach [**10, 11**]. Then, I consider the effects of electrostatic boundary

conditions on the definitions of the flexoelectric coefficient, deriving the relationship between the short-circuit flexoelectric coefficients measured in these experiments and open-circuit flexoelectric coefficients typically obtained from first principles calculations [**58**]. Lastly, I describe how physical measurables in TPB flexoelectric experiments are used to determine the magnitude and sign of the measured flexoelectric coefficient.

2.5.1. Phenomenological Description of Flexoelectricity (1D)

Consider the expansion of a one-dimensional energy density Φ which includes elastic, dielectric, and flexoelectric couplings [**10, 11**]. For simplicity, I ignore piezoelectric contribution to potential energy density, so this treatment formally applies to only centrosymmetric materials.

$$\Phi = \frac{(\varepsilon_0\chi)^{-1}}{2}P^2 + \frac{c}{2}\epsilon^2 - f^{(1)}P\frac{d\epsilon}{dx} - f^{(2)}\epsilon\frac{dP}{dx} - PE - \epsilon\sigma \tag{2.25}$$

where ε_0 is the permittivity of free space, χ is dielectric susceptibility, P is polarization, c is elastic stiffness, ϵ is strain, $f^{(1)}$ and $f^{(2)}$ mediate the gradient couplings, E is electric field, and σ is stress.

Solving the associated Euler-Lagrange equation with respect to polarization

$$\frac{\partial\Phi}{\partial P} = \frac{d}{dx}\left(\frac{\partial\Phi}{\partial\left(\frac{dP}{dx}\right)}\right) \tag{2.26}$$

yields

$$(\varepsilon_0\chi)^{-1}P - f^{(1)}\frac{d\epsilon}{dx} - E = \frac{d}{dx}\left(-f^{(2)}\epsilon\right) \tag{2.27}$$

which can be arranged as

$$P = \varepsilon_0 \chi E + \mu \frac{d\epsilon}{dx} \tag{2.28}$$

for homogeneous materials with $f = f^{(1)} - f^{(2)}$ and $\mu = \varepsilon_0 \chi f$. Thus, the constitutive equation for the direct flexoelectric effect has been derived [**10, 11**].

Similarly, the constitutive equation given in Eq. 2.2 for the converse flexoelectric effect can be obtained by using the Euler-Lagrange equation associated with the energy functional given in Eq. 2.25 with respect to strain. From the Euler-Lagrange equation

$$\frac{\partial \Phi}{\partial \epsilon} = \frac{d}{dx}\left(\frac{\partial \Phi}{\partial \left(\frac{d\epsilon}{dx}\right)}\right) \tag{2.29}$$

we obtain

$$c\epsilon - f^{(2)}\frac{dP}{dx} - \sigma = \frac{d}{dx}\left(-f^{(1)}P\right) \tag{2.30}$$

which can be rearranged as

$$\sigma = c\epsilon + f\frac{dP}{dx} \tag{2.31}$$

with the substitution $f = f^{(1)} - f^{(2)}$ for homogeneous materials.

The phenomenological treatment above shows direct and converse flexoelectric effects are dictated by the same materials parameters: the flexoelectric coefficient μ, and a normalized form of the flexoelectric coefficient $f = \mu\varepsilon_0\chi$ [**10, 11**]. The latter quantity is

called the flexocoupling voltage. It describes the gradient in the average Coulomb potential induced by a strain gradient [**58**] and is commonly used in theoretical formulations of flexoelectricity (Chapter 4 and 5).

2.5.2. The Role of Electrostatic Boundary Conditions

Measurements and calculations of flexoelectric responses can be done under different electrostatic boundary conditions. As described in Section 2.4, it is most common to perform flexoelectric measurements under short-circuit boundary conditions ($E = 0$) [**52**], but measurements under open-circuit boundary conditions ($D = 0$) are also possible. Since open-circuit boundary conditions are also used in the first principles theory of flexoelectricity ([**58**] and Chapter 4), I address the impact of electrostatic boundary conditions on the definition of flexoelectric coefficients here. The flexoelectric coefficients defined in Eq. 2.28 are short-circuit quantities. This can be easily seen by considering Eq. 2.28 in the $E = 0$ limit:

$$P = \mu \frac{d\epsilon}{dx}. \tag{2.32}$$

In order to define open-circuit flexoelectric coefficients, recall that polarization, electric field, and dielectric displacement [**73**] are related via

$$D = \varepsilon_0 E + P. \tag{2.33}$$

Therefore, $D = 0$ implies $P = -\varepsilon_0 E$, which when substituted into Eq. 2.28 yields

$$P = \varepsilon_0 \chi \left(-\frac{P}{\varepsilon_0} \right) + \mu \frac{d\epsilon}{dx}. \tag{2.34}$$

This can be rearranged as

$$P = \frac{\mu}{1+\chi}\frac{d\epsilon}{dx}. \tag{2.35}$$

Thus, the short-circuit and open-circuit flexoelectric coefficients, μ^E and μ^D, respectively, are related by

$$\mu^D = \frac{\mu^E}{1+\chi} \tag{2.36}$$

and both quantities are related to the flexocoupling voltage via

$$f = \frac{\mu^E}{\varepsilon_0 \chi} = \frac{\mu^D(1+\chi)}{\varepsilon_0 \chi}. \tag{2.37}$$

Note, it is also common to express Eq. 2.36 and 2.37 in terms of the dielectric constant κ [**73**] which is related to the dielectric susceptibility χ

$$\kappa = 1 + \chi. \tag{2.38}$$

2.5.3. Magnitude and Sign of Measured Flexoelectric Coefficients

Having defined the nature of the strain gradients in TPB, the polarization measured from such a stimulus, and the flexoelectric coefficients mediating the response, I now explain how the magnitude and sign of the flexoelectric coefficient are determined from the physical measurables in a TPB flexoelectric experiment.

To determine the magnitude of the flexoelectric coefficient, it is necessary to determine the polarization from the measured current and strain gradient from the measured displacement at the sample center. The average polarization across an electrode is given

by

$$\overline{P} = \frac{I}{2A\omega} \tag{2.39}$$

where I is the short-circuit current generated by an oscillatory strain gradient at frequency ω and A is the electrode area [**52**]. The strain gradient that generates this polarization is the average strain gradient across the electrode area. The displacement at the sample center measured from the DMA can be used to calculate the strain gradient profile in the sample according to Eq. 2.18, which can then be averaged over the electrode which has a half length a [**52**]

$$\overline{\frac{d\epsilon}{dx}} = \frac{1}{\frac{L}{2} - \left(\frac{L}{2} - a\right)} \int_{\frac{L}{2}-a}^{\frac{L}{2}} \frac{d\epsilon}{dx}(x)dx = 12u\frac{L-a}{L^3}. \tag{2.40}$$

Therefore, by measuring the short-circuit current as a function of oscillatory displacement, it is possible to obtain the change in polarization (Eq. 2.39) induced by the oscillatory strain gradient (Eq. 2.40), respectively. Then, according to the constitutive equation for the direct flexoelectric effect under short-circuit boundary conditions (Eq. 2.32), the magnitude of the flexoelectric coefficient is the slope of $\overline{P}$ vs $\overline{\frac{d\epsilon}{dx}}$.

Determining the sign of the flexoelectric coefficient is more subtle. Figure 2.8 demonstrates the sign of the flexoelectric coefficient dictates the relative direction between polarization and strain gradient, i.e. if the polarization and strain gradient are parallel or antiparallel. Experimentally, this manifests as opposite configurations of surface charge densities in the metal electrodes, which amount to a phase difference in the output of the LIA. Therefore, the sign of the flexoelectric coefficient can be deduced by comparing the relative phase between the DMA reference signal and flexoelectric current signal for

different samples. For simplicity, if two materials have flexoelectric coefficients equal in magnitude and opposite in sign, the LIA will measure currents with equal magnitude and 180° phase shifts.

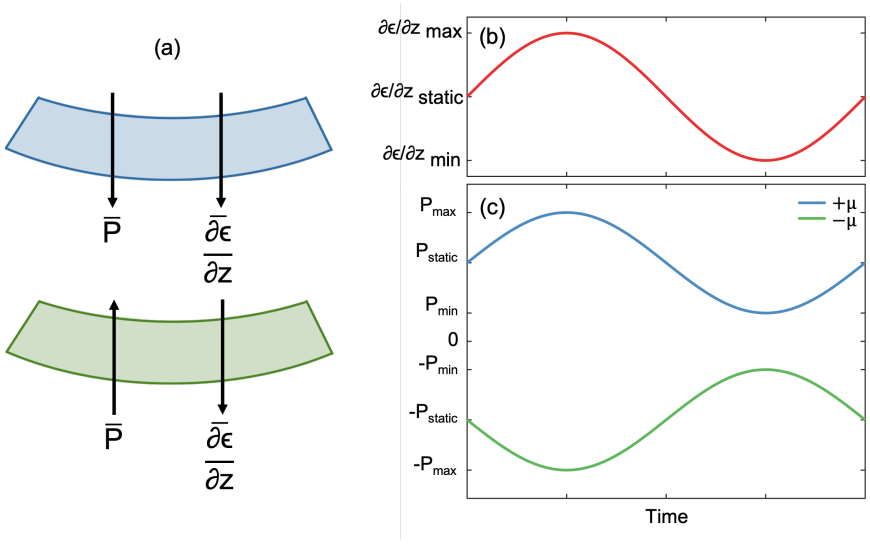

Figure 2.8. (a) Pictorial representation of the relationship between polarization and strain gradient in the bending direction for positive (blue) and negative (green) flexoelectric coefficients. (b) An oscillating strain gradient is applied to a sample. (c) As the strain gradient increases, the magnitude of polarization increases independent of the flexoelectric coefficient sign, so the sign cannot be determined from current magnitude. Instead, the 180° phase difference between the polarization responses of samples with opposite flexoelectric coefficient signs must be used to deduce the sign.

2.6. Benchmarking Apparatus with $SrTiO_3$ Single Crystals

2.6.1. Sample Preparation

Commercially available 0.5 mm thick single crystalline STO substrates with (100) and (110) surfaces were cut into 10 mm × 3 mm samples using a TechCut 5 Precision Sectioning Machine (Allied High Tech Products, Inc.) with a diamond wafering blade. Samples

were cleaned by sonication in acetone and then ethanol. Following a short bake to minimize surface contamination (typically 600°C for 6 hr in air), a Denton DESK III sputter coater was used to deposit 50 nm thick, 8 mm × 2 mm gold electrodes which were masked with aluminum foil. Thicknesses were monitored with Inficon SQM-160 Rate/Thickness Monitor. More precise measurements of the electrode areas were attained using optical microscopy and ImageJ. Following electrode deposition, copper wires were attached to the electrodes with silver paste (SPI Silver Paste Plus). Then the samples were baked at 300°C for 2 hours to improve mechanical stability and electrical conductivity of the electrodes. A multimeter was used to confirm low contact resistance between the copper wires and gold electrodes. Schematics of the samples and electrode configuration are shown in Figure 2.9.

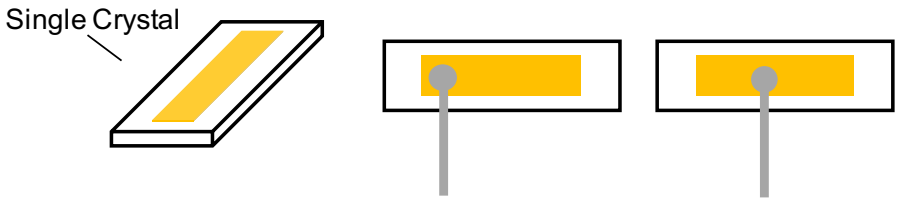

Figure 2.9. Electrode (gold) and wire configuration (grey) typically used for flexoelectric samples.

2.6.2. Experimental Details

Two DMAs were used throughout my dissertation research, the TA Instruments RSA-III and RSA-G2, in conjunction with a custom-machined TPB holder suitable for samples ~10 mm long (Figure 2.10). The spacing between the alumina supports on this holder was 8.41 mm. Both DMAs have an ability to measure elastic properties as a function of

frequency (2×10^{-5}-100 Hz) and temperature (77 K to 900 K) with a displacement resolution of 50 nm, force resolution of 10^{-6} N, maximum force of 35 N, and phase resolution of 0.1°. Temperatures above room temperature are controlled by forced-air convection oven. Typically, static forces ∼1.5 N, dynamic forces ∼0.5 N forces, displacements ∼ 1μm, and frequencies ∼40 Hz were used in the experiments reported here. These correspond to maximum strains ∼ 10^{-5} and oscillatory strain gradients ∼0.1 1/m.

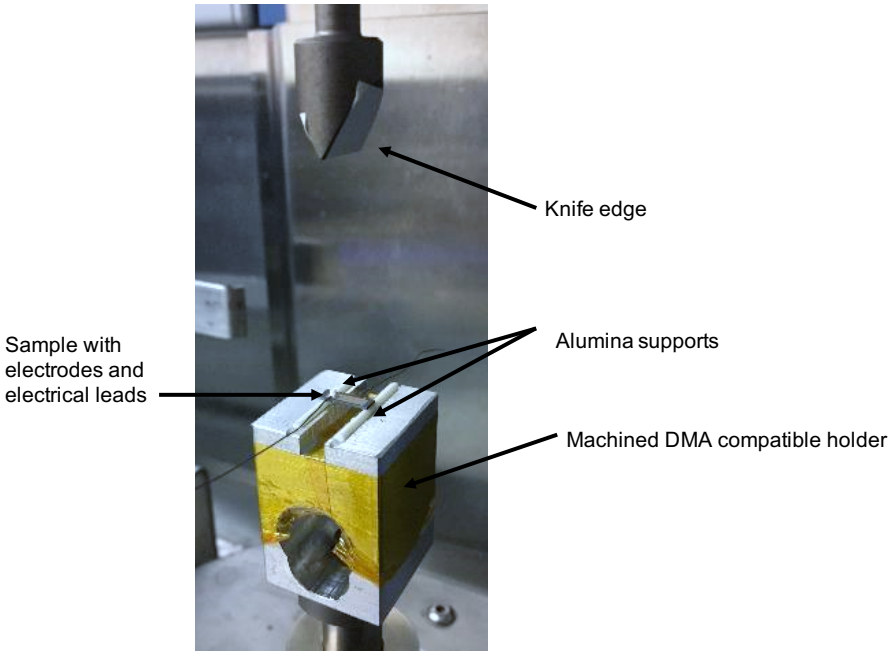

Figure 2.10. Image of a typical experimental set-up for flexoelectric characterization. The sample is supported on alumina rods which sit on a custom-machined DMA compatible holder. A knife edge is used to bend the sample.

After centering a sample on the alumina supports, the DMA knife edge (covered in an insulating tape to avoid short-circuiting) was brought into contact with the sample. In order to benchmark the apparatus, the short-circuit current induced by the flexoelectric

effect was measured for a variety of static force, oscillatory force, and frequency combinations, though typical flexoelectric characterization consists of measuring the short-circuit current as a function of oscillatory force with static force and frequency fixed.

The short-circuit current induced by the flexoelectric effect was measured by a 7265 Dual Phase DSP LIA This LIA has a frequency range of 1 mHz to 250 kHz, voltage sensitivity of 2 nV, and current sensitivity of 2 fA. The reference input for the amplifier is a voltage proportional to the oscillatory force measured by the DMA used to bend the sample and the signal input is the short-circuit current from the sample. Typically, frequencies $\sim$40 Hz were used on samples with electrode areas $\sim$16 mm^2. Assuming a flexoelectric coefficient of 1 nC/m and strain gradients $\sim$0.1 1/m (typical of the DMA), flexoelectric currents should be $\sim$1 pA.

2.6.3. System Validation

A number of predictions based upon the understanding of these measurements outlined in previous sections were tested in order to validate this system. The data shown in Figure 2.12 was acquired on STO single crystals with {100} faces. First, since the oscillatory force is responsible for the oscillatory strain gradient which induces changes in flexoelectric polarization, fixing oscillatory force while varying static force should have no impact on the measured flexoelectric current. This behavior is demonstrated in Figure 2.12(a), where no systematic changes in the measured current are observed as a function of static force. On the contrary, fixing static force and varying oscillatory force magnitude should cause a linear variation in the measured flexoelectric current. Figure 2.12(b) shows there is a linear variation in the measured current with oscillatory force as the theory predicts.

Since the oscillatory force is proportional to strain gradient and the current is proportional to the polarization, the flexoelectric coefficient of this sample is proportional to the slope of this plot. The understanding of flexoelectric characterization discussed above also indicates that at fixed oscillatory and static force, the measured current should linearly scale with frequency or, equivalently, the polarization should be frequency independent. Figure 2.12(c) demonstrates this is the case.

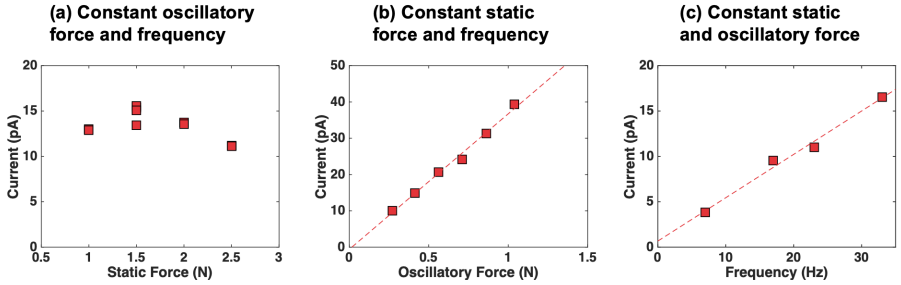

Figure 2.11. Testing of this flexoelectric characterization system using data acquired on a STO single crystal. (a) Flexoelectric current acquired at a constant frequency and oscillatory force shows that the flexoelectric response does not systematically vary with static force. (b) Flexoelectric current acquired at constant frequency and static force shows a linear relationship with oscillatory force. (c) Flexoelectric current acquired at fixed static force and oscillatory force linearly scales with frequency.

2.6.4. Magnitude of Flexoelectric Coefficient

Combining Eq. 2.39 for the average polarization and Eq. 2.40 for the average strain gradient allows conversion of the measured displacement and current to strain gradient and polarization using the known sample geometry. Then, the flexoelectric coefficient is determined from the slope of the polarization vs. strain gradient data. We solely focus on the magnitude and sign of the flexoelectric coefficients measured in this way for the purposes of benchmarking the system. A detailed analysis of the meaning of this

flexoelectric coefficient (e.g. how it relates to point group symmetry, flexoelectric tensor components, etc.) is left for Chapter 3.

Figure 2.12 shows the end results of flexoelectric characterization using the TPB approach explained above for STO single crystals with two different orientations. STO single crystals were used as a benchmark because STO is one of the few materials that has had its flexoelectric response experimentally [**52**] and theoretically [**58, 74**] characterized. In both cases the data are highly linear, and the measured coefficients are in good agreement with literature values which report coefficients ranging from 1 nC/m to 10 nC/m for both orientations of STO [**52**].

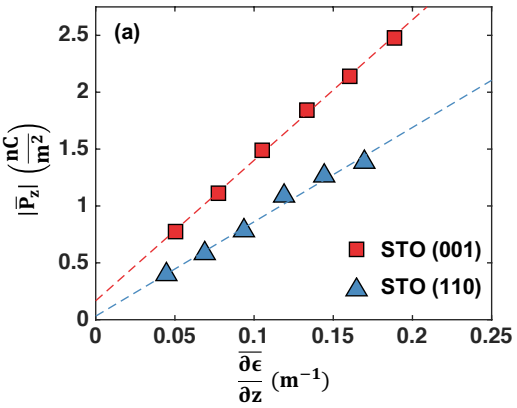

(b)

	STO (001)	STO (110)
μ (nC/m)	12.4 ± 0.6	- 8.3 ± 1.4
f (V)	4.7 ± 0.2	- 3.1 ± 0.5
r^2	0.9984	0.9819
RMSE	0.03	0.05

Figure 2.12. (a) Experimental results for STO single crystals with (001) and (110) surfaces. Dashed lines are linear fits to the data. (b) The STO (001) flexoelectric response is larger than the STO (110) flexoelectric response and the flexoelectric coefficients are of opposite signs. Uncertainties for the linear fits are given by the 95% confidence interval.

2.6.5. Sign Change Between Flexoelectric Response of (100) and (110) $SrTiO_3$ Single Crystals

As explained in Section 2.5, different signs of the flexoelectric coefficient manifest as phase shifts between the DMA reference signal and the flexoelectric current signal, with an anticipated phase shift of 180° between positive and negative flexoelectric coefficients. The example data shown in Figure 2.13 for STO single crystals with (001) and (110) surfaces are in good agreement with this predicted behavior and the sign of the flexoelectric coefficients of STO found in the literature [**52**].

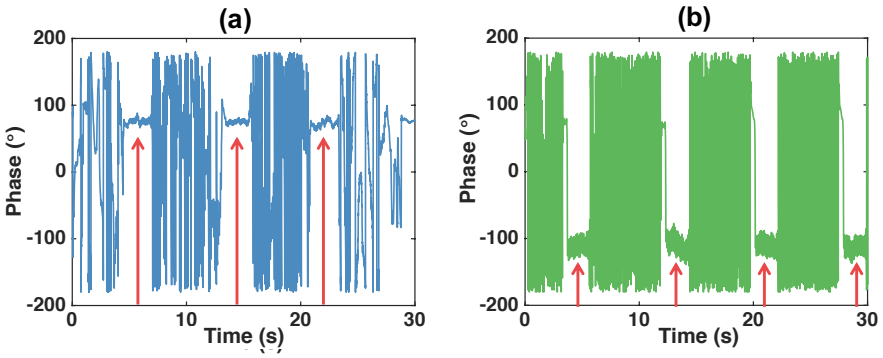

Figure 2.13. Measured phase between flexoelectric current and DMA output for (a) STO (001) and (b) STO (110) under identical conditions shows a 180° relative phase shift between the materials (red arrows indicate locked-in regions). STO samples with these two orientations are known to have different flexoelectric coefficient signs [**52**].

CHAPTER 3

Flexoelectric Characterization of Single Crystals

3.1. Introduction

This chapter expands upon the concepts introduced in Chapter 2 to explain the TPB approach to flexoelectric characterization. While the measurement of flexoelectric polarization as a short-circuit current with LIAs requires no further elaboration beyond what was stated in Chapter 2, quantitative flexoelectric characterization requires a more substantive treatment of the flexoelectric coefficient and TPB strain gradients.

In Section 3.2 I provide a tensorial description of the flexoelectric effect and, through a symmetry-based analysis, determine the non-trivial flexoelectric coefficients for each point group. Next, in Section 3.3 I analyze pure beam bending to develop the machinery to treat new characteristics of three-dimensional bending, including Poisson effects and material anisotropy, which are necessary to quantitatively analyze flexoelectric measurements. I combine these results with the tensorial description in Section 3.2 to develop general expressions for effective flexoelectric coefficients of anisotropic crystals subjected to pure bending. Following this, I use finite element analysis (FEA) simulations in Section 3.4 to modify the pure bending effective flexoelectric coefficients derived in Section 3.3 to account for the differences between pure bending and TPB. The flexoelectric measurements I have performed on single crystals are analyzed in Section 3.5 and the framework developed in Section 3.2- 3.4 is used to interpret the effective flexoelectric coefficients in

terms of elastic constants, flexoelectric tensor components, and geometric factors. The work in Chapter 3 benefitted from discussions with LDM group members, especially Dr. Pratik Koirala, Binghao (Evan) Guo, and Professor Laurence D. Marks. I performed all analyzes, simulations, and measurements, and Binghao (Evan) Guo assisted with some of the flexoelectric sample preparation and TPB measurements included in Seciton 3.5. The measurements on $LaAlO_3$ (LAO) and $DyScO_3$ (DSO) are described in Ref. [**27**] and [**75**], respectively.

3.2. Symmetry Analysis of Flexoelectric Tensor

The direct flexoelectric effect was introduced in Chapter 2 as a scalar equation describing the linear coupling of polarization (P) and strain gradient ($\frac{d\epsilon}{dx}$) [**10, 11**]. Under short-circuit electrostatic boundary conditions it was expressed as

$$P = \mu \frac{d\epsilon}{dx} \tag{3.1}$$

where μ is the flexoelectric coefficient. In three-dimensions, it is necessary to express Eq. 3.1 in terms of tensors. Since the flexoelectric coefficient relates a first-rank tensor response (polarization) with a third-rank tensor stimulus (strain gradient), it is a fourth-rank tensor property [**10, 11, 9, 8**]. Therefore, the three-dimensional analogue to Eq. 3.1 is

$$P_i = \mu_{ijkl} \epsilon_{kl,j}. \tag{3.2}$$

Note, this equation has been written using Einstein notation, where there is an implicit sum over repeated indices. This convention is used throughout the remainder of this dissertation.

3^n components are needed to fully describe an nth rank tensor, suggesting there are 81 flexoelectric coefficients [**9, 8**]. Fortunately, strain and point group symmetry greatly reduces the number of independent flexoelectric coefficients from the nominal value of 81. First, consider the effect of strain. Based upon the strain convention introduced in Chapter 2, the strain gradient tensor is symmetric with respect to the exchange of the first two indices

$$\epsilon_{kl,j} = \epsilon_{lk,j} \tag{3.3}$$

from which it follows that the flexoelectric tensor obeys

$$\mu_{ijkl} = \mu_{ijlk}. \tag{3.4}$$

This reduces the number of independent flexoelectric coefficients from 81 to 54 for all crystal systems, independent of point group symmetry.

The point group symmetry of a crystal acts as an additional constraint on the number of independent tensor components needed to fully describe flexoelectricity. This is a consequence of Neumann's Principle which states "The symmetry elements of any physical property of a crystal must include the symmetry elements of the point group of the crystal" [**9, 8**]. To exemplify Neumann's Principle, consider a matrix representation a_{ij} of a symmetry element contained within a point group. Under the operation of this symmetry

element, the flexoelectric coefficient tensor component μ_{ijkl} will be transformed to μ'_{ijkl} according to the definition of a fourth-rank tensor:

$$\mu'_{ijkl} = a_{im}a_{jn}a_{ko}a_{lp}\mu_{mnop}. \tag{3.5}$$

However, since the symmetry is contained within the point group of the crystal, Neumanns Principle dictates the tensor coefficient must be unchanged under the action of this symmetry operation. Therefore, Eq. 3.5 and

$$\mu'_{ijkl} = \mu_{ijkl} \tag{3.6}$$

must be simultaneously obeyed [**9, 8**].

Applying Eq. 3.5 and 3.6 for all symmetry operations contained within a point group leads to a massive reduction in the number of independent flexoelectric coefficient tensor components in a crystal, depending upon which of the 32 point group symmetries the crystal possesses [**76, 77**]. Figure 3.1 gives the specific non-trivial components for the $m\bar{3}m$, 4/mmm, and mmm point groups relevant to the experimental results reported in Section 3.5. The values I obtain match those reported in Ref. [**76**].

The above analysis holds for crystals oriented along principal crystal axes (x_i) according to the standard crystallographic settings. For the materials experimentally investigated in Section 3.5, the principal crystal axes are as follows [**9**].

- In cubic systems, x_i are along $\langle 100 \rangle$ directions.
- In tetragonal systems with lattice parameters $c \neq a = b$, x_3 is along the fourfold-symmetric c axis and x_1/x_2 are along a/b.

(a) m$\bar{3}$m

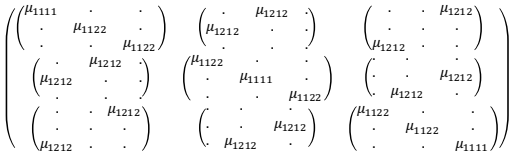

Type	Independent Coefficients
Longitudinal	μ_{1111}
Transverse	μ_{1122}
Shear	μ_{1212}

(b) 4/mmm

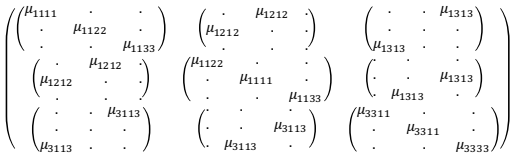

Type	Independent Coefficients
Longitudinal	μ_{1111}, μ_{3333}
Transverse	$\mu_{1122}, \mu_{1133}, \mu_{3311}$
Shear	$\mu_{1212}, \mu_{1313}, \mu_{3113}$

(c) mmm

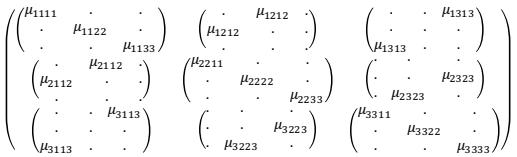

Type	Independent Coefficients
Longitudinal	$\mu_{1111}, \mu_{2222}, \mu_{3333}$
Transverse	$\mu_{1122}, \mu_{2211}, \mu_{1133}, \mu_{3311}, \mu_{2233}, \mu_{3322}$
Shear	$\mu_{1212}, \mu_{2112}, \mu_{1313}, \mu_{3113}, \mu_{2323}, \mu_{3223}$

Figure 3.1. Flexoelectric coefficient tensors for materials with m$\bar{3}$m, 4/mmm, and mmm point group symmetries. Dots indicate elements of the tensor which are zero. The table lists the independent coefficients according to the type of strain gradient-polarization response they mediate.

- In orthorhombic systems with lattice parameters $c < a < b$, x_1 is along c, x_2 is along a, and x_3 is along b.

Since measurement axes (x_i') do not need to coincide with principal crystal axes (x_i), the relationship between measurement and principal crystal axes must be defined to relate measured flexoelectric coefficients to the underlying tensor components [**9, 8**]. To analyze such situations, it is first necessary to identify the direction cosine matrix a_{ij} relating the

measurement and principal crystal axes. The direction cosine matrix is defined by

$$x'_i = a_{ij} x_j. \tag{3.7}$$

Then, the direction cosine matrix must be used to transform the flexoelectric coefficient tensor defined according to the principal crystal axes (μ_{ijkl}) to the flexoelectric coefficient tensor defined according to the measurement axes (μ'_{ijkl}) according to Eq. 3.5.

As an example, consider a sample of a material with point group m$\overline{3}$m oriented along its principal axes. If this sample is subjected to a longitudinal strain gradient ($\epsilon'_{11,1}$) applied along the x'_1=[100] axis, the flexoelectric response measured in the x'_1 direction (P'_1) is mediated by

$$\mu_{1111}^{[100]} = \mu_{1111}. \tag{3.8}$$

However, if this same sample is rotated so that $x'_1 = [110]$, the flexoelectric response P'_1 resulting from $\epsilon'_{11,1}$ is now dictated by

$$\mu_{1111}^{[110]} = \frac{1}{2}\left(\mu_{1111} + \mu_{1122}\right) + \mu_{1212}. \tag{3.9}$$

The relationship between the measurement and principal axes will be used to analyze the bending flexoelectric responses presented in Sections 3.3 and 3.4.

3.3. Pure Bending in Three-Dimensions

To understand the relationship between the flexoelectric coefficient measured in TPB and the underlying flexoelectric tensor components, it is necessary to conduct a three-dimensional analysis of bending strains. Such analysis is necessary to develop even a

qualitative understanding of the measured flexoelectric response because bending along the primary axis induces bending in other directions owing to Poisson effects [**54**]. Consequently, flexoelectric coefficients measured in TPB are linear combinations of tensor components [**52**]. Deriving formulae which relate measured flexoelectric coefficients to the underlying tensor components for samples made of materials with cubic, orthorhombic, and tetragonal symmetry cut in arbitrary directions is the ultimate goal of this section.

Before analyzing flexoelectricity from TPB, we will begin with a simpler bending configuration: pure bending [**54, 55, 56**]. Pure bending occurs when a sample is bent in such a way that there is a constant moment throughout the sample. Although distinct from TPB (which has a linear moment in the sample, see Figure 2.3 in Chapter 2), we will begin our analysis of three-dimensional bending here because pure bending is analytically tractable, captures much of the relevant physics (i.e. how materials symmetry affects which strain gradient components couple to polarization components), and builds intuition for interpreting flexoelectric experiments. While this pure bending analysis may seem oversimplified, the FEA simulations in Section 3.4 will rigorously demonstrate that the approach to interpreting the flexoelectric response to TPB is quite similar to the pure bending framework developed below and only requires minor modifications.

3.3.1. Beams vs. Planes

Unlike the one-dimensional samples considered in Chapter 2, samples in three-dimensions with rectangular cross-sections have three characteristic dimensions, namely, their length (L), width (b), and thickness (h). If b/h is large, it is common to refer to the sample as a plate, and if b/h is small, the sample is considered a beam (e.g. Figure 3.2 and Ref. [**56**]).

However, this distinction is somewhat ambiguous: e.g., what is the difference between a wide beam and a narrow plate?

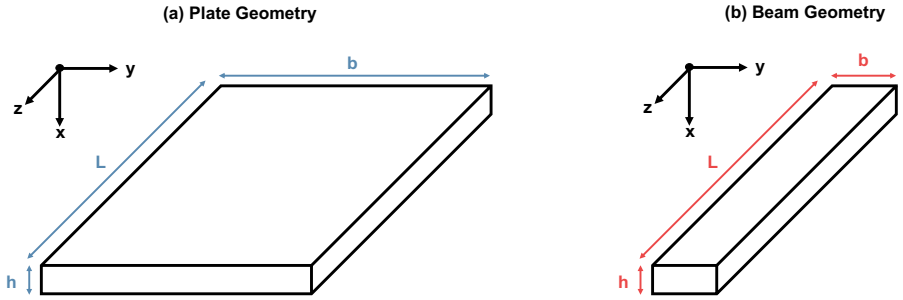

Figure 3.2. Comparison of plate and beam geometries with sample dimensions labeled. This coordinate system will be used throughout the remainder of this chapter.

A more precise definition for plates and beams relates to the extent to which anticlastic bending, i.e., a transverse curvature arising from Poisson effects in response to bending along a primary axis (Figure 3.3), is allowed to occur [**54**]. A sample under pure bending is considered a beam if anticlastic bending occurs unhindered, whereas a sample is considered a plate if anticlastic bending is completely suppressed. A convenient metric which encapsulates the transition from beam-like to plate-like behavior is the Searle parameter [**78**]:

$$\beta = \frac{b^2}{Rh}. \tag{3.10}$$

In Eq. 3.10, b is the sample width, h is the sample thickness, and R is the radius of curvature of the bent sample. When $\beta \gg 1$ samples bend like beams, and when $\beta \ll 1$ samples bend like plates [**78, 79, 80**].

Importantly, the Searle parameter [**78**] indicates that bent samples with nominally plate-like dimensions should be considered beams when the curvature ($\sim 1/R$) is small. The samples studied in the experiments described here typically have b ~3 mm, h ~0.5mm, and R ~1/(0.1 1/m)=10 m. Substituting these values in Eq. 3.10 yields $\beta \sim 10^{-3}$, which is firmly in the beam regime. Even if the samples were 10 mm wide, they would need to be <10 μm thick to be considered plates owing to the small curvatures in my experiments.

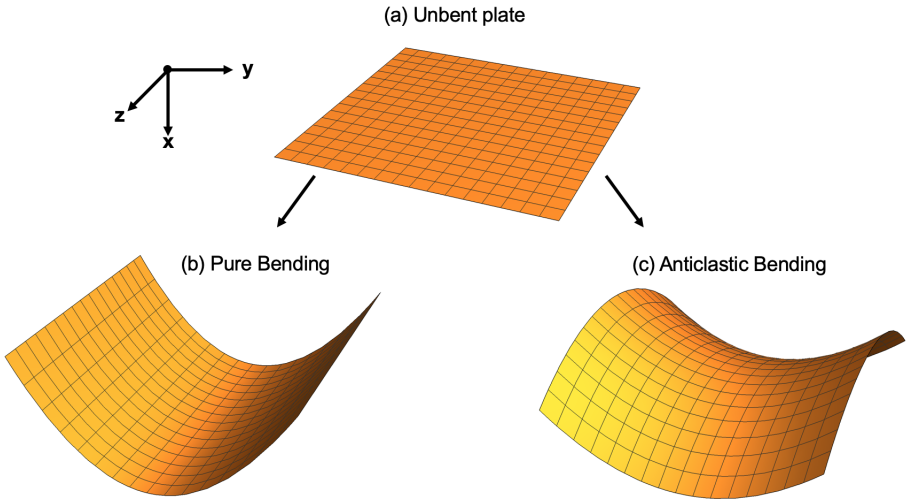

Figure 3.3. (a) A bent plate subjected to (b) pure bending or (c) anticlastic bending.

3.3.2. Pure Beam Bending Strains

As mentioned previously, pure bending occurs when a sample is bent in such a way that there is a constant moment throughout the sample. Since beams are often thin in two directions, it is typical to assume the only non-zero stress component is σ_{33} along the long axis of the beam [**54**]. Defining R to be the radius of curvature of the neutral plane of a beam under pure bending, the strain along the long axis of the beam under pure bending

is

$$\epsilon_{33} = \frac{dx_3' - dx_3}{dx_3} = \frac{(R - x_1)d\theta - Rd\theta}{Rd\theta} = -\frac{x_1}{R} \tag{3.11}$$

as shown in Figure 3.4. Note, in using the classical elastic solutions to the pure beam bending, I implicitly assume that the changes to the mechanical equilibrium conditions owing to the electrostatic body forces induced by flexoelectricity, and other electromechanical couplings, are negligible [**54**].

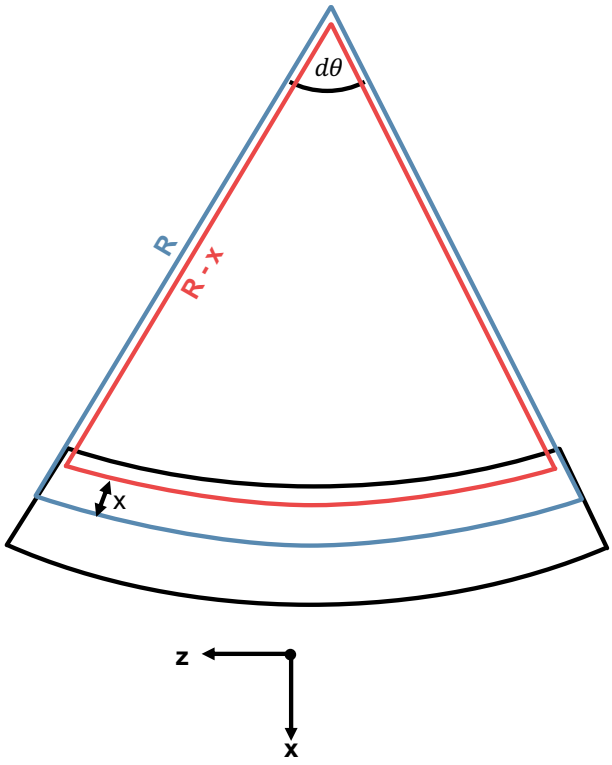

Figure 3.4. Pure bending derivation schematic. R is the radius of curvature of the neutral plane of a beam under pure bending.

Although there is only one non-trivial stress in pure bending, there will be additional strains besides the strain along the long axis of the beam owing to Poisson effects [**54**].

These additional strains cause pure bent beams to take the shape of an anticlastic surface (Figure 3.3). To understand the origin of these additional strains, consider the relationship between stress and strain in a linear elastic material expressed in terms of elastic compliance coefficients s_{ijkl}:

$$\epsilon_{ij} = s_{ijkl}\sigma_{kl}. \tag{3.12}$$

Since σ_{33} is the only non-zero stress, all strain components are given by

$$\epsilon_{ij} = s_{ij33}\sigma_{33} \tag{3.13}$$

or equivalently,

$$\epsilon_{ij} = \frac{s_{ij33}}{s_{3333}}\epsilon_{33} \tag{3.14}$$

since ϵ_{33} is known through Eq. 3.11. Defining the proportionality factor in Eq. 3.14 to be the anisotropic Poisson ratio [**81**]

$$\nu_{ij33} = -\frac{\epsilon_{ij}}{\epsilon_{33}} = -\frac{s_{ij33}}{s_{3333}} \tag{3.15}$$

we can now construct a strain matrix which completely describes pure bending of anisotropic crystals.

$$\epsilon_{ij} = \frac{x_1}{R}\begin{pmatrix} -\nu_{1133} & -\nu_{1233} & -\nu_{1333} \\ -\nu_{1233} & -\nu_{2233} & -\nu_{2333} \\ -\nu_{1333} & -\nu_{2333} & 1 \end{pmatrix}. \tag{3.16}$$

Note, as was shown in Section 3.2, any difference between measurements and principal crystal axes can be accounted for by modifying Eq. 3.15 with a rotation matrix a_{ij} describing the relationship between the measurement and principal crystal axes [**9, 8**]. This amounts to replacing each Poisson ratio in Eq. 3.16 with

$$\nu'_{ij33} = -\frac{s'_{ij33}}{s'_{3333}} = -\frac{a_{im}a_{jn}a_{3o}a_{3p}s_{mnop}}{a_{3m}a_{3n}a_{3o}a_{3p}s_{mnop}}. \tag{3.17}$$

From the strain matrix in Eq. 3.16, it is clear that the strain along the long beam axis is accompanied by other strain components which can be determined from the knowledge of ϵ_{33} and elastic constants. Since the experiments reported in Section 3.5 involve samples with $\mathrm{m\bar{3}m}$, 4/mmm, and mmm point group symmetry oriented along high symmetry axes, the off-diagonal terms are zero in pure beam bending and 3.16 reduces to

$$\epsilon_{ij} = \frac{x_1}{R}\begin{pmatrix} -\nu_{1133} & 0 & 0 \\ 0 & -\nu_{2233} & 0 \\ 0 & 0 & 1 \end{pmatrix}. \tag{3.18}$$

3.3.3. Flexoelectric Polarization of Anisotropic Beams under Pure Bending

The strain expression in Eq. 3.16 indicates that in general there will be a maximum of six unique strain gradients in an anisotropic, homogeneous crystal subjected to pure bending. These are given by

$$\epsilon_{ij,1} = -\nu_{ij33}\epsilon_{33,1} \tag{3.19}$$

Combining these non-trivial strain gradients with the expression for flexoelectric polarization (Eq. 3.2) yields

$$P_k = \mu_{k1ij}\epsilon_{ij,1} = -\mu_{k1ij}\nu_{ij33}\epsilon_{33,1}. \tag{3.20}$$

This equation represents a complete description of the flexoelectric response of an anisotropic, homogeneous crystal subjected to pure bending.

Since P_i in Eq. 3.20 are measurable as short-circuit currents (Section 2.4) and $\epsilon_{33,1}$ is obtained from measured bending displacements and sample geometry (Section 2.3), it is convenient to define an effective flexoelectric coefficient which corresponds to the measured slope that would characterize the flexoelectric response in a pure bending experiment [**52**].

$$P_k = \mu^{eff}_{k133}\epsilon_{33,1}, \quad \mu^{eff}_{k133} = -\mu_{k1ij}\nu_{ij33} \tag{3.21}$$

Eq. 3.21 makes it clear that even under the relatively simple strain gradients present under pure bending, flexoelectric characterization involves measuring linear combinations of tensor coefficients [**52**]. The following procedure should be used to generate the formulae for μ^{eff}_{k133} for a specific sample:

- Determine the relationship between the measurement and principal crystal axes (a_{ij}).
- Compute the anisotropic Poisson ratio components ν'_{ij33} using elastic compliance coefficients s_{ijkl} and a_{ij}.
- Transform the flexoelectric coefficient tensor from μ_{ijkl} to μ'_{ijkl} using a_{ij}.

- Combine (2) and (3) to calculate $\mu'^{eff}_{k133} = -\mu'_{k1ij}\nu'_{ij33}$, the effective coefficient relating P'_k and $\epsilon'_{33,1}$.

3.3.4. Example: Effective Flexoelectric Coefficients of m$\bar{3}$m Beam under Pure Bending

As an example of the procedure outlined above, consider a m$\bar{3}$m beam aligned along its principal axes so that $a_{ij} = \delta_{ij}$, where δ_{ij} is the Kronecker delta. In this case, the strain matrix from Eq. 3.16 reduces to

$$\epsilon_{ij} = \frac{x_1}{R}\begin{pmatrix} -\nu & 0 & 0 \\ 0 & -\nu & 0 \\ 0 & 0 & 1 \end{pmatrix} \tag{3.22}$$

where $\nu = -s_{1122}/s_{1111}$ owing to the m$\bar{3}$m point group symmetry. This strain matrix indicates there are three non-trivial strain gradients which can couple to flexoelectric polarization components: $\epsilon_{11,1}$, $\epsilon_{22,1}$, and $\epsilon_{33,1}$. Written explicitly the three possible polarization components are

$$\begin{aligned} P_1 &= (-\nu\mu_{1111} - \nu\mu_{1122} + \mu_{1133})\epsilon_{33,1} \\ P_2 &= (-\nu\mu_{2111} - \nu\mu_{2122} + \mu_{2133})\epsilon_{33,1} \\ P_3 &= (-\nu\mu_{3111} - \nu\mu_{3122} + \mu_{3133})\epsilon_{33,1} \end{aligned} \tag{3.23}$$

which reduces to

$$P_1 = (-\nu\mu_{1111} - \nu\mu_{1122} + \mu_{1122})\epsilon_{33,1}$$
$$P_2 = P_3 = 0 \tag{3.24}$$

after considering the symmetry of the flexoelectric coefficient tensor for the point group m$\bar{3}$m. Therefore, the effective flexoelectric coefficient measured in the x_1 direction this sample is

$$\mu_{1133}^{eff,(100)} = (1-\nu)\mu_{1122} - \nu\mu_{1111}, \quad \nu = -\frac{s_{1133}}{s_{3333}}. \tag{3.25}$$

If we were to cut additional beams from this same material oriented along other high symmetry directions, we could repeat the procedure described above to find expressions for the effective flexoelectric coefficient in the x_1' measurement direction. The results of this process are included for a m$\bar{3}$m sample with $x_1' = [110]$, $x_2' = [1\bar{1}0]$, and $x_3' = [001]$

$$\mu_{1133}^{eff,(110)} = \frac{s_{1111}+s_{1122}}{s_{1111}+s_{1122}+2s_{1212}}\mu_{1111} + \frac{s_{1111}+3s_{1122}}{s_{1111}+s_{1122}+2s_{1212}}\mu_{1122} - \frac{4s_{1212}}{s_{1111}+s_{1122}+2s_{1212}}\mu_{1212} \tag{3.26}$$

and with $x_1' = [111]$, $x_2' = [1\bar{2}1]$, and $x_3' = [\bar{1}01]$

$$\mu_{1133}^{eff,(111)} = \frac{2(s_{1111}+2s_{1122})}{3(s_{1111}+s_{1122}+2s_{1212})}\mu_{1111} + \frac{4(s_{1111}+2s_{1122})}{3(s_{1111}+s_{1122}+2s_{1212})}\mu_{1122} - \frac{8s_{1212}}{3(s_{1111}+s_{1122}+2s_{1212})}\mu_{1212}. \tag{3.27}$$

It is worth mentioning that Eq. 3.25- 3.27 are not linearly dependent, meaning that pure bending measurements on three samples with different crystallographic orientations cannot be used to solve for the individual flexoelectric tensor components, even in a cubic material [**52**].

3.4. Three-Point Beam Bending in Three-Dimensions

The analysis of pure beam bending in the previous section provided the machinery to treat new characteristics of three-dimensional bending, including Poisson effects and material anisotropy, that were not introduced in Chapter 2 but are necessary to quantitatively analyze flexoelectric measurements. While TPB is not pure bending (samples under TPB have a linear moment (Section 2.3) whereas those under pure bending possess a constant moment), the FEA simulations presented in this section demonstrate that, on average, TPB strain gradients are related to pure bending strain gradients via simple geometric modification. After introducing FEA modelling, we analyze the strain fields calculated with this approach to determine which TPB strain gradients can couple to flexoelectric polarization. Then, modifications for pure bending strain gradient expressions are developed which allow for the representation of TPB as an altered form of pure bending. Lastly, we quantify the accuracy of using the Euler-Bernoulli approximation to determine $\overline{\epsilon}_{33,1}$ from measured displacements.

3.4.1. Finite Element Analysis

FEA is a powerful technique capable of finding numerical solutions to differential equations. Interested readers are directed to textbooks, e.g. Ref. [**82**], for detailed explanations on this technique. In this chapter, FEA was performed using Abaqus to numerically simulate TPB. Unless otherwise stated, the results shown in subsequent sections correspond to a 10 mm $\times$ 3 mm $\times$ 0.5 mm beam resting on rigid supports spaced 8.4 mm apart with a rigid knife edge centered on the beam. TPB was simulated by applying a given displacement (typically $5 - 50$ μm) to the knife edge and the resulting strain

fields were analyzed. Since these simulations were displacement controlled, the strains that developed were independent of the elastic properties of the beam material for the high symmetry orientations considered here. Most commonly, the elastic properties of aluminum ($Y = 70$ GPa, $\nu = 0.3$) were used in the FEA simulations described below, but these were varied to confirm the results were insensitive to the elastic properties.

An example of a TPB simulation is shown in Figure 3.5. Tests were performed to ensure all quantities were adequately converged with respect to mesh density. C3D8R mesh elements with reduced integration were used, and tests performed with C3D8I incompatible, second-order elements yielded no changes within the precision of these calculations. Contact was modelled as hard-contact with surface-to-surface discretization and tangential friction (friction coefficient of 0.15). Mirror symmetries present in TPB were included in the model to minimize the computational cost of the simulations. Therefore, the simulations were only performed on 1/4 of the bent beam. The supports beams were not allowed to rotate or displace, and displacement and rotation of the knife edge in directions other than the main bending direction were prohibited.

3.4.2. Three Point Bending Strains from Finite Element Modelling

The stresses and strains determined from the FEA simulations of TPB described in the previous section are shown in Figure 3.6 and 3.7. Recall that pure bending (Section 3.3) predicted a stress matrix [**54**] with a single non-zero component (σ_{33}), the absence of shear strains except in low symmetry cases, and diagonal strains related according to

$$\epsilon_{11}(x_1) = \epsilon_{22}(x_1) = -\nu\epsilon_{33}(x_1) = -\frac{\nu}{R}x_1. \tag{3.28}$$

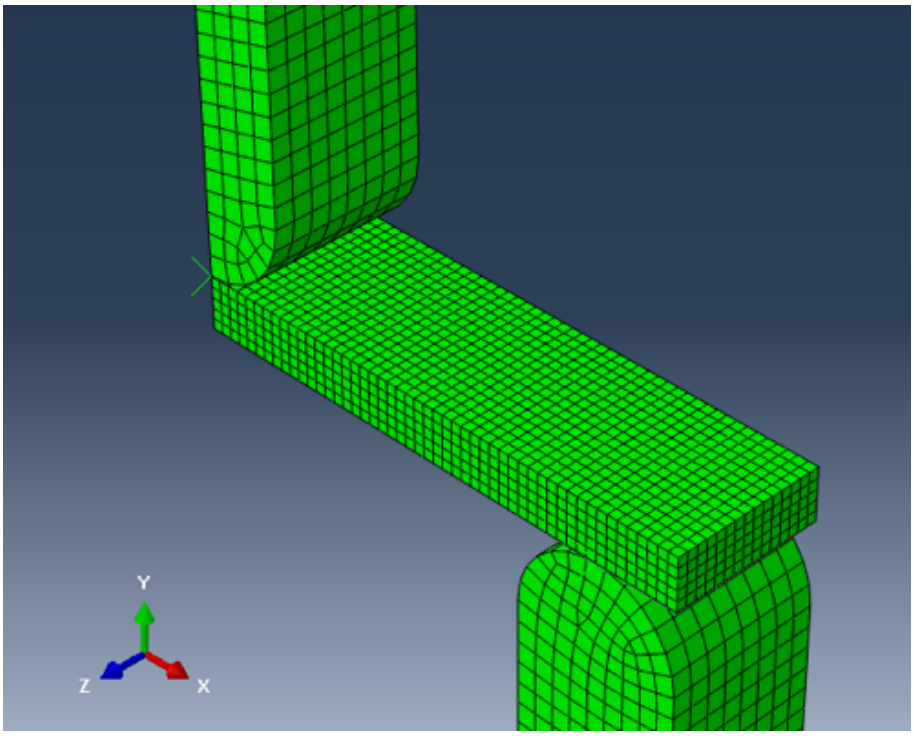

Figure 3.5. Abaqus simulation of TPB showing the sample resting between the rigid support and knife edge. x and z mirror symmetry was used for computational efficiency. For image clarity, this image contains a lower resolution mesh than was used in calculations.

Contrary to these predictions, the FEA simulations indicate the presence of multiple non-zero stress components (Figure 3.6) and shear strains (Figure 3.7) throughout the sample in TPB. Additionally, the diagonal strains deviate from the equalities in Eq. 3.28 and vary with x_2 and x_3.

For flexoelectric measurements, we are interested in the gradients of the strains shown in Figure 3.7. These 18 possible strain gradients will, in general, have complex spatial variations, but only those whose average is non-zero throughout the electrode area are relevant for the polarization measured in a typical flexoelectric experiment (Chapter 2). A convenient method to compute the average of a particular strain gradient component

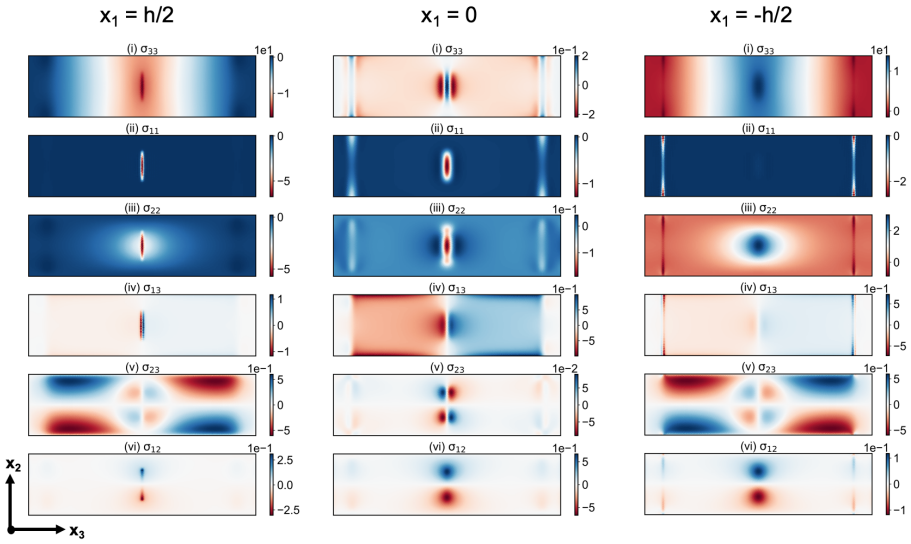

Figure 3.6. Stresses in a beam subjected to TPB according to the axes convention defined in Figure 3.2 calculated with FEA modelling. Each column shows cross-sections of the six stress components at the top, middle, and bottom surfaces, respectively. Note, the color scale varies in each plot.

over the electrode area is via a linear fit to the strain over the electrode area. For example, $\overline{\epsilon}_{33,1}$ can be found by taking the slope of a linear fit to ϵ_{33} as a function of x_1. The results of this process are summarized in Table 3.1.

	x_1	x_2	x_3
ϵ_{11}	-0.319	-0.001	-0.001
ϵ_{22}	-0.249	0.000	0.000
ϵ_{33}	1.000	0.000	0.000
ϵ_{12}	0.000	0.000	0.003
ϵ_{13}	-0.002	-0.006	0.000
ϵ_{23}	0.077	0.000	0.000

Table 3.1. Strain gradient values averaged over the electrode normalized to the average of the principal strain gradient $\epsilon_{33,1}$ over the electrode (i.e. $\overline{\epsilon}_{ij,k}/\overline{\epsilon}_{33,1}$). Columns indicate the direction of the gradient for the strains in each row. Values correspond to a finite element simulation of a 10 mm $\times$ 3 mm $\times$ 0.5 mm beam sitting on supports with a separation of 8.4 mm displaced by 5 μm at the beam center.

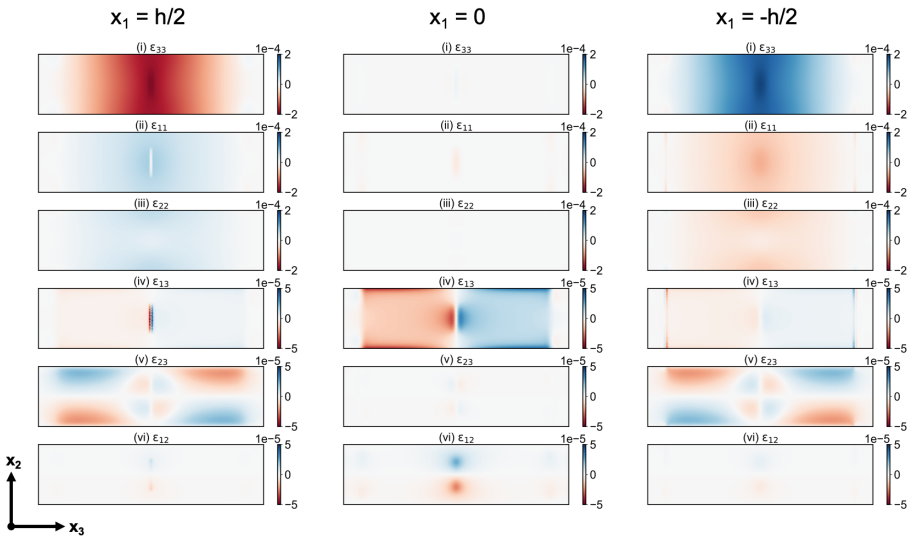

Figure 3.7. Strains in a beam subjected to TPB according to the axes convention defined in Figure 3.2 calculated with FEA modelling. Each column shows cross-sections of the six strain components at the top, middle, and bottom surfaces, respectively. Note, the color scale of the shear strains differs from the normal strains.

It is clear from Table 3.1 that only $\bar{\epsilon}_{11,1}$, $\bar{\epsilon}_{22,1}$ and $\bar{\epsilon}_{33,1}$ make substantial contributions to a measured flexoelectric response, even without considering materials symmetry. This reduces the general expression for flexoelectric polarization in Eq. 3.2 to

$$\begin{aligned} \overline{P}_1 &= \mu_{1111}\bar{\epsilon}_{11,1} + \mu_{1122}\bar{\epsilon}_{22,1} + \mu_{1133}\bar{\epsilon}_{33,1} \\ \overline{P}_2 &= \mu_{2111}\bar{\epsilon}_{11,1} + \mu_{2122}\bar{\epsilon}_{22,1} + \mu_{2133}\bar{\epsilon}_{33,1} \\ \overline{P}_3 &= \mu_{3111}\bar{\epsilon}_{11,1} + \mu_{3122}\bar{\epsilon}_{22,1} + \mu_{3133}\bar{\epsilon}_{33,1}. \end{aligned} \tag{3.29}$$

Since the materials measured in Section 3.5 have m$\bar{3}$m, 4/mmm, and mmm point group symmetries, the flexoelectric coefficients in the expressions for P_2 and P_3 are all zero. For the rest of this chapter, we will limit our analysis to the strain gradients $\bar{\epsilon}_{11,1}$, $\bar{\epsilon}_{22,1}$ and $\bar{\epsilon}_{33,1}$. Note, besides the shear strain gradients being much smaller than the longitudinal

and transverse strain gradients in Table 3.1, first principles calculations also indicate shear flexoelectric coefficients for oxides are an order of magnitude smaller than longitudinal and transverse flexoelectric coefficients (Chapter 4). This further supports neglecting shear strain gradient contributions to the flexoelectric measurements reported in Section 3.5.

3.4.3. Deviations from Pure Bending

At the start of this chapter we were careful to differentiate between TPB and pure bending because the two forms of bending appeared to be rather different. However, within the context of flexoelectric characterization, the analysis of TPB presented above suggests TPB has much in common with pure bending. Not only have we demonstrated that only the $\overline{\epsilon}_{11,1}$, $\overline{\epsilon}_{22,1}$ and $\overline{\epsilon}_{33,1}$ strain gradients can couple to flexoelectric polarization (these are the same strain gradients found in Section 3.3 to exist in pure bending), but Table 3.1 indicates $\overline{\epsilon}_{11,1}/\overline{\epsilon}_{33,1}$ and $\overline{\epsilon}_{22,1}/\overline{\epsilon}_{33,1}$ are close to the pure bending value of $-\nu$. The deviation from the pure bending value of these ratios is a consequence of the well-known phenomenon of anticlastic suppression [**56, 78, 83, 84, 79, 80**]: anticlastic bending does not occur freely in TPB, tending to be suppressed particularly near the supports and knife edge (see stresses in Figure 3.6). This means that even though the Searle parameter [**78**] would predict the samples used here to be firmly in the beam-bending regime ($\beta \sim 10^{-3}$), beam samples in TPB have some plate-like tendencies [**83, 84, 79, 80**].

In the fully clamped limit of TPB (i.e. where anticlastic bending has been completely suppressed), the sample will act like a plate subjected to pure bending [**54, 83, 84, 79,**

80]. The strains of a clamped plate under pure bending [**54**] are

$$\begin{aligned} \epsilon_{22} &= 0 \\ \epsilon_{33} &= -\frac{x_1}{R} \\ \epsilon_{11} &= -\frac{\nu}{1-\nu}\epsilon_{33} \end{aligned} \tag{3.30}$$

which have the following relationship between strain gradient components:

$$\begin{aligned} \epsilon_{11,1} &= -\frac{\nu}{1-\nu}\epsilon_{33,1} \\ \epsilon_{22,1} &= 0. \end{aligned} \tag{3.31}$$

These expressions represent an upper bound for the relationship between the average strain gradients in TPB, i.e. one in which anticlastic bending has been completely suppressed. On the other hand, the pure beam bending strains [**54**] reproduced below

$$\begin{aligned} \epsilon_{11,1} &= -\nu\epsilon_{33,1} \\ \epsilon_{22,1} &= -\nu\epsilon_{33,1} \end{aligned} \tag{3.32}$$

are lower bounds for the relationship between the average strain gradients in TPB, i.e. the limit in which anticlastic bending occurs completely unhindered. The real strain gradients for a given sample will be somewhere between these two limits.

The above discussion motivates introducing a parameter ϕ which is equal to 0 in the beam bending limit and 1 in the plate bending limit [**83, 84**]. The strain gradient

relationships in Eq. 3.31 and 3.32 can then be expressed in terms of ϕ as

$$\begin{aligned} -\frac{\overline{\epsilon}_{11,1}}{\overline{\epsilon}_{33,1}} &= \nu\left(1-\frac{\nu}{\nu-1}\phi\right) \\ -\frac{\overline{\epsilon}_{22,1}}{\overline{\epsilon}_{33,1}} &= \nu\left(1-\phi\right) \end{aligned}. \tag{3.33}$$

Ashwell [**83**] and Pomeroy [**84**] have shown that in the case of pure bending, the dimensionless parameter ϕ has the functional form

$$\phi(x) = 1 - \frac{2}{x}\left(\frac{\cosh(x)-\cos(x)}{\sinh(x)+\sin(x)}\right). \tag{3.34}$$

$x = \left(3(1-\nu^2)\right)^{1/4}\sqrt{\beta}$ where $\beta = \frac{w^2}{Rb}$ is the Searle parameter [**78**]. For TPB $1/R$ is approximately the average of the Euler-Bernoulli strain gradient (Section 3.5), so the average of β over the entire sample is given by

$$\overline{\beta} = \frac{12w^2u}{bL^2}. \tag{3.35}$$

Rearranging Eq. 3.33 allows for the expression of the ratio of the strain gradients in terms of the dimensionless parameter ϕ which is purely a function of sample geometry and ν.

$$\begin{aligned} 1-\phi(x) &= -\frac{1}{\nu}\frac{\overline{\epsilon}_{22,1}}{\overline{\epsilon}_{33,1}} \\ \phi(x) &= \frac{\nu-1}{\nu^2}\left(\frac{\overline{\epsilon}_{11,1}}{\overline{\epsilon}_{33,1}}+\nu\right) \end{aligned} \tag{3.36}$$

Therefore, bending an arbitrary sample should yield a point on the universal curves defined by Eq. 3.36, where ϕ is solely defined by ν, sample dimensions, support spacing, and displacement at the beam center through Eq. 3.35.

After performing a series of FEA simulations in which the sample dimensions, elastic properties, support spacing, and displacement at the beam center were varied, we found the beam-to-plate transition in for TPB is poorly described when the pure bending solution $x = (3(1-\nu^2))^{1/4}\sqrt{\overline{\beta}}$ is used in Eq. 3.34-3.36. This is demonstrated in Figure 3.8(a) where Eq. 3.36 is plotted for the different FEA simulations. There is clearly a missing dependency in Eq. 3.34-3.36 because neither $-\frac{1}{\nu}\frac{\overline{\epsilon}_{22,1}}{\overline{\epsilon}_{33,1}}$ nor $\frac{\nu-1}{\nu^2}\left(\frac{\overline{\epsilon}_{11,1}}{\overline{\epsilon}_{33,1}}+\nu\right)$ fall on universal curves given by 1-ϕ and ϕ.

Empirically we have found that if the Searle parameter [**78**] in Eq. 3.35 is replaced by a modified Searle parameter $\overline{\beta}^*$ defined as

$$\overline{\beta}^* = \frac{2b}{u}\overline{\beta} = \frac{24w^2}{L^2}. \tag{3.37}$$

Eq. 3.37 accurately captures the beam-to-plate transition for TPB. Figure 3.8(b) demonstrates the quantitative agreement between $-\frac{1}{\nu}\frac{\overline{\epsilon}_{22,1}}{\overline{\epsilon}_{33,1}}$ and $\frac{\nu-1}{\nu^2}\left(\frac{\overline{\epsilon}_{11,1}}{\overline{\epsilon}_{33,1}}+\nu\right)$ with 1-ϕ and ϕ, respectively, for all combinations of sample dimensions, elastic properties, support spacing, and beam displacements investigated with FEA simulations and zero fit parameters. For small $\overline{\beta}^*$, the strain gradients approach the beam bending limit with $\overline{\epsilon}_{22,1}/\overline{\epsilon}_{33,1} = \overline{\epsilon}_{11,1}/\overline{\epsilon}_{33,1} = -\nu$. For large $\overline{\beta}^*$, the strain gradients approach the plate bending limit with $\overline{\epsilon}_{22,1}/\overline{\epsilon}_{33,1} = 0$ and $\overline{\epsilon}_{11,1}/\overline{\epsilon}_{33,1} = -\frac{\nu}{1-\nu}$.Ultimately, these results indicate that the extent of anticlastic bending can be determined solely from geometric factors and elastic constants through Eq. 3.34 with $x^* = (3(1-\nu^2))^{1/4}\sqrt{\overline{\beta}^*}$.

For convenience we have included the value of the anticlastic correction factors for a 10×3×0.5 mm beam sitting on supports 8.4 mm apart displaced 5 μm at its center in Table 3.2 as these conditions are close to the conditions typically used in the experiments

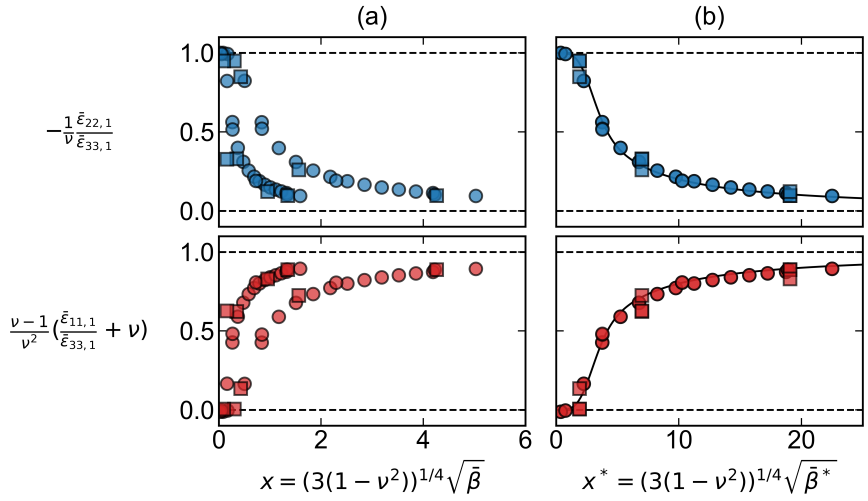

Figure 3.8. Beam to plate transition using (a) the Searle parameter and (b) the modified Searle parameter $\overline{\beta}^* = \frac{2b}{u}\overline{\beta}$. Each data point corresponds to a different combination of sample dimensions, elastic properties, support spacing, and beam displacements, with circles and squares indicating simulations using the elastic properties of Al and STO, respectively. The entire data set collapses onto a single curve given by $\phi(x^*)$ (black line) when $\overline{\beta}^*$ is used.

reported in Section 3.5. The correction factors k_1 and k_2 are defined as

$$\begin{aligned} \left.\frac{\overline{\epsilon}_{11,1}}{\overline{\epsilon}_{33,1}}\right|_{TPB,FEA} &= -k_1\nu \left.\frac{\overline{\epsilon}_{11,1}}{\overline{\epsilon}_{33,1}}\right|_{PureBeamBending} \\ \left.\frac{\overline{\epsilon}_{22,1}}{\overline{\epsilon}_{33,1}}\right|_{TPB,FEA} &= -k_2\nu \left.\frac{\overline{\epsilon}_{22,1}}{\overline{\epsilon}_{33,1}}\right|_{PureBeamBending} \end{aligned} \tag{3.38}$$

In summary, the above analysis indicates the effective flexoelectric coefficients measured in TPB are not purely functions of the flexoelectric tensor components and elastic constants, but also include anticlastic correction factors. Reintroducing the anisotropic

Strain Gradient	FEA (1/m)	Pure Beam Bending (1/m)	Correction Factor
$\epsilon_{33,1}$	-0.43	-0.43	1.00
$\epsilon_{11,1}$	0.14	0.13	1.08
$\epsilon_{22,1}$	0.11	0.13	0.85

Table 3.2. Average strain gradients calculated for 10×3×0.5 mm beam displaced 5 μm at its center from FEA simulations compared to the average strain gradients predicted from pure beam bending (assuming the same $\epsilon_{33,1}$ value). The values reported here correspond to the dimensions and strain gradients used in experiments reported in Section 3.5.

Poisson ratios into Eq. 3.33 yields

$$-\frac{\overline{\epsilon}_{11,1}}{\overline{\epsilon}_{33,1}} = \nu_{1133}\left(1 - \frac{\nu_{1133}}{\nu_{1133}-1}\phi\right) \qquad -\frac{\overline{\epsilon}_{22,1}}{\overline{\epsilon}_{33,1}} = \nu_{2233}\left(1-\phi\right) \tag{3.39}$$

which can be used to rewrite Eq. 3.29, yielding general expressions for the flexoelectric polarization components measured in TPB:

$$\begin{aligned}
\overline{P}_1 &= \left(-\nu_{1133}\mu_{1111} - \nu_{2233}\mu_{1122} + \mu_{1133} + \phi\left(\frac{\nu_{1133}^2}{\nu_{1133}-1}\mu_{1111} + \nu_{2233}\mu_{1122}\right)\right)\overline{\epsilon}_{33,1} \\
\overline{P}_2 &= \left(-\nu_{1133}\mu_{2111} - \nu_{2233}\mu_{2122} + \mu_{2133} + \phi\left(\frac{\nu_{1133}^2}{\nu_{1133}-1}\mu_{2111} + \nu_{2233}\mu_{2122}\right)\right)\overline{\epsilon}_{33,1} \\
\overline{P}_3 &= \left(-\nu_{1133}\mu_{3111} - \nu_{2233}\mu_{3122} + \mu_{3133} + \phi\left(\frac{\nu_{1133}^2}{\nu_{1133}-1}\mu_{3111} + \nu_{2233}\mu_{3122}\right)\right)\overline{\epsilon}_{33,1}.
\end{aligned} \tag{3.40}$$

The remaining step to complete the analysis of the flexoelectric response of a sample to TPB is to determine the average strain gradient $\overline{\epsilon}_{33,1}$ from measurable quantities. For this we return to Euler-Bernoulli beam bending theory.

3.4.4. Application of Euler Bernoulli Beam Bending Solutions

In Chapter 2, it was shown that bending a one-dimensional beam in a TPB geometry yielded a displacement profile of

$$u(x) = -\frac{F}{48D}\left(4x^3 - 3L^2x\right), \quad 0 \leq x \leq \frac{L}{2}. \tag{3.41}$$

Extending this Euler-Bernoulli beam theory solution [**54, 56, 55**] to three-dimensions using the axes convention defined in Figure 3.2 gives

$$u_1(x_3) = -\frac{F}{48D}\left(4x_3^3 - 3L^2x_3\right), \quad 0 \leq x_3 \leq \frac{L}{2}. \tag{3.42}$$

There is an *unsymmetrized* strain gradient associated with this displacement

$$\eta_{1,33} = \frac{\partial^2 u_1}{\partial x_3^2} = -\frac{F}{2D}x_3, \quad 0 \leq x_3 \leq \frac{L}{2} \tag{3.43}$$

which is related to the symmetric strain gradients [**59**] we have been working with via

$$\eta_{1,33} = 2\epsilon_{13,3} - \epsilon_{33,1}. \tag{3.44}$$

When the shear strain gradient $\epsilon_{13,3}$ is negligible (see Table 3.1), Eq. 3.44 reduces to

$$\epsilon_{33,1} = \frac{F}{2D}x_3, \quad 0 \leq x_3 \leq \frac{L}{2}. \tag{3.45}$$

Therefore, if Euler-Bernoulli beam theory is obeyed in three-dimensional samples and the shear strain gradient $\epsilon_{13,3}$ is small, then Eq. 3.45 provides a means to determine $\epsilon_{33,1}$ using measurable quantities available from TPB.

To assess the quality of using Euler-Bernoulli beam theory on three-dimensional beams, we perform FEA modelling of TPB, matching the sample dimensions and geometry used in experiments. Figure 3.9 shows $\overline{u}_1(x_3)$, u_1 computed from FEA and averaged over the width and thickness, as a function of x_3. We find $\overline{u}_1 \sim x_3^3$ as Euler-Bernoulli beam theory predicts, as well as good quantitative agreement between the polynomial coefficients calculated from FEA and predicted by the analytic theory.

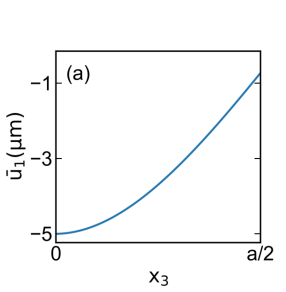

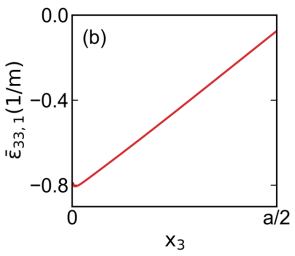

(c)

$u_1(x_3) = A\,x^3 + B\,x^2 + C\,x + D$

	Euler-Bernoulli	Finite Element
A	-3.37e-5 mm^{-2}	-3.35e-05 mm^{-2}
B	8.50e-4 mm^{-1}	8.42e-4 mm^{-1}
C	-5.4e-3	-5.30e-3
D	5.00e-3 mm	4.87e-3 mm

$\epsilon_{33,1}(x_3) = A\,x + B$

	Euler-Bernoulli	Finite Element
A	2.02e-4 mm^{-2}	1.98e-4 mm^{-2}
B	-1.70e-3 mm^{-1}	-1.66e-3 mm^{-1}

Figure 3.9. Comparison between displacements and strain gradients computed with FEA simulations and predicted by analytic Euler-Bernoulli beam-bending theory. As predicted by Euler-Bernoulli theory, (a) the average displacement $\overline{u}_1$ is found to scale with the cube of x_3 and (b) the average strain gradient $\overline{\epsilon}_{33,1}$ is found to scale linearly with x_3. (c) In both cases there is quantitative agreement between the polynomial coefficients.

This quantitative agreement between the TPB displacements and Euler-Bernoulli theory is an indication that it is proper to use Euler-Bernoulli to describe the experimental TPB strain gradients. However, to directly confirm this we compute $\overline{\epsilon}_{33,1}$, which is $\epsilon_{33,1}$ calculated from finite element analysis and averaged over the width and thickness, and compare this value to Euler-Bernoulli theory. Figure 3.9(b) shows that as with $\overline{u}_1$, $\overline{\epsilon}_{33,1}$ obeys the proper Euler-Bernoulli scaling, although there are some small deviations at the point of contact between the knife edge and sample. Figure 3.9(c) also demonstrates

the quantitative agreement between $\overline{\epsilon}_{33,1}$ calculated from FEA and predicted by Euler-Bernoulli theory. Ultimately, it is necessary to average the strain gradient in Figure 3.9(b) over the electrode area to connect with experiments [**52**]. This yields $\overline{\epsilon}_{33,1}$=0.43 1/m from FEA, which is within 5% of the Euler-Bernoulli average value of 0.45 1/m. The agreement between the average behavior of the u_1 and $\epsilon_{33,1}$ computed from FEA and the analytic predictions based upon 1D Euler-Bernoulli theory support our use of 1D Euler-Bernoulli values to calculate $\overline{\epsilon}_{33,1}$ in experiments.

3.5. Experimental Measurements for Single Crystals

The analyses above provide the framework to write formulae for the effective flexoelectric coefficient of an arbitrary crystal with a known geometry, crystallographic orientation, and point group measured in TPB. In general, these expressions will be linear combinations of flexoelectric tensor components, elastic constants, and anticlastic factors. In each of the measurements reported in the following subsections, the effective flexoelectric coefficient corresponds to the slope of the x_1 component of polarization and the average strain gradient $\overline{\epsilon}_{33,1}$ determined from the Euler-Bernoulli approximation.

$$\overline{P}_1 = \mu_{1133}^{eff} \overline{\epsilon}_{33,1} \tag{3.46}$$

The sign of the effective flexoelectric coefficient is determined according to the phase difference method described in Chapter 2. After introducing each material and presenting the flexoelectric measurements, the exact form of μ_{1133}^{eff} will be given and discussed. Note, the measurements reported in this section are limited to those performed on high quality single crystals and materials are grouped in subsections according to their point group

symmetry. The role of defects in flexoelectricity is considered in Chapters 5 and 6. In all the samples reported below, b = 3 mm, L = 8.41 mm, h = 0.5 mm, a = 4 mm, and $\nu \approx 0.24$, so $\phi \approx 0.1$ indicating there are non-negligible effects from anticlastic bending.

3.5.1. Cubic Perovskites $SrTiO_3$ and $KTaO_3$

STO and $KTaO_3$ (KTO) have the archetypal ABO_3 cubic perovskite structure with space group $Pm\overline{3}m$ at room temperature and atmospheric pressure [**85, 86**]. This structure consists of a network of corner-sharing BO_6 octahedra with the A-site cation positioned in the middle of each 8 octahedra [**87**]. Both STO and KTO are wide bandgap insulators [**88, 89**] with high dielectric constants (310 and 242 for STO [**90**] and KTO [**91**], respectively) which have been the focus of extensive research in bulk and thin-film form. More recently, they have been of interest owing to their incipient ferroelectric [**92**] and superconducting properties [**93, 94, 95**]. In the context of flexoelectricity, STO is significant because it is one the few materials that has had its flexoelectric response experimentally [**52**] and theoretically characterized [**58, 74**]. Therefore, it represents an important benchmark material for the flexoelectric effect.

Figure 3.10 shows the flexoelectric characterization of single crystals of STO and KTO. In both cases, a highly linear polarization is induced from the applied strain gradient and flexoelectric coefficients are found to range between ∼1-10 nC/m. The measured values for STO are in good agreement with the literature values [**52**] and these are the first flexoelectric coefficient measurements in KTO. As established in this chapter, the effective flexoelectric coefficient measured in TPB can be related to the underlying tensor coefficients if the sample geometry, orientation, and elastic constants are known. Since

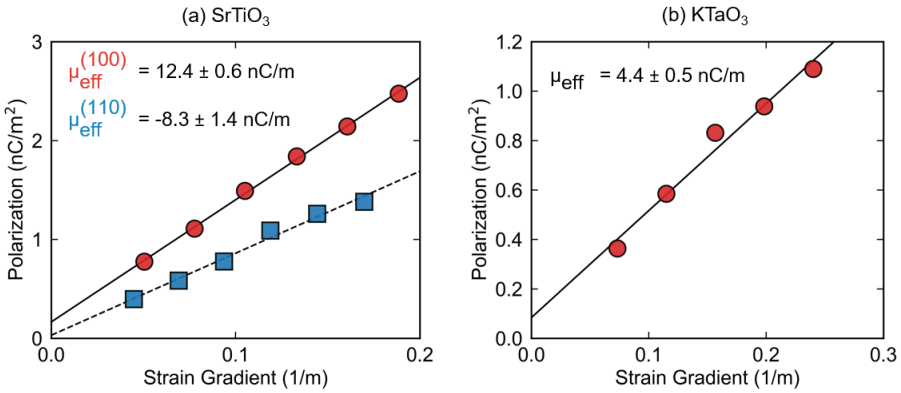

Figure 3.10. Flexoelectric characterization of (a) STO and (b) KTO single crystals. The flexoelectric response is highly linear ($r^2 > 0.98$ with root mean square error (RMSE) < 0.05) and magnitude of the flexoelectric coefficients ranges between ∼1-10 nC/m.

both materials have m$\bar{3}$m point group symmetry, the KTO and STO samples with {100} faces have the same expression for the effective flexoelectric coefficient:

$$\mu_{eff}^{(100)} = \frac{s_{1122}}{s_{1111}}\mu_{1111} + \frac{s_{1111}+s_{1122}}{s_{1111}}\mu_{1122} - \phi\frac{s_{1122}}{s_{1111}}\left(\frac{s_{1122}}{s_{1111}+s_{1122}}\mu_{1111} + \mu_{1122}\right) \tag{3.47}$$

The STO sample with the (110) surface was oriented such that $x_2 = [1\bar{1}0]$ and $x_3 = [001]$. For this orientation, the effective flexoelectric coefficient has the form

$$\mu_{eff}^{(110)} = \frac{s_{1111}+s_{1122}}{s_{1111}+s_{1122}+2s_{1212}}\mu_{1111} + \frac{s_{1111}+3s_{1122}}{s_{1111}+s_{1122}+2s_{1212}}\mu_{1122} - \frac{4s_{1122}}{s_{1111}+s_{1122}+2s_{1212}}\mu_{1212} + \frac{\phi}{2}\mu_{anticlastic}^{(110)}. \tag{3.48}$$

where

(3.49)

$$\mu^{(110)}_{anticlastic} = -\frac{4s_{1122}\mu_{1122}}{s_{1111}+s_{1122}+2s_{1212}} + \frac{(s_{1111}+s_{1122}-2s_{1212})\,s_{1212}\,(\mu_{1111}+\mu_{1122}+2\mu_{1212})}{(s_{1111}+s_{1122})\,(s_{1111}+s_{1122}+2s_{1212})} + \frac{(-s_{1111}-s_{1122}+2s_{1212})\,(\mu_{1111}+\mu_{1122}+2\mu_{1212})}{2\,(s_{1111}+s_{1122}+2s_{1212})}$$

3.5.2. Pseudocubic Rhombohedral Perovskite $LaAlO_3$

LAO is a rhombohedral perovskite with space group R$\overline{3}$c at room temperature and atmospheric pressure [**96**]. The deviations from the cubic perovskite structure are very small (the pseudocubic angle is 90.086° [**97**]), so it is common to approximate LAO as a cubic material. LAO is frequently used as a substrate for thin film growth, especially for superconductors [**98**], and has achieved popularity in recent years due to the discovery of a two-dimensional electron gas at the LAO/STO interface [**99**]. It is an interesting material in its own right because it has a moderately large dielectric constant [**100**], anomalous Born charges [**101**], and is heavily twinned at room temperature as a result of its cubic to rhombohedral phase transition at 550°C [**97**]. The structure of these twins has been studied extensively [**102, 103, 66, 104, 105, 106**], and LAO twins are intriguing because there is evidence of polarity [**107, 108, 109**] at LAO twin boundary (TB)s (for more details on the effects of twin boundaries on flexoelectricity see Chapter 6).

Although LAO is normally twinned at room temperature, it is possible to cut a twin-free portion out of a larger crystal. Such a sample is shown in Figure 3.11 along with its flexoelectric response. The twin-free sample shows very linear behavior with an effective flexoelectric coefficient of 3.2 nC/m, which is comparable to the effective coefficients

measured for STO and KTO even though LAO has a dielectric constant an order of magnitude smaller than these two materials. This flexoelectric coefficient is in agreement with a recent measurement of the flexoelectric response of LAO using a different approach [**110**]. Polarized optical microscopy was used after the experiment to confirm the sample remained twin-free throughout the course of the experiment (see Chapter 6 for a detailed discussion of polarized optical microscopy and a further analysis of twin-boundary effects on flexoelectricity).

Since the axes of this sample are oriented along the ⟨100⟩pseudo-cubic directions and LAO is nearly cubic [**97**], the effective flexoelectric coefficient of LAO will be approximately given by the Eq. 3.48.

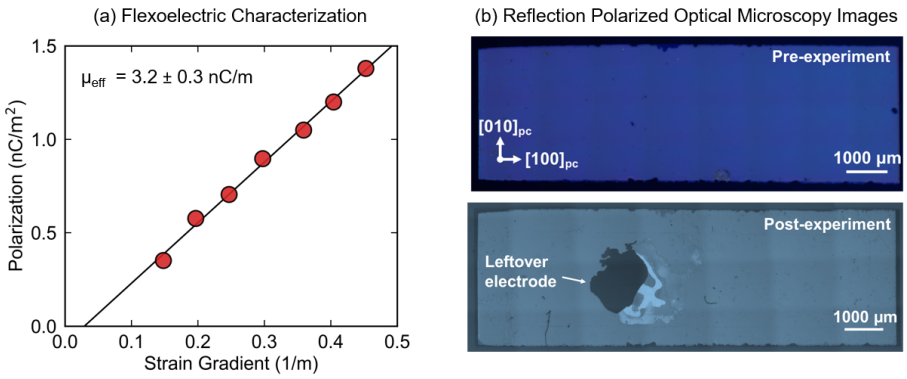

Figure 3.11. (a) Flexoelectric characterization of twin-free LAO single crystal and (b) polarized optical microscopy confirming the sample remained twin-free throughout the course of the bending experiments. The flexoelectric response is highly linear ($r^2 > 0.99$ with RMSE < 0.03). Note, the vertical and horizontal lines in the images are stitching artifacts.

3.5.3. Tetragonal Oxide TiO_2

TiO_2 exists as a number of polymorphs [**111**], the two most common being rutile and anatase. The rutile phase of TiO_2 studied here has the space group $P4\frac{2}{m}nm$ at room temperature and atmospheric pressure. It consists of chains of edge-sharing TiO_6 octahedra which are connected via shared corners, and is most commonly studied for high dielectric constant [**112**] and catalytic [**113**] applications. Rutile TiO_2 was analyzed here because high dielectric constants are typically used as a proxy for strong flexoelectric couplings [**10, 11**]. Although the flexoelectric response of TiO_2 has been measured in the literature [**114, 115**], the functional form of the effective flexoelectric coefficient has not been provided.

The flexoelectric response of TiO_2 shown in Figure 3.12 is highly linearly and yields an effective flexoelectric coefficient of the same magnitude as the cubic (and pseudo-cubic) perovskites studied in the previous two sections. Literature values for the flexoelectric coefficient are in good agreement with measurements indicating ∼1-2 nC/m [**114, 115**], however a direct comparison is with existing measurements difficult because (1) the reported flexoelectric coefficient for single crystal TiO_2 measured with TPB did not report crystallographic orientation [**114**] and (2) the other measurement in the literature was performed on polycrystalline thin films using a cantilever based approach [**115**]. In both cases, it is not possible to deduce the functional form of the effective flexoelectric coefficient, but the order of magnitude agreement between these two measurements and my own is encouraging.

My measurements were performed on TiO_2 beams with $x_1 = [100]$, $x_3 = [001]$, and $x_2 = [010]$. Note, according to the standard crystallographic convention [001] is the four-fold axis. The functional form of the effective flexoelectric coefficient for this orientation is

$$\mu_{eff}^{(100)} = \frac{s_{1133}}{s_{3333}}(\mu_{1111} + \mu_{1122}) + \mu_{1133} - \phi\frac{s_{1133}}{s_{3333}}\left(\frac{s_{1133}}{s_{3333} + s_{1133}}\mu_{1111} + \mu_{1122}\right). \tag{3.50}$$

For completeness, if the sample had rotated 90° along the surface normal so that $x_2 = [001]$ and $x_3 = [010]$, the functional form of the effective flexoelectric coefficient would be

$$\mu_{eff}^{(100)} = \frac{s_{1122}}{s_{3333}}\mu_{1111} + \mu_{1122} + \frac{s_{1133}}{s_{1111}}\mu_{1133} - \phi\frac{1}{s_{1111}}\left(\frac{s_{1122}^2}{s_{1111} + s_{1122}}\mu_{1111} + s_{1133}\mu_{1133}\right). \tag{3.51}$$

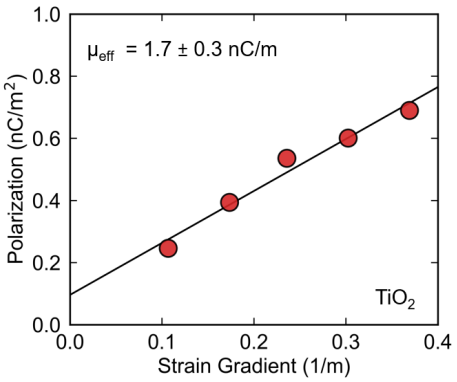

Figure 3.12. Flexoelectric characterization of TiO_2 single crystals. The flexoelectric response is highly linear ($r^2 > 0.97$ with RMSE < 0.03) with an effective flexoelectric coefficient of 1.7 nC/m.

3.5.4. Orthorhombic Perovskites $YAlO_3$ and $DyScO_3$

The majority of perovskite materials do not possess the archetypal cubic perovskite structure, but instead have a distorted orthorhombic structure with space group Pnma at room temperature and atmospheric pressure [**116**]. These structures are characterized by combinations of octahedral rotations and anti-polar A-site displacements [**117**]. $YAlO_3$ (YAO) and DSO are two materials which possess this structure [**118, 119**]. From a fundamental science perspective, DSO is an interesting material because of its low-temperature magnetic ordering [**120**], a highly anisotropic magnetic response [**121**], and polar phonons [**122**], and YAO is widely studied for its optical properties [**123**]. From an applications perspective, high dielectric constants make YAO and DSO potential gate oxide materials [**124, 125, 126**]. Also, their use as thin film substrates has led to discoveries such as an enhanced ferroelectric response in epitaxially grown STO [**127**].

As shown in Figure 3.13, the flexoelectric responses of both YAO and DSO are highly linear and characterized by effective flexoelectric coefficients which are the same order of magnitude as those measured above [**27**]. In both cases, the materials are oriented such that $x_1 = [101]$, $x_3 = [010]$, and $x_2 = [10\bar{1}]$ in the Pnma setting. Accordingly, the measured effective flexoelectric coefficient has the form:

$$\mu_{eff}^{(101)} = \mu_{1122} + \mu_{3322} + \frac{4s_{1122}}{s_{2222}}\left(\mu_{1111} + \mu_{3311}\right) + \frac{4s_{2233}}{s_{2222}}\left(\mu_{3333} + \mu_{1133}\right) + \phi\mu_{anticlastic}^{(101)} \tag{3.52}$$

where

(3.53)

$$\mu^{(101)}_{anticlastic} = -\frac{s_{1122}+s_{2233}}{s_{2222}\left(s_{1122}+s_{2222}+s_{2233}\right)}\left(\left(2s_{1122}+2s_{2233}\right)\left(\mu_{1111}+\mu_{1133}+\mu_{3311}+\mu_{3333}\right)+ s_{2222}\left(\mu_{1111}+\mu_{1133}+\mu_{3311}+\mu_{3333}-2\mu_{1313}-2\mu_{3113}\right)\right)$$

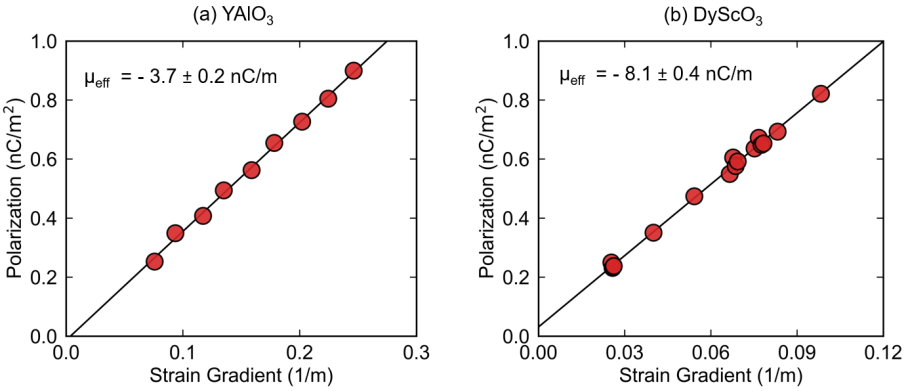

Figure 3.13. Flexoelectric characterization of (a) YAO and (b) DSO single crystals. The flexoelectric response is highly linear ($r^2 > 0.99$ with RMSE $<$ 0.01) and magnitude of the flexoelectric coefficients ranges between ∼1-10 nC/m.

3.5.5. Flexocoupling Voltage Comparison

Recall that it is common practice to characterize flexoelectricity by the short-circuit flexoelectric coefficient defined as

(3.54)
$$P_i = \mu^E_{ijkl}\epsilon_{kl,j}$$

which describe the linear coupling between polarization and strain gradient in the absence of an electric field. An alternative formulation of flexoelectricity can be made in terms of flexocoupling voltages, which are the materials parameters describing the gradient in the average Coulomb potential in a crystal that arises from a strain gradient [**58**]. Flexocoupling voltages were introduced as scalar quantities in Chapter 2, but formally are fourth-rank tensors like the flexoelectric coefficient. Flexocoupling voltages and short-circuit flexoelectric coefficients are related via

$$f_{ijkl} = \frac{\mu^{E}_{ijkl}}{\varepsilon_0 \chi_{eff}} \tag{3.55}$$

where χ_{eff} is the effective dielectric susceptibility in a given crystallographic direction.

Flexocoupling voltages tend to be a more convenient metric for the flexoelectric effect in theoretical considerations of flexoelectricity. Early estimates of the flexocoupling voltage based upon phenomenological theory indicated that their magnitude should be within 1-10 V and largely insensitive to differences in crystal structure [**128, 41, 11, 10**]. This estimate was supported by more recent phenomenological analyses as well [**129**], however there has not been a sufficient number of measurements in the literature to robustly test this 1-10 V prediction. Table 3.3 includes the magnitudes of the measured flexoelectric coefficients from the single crystal measurements shown in Figures 3.10- 3.13, the literature values for the effective dielectric susceptibilities [**112, 125, 126, 100, 90, 91**] in the relevant crystallographic direction, and the flexocoupling voltages calculated according to Eq. 3.55.

Material (surface)	$\lvert\mu_{eff}\rvert$ (nC/m)	χ_{eff}	$\lvert f_{eff}\rvert$ (V)
$SrTiO_3$ (100)	12.4 ± 0.6	309	4.5 ± 0.2
$SrTiO_3$ (110)	8.3 ± 1.4	309	3.0 ± 0.5
$KTaO_3$ (100)	4.4 ± 0.5	241	2.1 ± 0.2
$LaAlO_3$ $(100)_{pc}$	3.2 ± 0.3	25	14.5 ± 1.4
TiO_2 (100)	1.7 ± 0.3	85	2.3 ± 0.6
$YAlO_3$ (101)	3.7 ± 0.2	14.7	28 ± 1.5
$DyScO_3$ (101)	8.1 ± 0.4	19.4	47.2 ± 2.3

Table 3.3. Summary of effective flexoelectric coefficients, dielectric constants, and effective flexocoupling voltages of all the materials investigated in this chapter.

These measurements indicate that while the effective flexoelectric coefficients across all the measured materials are between ∼1-10 nC/m, the corresponding flexocoupling voltages show substantially larger variation and do not appear to be structurally insensitive. Instead, it appears that low dielectric constant oxides possess flexocoupling voltages 5-10× larger than the flexocoupling voltages of high dielectric constant oxides. Figure 3.14 summarizes these results by depicting the flexocoupling voltage averaged over all samples and crystallographic orientations for a particular materials system as a function of dielectric constant.

Flexocoupling voltages are the more fundamental quantities describing the flexoelectric response of a solid rather than the measured short-circuit flexoelectric coefficients [**58**]. This is because short-circuit flexoelectric coefficients measured experimentally have a dielectric contribution (recall, $\mu = f\varepsilon_0\chi$), and flexocoupling voltages are the materials parameters entering into the Landau energy density expansion (see discussion in Chapter 2 and Ref. [**10, 11**]). Therefore, the relationship in Figure 3.14 suggests that the intrinsic flexoelectric properties of the low dielectric constant materials are larger than those of

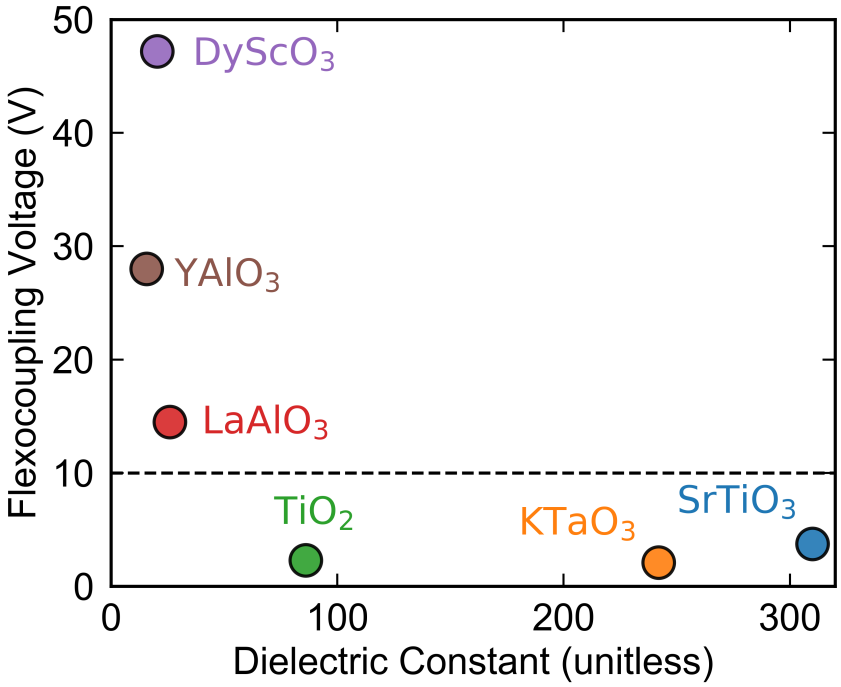

Figure 3.14. The average effective flexocoupling voltages measured for each single crystal oxide investigated in this work as a function of dielectric constant. Theoretically, the flexocoupling voltage should be a constant between 1-10 V for all materials.

the high dielectric constant materials. Since the dielectric constant is often considered a proxy for the polarizability of a solid, the indication that lower dielectric constant materials exhibit a stronger propensity for flexoelectric polarization is somewhat counter-intuitive. It is worth noting that counting arguments do not account for the difference in the flexocoupling voltage: if the large flexocoupling voltages in DSO and YAO were merely a consequence of the effective flexoelectric coefficient expression in Eq. 3.52 having contributions from more flexoelectric coefficients than STO and KTO in Eq. 3.48, then *both* the flexoelectric coefficients and flexocoupling voltages should be anomalously large.

At the moment the origin of this observation is unclear, but some possible explanations are explored in future chapters using DFT including the role of site symmetry (Chapter 4) and surfaces (Chapter 5).

CHAPTER 4

First Principles Theory of Bulk Flexoelectricity

4.1. Historical Context

The first theoretical treatments of flexoelectricity in solids arose in the context of lattice dynamics in the 1950s and 1960s [**12, 41**]. This work was rooted in phenomenological frameworks and led to order of magnitude estimates for the flexoelectric coefficient (i.e. $\mu \sim e/a$, where e is the electron charge and a is the lattice parameter [**41**]), and in one case estimates of flexoelectric coefficients in a few cubic ionic insulators based upon lattice dynamic shell models [**130**]. The phenomenological description of flexoelectricity was refined over the next 20 years, culminating in a formalized method for calculating flexoelectric coefficients from a crystal's dynamical matrix [**128**].

With the benefit of hindsight, it is apparent that the roots of the first principles theory of bulk flexoelectricity were planted in work addressing absolute deformation potentials[**131, 132, 133, 134**], but the first explicit attempt at such a theory was put forward by Resta in 2010 [**135**]. Using an approach analogous to Martin's description of piezoelectricity [**4**], Resta demonstrated that electronic contributions to the flexoelectric coefficient are given in terms of induced octupole moments. Resta's analysis, which formally only applied to elemental, cubic insulators, was generalized by Hong and Vanderbilt to work for arbitrary insulators in 2011 [**136**] and then expanded to include lattice contributions in 2013 [**58**]. Simultaneously and independently, Stengel developed a theory of

flexoelectricity rooted in density functional perturbation theory (DFPT) [**59, 137**]. These works approached the same problem from different perspectives, and ultimately arrived at a unified, first principles description of flexoelectricity. More recently, these descriptions have been generalized as current-density responses [**138**], implemented in ab initio codes with DFPT capabilities [**139**], extended to describe arbitrary spatial dispersions [**140**], and examined for lower dimensional materials [**141**].

In this chapter, I first provide an overview of the first principles theory of flexoelectricity put forth by Hong and Vanderbilt [**58**] in Section 4.2 In Section 4.3 I discuss some of the technical details concerning implementing this theory in DFT calculations and then provide some benchmark calculations on STO in Section 4.4. Section 4.5 studies the effects of the exchange and correlation functional on the flexoelectric response of STO. Then, Section 4.6 and 4.7 includes a comparison of the first principles flexoelectric coefficients of STO, KTO, LAO, and $GdScO_3$ (GSO) with the measurements in Chapter 3. Short-comings of the first principles theory of bulk flexoelectricity and approach adopted here are addressed in Section 4.8 and Section 4.9. I performed all DFT calcultions and analyses described in this chapter and benefitted from discussions with Professor Laurence D. Marks.

4.2. Theory of Bulk Flexoelectricity

4.2.1. Overview

Here I provide a brief overview of the first principles theory of bulk flexoelectricity developed by Hong and Vanderbilt [**58**], stating the main conclusions and focusing on the

physical interpretation of the theory. For technical details, including derivations, please see Ref. [**58**].

Hong and Vanderbilt developed expressions for flexoelectric coefficients in terms of charge density and force responses to long wavelength phonon perturbations. They showed it is possible to decompose a flexoelectric tensor component $\mu_{\alpha\beta\gamma\delta}$ into three terms

$$\mu_{\alpha\beta\gamma\delta} = \mu^{el}_{\alpha\beta\gamma\delta} + \mu^{ld}_{\alpha\beta\gamma\delta} + \mu^{lq}_{\alpha\beta\gamma\delta}. \tag{4.1}$$

$\mu^{el}_{\alpha\beta\gamma\delta}$ is the purely electronic contribution to the flexoelectric coefficient and the other two terms are lattice-mediated contributions, the lattice-dipole interaction $\mu^{ld}_{\alpha\beta\gamma\delta}$ and lattice-quadrupole interaction $\mu^{lq}_{\alpha\beta\gamma\delta}$.

4.2.2. Pure Electronic Contributions

The pure electronic contribution to the flexoelectric response, also known as the frozen-ion or clamped-ion contribution, is the sum of the octupole moments of the change in charge density induced by all sublattice displacements. In the approximation that atomic positions are unable to relax in response to an applied deformation, this term represents the entire flexoelectric response.

$$\mu^{el}_{\alpha\beta\gamma\delta} = \frac{1}{6\Omega} \sum_{I} Q^{(3)}_{I\alpha\beta\gamma\delta} \tag{4.2}$$

In Eq. 4.2, Ω is the unit cell volume and $Q^{(3)}_{I\alpha\beta\gamma\delta}$ is the third moment (octupole) of the change in charge density $\rho(\mathbf{r})$ caused by the displacement $u_{lI\tau}$ of atom I in cell l in the

direction τ

$$Q^{(3)}_{I\alpha\tau\beta\gamma} = \int d\mathbf{r} r_\alpha \frac{\partial \rho(\mathbf{r})}{\partial u_{lI\tau}} r_\beta r_\gamma \tag{4.3}$$

and r are spatial coordinates.

4.2.3. Lattice-Dipole Contributions

The lattice-mediated, or relaxed-ion, contributions to flexoelectric coefficients come in two forms. The first contribution, which is active in all insulators with finite dynamical charges, is the lattice-dipole term. It relates the dipole moment of the change in charge density induced by a sublattice displacement to the forces induced by that sublattice displacement.

$$\mu^{ld}_{\alpha\beta\gamma\delta} = \frac{1}{\Omega} \sum_{I\tau, J\tau'} Q^{(1)}_{I\alpha\tau} (K^{-1})_{I\tau, J\tau'} T_{J\tau'\beta\gamma\delta} \tag{4.4}$$

$Q^{(1)}_{I\alpha\tau}$ is the first moment (dipole) of the change in charge density induced by the displacement of atom I in cell l in the direction τ

$$Q^{(1)}_{I\alpha\tau} = \int d\mathbf{r} r_\alpha \frac{\partial \rho(\mathbf{r})}{\partial u_{lI\tau}}. \tag{4.5}$$

It is a measure of dynamical charge [**142**] known as the Callen charge under fixed dielectric displacement boundary conditions [**143**], or Born charge under fixed electric field boundary conditions [**144**].

The force response tensor $T_{I\tau\beta\gamma\delta}$ describes the force on atom I in direction τ ($F_{I\tau}$) caused by a strain gradient and has the physical interpretation of sub-lattice resolved

elastic constants (see Ref. [**59**] and Section 4.5). It is typically defined in terms of unsymmetrized strain gradients $\eta_{i,jk} = \frac{\partial^2 u_i}{\partial x_j \partial x_k}$ as

$$T_{I\tau\beta\gamma\delta} = \frac{\partial F_{I\tau}}{\partial \eta_{\beta,\gamma\delta}}. \tag{4.6}$$

In practice, the force response tensor is calculated as the second moment of the change in forces induced by the displacement of atom I

$$T_{I\tau\beta\gamma\delta} = -\frac{1}{2u_I} \sum_J \Delta F_{I\tau,J\beta} \Delta R_\gamma \Delta R_\delta \tag{4.7}$$

where $\Delta F_{I\tau,J\beta}$ is the force on atom J in direction β caused by the displacement of atom I in direction τ. ΔR is the distance between atom J and I.

The remaining term in Eq. 4.4, $(K^{-1})_{I\tau,J\tau'}$, is the (pseudo)inverse [**58, 46**] of the zone-center force-constant matrix

$$K_{I\tau,J\tau'} = -\frac{\partial F_{J\tau}}{\partial u_{I\tau'}}. \tag{4.8}$$

Note, by converting Eq. 4.4 to symmetry-adapted mode variables it is apparent that only infrared active modes contribute to the lattice-dipole flexoelectric terms [**58**].

4.2.4. Lattice-Quadrupole Contributions

The other lattice-mediated contribution is the lattice-quadrupole contribution.

$$\mu^{lq}_{\alpha\beta\gamma\delta} = -\frac{1}{4\Omega} \sum_{I\tau,J\tau'} \left(Q^{(2)}_{I\alpha\tau\delta} (K^{-1})_{I\tau,J\tau'} \Lambda_{J\tau'\beta\gamma} + Q^{(2)}_{I\alpha\tau\gamma} (K^{-1})_{I\tau,J\tau'} \Lambda_{J\tau'\beta\delta} \right) \tag{4.9}$$

In Eq. 4.9, $Q^{(2)}_{I\alpha\tau\delta}$ is second moment (quadrupole) of the change in charge density induced by the displacement of atom I in cell l in the direction τ

$$Q^{(2)}_{I\alpha\tau\beta} = \int d\mathbf{r} r_\alpha \frac{\partial \rho(\mathbf{r})}{\partial u_{lI\tau}} r_\beta. \tag{4.10}$$

The force response tensor $\Lambda_{J\tau'\beta\gamma}$ describes the force on atom I in direction τ caused by a uniform strain

$$\Lambda_{I\tau\beta\gamma} = \frac{\partial F_{I\tau}}{\partial \eta_{\beta,\gamma}}. \tag{4.11}$$

In practice, the force response tensor is calculated as the first moment of the change in forces induced by the displacement of atom I

$$\Lambda_{I\tau\beta\gamma} = -\frac{1}{u_I} \sum_J \Delta F_{I\tau,J\beta} \Delta R_\gamma. \tag{4.12}$$

The lattice-quadrupole contribution is non-zero only for sites which lack inversion symmetry and recasting Eq. 4.9 in terms of symmetry-adapted modes indicates that lattice-quadrupole moments are only non-zero for Raman active modes [**58**].

4.2.5. Limitations of Approach: Current Density Terms

The above approach relied upon expressing contributions to the flexoelectric tensor component in terms of changes in charge density, but there is a fundamental limitation with this approach: charge density is only sensitive to longitudinal polarization because charge density and polarization are related via

$$\nabla \cdot \mathbf{P} = -\rho. \tag{4.13}$$

This means that the charge density contains no information on any transverse parts of a polarization given by $\nabla \times \mathbf{P}$ [**58**].

Generalizing Eq. 4.2, 4.4, and 4.9 to account for these missing contributions amounts to replacing $\frac{\partial \rho}{\partial u_{lI\tau}}$ with $\frac{\partial J_\alpha}{\partial \dot{u}_{lI,\tau}}$, i.e. reformulating the problem in terms of the change in adiabatic current with velocity. Performing this analysis yields two additional contributions to the total expression for a flexoelectric tensor component, current-density contributions to the electronic ($\mu^{el,J}_{\alpha\beta\gamma\delta}$) and lattice-quadrupole ($\mu^{lq,J}_{\alpha\beta\gamma\delta}$) terms [**58, 138**].

$$\mu_{\alpha\beta\gamma\delta} = \mu^{el}_{\alpha\beta\gamma\delta} + \mu^{el,J}_{\alpha\beta\gamma\delta} + \mu^{ld}_{\alpha\beta\gamma\delta} + \mu^{lq}_{\alpha\beta\gamma\delta} + \mu^{lq,J}_{\alpha\beta\gamma\delta}. \tag{4.14}$$

Presently, calculation of $\mu^{el,J}_{\alpha\beta\gamma\delta}$ and $\mu^{lq,J}_{\alpha\beta\gamma\delta}$is difficult [**138**]. Calculations have shown $\mu^{el,J}_{\alpha\beta\gamma\delta}$ is rather small and a good approximation is to take $\mu^{el,J}_{\alpha\beta\gamma\delta} = 0$ [**138**]. There have been no calculations of $\mu^{lq,J}_{\alpha\beta\gamma\delta}$, so it is difficult to know the impact of this term. Throughout the remainder of this work we will focus on structures which by symmetry do not have lattice-quadrupole contributions making $\mu^{lq,J}_{\alpha\beta\gamma\delta} = 0$ and we will assume $\mu^{el,J}_{\alpha\beta\gamma\delta} = 0$ [**58**].

4.3. Density Functional Theory Implementation

4.3.1. General Considerations

Eq. 4.2, 4.4, and 4.9 make clear that to utilize the first principles theory of flexoelectricity, it is necessary to compute the charge and force changes induced by all unique sub-lattice displacements in a structure. We calculate these quantities using DFT as implemented in the all-electron augmented plane wave + local orbitals WIEN2k code [**145**]. Readers wishing to learn more about DFT and WIEN2k, are directed to Ref. [**146**], [**147**], and [**145**].

Before considering the specific forms of Eq. 4.2, 4.4, and 4.9 for a cubic perovskite structure in Section 4.3.2 and 4.3.3 , I first comment on how these calculations are performed using a supercell geometry, the impact of electrostatic boundary conditions (also see Section 2.5), and the strain convention used in the quantities defined above (also see Section 2.3).

4.3.1.1. Supercell Geometry. The method of calculating the moments in Eq. 4.2, 4.4, and 4.9 is similar to the supercell approach to phonons. After structural optimization has been performed on a bulk cell and the number of unique sublattice displacements has been identified, $Nx1x1$ supercells are constructed using the bulk optimized structural parameters (where N is sufficiently large to minimize spurious effects from periodic boundary conditions) in directions consistent with the required sublattice displacements [**58**]. For example, see Figure 4.1. Electronic relaxations are then performed on all the supercells and the differences in the charge density and forces between each supercell with a displaced atom and the unperturbed supercell are used to compute the moments needed to calculate the flexoelectric coefficients according to 4.2, 4.4, and 4.9 .

4.3.1.2. Electrostatic Boundary Conditions. The atomic displacements described above can be imposed according to different electrostatic boundary conditions. Although the experimental measurements described in Chapter 3 are performed under short-circuit ($E = 0$ or fixed E) boundary conditions, it is computationally advantageous to work under open-circuit ($D = 0$ or fixed D) boundary conditions because long-range electric fields lead to slower convergence. A depiction of the atomic displacement pattern used in a typical supercell calculation, as well as the induced change in charge density, electric field, and potential, are shown in Figure 4.2.

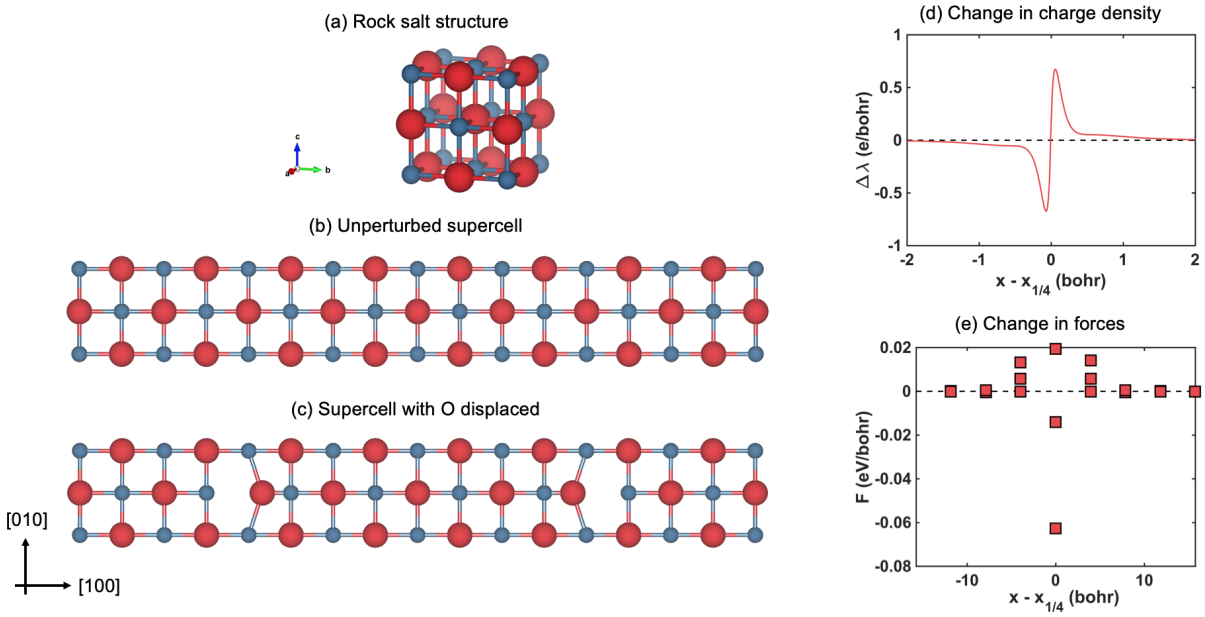

Figure 4.1. Example of supercell procedure for a rock salt structure. (a) The bulk structure is used to generate supercells with (b) no sublattice displacements and (c) sublattice displacements. The electron density and forces are relaxed in both supercells and the difference in the (d) charge density and (e) forces are computed (shown here for the left half of the supercells in (b) and (c)). Moments of (d) and (e) are used to determine the flexoelectric response.

Throughout the remainder of this chapter, a superscript D and E will be used to denote fixed D and fixed E quantities, respectively. Once the flexoelectric coefficients have been computed as fixed D quantities, they are converted to fixed E quantities to compare to experiment using

$$\mu^{E}_{\alpha\beta\gamma\delta} = \varepsilon^{0}_{\alpha\lambda}\mu^{D}_{\lambda\beta\gamma\delta} \tag{4.15}$$

for the total flexoelectric coefficient and

$$\mu^{el,E}_{\alpha\beta\gamma\delta} = \varepsilon^{\infty}_{\alpha\lambda}\mu^{el,D}_{\lambda\beta\gamma\delta} \tag{4.16}$$

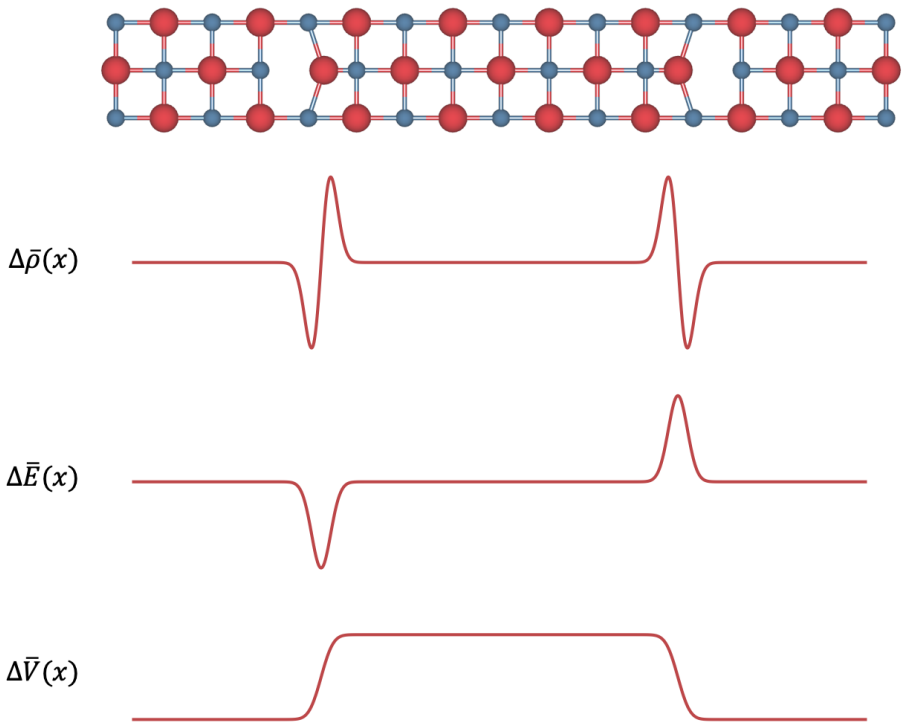

Figure 4.2. Example of a supercell with a displacement pattern consistent with $D = 0$ boundary conditions. The change in the charge density, electric field, and potential from the unperturbed case are also shown.

for the electronic contributions. $\varepsilon^0_{\alpha\lambda}$ is the static dielectric constant and $\varepsilon^\infty_{\alpha\lambda}$ is the high frequency dielectric constant [**58**].

4.3.1.3. Strain Convention. The flexoelectric coefficients in Eq. 4.2, 4.4, and 4.9 were defined in terms of the polarization response to an unsymmetrized strain gradient

$$\eta_{\alpha,\beta\gamma} = \frac{\partial^2 u_\alpha}{\partial x_\beta \partial x_\gamma} \tag{4.17}$$

however, the experimental treatment described in Chapters 2 and 3 relied upon symmetrized strain gradients of the form

$$\epsilon_{\alpha\beta,\gamma} = \frac{\partial \epsilon_{\alpha\beta}}{\partial x_\gamma}. \tag{4.18}$$

These strain gradients are related [**59**] by

$$\eta_{\alpha,\beta\gamma} = \epsilon_{\alpha\beta,\gamma} + \epsilon_{\gamma\alpha,\beta} - \epsilon_{\beta\gamma,\alpha}. \tag{4.19}$$

Similarly, the flexoelectric coefficients defined according to the unsymmetrized and symmetrized convention are related [**59**] via

$$\mu^{sym}_{\alpha\delta\beta\gamma} = \mu^{unsym}_{\alpha\beta\gamma\delta} + \mu^{unsym}_{\alpha\gamma\beta\delta} - \mu^{unsym}_{\alpha\delta\beta\gamma}. \tag{4.20}$$

For cubic materials, which only have three independent flexoelectric tensor components (μ_{1111},μ_{1122}, and μ_{1212}), Eq. 4.20 gives

$$\begin{aligned} \mu^{sym}_{1111} &= \mu^{unsym}_{1111} \\ \mu^{sym}_{1122} &= 2\mu^{unsym}_{1221} - \mu^{unsym}_{1122} \\ \mu^{sym}_{1212} &= \mu^{unsym}_{1122}. \end{aligned} \tag{4.21}$$

Throughout the remainder of this chapter, all flexoelectric coefficients are computed as unsymmetrized quantities and reported as symmetrized quantities using the conversion in Eq. 4.21.

4.3.2. Cubic Perovskite: μ_{1111}

Now I consider the specific forms of Eq. 4.2, 4.4, and 4.9 for a cubic perovskite. Focusing first on the longitudinal component $\mu_1 111$ (the relevant supercell is in Figure 4.3(a)) we need to compute $Q^{(1),D}_{I,11}$, $Q^{(3),D}_{I,1111}$, and $T^{D}_{I,1111}$ for I=$\{A, B, O1, O2,$ and $O3\}$ in addition to the zone-center force constant matrix. The electronic contributions to μ^{D}_{1111} can be obtained directly from the values for $Q^{(3),D}_{I,1111}$.

$$\mu^{el,D}_{1111} = \frac{1}{6\Omega}\left(Q^{(3),D}_{A,1111} + Q^{(3),D}_{B,1111} + Q^{(3),D}_{O1,1111} + Q^{(3),D}_{O2,1111} + Q^{(3),D}_{O3,1111}\right) \tag{4.22}$$

$\mu^{ld,D}_{1111}$ requires combining

$$\left[Q^{(1),D}\right] = \left[Q^{(1),D}_{A,11} + Q^{(1),D}_{B,11} + Q^{(1),D}_{O1,11} + Q^{(1),D}_{O2,11} + Q^{(1),D}_{O3,11}\right] \tag{4.23}$$

and

$$\left[T^{D}\right] = \left[T^{D}_{A,1111} + T^{D}_{B,1111} + T^{D}_{O1,1111} + T^{D}_{O2,1111} + T^{D}_{O3,1111}\right] \tag{4.24}$$

according to

$$\mu^{ld,D}_{1111} = \frac{1}{\Omega}\left[Q^{(1),D}\right] \cdot \left[K^{D}\right]^{-1} \cdot \left[T^{D}\right]^{T} \tag{4.25}$$

where $[K]$ is the zone-center force-constant matrix

$$[K] = \begin{pmatrix} \frac{\partial F_A}{\partial u_A} & \frac{\partial F_B}{\partial u_A} & \frac{\partial F_{O1}}{\partial u_A} & \frac{\partial F_{O2}}{\partial u_A} & \frac{\partial F_{O3}}{\partial u_A} \\ \frac{\partial F_A}{\partial u_B} & \frac{\partial F_B}{\partial u_B} & \frac{\partial F_{O1}}{\partial u_B} & \frac{\partial F_{O2}}{\partial u_B} & \frac{\partial F_{O3}}{\partial u_B} \\ \frac{\partial F_A}{\partial u_{O1}} & \frac{\partial F_B}{\partial u_{O1}} & \frac{\partial F_{O1}}{\partial u_{O1}} & \frac{\partial F_{O2}}{\partial u_{O1}} & \frac{\partial F_{O3}}{\partial u_{O1}} \\ \frac{\partial F_A}{\partial u_{O2}} & \frac{\partial F_B}{\partial u_{O2}} & \frac{\partial F_{O1}}{\partial u_{O2}} & \frac{\partial F_{O2}}{\partial u_{O2}} & \frac{\partial F_{O3}}{\partial u_{O2}} \\ \frac{\partial F_A}{\partial u_{O3}} & \frac{\partial F_B}{\partial u_{O3}} & \frac{\partial F_{O1}}{\partial u_{O3}} & \frac{\partial F_{O2}}{\partial u_{O3}} & \frac{\partial F_{O3}}{\partial u_{O3}} \end{pmatrix}. \tag{4.26}$$

Note, only derivatives along the [100] direction are needed in Eq. 4.26 because forces in other directions are zero by symmetry. In more general cases (e.g. Section 4.3.3), more spatial dimensions must be included in the zone-center force-constant matrix. Combining Eq. 4.22 and 4.25 yields the longitudinal flexoelectric coefficient

$$\mu_{1111}^{D} = \mu_{1111}^{el,D} + \mu_{1111}^{ld,D}. \tag{4.27}$$

4.3.3. Cubic Perovskite: μ_{1122} and μ_{1212}

Next we would like to compute the remaining two independent flexoelectric tensor components. Unfortunately, owing to the limitations of the current-density approach [**58, 138**], only a linear combination of them is accessible. If we consider a supercell of the rotated perovskite structure shown in Figure 4.3(b), the longitudinal flexoelectric coefficient in the rotated frame (denoted by $'$) is

$$\mu'_{1111} = \frac{1}{2}\left(\mu_{1111} + \mu_{1122}\right) + \mu_{1212} \tag{4.28}$$

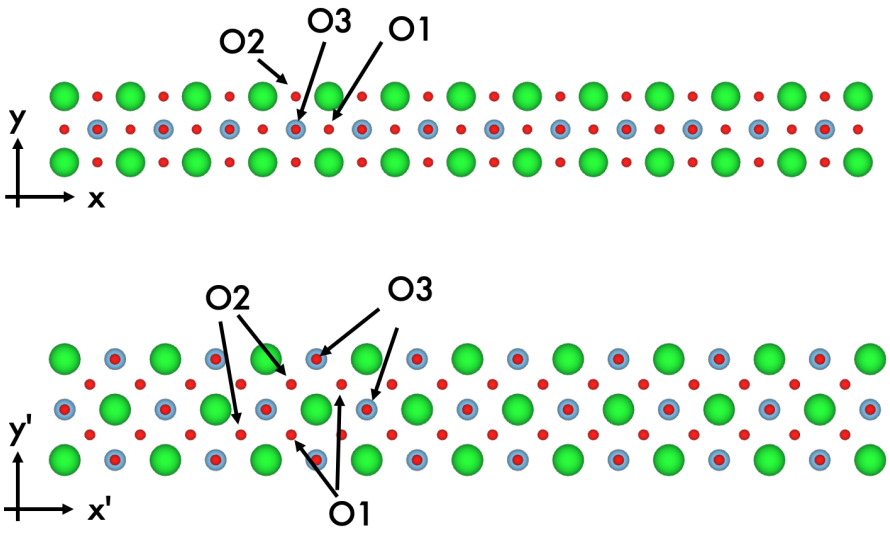

Figure 4.3. Supercells needed to compute the flexoelectric response of a cubic perovskite. (a) A supercell oriented along ⟨100⟩ directions provides access to μ_{1111}. (b) A supercell rotated 45° such that $x' = [110]$ provides access to $\mu'_{1111} = \frac{1}{2}(\mu_{1111} + \mu_{1122}) + \mu_{1212}$. The three oxygens in the cubic perovskite structure are labeled in both (a) and (b).

which can be rearranged in terms of the two unknown quantities, μ_{1122} and μ_{1212}.

$$\mu_{L2} = 2\mu'_{1111} - \mu_{1111} = \mu_{1122} + 2\mu_{1212} \tag{4.29}$$

The electronic contributions in this rotated frame are computed analogously to Eq. 4.22, where each $Q^{(3),D}_{I,1111}$ is replaced by $Q^{'(3),D}_{I,1111}$.

$$\mu'^{el,D}_{1111} = \frac{1}{6\Omega}\left(Q'^{(3),D}_{A,1111} + Q'^{(3),D}_{B,1111} + Q^{('3),D}_{O1,1111} + Q'^{(3),D}_{O2,1111} + Q^{('3),D}_{O3,1111}\right) \tag{4.30}$$

The lattice-dipole term is more complex owing the tetragonal site symmetry of the anion in cubic perovskites [**58**]. While $\mu^{ld,D}_{1111}$ only had contributions arising from longitudinal

displacements, $\mu_{1111}^{\prime ld,D}$ has additional contributions from transverse displacements so that

$$\mu_{1111}^{\prime ld,D} = \frac{1}{\Omega}\left[Q^{\prime(1),D}\right]\cdot\left[K^{\prime D}\right]^{-1}\cdot\left[T^{\prime D}\right]^{T} \tag{4.31}$$

where

$$\left[Q^{\prime(1),D}\right] = \left[Q_{A,11}^{\prime(1),D} + Q_{B,11}^{\prime(1),D} + Q_{O1,11}^{\prime(1),D} + Q_{O2,11}^{\prime(1),D} + Q_{O1,12}^{\prime(1),D} + Q_{O2,12}^{\prime(1),D} + Q_{O3,11}^{\prime(1),D}\right] \tag{4.32}$$

$$\left[T^{\prime D}\right] = \left[T_{A,1111}^{\prime D} + T_{B,1111}^{\prime D} + T_{O1,1111}^{\prime D} + T_{O2,1111}^{\prime D} + T_{O1,2111}^{\prime D} + T_{O2,2111}^{\prime D} + T_{O3,1111}^{\prime D}\right] \tag{4.33}$$

and

$$[K'] = \begin{pmatrix} \frac{\partial F'_{A,1}}{\partial u'_{A,1}} & \frac{\partial F'_{B,1}}{\partial u'_{A,1}} & \frac{\partial F'_{O1,1}}{\partial u'_{A,1}} & \frac{\partial F'_{O2,1}}{\partial u'_{A,1}} & \frac{\partial F'_{O1,2}}{\partial u'_{A,1}} & \frac{\partial F'_{O2,2}}{\partial u'_{A,1}} & \frac{\partial F'_{O3,1}}{\partial u'_{A,1}} \\ \frac{\partial F'_{A,1}}{\partial u'_{B,1}} & \frac{\partial F'_{B,1}}{\partial u'_{B,1}} & \frac{\partial F'_{O1,1}}{\partial u'_{B,1}} & \frac{\partial F'_{O2,1}}{\partial u'_{B,1}} & \frac{\partial F'_{O1,2}}{\partial u'_{B,1}} & \frac{\partial F'_{O2,2}}{\partial u'_{B,1}} & \frac{\partial F'_{O3,1}}{\partial u'_{B,1}} \\ \frac{\partial F'_{A,1}}{\partial u'_{O1,1}} & \frac{\partial F'_{B,1}}{\partial u'_{O1,1}} & \frac{\partial F'_{O1,1}}{\partial u'_{O1,1}} & \frac{\partial F'_{O2,1}}{\partial u'_{O1,1}} & \frac{\partial F'_{O1,2}}{\partial u'_{O1,1}} & \frac{\partial F'_{O2,2}}{\partial u'_{O1,1}} & \frac{\partial F'_{O3,1}}{\partial u'_{O1,1}} \\ \frac{\partial F'_{A,1}}{\partial u'_{O2,1}} & \frac{\partial F'_{B,1}}{\partial u'_{O2,1}} & \frac{\partial F'_{O1,1}}{\partial u'_{O2,1}} & \frac{\partial F'_{O2,1}}{\partial u'_{O2,1}} & \frac{\partial F'_{O1,2}}{\partial u'_{O2,1}} & \frac{\partial F'_{O2,2}}{\partial u'_{O2,1}} & \frac{\partial F'_{O3,1}}{\partial u'_{O2,1}} \\ \frac{\partial F'_{A,1}}{\partial u'_{O1,2}} & \frac{\partial F'_{B,1}}{\partial u'_{O1,2}} & \frac{\partial F'_{O1,1}}{\partial u'_{O1,2}} & \frac{\partial F'_{O2,1}}{\partial u'_{O1,2}} & \frac{\partial F'_{O1,2}}{\partial u'_{O1,2}} & \frac{\partial F'_{O2,2}}{\partial u'_{O1,2}} & \frac{\partial F'_{O3,1}}{\partial u'_{O1,2}} \\ \frac{\partial F'_{A,1}}{\partial u'_{O2,2}} & \frac{\partial F'_{B,1}}{\partial u'_{O2,2}} & \frac{\partial F'_{O1,1}}{\partial u'_{O2,2}} & \frac{\partial F'_{O2,1}}{\partial u'_{O2,2}} & \frac{\partial F'_{O1,2}}{\partial u'_{O2,2}} & \frac{\partial F'_{O2,2}}{\partial u'_{O2,2}} & \frac{\partial F'_{O3,1}}{\partial u'_{O2,2}} \\ \frac{\partial F'_{A,1}}{\partial u'_{O3,1}} & \frac{\partial F'_{B,1}}{\partial u'_{O3,1}} & \frac{\partial F'_{O1,1}}{\partial u'_{O3,1}} & \frac{\partial F'_{O2,1}}{\partial u'_{O3,1}} & \frac{\partial F'_{O1,2}}{\partial u'_{O3,1}} & \frac{\partial F'_{O2,2}}{\partial u'_{O3,1}} & \frac{\partial F'_{O3,1}}{\partial u'_{O3,1}} \end{pmatrix}. \tag{4.34}$$

In Eq. 4.32- 4.34 displacements/forces in the x and y directions are denoted by 1 and 2, respectively. Once $\mu_{1111}^{\prime el,D}$ and $\mu_{1111}^{\prime ld,D}$ are computed, they can be used in conjunction with μ_{1111}^{D} to obtain $\mu_{L2}^{D} = \mu_{1122}^{D} + 2\mu_{1212}^{D}$ according to Eq. 4.29.

The ultimate goal is to isolate μ^D_{1122} and μ^D_{1212}. The lattice-dipole contribution to the transverse flexoelectric coefficient ($\mu^{ld,D}_{1122}$) can be directly computed according to

$$\mu^{ld,D}_{1122} = \frac{1}{\Omega}\left[Q^{(1),D}_{11}\right] \cdot \left[K^D\right]^{-1} \cdot \left[T^D_{1122}\right]^T \tag{4.35}$$

using the available information in Eq. 4.23 and 4.26 in addition to

$$\left[T^D_{1122}\right] = \left[T^D_{A,1122} + T^D_{B,1122} + T^D_{O1,1122} + T^D_{O2,1122} + T^D_{O3,1122}\right]. \tag{4.36}$$

Each $T^D_{I,1122}$ component corresponds to the second moment of the change in force along the x-direction in Figure 4.3(a) from a displacement in the y-direction. Then $\mu^{ld,D}_{1122}$ can be used with $\mu^{ld,D}_{L2}$ to solve for $\mu^{ld,D}_{1212}$ according to Eq. 4.29.

Isolating the electronic contributions to the shear and transverse flexoelectric coefficients requires an approximation without the current-density information. We follow Hong and Vanderbilt [**58**] in assuming the transverse contribution to the electronic flexoelectric coefficient is zero, i.e. $\mu^J_{el} = 0$, which is equivalent to assuming

$$\mu^{el}_{1122} = \mu^{el}_{1212}. \tag{4.37}$$

Then, from Eq. 4.37 we get

$$\mu^{el}_{1122} = \mu^{el}_{1212} = \frac{\mu^{el,D}_{L2}}{3}. \tag{4.38}$$

Ultimately $\mu_e l^J$ is rather small, so this approximation is moderately good [**138**].

4.4. Benchmark Calculations with $SrTiO_3$

4.4.1. DFT Parameters

DFT calculations were performed with the all-electron augmented plane wave + local orbitals WIEN2k code [**145**] on cubic STO ($Pm\bar{3}m$) using the local density approximation (LDA) functional [**148**] to approximate the exchange-correlation term. STO was used as a benchmark because its flexoelectric coefficients have been calculated using other (plane-wave pseudopotential) DFT implementations [**136, 58, 74, 140**]. Muffin-tin radii of 2.44, 1.72, 1.64 bohr were used for Sr, Ti, and O, respectively with a plane-wave expansion parameter RKMAX of 6, energy cut-off of -6 Ry, and k-mesh equivalent to 8×8×8 per bulk conventional unit cell. All calculations used a Mermin functional at room temperature. Convergence criteria of 10^{-6} e, 10^{-4} Ry, and 10^{-3} mRy/bohr were used. Results were found to be particularly sensitive to plane wave convergence.

First, bulk calculations were performed to find the optimized lattice constant (7.290 bohr). The supercells depicted in Figure 4.3 were then constructed using the bulk optimized lattice constants. The supercell with the [100] long axis in Figure 4.3(a) was 12 unit cells long and the supercell with the [110] long axis in Figure 4.3(b) was 8 unit cells long. After the unperturbed supercells were converged, supercells containing the displacements necessary to obtain the required charge density moments, force moments, and force-constant matrices were created and converged. Numerical tests confirmed the supercells were sufficiently large and varying the muffin-tin radii, RKMAX, and k-mesh reported above yielded consistent values.

Once the required supercells were converged, the 3DDENS program within WIEN2k was used to compute the real space charge density of each supercell. The charge density output from 3DDENS and the forces from WIEN2k were used to compute the charge density moments, force moments, and zone-center force-constant matrices which were then used to calculate the flexoelectric coefficients according to Eq. 4.2, 4.4, and 4.9. Python/Matlab scripts were written to perform this analysis. It was found using 3DDENS for heavier elements lead to an underestimation of the Callen [**143**] charge ($Q^{(1),D}$). To correct for this, Born [**144**] charges ($Q^{(1),E}$) were calculated using a Berry phase approach [**70, 69, 149**] and $Q^{(1),D}$ for heavy elements was replaced by $\frac{Q^{(1),E}}{\varepsilon^{\infty}}$. This lead to an improvement in the acoustic sum rule for the Callen charges.

4.4.2. Charge Density and Force Moments for $SrTiO_3$

First, I focus on the change in the charge density and the induced dipole and octupole moments for the Sr, Ti, O1, and O2/O3 sites (O2 and O3 are equivalent for this case) in the supercell with the [100] long axis. Owing to the symmetry of the supercell, the three-dimensional charge density can be replaced by the one-dimensional planar averaged charge density.

$$\overline{\rho}(x) = \frac{1}{A}\int_{yz} \rho(x,y,z)dydz \tag{4.39}$$

Figure 4.4 shows the change in charge density between a supercell with a displaced species and an unperturbed supercell

$$\Delta\lambda(x) = \overline{\rho}_{displaced}(x) - \overline{\rho}_{unperturbed}(x) \tag{4.40}$$

for Sr, Ti, O1, and O2/O3. In all cases $\Delta\lambda(x)$ has the form of a dipolar distribution and is localized to within 1 bohr of the displaced atom, quickly falling to zero.

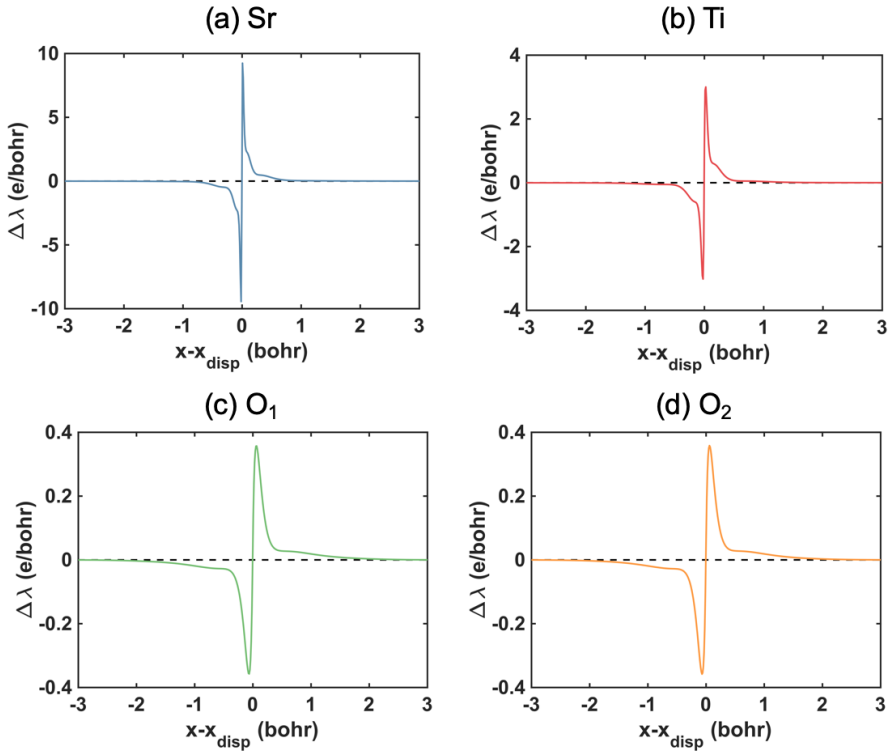

Figure 4.4. Differences in the planar-averaged charge density of supercells with displaced atoms and an unperturbed supercell. (a)-(d) show this difference for each displacement contributing to μ_{1111} in STO.

Because of this localization, moments of this charge density distribution,

$$Q^{(n)} = \frac{1}{u}\int \Delta\lambda(x - x_{disp})\,(x - x_{disp})^n\,dx \tag{4.41}$$

where $Q^{(n)}$ is the nth moment of the change in the charge density about the displaced atom $\Delta\lambda(x - x_{disp})$ which has been displaced by u, are well converged. Cumulative integrals of the first and third moments of Sr, Ti, O1, and O2/O3 are shown in Figure 4.5 to depict the numerical stability of these quantities. While we have found there are some

oscillations in the 3rd order moments at large distances from the displaced atom (e.g. Figure 4.5(f) at $x - x_{disp} = 20$ bohr), these oscillations do not affect the overall result and can be easily filtered with a low pass filter.

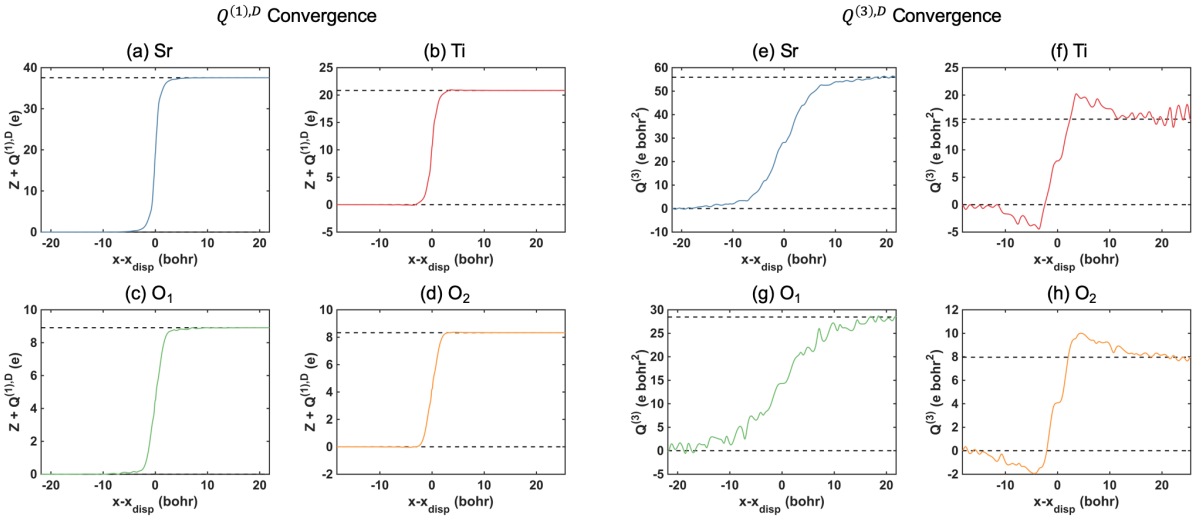

Figure 4.5. Cumulative integrals of moments of the differences in the planar-averaged charge density of supercells with displaced atoms and an unperturbed supercell for each displacement contributing to μ_{1111} in STO. (a)-(d) show the first moment convergence and (e)-(h) show the third moment convergence.

Like the changes in charge density brought about by sub-lattice displacements, the forces induced by sub-lattice displacements are also localized to within a few bohr of the displaced atom. The forces arising from Sr, Ti, O1, and O2/O3 displacements are shown in Figure 4.6. As a result, second moments of the force distribution about the position of the displaced atom, given by

$$T_j = -\frac{1}{2u} \sum_i F_{i,j} \left(x_i - x_{disp}\right)^2 \tag{4.42}$$

where $F_{i,j}$ is the force on atom i owing to the displacement u of atom j and $x_i - x_{disp}$ is the distance from atom i to the displaced atom, are well-behaved quantities. Cumulative sums of the second moments of the forces are shown in Figure 4.7 for Sr, Ti, O1, and O2/O3 displacements to demonstrate the numerical stability of the second-order force moments.

Similar levels of convergence were found for the charge density and force moments computed from the rotated supercell, so those plots are not shown here.

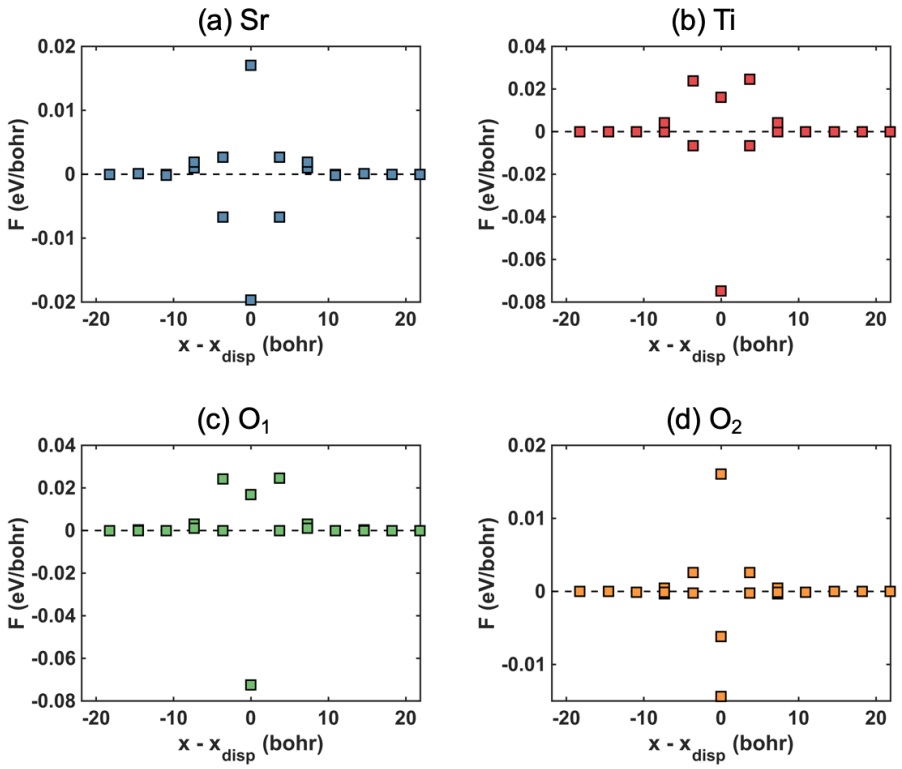

Figure 4.6. Differences in the forces of supercells with displaced atoms and an unperturbed supercell. (a)-(d) show this for each displacement contributing to μ_{1111} in STO.

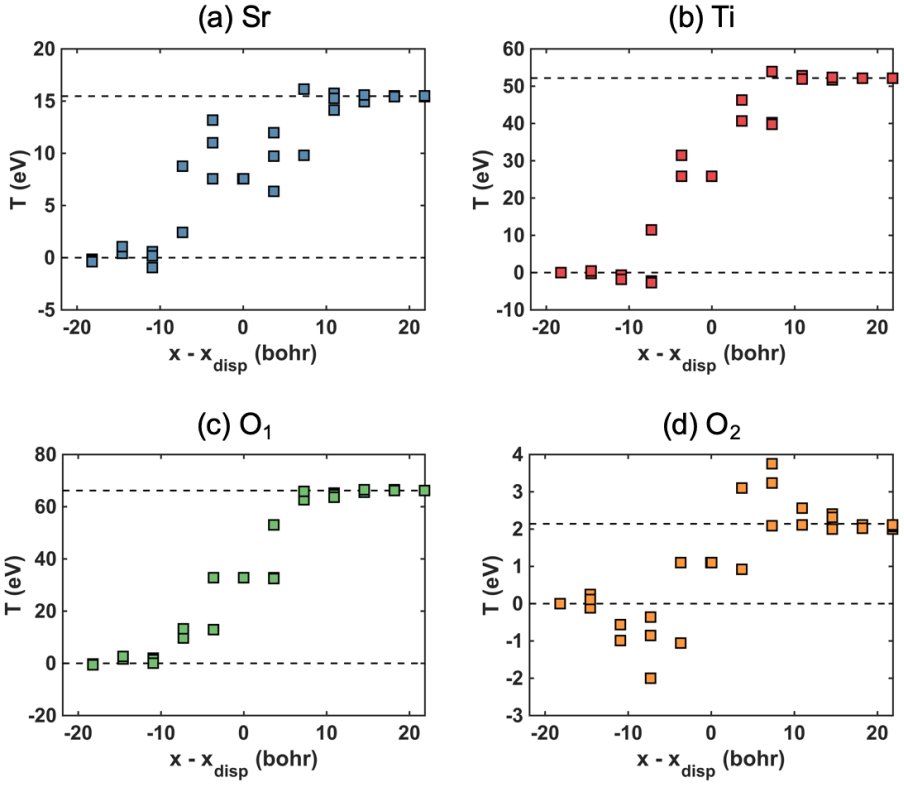

Figure 4.7. Cumulative sum of the second moment of the differences in the forces of supercells with displaced atoms and an unperturbed supercell. (a)-(d) show this for each displacement contributing to μ_{1111} in STO.

4.4.3. Comparison to Literature

Having shown how the various "microscopic flexoelectric coefficient ingredients" are computed with WIEN2k and demonstrated that they are well-behaved quantities, we now compare the results of these calculations with those in the literature. Literature values have been reported in terms of symmetry-adapted modes (ξ_i) instead of atomic quantities, so we report our quantities in Table 4.1 according to this same convention. See Ref. [**58**] for the definitions of these modes. Note, in this section we will merely compare the values shown in Table 4.1; their physical significance is discussed in Section 4.5 and 4.6.

In general, we find good agreement with literature values. The Callen charges in our calculations are nearly identical to the Callen charges reported by Hong and Vanderbilt [**58**], as well as those reported by Stengel [**150**]. We find the acoustic sum rule for the Callen charges is also well-maintained with

$$Q_{Sr}^{(1),D} + Q_{Ti}^{(1),D} + Q_{\xi_3}^{(1),D} + Q_{\xi_4}^{(1),D} = -0.01 \tag{4.43}$$

according to the definitions of the symmetry adapted modes [**58**].

The T and $Q^{(3)}$ values reported here and in the literature are also close. Our calculations agree with those performed by Stengel [**150**] (which is encouraging because those calculations were performed with an entirely different approach) and largely match those reported by Hong and Vanderbilt [**58**]. There are some slight differences with the Hong and Vanderbilt [**58**] values, particularly with respect to oxygen contributions (ξ_3 and ξ_4). It is unclear if this is a consequence of the choice of oxygen pseudopotential, an artifact of the rigid-core correction needed for pseudopotential codes, a typographical error (there are several in Ref. [**58**]), or something else entirely. Without other calculations for comparison it is difficult to address the origin of these differences. Ultimately, these differences do not have a significant impact on the flexoelectric coefficients as our values and the Ref. [**58**] values are within a few nC/m of one another.

4.5. Impact of the Exchange and Correlation Functional on the Bulk Flexoelectric Coefficients of $SrTiO_3$

Having demonstrated that the implementation of the first principles theory of flexoelectricity in WIEN2k yields comparable values to the literature, now I investigate the

(a) $Q^{(1),D}$ (e)

	MM	HV	S
Sr	0.41	0.39	0.41
Ti	1.15	1.20	1.17
ξ_3	-0.91	-0.92	-0.92
ξ_4	-0.47	-0.47	-0.47

(b) $Q_{L1}^{(3),D}$ (e bohr^2)

	MM	HV
Sr	-55.92	-57.5
Ti	-15.61	-16.2
ξ_3	-28.47	-28.6
ξ_4	-11.27	-9.5

(c) $Q_{L2}^{(3),D}$ (e bohr^2)

	MM	HV
Sr	-45.42	-43.5
Ti	-44.54	-45.0
ξ_3	-30.61	-44.0
ξ_4	4.65	7.7

(g) μ_{ijkl}^{E} (nC/m)

	MM	HV
μ_{1111}^{E}	-40.98	-36.9
μ_{1122}^{E}	-42.67	-40.2
μ_{1212}^{E}	-1.63	-1.4

(d) T_{L1}^{D} (eV)

	MM	HV	S
Sr	15.43	17.0	16.3
Ti	52.18	52.3	49.1
ξ_3	66.15	68.7	67.2
ξ_4	2.99	3.6	3.0

(e)T_{L2}^{D} (eV)

	MM	HV	S
Sr	32.48	35.7	33.2
Ti	36.87	38.9	36.3
ξ_3	25.73	13.1	24.9
ξ_4	21.06	18.2	22.7

(f) T_{1122}^{E} (eV)

	MM	HV	S
Sr	7.71	8.4	7.9
Ti	4.08	3.0	3.8
ξ_3	15.57	15.7	15.3
ξ_4	11.44	12.0	11.6

Table 4.1. Comparison between the flexoelectric $Q^{(n)}$ and T components and flexoelectric tensor coefficients computed here with LDA and reported in the literature. MM = Mizzi and Marks, HV = Hong and Vanderbilt [**58**], S=Stengel [**150**].

impact of the exchange and correlation functional on the bulk flexoelectric coefficients of STO. Analyzing the sensitivity of DFT predictions to the exchange and correlation functional is standard, but has not been performed for flexoelectric calculations. The same computational approach described in Section 4.4 is utilized here except the exchange and correlation terms are approximated using LDA, PBE [**151**], PBEsol [**152**], and PBEsol + on-site hybrid [**153, 154**] approach (on-site hybrid fraction of 0.25 applied to Ti3d).

First, the optimized lattice parameters are compared in Table 4.2. Our calculations reproduced the documented under- and over-estimation of the lattice parameter when using LDA and PBE, respectively, and the good agreement between the experimental lattice parameter [**118**] and the optimized lattice parameter with PBEsol [**155**]. The on-site hybrid approach does the best job of reproducing the experimental lattice parameter among the investigated functionals.

Born charges are a dynamical charge which reflect hybridization [**142**]. It is common for ABO_3 perovskites to have anomalous Born charges, i.e. values which differ from nominal charges expected in an ionic limit [**156**]. The Born charges shown in Table 4.2 agree with those reported in the literature, with large anomalies for Ti and O1 (∼3e), a smaller anomaly for Sr (∼0.55 e), and minimal deviation from the nominal value for O2/O3 (∼0.01 e) [**142**]. The values of the Sr and O2 Born charges are found to be largely insensitive to the choice of functional, whereas the Ti and O1 Born charges anomalies are slightly larger for PBE and significantly smaller for the PBEsol + on-site hybrid approach. This reduction in the anomalous Born charges on the Ti and O1 sites is a consequence of the improved treatment of hybridization between Ti and O1 with the PBEsol+on-site hybrid scheme. Similar behavior in the Born charges with respect to functional have been reported in the literature for rutile and anatase TiO_2 [**157**].

(a) Lattice Parameters (bohr)

LDA	PBE	PBEsol	PBEsol + hybrid	Exp.
7.290	7.446	7.362	7.380	7.379

(b) Born Charge (e)

	LDA	PBE	PBEsol	PBEsol + hybrid
Sr	2.55	2.55	2.55	2.56
Ti	7.12	7.16	7.12	6.58
O1	-5.63	-5.72	-5.66	-5.19
O1	-2.04	-2.01	-2.02	-1.99

Table 4.2. (a) Optimized lattice parameter versus experiment and (b) Born charges for STO computed with different exchange and correlation functionals. Lattice parameters are in bohr and Born charges are in e.

Unlike the variations in the STO Born charges ($Q^{(1),E}$ or Z^*) with the choice of functional, we find the Callen charges ($Q^{(1),D}$) reported in Table 4.3 are nearly identical when the functional is changed. Both are measures of dynamical charge which are defined for different electrostatic boundary conditions and related via the high frequency dielectric constant [**142, 58**]. For cubic materials this relationship is

$$Q^{(1),E} = Q^{(1),D}\varepsilon^{\infty}. \tag{4.44}$$

Our results indicate the decrease in the Born charge anomalies in Ti and O1 through the use of the on-site hybrid are matched by a decrease in the high frequency permittivity: high frequency dielectric constants from Eq. 4.44 are 6.18, 6.18, 6.22, and 5.64 with the LDA, PBE, PBEsol, and PBEsol+hybrid functionals, respectively.

The octupole moments in Table 4.3 have larger variations with the choice of functional than the Callen charges. The most significant changes in $Q^{(3),D}$ with functional are associated with oxygen displacements (as much as $\sim$15% compared to the LDA values), while the Sr and Ti octupolar moments are largely unaffected by functional ($<$5% change compared to the LDA values). All computed $Q^{(3),D}$ describing the longitudinal change in charge density to a longitudinal displacement are negative and those describing the longitudinal change in charge density to a transverse displacement (i.e. $Q^{'(3),D}_{O1,12}$) are positive. The negative, largely consistent $Q^{(3),D}$ values suggest the longitudinal response is dominated by the mostly rigid shift in the electron density caused by the atomic displacement [**58, 59**]. Across all functionals $Q^{(3),D}$ values are much larger for Sr than Ti, which is somewhat surprising since the opposite is true for $Q^{(1),D}$. This is explored further in Section 4.6.

(a) $Q_{11}^{(1),D}$ (e)

	LDA	PBE	PBEsol	PBEsol +hybrid
Sr	0.41	0.41	0.41	0.45
Ti	1.15	1.16	1.15	1.17
O1	-0.91	-0.93	-0.91	-0.93
O2	-0.33	-0.32	-0.33	-0.35

(b) $Q_{1111}^{(3),D}$ (e bohr^2)

	LDA	PBE	PBEsol	PBEsol +hybrid
Sr	-55.92	-57.44	-56.50	-54.74
Ti	-15.61	-14.67	-15.28	-15.74
O1	-28.47	-29.39	-28.73	-27.88
O2	-7.97	-7.31	-7.70	-8.68

(c) $Q'^{(3),D}_{1111}$ (e bohr^2)

	LDA	PBE	PBEsol	PBEsol +hybrid
Sr	-50.67	-51.59	-51.01	-49.71
Ti	-30.07	-30.21	-30.14	-30.51
$O1_{(11)}$	-17.70	-17.94	-17.79	-17.89
$O1_{(12)}$	5.80	6.64	6.08	5.55
O3	-6.10	-5.34	-5.74	-6.78

(d) T_{1111}^{D} (eV)

	LDA	PBE	PBEsol	PBEsol +hybrid
Sr	15.43	13.63	14.85	14.69
Ti	52.18	43.07	48.32	50.31
O1	66.15	57.24	62.97	64.42
O2	2.12	2.27	1.97	2.35

(e) T'^{D}_{1111} (eV)

	LDA	PBE	PBEsol	PBEsol +hybrid
Sr	23.95	21.91	22.86	22.96
Ti	44.52	39.67	42.26	43.65
$O1_{(11)}$	33.16	30.63	32.12	32.52
$O1_{(12)}$	-12.78	-10.43	-12.18	-12.62
O_3	-3.36	-3.95	-3.60	-3.72

(f) T_{1122}^{E} (eV)

	LDA	PBE	PBEsol	PBEsol +hybrid
Sr	7.71	6.5	7.37	7.73
Ti	4.08	4.51	4.22	5.38
O1	17.30	16.99	16.80	16.26
O2	15.57	15.44	15.26	14.95
O3	-1.12	-2.06	-1.45	-1.61

Table 4.3. Variation in components used to calculate flexoelectric coefficients with functional. (a) Callen charges, (b) octupole moments, and (d) second order force moments computed from the supercell with the [100] long axis. (c) Octupole moments and (e) second order force moments computed from the supercells with the [110] long axis. (f) Transverse second order force moments computed from the supercell with the [100] long axis. O1, O2, and O3 are defined in Figure 4.3. The (11) and (12) subscripts denote the longitudinal and transverse displacements needed for $Q'^{(3),D}$ and T'^{D}.

The T values correspond to sub-lattice resolved elastic constants [**59**] which are related to the stiffness coefficients via

$$c_{\alpha\beta\gamma\delta} = \frac{1}{\Omega}\sum_I T_{I,\alpha\beta\gamma\delta}. \tag{4.45}$$

The values in Table 4.3 combined with the lattice parameters in Table 4.2 yield the stiffness constants given in Table 4.4. These values are consistent with literature calculations computed through the traditional energy-based approach [**158, 159, 150**]. The elastic constants in Table 4.4 suggest PBE does the best job of modeling elasticity in STO with LDA, PBEsol, and PBEsol+hybrid predicting far too large a longitudinal stiffness.

Importantly, unlike traditional elastic constant calculations, the data in Table 4.3 gives a site-by-site breakdown of the contributions to the elastic constants [**59**]. For instance, these calculations indicate c_{1111} in STO is dominated by Ti and O1 contributions and oxygen contributions largely dictate c_{1122}. When combined with elastic stability conditions (e.g. for cubic materials $c_{1111} - c_{1122} > 0$ [**144, 160**]), the data in Table 4.3 is an alternative way to interpret structural instabilities. As an example, $T_{O2,1111} - T_{O2,1122} < 0$ which suggests a structural instability associated with O2 [**155**]. The relationship between $T_I, ijkl$ and c_{ijkl} demonstrates first principles flexoelectric theory and calculations of the sort described here could be of use in other contexts.

	LDA	PBEsol	PBE	PBEsol + hybrid	Exp.
c_{1111}	384.6	309.8	351.9	360.3	317
c_{1122}	121.4	108.4	114.2	114.7	103
c_{1212}	113.3	101.8	107.1	106.2	123

Table 4.4. Elastic constants computed from T values in Table 4.3 and optimized lattice parameters in Table 4.2 compared to experimental values from Ref. [**161**]. All values are in GPa.

Ultimately, using the values of $Q^{(n)}$ and T in Table 4.3 with Eq. 4.2, 4.4, and 4.9 allows one to calculate the three flexoelectric coefficients of STO. We find the differences in $Q^{(n)}$ and T stemming from the use of different functionals only lead to minor variations in the flexoelectric coefficients $\sim$1 nC/m as shown in Table 4.5. The effects of these differences

are most significant on the shear coefficient owing to its small magnitude, but these differences are well within the currently available experimental precision of flexoelectric coefficient measurements.

	LDA	PBEsol	PBE	PBEsol + hybrid
μ^E_{1111}	-40.98	-40.82	-41.03	-40.42
μ^E_{1122}	-42.67	-42.18	-41.69	-40.18
μ^E_{1212}	-1.63	-1.40	-1.09	-2.00

Table 4.5. Variation in the three independent flexoelectric coefficients under short-circuit boundary conditions with the exchange and correlation functional. All values are in nC/m.

4.6. Flexoelectricity in (Pseudo) Cubic Perovskites

4.6.1. Materials and Computational Parameters

Now we utilize the first principles of theory introduced in Section 4.2 with the implementation using WIEN2k described in Section 4.3 to calculate the flexoelectric coefficients in some of the materials measured in Chapter 3. We will focus on four (pseudo) cubic perovskites: STO, KTO, LAO, and GSO. Both STO and KTO are cubic perovskites with space group $Pm\overline{3}m$ at room temperature and atmospheric pressure, so the flexoelectric coefficient computed from first principles should be directly comparable to the measured flexoelectric coefficients. LAO is a rhombohedral perovskite with space group $R\overline{3}c$ at room temperature and atmospheric pressure, however the deviations from the cubic structure are small (pseudocubic angle is 90.086°[**97**]) so we approximate LAO as a cubic perovskite with space group $Pm\overline{3}m$ for these calculations. GSO is an orthorhombic perovskite with space group Pnma at room temperature and atmospheric pressure. It is investigated in this section because it is isostructural with Pnma perovskites which exhibited large

flexoelectric responses in Chapter 3, but chosen over DSO because it lacks the f electron complexity (Gd is 4f7) and over YAO because it has been studied extensively in WIEN2k (e.g., Chapter 7). I also make the crude approximation to treat GSO as a cubic perovskite with space group $Pm\overline{3}m$ for these calculations. While this structure is not physical, the calculated flexoelectric coefficients are still informative and we address the shortcomings of this approximation in Section 4.8.

It was shown in Section 4.5 that different exchange and correlation functionals yielded internal differences in the components used to calculate flexoelectric coefficients in STO, but that these differences largely canceled such that the flexoelectric coefficients were not particularly sensitive to the functional choice. As such, the calculations in this section use the PBEsol [**152**] functional for STO, KTO, and LAO, and a PBEsol + hybrid [**153, 154**] approach (with on-site hybrid fractions of 0.80, 0.50, and 0.38 for Sc3d, Gd5d, and Gd4f, respectively [**162**]) for GSO. The procedure outlined in Section 4.3 was followed here with regards to supercell construction and all calculations were performed with the all-electron augmented plane wave + local orbitals WIEN2k code. Muffin-tin radii of 2.44, 1.72, 2.36, 1.65, 2.26, 1.80, 2.02, 1.82, 1.64 bohr were used for Sr, Ti, La, Al, K, Ta, Gd, Sc, and O, respectively. A plane-wave expansion parameter RKMAX of 6, energy cut-off of -6 Ry, k-mesh equivalent to 8x8x8 per bulk conventional unit cell, and Mermin functional at room temperature were used in all calculations with convergence criteria of 10^{-6} e, 10^{-4} Ry, and 10^{-3} mRy/bohr. The optimized lattice constants provided in Table 4.6 largely agree with the experimental values [**118, 86, 97, 125**].

	$SrTiO_3$	$KTaO_3$	$LaAlO_3$	$GdScO_3$
a_{DFT}	7.362	7.537	7.131	7.625
a_{exp}	7.379	7.538	7.156	7.502

Table 4.6. Comparison between optimized and (pseudo)-cubic experimental [**118, 86, 97, 125**] lattice parameters in bohr.

4.6.2. Flexoelectric Coefficient Calculations

Table 4.7 includes all the internal components used in Eq. 4.2, 4.4, and 4.9 to compute the flexoelectric coefficients for the four investigated materials. Beginning with the Callen charge, we find the $Q^{(1),D}$ values track with the known Born charge anomalies in these materials: STO and KTO have anomalous charges on the B and O1 sites, and LAO and GSO have smaller charge anomalies present on all sites. In all materials the acoustic sum rule is obeyed to $\sim$0.01e.

The octupole moments in the four materials are negative (except for the transverse components of STO and KTO) and exhibit large variations in their magnitudes depending on the chemical species. The magnitudes of the octupole moments do not track with dynamical charge anomalies nor simply scale with atomic number. For example, KTO has nearly equal A, B, and O1 $Q^{(3),D}_{1111}$ values and STO has a much larger $Q^{(3),D}_{1111}$ A value than B value, even though both materials have sizable charge anomalies on the B site and the atomic numbers of K and Ta differ significantly. This suggests the dynamical charge intuition developed in the context of ferroelectricity might require revisiting for octupole moments and indicates that flexoelectricity obeys different design rules than more familiar properties.

To further understand the octupole moments, consider an isolated atom in volume Ω with a spherically symmetric charge distribution $\rho(\mathbf{r})$ and corresponding potential $V(\mathbf{r})$

(a) $Q_{11}^{(1),D}$ (e)

	STO	KTO	LAO	GSO
A	0.41	0.21	0.93	0.90
B	1.15	1.57	0.60	0.67
O1	-0.91	-1.19	-0.50	-0.61
O2	-0.33	-0.30	-0.51	-0.46

(b) $Q_{1111}^{(3),D}$ (e bohr^2)

	STO	KTO	LAO	GSO
A	-56.50	-37.01	-64.82	-67.37
B	-15.28	-34.43	-20.10	-30.03
O1	-28.73	-37.69	-9.93	-14.87
O2	-7.70	-7.89	-12.69	-11.58

(c) $Q'^{(3),D}_{1111}$ (e bohr^2)

	STO	KTO	LAO	GSO
A	-51.01	-33.49	-64.38	-62.81
B	-30.14	-53.64	-24.45	-38.20
$O1_{(11)}$	-17.79	-21.68	-11.95	-12.50
$O1_{(12)}$	6.08	9.15	-1.26	-1.30
O3	-5.74	-5.02	-15.79	-11.44

(d) T_{1111}^{D} (eV)

	STO	KTO	LAO	GSO
A	14.85	11.65	35.90	20.85
B	48.32	78.56	21.83	53.52
O1	62.97	100.62	33.36	73.81
O2	1.97	-0.39	14.28	1.81

(e) T'^{D}_{1111} (eV)

	STO	KTO	LAO	GSO
A	22.03	17.93	36.77	16.00
B	42.26	51.77	34.06	46.23
$O1_{(11)}$	32.12	39.02	29.37	33.37
$O1_{(12)}$	-12.18	-21.44	-3.79	-15.04
O3	-3.60	-1.61	2.68	-15.60

(f) T_{1122}^{E} (eV)

	STO	KTO	LAO	GSO
A	7.37	7.08	10.42	3.31
B	4.22	1.85	13.07	6.90
O1	16.80	16.62	14.45	11.85
O2	15.26	14.10	16.20	12.06
O3	-1.45	-0.10	0.81	-7.22

Table 4.7. Components used to calculate flexoelectric coefficients for STO, KTO, LAO, and GSO. (a) Callen charges, (b) octupole moments, and (d) second order force moments computed from the supercell with the [100] long axis. (c) Octupole moments and (e) second order force moments computed from the supercells with the [110] long axis. (f) Transverse second order force moments computed from the supercell with the [100] long axis. A, B, O1, O2, and O3 refer to the sites in the ABO_3 cubic perovskite. O1, O2, and O3 are defined in Figure 4.3. The (11) and (12) subscripts denote the longitudinal and transverse displacements needed for $Q'^{(3),D}$ and T'^{D}.

given by Poisson's Equation

$$\nabla^2 V(\mathbf{r}) = -\frac{\rho(\mathbf{r})}{\varepsilon_0}. \tag{4.46}$$

In reciprocal space, this equation can be rewritten as

$$v(\mathbf{k}) = -\frac{1}{4\pi^2 k^2 \varepsilon_0} f(\mathbf{k}) \tag{4.47}$$

where $v(\mathbf{k})$ and $(\mathbf{k})$ are the Fourier transforms of $V(\mathbf{r}$ and $\rho(\mathbf{r}$, respectively [**163**].

Following Ref. [**163**], the $\mathbf{k} = 0$ component of $v(\mathbf{k})$ is related to the average Coulomb potential in Ω which, as discussed in Chapter 5, can be expressed in terms of electron scattering factors [**163, 164**]

$$\overline{V} = \frac{1}{\Omega}\int V(\mathbf{r}) d\Omega = \frac{v(0)}{\Omega} = \frac{h^2}{2\pi m e \Omega} f^{el}(0) \tag{4.48}$$

from which it follows that

$$v(0) = \frac{h^2}{2\pi m e} f^{el}(0). \tag{4.49}$$

Becker and Coppens [**165**] have shown that an alternative expression for $v(0)$ can be obtained from taking Eq. 4.47 in the $k \to 0$ limit:

$$v(0) = \lim_{k\to 0}\left(-\frac{1}{4\pi^2 k^2 \varepsilon_0}\langle f(k)\rangle\right). \tag{4.50}$$

In Eq. 4.50 $\langle f(k)\rangle$ is the orientational average of $f(\mathbf{k})$ which to leading order in k is

$$\langle f(k)\rangle = -\frac{2\pi^2}{3} k^2 \int r^2 \rho(r) d\Omega. \tag{4.51}$$

Combining Eq. 4.51 with Eq. 4.50 leads to

$$v(0) = -\frac{1}{6\varepsilon_0}\int r^2 \rho(r) d\Omega. \tag{4.52}$$

This new form for $v(0)$ is of interest because the integral in Eq. 4.52 represents the *static* quadrupole moment of the charge distribution on an isolated atom. Stengel [**137**] has shown that this quantity is equal to the octupole moment of the change in charge density induced by a longitudinal atomic displacement defined by Eq. 4.3. Therefore, Eq. 4.52 can be rewritten as

$$v(0) = -\frac{1}{6\varepsilon_0} Q^3_{1111} \tag{4.53}$$

which can be combined with Eq. 4.48 to express the induced octupole moments in terms of electron scattering factors and fundamental constants.

$$Q^3_{I,1111} = -\frac{3\varepsilon_0 h^2}{\pi m e} f^{el}_I(0) \tag{4.54}$$

Therefore, electron scattering factors can be used to compare the DFT computed values of $Q^{(3)}_{I,1111}$ to their atomic and ionic limits. Note, these limits do not represent bounds on the values of $Q^{(3)}_{I,1111}$ because Eq. 4.53 is derived assuming the charge densities are rigid. Instead, these limits indicate the similarity between the spatial distribution of the charge density of a chemical species in a crystal and the isolated atomic and ionic charge densities.

The values of $Q^{(3)}_{I,1111}$ calculated for each chemical species in Table 4.7 using the atomic and ionic electron scattering factors taken from Ref. [**166**] are shown in Table 4.8. We find that all values are negative, which must be true since the fundamental constants and electron scattering factors in Eq. 4.53 are positive quantities. The values in Table 4.7 for the A and B sites in each perovskite (except for Ti in STO) are approximately halfway between the atomic and ionic charge densities in Table 4.8 indicating a significant redistribution

of charge is associated with A and B site displacements. The DFT computed Ti octupole moment is much closer to the ionic charge density value than the other moments which is surprising given the Born charge anomaly on the Ti site in STO. This further indicates that the octupole moments cannot be simply considered higher order Born charges. The O1 site in STO and KTO has much larger octupole moments than the ionic values in Table 4.8, indicating the O1 site displacement leads to significant charge redistribution. The O1 site in LAO and GSO as well as the O2/O3 sites in all the perovskites have similar octupole moments to the atomic values in Table 4.8 . Ultimately, this comparison demonstrates the necessity of performing the DFT calculations to accurately model the changes in charge density caused by an atomic displacement, but also suggests Eq. 4.53 provides a back-of-the-envelope method to predict the electronic contributions to bulk flexoelectric coefficients and interpret DFT computed values.

	Atomic $f^{el}(0)$	Ionic $f^{el}(0)$
Sr	-73.71	-26.27
Ti	-49.46	-10.45
K	-50.43	-19.44
Ta	-73.30	
La	-100.35	-39.02
Al	-33.25	-3.62
Gd	-86.49	-35.12
Sc	-52.43	-12.51
O	-11.24	-23.23

Table 4.8. $Q^{(3)}$ values computed using atomic and ionic electron scattering factors according to Eq. 4.53. Scattering factors are taken from Ref. [**166**]. Note, an ionic electron scattering factor for Ta was not included in Ref. [**166**].

Next, we focus on the second order force moments in Table 4.7. Cubic STO, KTO, LAO, and GSO are found to have rather different elastic properties. Converting the

second order force moments to stiffness constants using Eq. 4.45 and the optimized lattice parameters in Table 4.6 yields the values in Table 4.9. These stiffness coefficients are in moderately good agreement with other calculations, but poor agreement with experiment [**167, 159, 168**], as expected with using the PBEsol functional (e.g. Table 4.4). Although the agreement with experiment is poor, the second order force moments in Table 4.7 still provide insight as sub-lattice resolved stiffness coefficients. The longitudinal stiffness of STO, KTO, and GSO are found to be dominated by O1 contributions with minimal O2/O3 contributions whereas LAO has comparable contributions from all atoms in in the structure. Additionally, the T values indicate an elastic instability in the O2 site [**144, 160**] is in all investigated materials.

	$SrTiO_3$	$KTaO_3$	$LaAlO_3$	$GdScO_3$
c_{1111}	351.9	476.6	356.3	369.7
c_{1122}	114.2	99.8	163.5	65.5
c_{1122}	107.1	78.4	133.9	58.5

Table 4.9. Elastic constants computed from T values in Table 4.7 and optimized lattice parameters in Table 4.6. All values are in GPa.

Combining the values in Table 4.7 with Eq. 4.2, 4.4, and 4.9 yields the three independent flexoelectric coefficients for STO, KTO, LAO, and GSO given in Table 4.10(a). In all materials, we find longitudinal and transverse coefficients of similar magnitude with shear coefficient an order of magnitude smaller, independent of the choice of electrostatic boundary condition. Under the short-circuit boundary conditions, the large dielectric constant of STO and KTO (an order of magnitude larger than the dielectric constant in LAO and GSO) manifests in proportionally larger flexoelectric coefficients. The open-circuit values are given as flexocoupling voltages in Table 4.10(b). They are determined

according to

$$f_{ijkl} = \frac{\mu^E_{ijkl}}{\chi \varepsilon_0} \tag{4.55}$$

where χ is the dielectric susceptibility [**112, 125, 126, 100, 90, 91**] and ε_0 is the permittivity of free space, and are essentially constant across all the materials.

(a) μ^E_{ijkl} (nC/m)

	$SrTiO_3$	$LaAlO_3$	$KTaO_3$	$GdScO_3$
μ^E_{1111}	-40.82	-30.26	-3.86	-3.50
μ^E_{1122}	-42.18	-36.07	-3.98	-3.46
μ^E_{1212}	-1.40	-2.05	-0.16	0.10

(b) f (V)

	$SrTiO_3$	$LaAlO_3$	$KTaO_3$	$GdScO_3$
f_{1111}	-14.93	-14.19	-17.45	-14.56
f_{1122}	-15.42	-16.91	-17.99	-20.15
f_{1212}	-0.51	-0.96	-0.72	0.58

Table 4.10. Independent (a) flexoelectric coefficients and (b) flexocoupling voltages in STO, KTO, LAO, and GSO.

4.7. Experimental Comparison

Using the values for the flexoelectric tensor components in Table 4.10 and the formulas developed in Chapter 3, it is possible to predict the effective flexoelectric response to TPB. Table 4.11 provides the effective flexoelectric coefficient for samples with ⟨100⟩ (pseudo)-cubic edges in the beam bending (unclamped) and plate bending (fully clamped) limits (as defined in Chapter 3). The predicted flexoelectric responses significantly differ from the measured responses in all cases. In STO, KTO, and LAO, the sign and magnitude do not

agree with experiment, and in GSO the magnitude is four times too small. Admittedly, it is possible that the poor agreement between the LAO and GSO predictions/experiments could stem from the approximations made in treating the two structures as cubic perovskites, but the agreement with the simpler, truly cubic perovskites STO and KTO is even worse. This indicates some missing physics in the theory described in this chapter.

	Beam (ϕ=0)	Plate (ϕ=1)	Exp.
$SrTiO_3$	-22.36	-29.38	+12.4±0.6
$KTaO_3$	-25.92	-30.60	+4.4±0.5
$LaAlO_3$	-1.83	-2.52	+3.2±0.3
$GdScO_3$	-1.70	-2.41	-8.1±0.4

Table 4.11. Effective short-circuit flexoelectric coefficients for cubic samples with ⟨100⟩ edges computed from the tensor components in Table 4.10 for the beam and plate bending limits compared with experimental values from Chapter 3. All values are in nC/m.

4.8. Lattice Quadrupole Contribution in $LaAlO_3$ and $GdScO_3$

The poor agreement between the first principles flexoelectric coefficients calculated here and the measured flexoelectric coefficients for STO and KTO is resolved in Chapter 5. However, the mean-inner potential (MIP) correction introduced in the next chapter does not fix the disagreement between the predicted and measured coefficients for LAO and GSO. This issue likely originates from approximating LAO, a rhombohedral perovskite, and GSO, an orthorhombic perovskite, as cubic perovskites. While this is a common approximation for LAO given its small structural distortions, this approximation dramatically oversimplifies the highly distorted lanthanide scandate structure.

Within the context of the first principles theory of bulk flexoelectricity, approximating both structures as cubic artificially sets all lattice-quadrupole contributions to the bulk

flexoelectric coefficient, i.e. terms associated with Raman active modes, to zero (Section 4.2). In reality, O and La sites in R$\overline{3}$c LAO contribute to 4 and 1 zone-center Raman active modes, respectively. Gd/O1 and O2 sites in Pnma GSO contribute to 6 and 12 zone-center Raman active modes, respectively [**169**]. The supercell approach adopted for these calculations is ill-suited for investigating this large number of modes, and it is difficult to estimate the magnitude of these contributions for these structures because, to my knowledge, lattice-quadrupole terms have not been computed in distorted perovskites (Hong and Vanderbilt [**58**] calculated this term for C and Si, but there is no reason to think those values apply in oxides). Suggestions for how to approach this problem are provided as future research directions Chapter 9.

4.9. Shortcomings of Bulk Flexoelectric Theory

Not only is the agreement poor between the experimental measurements of flexoelectricity in single crystals and the first principles calculations, but even more troubling is that the first principles theory of flexoelectricity predicts metals to have non-zero flexoelectric coefficients. To illustrate the latter point, DFT calculations were performed with the all-electron augmented plane wave + local orbitals WIEN2k code on FCC Al using the LDA functional [**148**] to treat exchange and correlation effects. Muffin-tin radius of 2.5 bohr was used for Al with a plane-wave expansion parameter RKMAX of 7, energy cut-off of -6 Ry, k-mesh equivalent to 20×20×20 per bulk conventional unit cell, and Mermin functional at room temperature. Convergence criteria of 10^{-6} e, 10^{-4} Ry, and 10^{-3} mRy/bohr were used. Together, this yielded a bulk optimized lattice parameter of

7.54 bohr (experimental 7.65 bohr). The procedure outlined in Section 4.3 was followed regarding to the construction of an 8 unit cell long supercell with a [100] long axis.

Figure 4.8 contains the change in the charge density associated with the displacement of an Al atom in FCC Al and the moments of the change in charge density associated with this displacement. We find the dipole and quadrupole moments are zero: the former is a requirement for a metal because a metal has a dielectric constant of infinity and the latter is a consequence of the Al site possessing inversion symmetry. As a result, any lattice-dipole and lattice-quadrupole contributions to flexoelectric coefficients in Al are zero.

Unlike the dipole and quadrupole moments, the octupole moment in Figure 4.8 is finite. Simplifying Eq. 4.2 with this charge density moment indicates a non-zero flexoelectric coefficient of

$$\mu^D_{1111} = \frac{Q^{(3),D}_{Al}}{6\Omega} = -122.17\frac{pC}{m} \tag{4.56}$$

and non-zero flexocoupling voltage

$$f_{1111} = \frac{\mu^D_{1111}}{\varepsilon_0} = -13.80V. \tag{4.57}$$

These calculations suggest that a metal subjected to a strain gradient would become polarized, which we know is not possible. While the theoretical framework developed in this chapter is sound, we will see in the next chapter it is incomplete: the physical interpretation of the flexoelectric coefficients given by Eq. 4.2, 4.4, and 4.9, and flexoelectricity in general, requires careful consideration of surfaces. Through treating the integral role

(a)

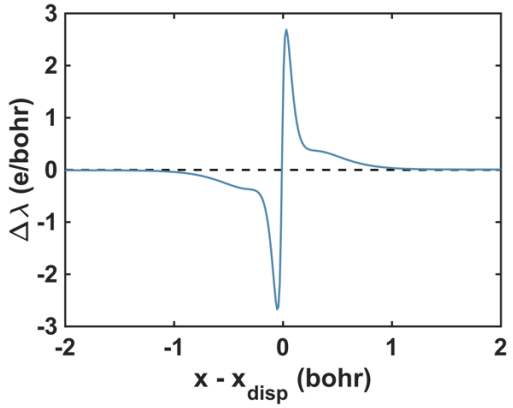

(b)

$Q^{(1),D}$ (e)	-0.0023
$Q^{(2),D}$ (e bohr)	0.0001
$Q^{(3),D}$ (e bohr^2)	-26.6515

Figure 4.8. (a) Differences in the planar-averaged charge density of supercells with a displaced Al atom and an unperturbed supercell. (b) Moments of the charge distribution in (a) about the position of the displaced atom.

of the MIP in flexoelectricity in Chapter 5, we resolve the disagreement with experiment in Table 4.11 for KTO and STO, and the notion of flexoelectric polarization in a metal indicated by Figure 4.8.

CHAPTER 5

The Role of Surfaces in Flexoelectricity

5.1. Introduction

The first principles theory of flexoelectricity [**135, 136, 58, 59, 138**] described in Chapter 4 makes significant progress toward a predictive, microscopic model for flexoelectricity. Unfortunately, as described at the end of Chapter 4, this theory has some serious shortcomings:

(1) The bulk flexoelectric coefficients predicted by this theory and experimental measurements on high-quality, single crystalline samples often differ in both magnitude and sign.
(2) The theory predicts non-zero bulk flexoelectric coefficients for metals.

It is common in the literature to attribute this discrepancy to surface contributions to the measured flexoelectric response, which are not present in the theory used in Chapter 4. The first identification of the importance of surfaces in the flexoelectric response of finite bodies can be traced to phenomenological theory [**128**]. This work was initially controversial [**135**], but subsequent work has rigorously shown that the polarization of a finite crystal induced by inhomogeneous strain has surface sensitive contributions, arising from changes in what has been called a "surface dipole" with strain, which do not go to zero in the bulk limit and are comparable in magnitude to the bulk flexoelectric response

[**137, 74, 150**]. Although some of the first ab initio calculations of flexoelectric coefficients supported this interpretation, these surface contributions have only been explicitly considered for bulk truncated (100) STO surfaces [**74**], which are unrealistic (e.g. Ref. [**170**]).

In Section 5.2 I motivate how surfaces contribute to the flexoelectric response of a finite system and connect this contribution to the strain derivative of the MIP, i.e. the difference between the average Coulomb potential and vacuum energy. Next, I use DFT calculations on a range of experimentally observed, low energy surfaces on archetypal ionic (MgO), covalent (Si), and mixed ionic-covalent (STO) crystals to investigate the role of surface structure, chemistry, polarity, and adsorbates on the MIP (Section 5.3) and MIP contributions to the flexoelectric response (Section 5.4). This work demonstrates that small variations in surface structure, chemistry, and adsorbates lead to significant changes in the MIP and total flexoelectric response. In Section 5.5 I combine the MIP contributions to the flexoelectric response with the bulk flexoelectric coefficient calculated in Chapter 4, allowing for a complete comparison with the measurements presented in Chapter 3. Lastly, I demonstrate how the issue of finite bulk flexoelectric coefficients in metals is resolved by considering the MIP contribution in Section 5.6. I performed all DFT calcultions and analyses described in this chapter and benefitted from discussions with Professor Laurence D. Marks.

5.2. The Flexoelectric Response of a Bent Slab

5.2.1. Contributions from the Bulk Flexoelectric Effect

To analyze the flexoelectric response of a bent slab, we will first summarize the effects of bulk flexoelectricity. In Chapters 2, 3, and 4 we have shown that short-circuit flexoelectric coefficients μ^E_{ijkl} mediate the electromechanical coupling of polarization (P_i) and strain gradient ($\epsilon_{kl,j}$) in the absence of an electric field [**10, 11**] according to

$$P_i = \mu^E_{ijkl}\epsilon_{kl,j}. \tag{5.1}$$

Alternatively, this effect can be described in terms of flexocoupling voltages (f_{ijkl}) which give the gradient of the average Coulomb potential arising from strain gradients [**10, 11, 58**]. Short-circuit flexoelectric coefficients and flexocoupling voltages are related through

$$f_{ijkl} = \frac{\mu^E_{ijkl}}{\varepsilon_0 \chi} \tag{5.2}$$

where χ is dielectric susceptibility and ε_0 is the permittivity of free space. Flexocoupling voltages will be used in this chapter because they are a more convenient description of flexoelectricity in this context.

Now consider the slab shown in Figure 5.1. If we assume the slab is composed of a centrosymmetric material, then there is no potential difference across an unperturbed slab. Subjecting the slab to a constant, longitudinal strain gradient as shown in Figure 5.1(b) leads to a potential difference across the slab owing to the bulk flexoelectric effect. If the

longitudinal strain gradient is taken to be one-dimensional

$$\frac{d\epsilon}{dx}(x) = \kappa \tag{5.3}$$

and the material has a single flexocoupling voltage (f), then the potential difference across the slab of thickness t is

$$\Delta V_{bulk} = -\int E dx = \int f \frac{d\epsilon}{dx}(x) dx = f\kappa t. \tag{5.4}$$

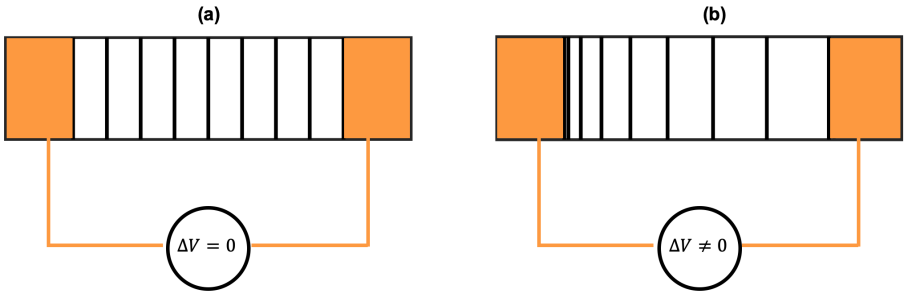

Figure 5.1. (a) An unperturbed slab of a centrosymmetric crystal has no potential difference across it. (b) A slab of a centrosymmetric crystal subjected to a constant longitudinal strain gradient has a potential difference across it from the flexoelectric effect. In both (a) and (b), black lines indicate atomic planes and gold electrodes on either end would measure the open-circuit voltage.

Importantly, ΔV_{bulk} is equal to the total potential difference across the slab only if the average Coulomb potential in a material is zero, which we know is not the case: the Coulomb potential in a solid is periodic and the (macroscopic) average of the Coulomb potential is a non-zero constant [**163, 171, 165, 164**]. An example of a DFT Coulomb potential for a STO slab with a TiO_2 bulk truncation is shown in Figure 5.2.

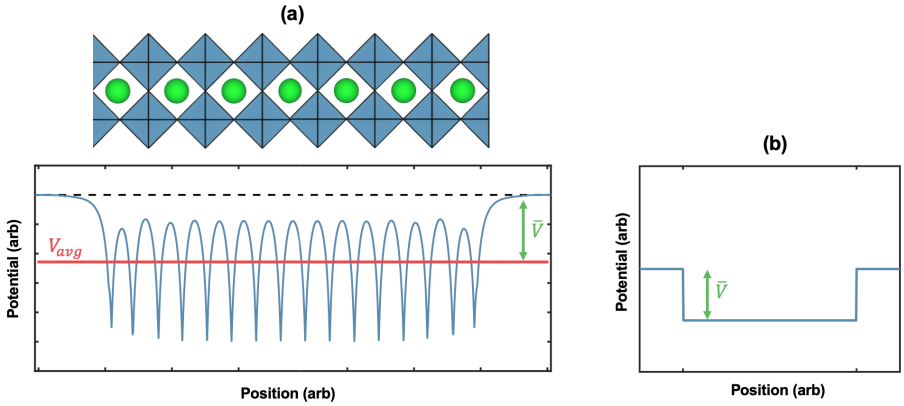

Figure 5.2. (a) Planar averaged Coulomb potential calculated with DFT in a STO slab with a bulk TiO_2 truncation. The periodic Coulomb potential has a well-defined macroscopic average V_{avg} (red). There is a potential step $\overline{V}$ (green) associated with the change in the average Coulomb potential inside and outside the slab. (b) It is convenient to work with an abstraction of the crystal slab where only the potential step is considered.

Before formally treating the average Coulomb potential in a solid, we will qualitatively demonstrate why a non-zero average Coulomb potential leads to additional contributions to the flexoelectric response of a bent slab [**137, 74, 150**]. Consider a finite centrosymmetric crystal with a slab geometry as shown in Figure 5.3. There are electric fields near the surface of the slab from the potential step corresponding to the change in the average Coulomb potential going from inside the crystal to vacuum. Even though there are finite electric fields near the surface, the potential difference across the slab is zero because it is centrosymmetric. Note, these electric fields can also be interpreted as a consequence of the inherent inversion-symmetry breaking nature of surfaces and are sometimes referred to as the surface piezoelectric effect [**172, 173**].

If the slab were to be homogeneously strained, as in Figure 5.3(b), the magnitude of the electric fields near the surfaces would change because the difference between the

average Coulomb potential and vacuum depends on lattice spacing. However, there is still zero potential difference across the slab because a homogeneous strain does not break inversion symmetry.

If a constant strain gradient, such as the one described by Eq. 5.3, is applied to the slab there will be a constant electric field in the bulk owing to the bulk flexoelectric effect leading to the potential difference described by Eq. 5.4. Additionally, there will be a contribution to the total potential difference from the electric fields near the surface: strain gradients break inversion symmetry, so the electric fields at either surface arising from the potential step between the bulk and vacuum no longer cancel. Figure 5.3(c) shows how the total potential difference across the bent slab is the sum of these two terms. Importantly, the contributions from the potential step at the surface do not go to zero in the thermodynamic bulk limit [**137, 172**] and are comparable in magnitude to the bulk flexoelectric effect [**74**].

5.2.2. The Mean-Inner Potential

To properly treat the electric field associated with the non-zero average Coulomb potential in Figure 5.3, it is necessary to define some terms. Figure 5.3 shows that it is actually not the average Coulomb potential that is the relevant quantity for the flexoelectric response of a bent slab; rather, it is the difference between the average Coulomb potential in the slab (V_{avg}) and the vacuum energy (E_{vac}) outside the solid. This quantity is known as the MIP ($\overline{V}$). See Ref. [**163**] and [**171**] for reviews of the MIP.

$$\overline{V} = V_{avg} - E_{vac} \tag{5.5}$$

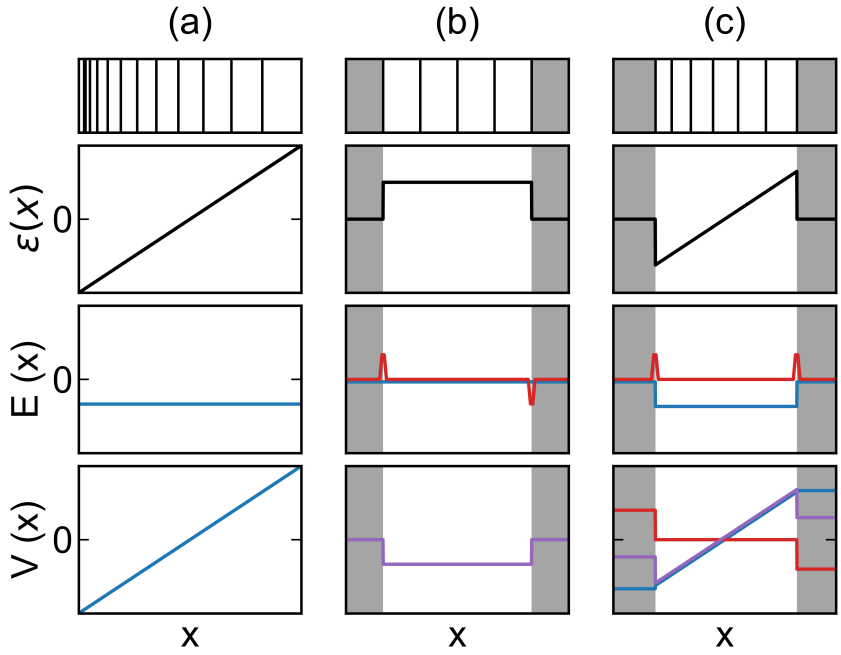

Figure 5.3. Changes in the electric field (E) and electrostatic potential (V) with strain (ϵ) in an infinite centrosymmetric crystal and finite centrosymmetric crystal with a slab geometry. Black lines in the top row indicate the position of atomic planes and grey shaded regions are vacuum. (a) An infinite crystal subjected to a constant strain gradient has a constant, non-zero electric field owing to the bulk flexocoupling voltage. (b) A finite crystal under constant strain will have no electric field in the bulk (blue), but will have equal and opposite electric fields (red) at the surface arising from the potential step (purple). There is no potential difference across the slab because inversion symmetry has not been broken. (c) The symmetry of the electric fields associated with the surface in a finite crystal (red) is broken by a constant strain gradient. This contribution and the constant electric field from the bulk flexoelectric effect (blue) yield a measurable potential difference across the slab (purple).

The MIP has been extensively studied due to its importance in electron microscopy [**163, 171, 174**], and there have been significant efforts to measure [**175**] and calculate MIPs [**176, 177, 178, 179, 180**] in a wide range of materials. At a fundamental level, the

MIP is only defined for finite-sized systems [**181**] because there is no reference potential in an infinite crystal [**163, 171**], making the MIP an inherently surface-sensitive property. It has been demonstrated that the MIP is sensitive to surface orientation, structure, chemistry, and adsorbates (e.g. Ref. [**176**]).

Figure 5.4 provides a band diagram description of the MIP in which the surface-sensitivity of this quantity is clear. The MIP in an insulator can be considered as

$$\overline{V} = \Delta + I. \tag{5.6}$$

In Eq. 5.6, Δ is the difference between V_{avg} and the bulk valence band maximum (E_{VBM}^{bulk}) and I is the ionization potential, i.e. the difference between E_{vac} and E_{VBM}^{bulk}. Δ is a bulk property and I is a surface property [**182**]. For the purposes of this work, it will be useful to decompose I further into the work function (ϕ, the difference between E_{vac} and the surface valence band maximum (VBM), E_{VBM}^{surf}) and surface valence band offset (δ, the difference between E_{VBM}^{bulk} and E_{VBM}^{surf}).

5.2.3. The Ibers Approximation

While the MIP is only defined for finite-sized systems [**181, 163, 171**], it is possible to estimate the MIP of a crystal from only its bulk structure if the crystal is approximated as a collection of non-interacting atoms or ions [**164, 163**]. Within this approximation, the issue of the reference potential is resolved because atomic/ionic energy levels have a well-defined zero infinitely far away from the atom/ion. Ibers [**164**] has demonstrated that within this approximation the MIP can be expressed in terms of electron scattering

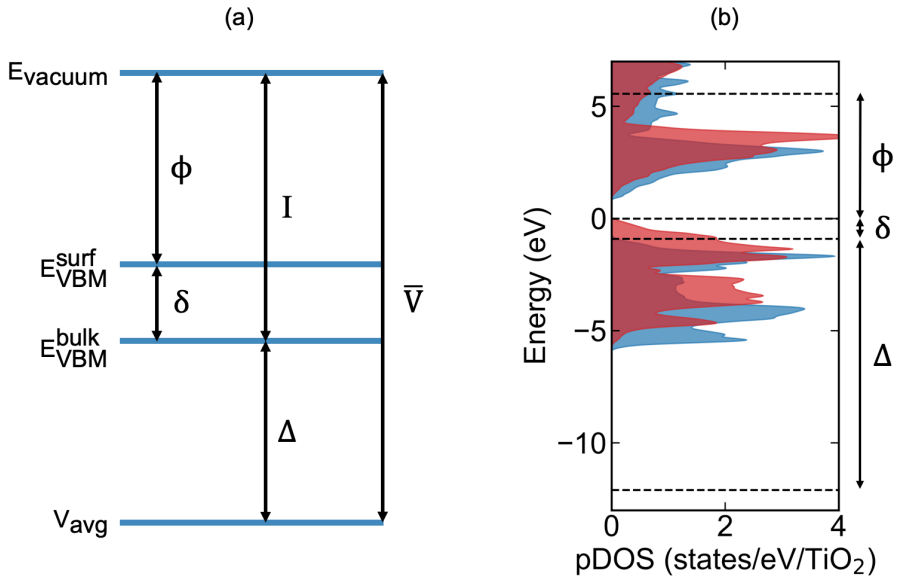

Figure 5.4. (a) Band diagram definition of the MIP for an insulator with finite size. All quantities are defined in the text. (b) Partial density of states of a (100) STO slab with a TiO_2 single-layer termination (structure shown in Figure 5.5) calculated with DFT depicting quantities defined in (a). Blue corresponds to the partial density of states of the inner-most TiO_2 layer and red corresponds to the partial density of states (pDOS) of the outer-most TiO_2 layer.

factors according to

$$\overline{V} = \frac{h^2}{2\pi m e \Omega} \sum_i f_i^{el}(0) \tag{5.7}$$

where h is Plancks constant, m is the electron rest mass, e is the electron charge, Ω is the unit cell volume, and $f_i^{el}(0)$ is the electron scattering factor of species i in the unit cell (atomic and ionic electron scattering factor values are tabulated for each element from Dirac-Fock calculations, e.g. Ref [**166**]).

5.2.4. Mean-Inner Potential Contributions to Flexoelectricity

Based upon the definition of the MIP provided above and the arguments summarized in Figure 5.3, the total flexocoupling voltage of a finite crystal is

$$f_{total} = f_{bulk} + f_{MIP} \tag{5.8}$$

where f_{bulk} is the bulk flexocoupling voltage defined in Eq. 5.2 and f_{MIP} is the change in the MIP with strain

$$f_{MIP} = \frac{d\overline{V}}{d\epsilon}. \tag{5.9}$$

A rigorous proof of Eqs. 5.8 and 5.9 are provided in Ref. [**137, 150**], but they can be motivated from the definition of f_{bulk} and MIP: the total potential difference will not only depend on the gradient of the average Coulomb potential (f_{bulk}), but also the difference between the average Coulomb potential and the vacuum energy (MIP). Note, Eq. 5.8 assumes contributions from defects are negligible which is not always the case (e.g. see Chapter 6).

While f_{MIP} has been called the surface flexocoupling voltage in the literature [**137, 74**], we refer to it as f_{MIP} because only some of Eq. 5.9 is truly surface sensitive. The bulk and surface components of f_{MIP} can be explicitly defined by combining Eq. 5.9 with Eq. 5.6 and Figure 5.4:

$$f_{MIP} = \frac{d\left(\Delta + I\right)}{d\epsilon} = f_{MIP}^{bulk} + f_{MIP}^{surf}. \tag{5.10}$$

f_{MIP}^{surf}, the surface-sensitive component of f_{MIP}, describes the strain derivative of the ionization potential. In the ensuing work, this quantity will be shown to be very sensitive to surface structure, chemistry, and adsorbates. The bulk component of f_{MIP}, f_{MIP}^{bulk}, is given by the strain derivative of the difference between the average Coulomb potential and the bulk VBM. This term depends only upon the bulk crystal structure and crystallographic orientation. Note, Eq. 5.5 and 5.10 use the VBM to distinguish between bulk and surface contributions to the MIP and f_{MIP}, but this breakdown is not unique: for other materials it may be more sensible to use another energy, e.g. the conduction band minimum in n-type semiconductors. This choice is arbitrary and has no impact on the physical measurement: it will cancel in Eq. 5.10.

5.3. Mean-Inner Potential Calculations

5.3.1. Background

Stengel clearly demonstrated the importance of surfaces in flexoelectricity in Ref. [**74**] through DFT calculations on bulk truncated STO surfaces. While this work represents an important step towards understanding flexoelectricity, the surfaces examined in that work are not experimentally relevant: experimentally observed surfaces, including those in nominally simple systems such as STO, deviate significantly from bulk truncations (e.g. Ref. [**183**] and references therein). Here we consider the flexoelectric response associated with surfaces which have been experimentally observed and/or lie near the theoretical convex hull for archetypal mixed ionic-covalent (STO, [**184, 185, 186, 187, 188, 189, 190, 191, 192, 193, 194, 195, 196**]), ionic (MgO, [**197, 198, 199, 200**]), and covalent (Si, [**201**]) crystals. This wide range of surfaces allows us to study the impact of surface

structure, chemistry, polarity, and adsorbates on flexoelectricity. Before investigating the impact of these factors on flexoelectricity, we first examine their impact on the MIP because of the intimate relationship between flexoelectricity and the MIP.

5.3.2. Methods

DFT calculations were performed with the all-electron augmented plane wave + local orbitals WIEN2k code [**145**]. Bulk calculations were used to obtain optimized lattice constants for STO ($Pm\overline{3}m$), MgO ($Fm\overline{3}m$), and Si ($Fd\overline{3}m$). Then, conventional slab models (consisting of 15-20 atomic layers with 1015 $\mathring{A}$ of vacuum and the highest available symmetry) were constructed for each investigated surface using the bulk optimized lattice constants. Numerical tests confirmed these surface slabs were sufficiently large. Atomic positions in the surface slabs were simultaneously converged with the electron density using a quasi-Newton algorithm [**202**]. The exchange-correlation term was approximated with the LDA functional [**148**]; calculations with the PBEsol functional [**152**] and a PBEsol + on-site hybrid [**153, 154**] approach (only for STO, with an on-site hybrid fraction of 0.25 applied to Ti 3d states) yielded qualitatively similar results.

For STO, muffin-tin radii of 2.31, 1.54, 1.40 bohr were used for Sr, Ti, and O, respectively with a plane-wave expansion parameter RKMAX of 5.98, energy cut-off of -6 Ry, and k-mesh equivalent to 4x4x4 per bulk conventional unit cell. For MgO, muffin-tin radii of 1.63, 1.20, 0.60 bohr were used for Mg, O, and H, respectively with a RKMAX of 4.42 (2.21 with H), energy cut-off of -6 Ry, and k-mesh equivalent to 10x10x10 per bulk conventional unit cell. For Si, a muffin-tin radius of 2.00 bohr was used with a RKMAX of 7, energy cut-off of -8 Ry, and k-mesh equivalent to 7x7x7 per bulk conventional unit

cell. Numerical tests in which the muffin-tin radii, RKMAX, and k-mesh reported above were varied yielded consistent MIP values. All calculations used a Mermin functional at room temperature. For bulk calculations, convergence criteria of 10^{-4} e and 10^{-3} Ry were used. This yielded optimized lattice parameters of 7.290 bohr, 7.874 bohr, and 10.208 bohr for STO, MgO and Si, respectively. For surface calculations, convergence criteria of 10^{-4} e, 10^{-3} Ry, and 10^{-3} mRy/bohr were used with a force tolerance of 0.1 mRy/bohr.

A core-level approach [**203, 204**] was used to calculate the MIP for each surface according to

$$\overline{V} = V_{avg} - E_{vac} = (V_{avg} - E_{core})_{bulk} + (E_{core} - E_{vac})_{surf} \,. \tag{5.11}$$

A bulk calculation was used to determine the difference between a deep core eigenvalue, E_{core}, and the average Coulomb potential, V_{avg}. Then, a surface slab calculation was used to determine the difference between the Coulomb potential in the center of vacuum, E_{vac}, and the same deep core eigenvalue from the innermost atomic plane of the slab. Checks were made to ensure the slab and vacuum were large enough to minimize oscillations in the Coulomb potential in vacuum and to recover the bulk structure in the innermost slab layer. Tests were also performed using different deep core eigenvalues for a particular structure to confirm consistency in $\overline{V}$ calculations. The computational parameters and method used here yielded uncertainties in $\overline{V}$ $\sim$0.2 V. Once $\overline{V}$ was known, the energies of the bulk and surface VBM were used to decompose $\overline{V}$ according to Figure 5.4.

5.3.3. (100) $SrTiO_3$ Surfaces

We begin with the MIP of (100) STO surfaces to determine how surface chemistry and structure affect the MIP. Cubic (100) perovskite surfaces have two bulk truncations corresponding to (1x1) TiO_2 and SrO single-layer (SL) terminations for STO. The (100) surface of STO also has many TiO_2 double-layer (DL) reconstructions (e.g. Ref. [**183**] and references therein). The DL reconstructions studied here ((1x1), (2x2)A, (2x2)C, (2x1), and c(4x2), see Figure 5.5 and Ref. [**184, 185, 186, 187, 188, 189, 190, 191, 192, 193, 194, 195, 196**]) allow for the separation of surface structure effects from surface chemistry effects because they have minor structural differences and identical stoichiometries.

First we focus on surface chemistry. Table 5.1 indicates the MIP increases with excess TiO_2 on the surface from a value of 15.2 V for bulk-truncated SrO (-0.5 TiO2/1×1) to 17.7 V for bulk-truncated TiO2 (0.5 TiO2/1×1) to an average of 18.4 V for TiO_2 DL reconstructions (1.5 TiO2/1×1). This demonstrates the importance of surface chemistry in determining the MIP. Table 1 shows MIPs are similarly sensitive to surface structure: the stoichiometrically-identical DL reconstructions have a 1.7 V MIP range, reflecting the role of differences in the surface Ti-O polyhedra coordination environment. The MIP difference between the chemically distinct SrO and TiO_2 SL bulk terminations is comparable to the MIP range for the DL reconstructions, suggesting both surface chemistry and structure play a large role in determining the MIP.

Unfortunately, there have been limited experimental investigations of MIP in STO, making it difficult to compare our calculations; there are no MIP measurements on DL structures and one measurement on bulk (100) STO terminations [**205**]. Although it is

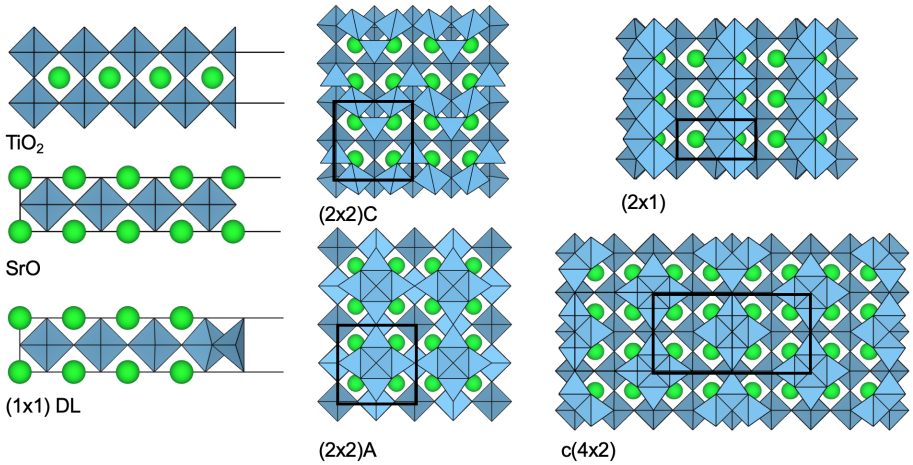

Figure 5.5. DFT relaxed (100) STO surface structures studied in this work with Sr atoms in green, Ti-O polyhedral in blue, and reconstructed unit cells outlined in black. The (100) surface of the TiO_2, SrO, and (1x1) double-layer structures correspond to the right-most atomic planes. The (100) surface of the (2x2)A, (2x2)C, c(4x2) and (2x1) double-layer reconstructions are shown sitting atop a bulk (100) plane.

Surface	$\overline{V}$ (V)	ϕ (V)	δ (V)	Δ (V)	$\overline{V}_{exp}$ (V)
SrO	15.2	4.0	0.0	11.2	13.3
TiO_2	17.7	5.6	0.9	11.2	14.6
(1x1) DL	17.6	6.0	0.7	11.0	
(2x2)A	18.2	6.7	0.4	11.1	
(2x2)C	18.5	7.4	0.0	11.0	
c(4x2)	18.3	7.2	0.0	11.1	
(2x1)	19.3	8.2	-0.1	11.0	

Table 5.1. DFT calculated MIP for (100) STO surfaces. All values are defined in Figure 5.4. All surfaces have the same Δ values (within the uncertainty of these calculations), whereas the work function and surface valence band offsets vary significantly, yielding a large MIP spread for nominally similar surfaces. The experimental values are taken from Ref. [**205**].

unlikely that pure bulk-like SrO and TiO_2 terminated surfaces are realistic [**170**], we compare our calculations to the existing literature [**205**]. The one experimental measurement on bulk terminations of (100) STO surfaces found MIPs of 13.3 V (14.6 V) for SrO (TiO_2)

terminations [**205**], whereas we calculated MIPs of 15.2 V (17.7 V) for SrO (TiO_2) terminations. Our calculations qualitatively capture the experimental relationship between the MIP of the bulk terminations, but the source of the discrepancy in the magnitude of the values is unclear.

To investigate further, additional MIP calculations were performed with the PBEsol functional and a PBEsol + hybrid approach. As shown in Table 5.2, these calculations yielded qualitatively similar MIP to those using the LDA functional. We also cannot attribute the discrepancy to the difference between the DFT optimized and experimental lattice parameters because the product of the MIP and the optimized unit cell volume is constant across all functionals [**179**]. The SrO and TiO_2 SL work functions we calculated are in good agreement with other DFT calculated work functions [**206**] and our MIP calculations agree with electron holography measurements for MgO and Si surfaces (see Section 5.3.4 and 5.3.5). These findings suggest that either (1) STO surfaces are poorly modeled with functionals used here, (2) reflection high-energy electron diffraction and electron holography measurements of the MIP are inconsistent, or (3) some contamination affected the MIP measurements reported in Ref. [**205**].

5.3.4. (100) and (111) MgO Surfaces

Now we turn to the MIP of MgO (100) and (111) surfaces. MgO has archetypal polar surfaces: bulk truncations of the (111) rock salt structure are not valence-neutral so (111) surfaces must reconstruct, metallize, or adsorb species to stabilize [**183**]. First, we calculate the MIP of bulk truncated MgO (100) to serve as a baseline for comparison

(a) $\overline{V}$ (V)

Surface	Exp.	LDA	PBEsol	PBEsol + hybrid
SrO	13.3	15.2	14.7	14.8
TiO_2	14.6	17.7	17.4	17.0

(b) $\overline{V} \times \Omega$ (V nm^3)

Surface	Exp.	LDA	PBEsol	PBEsol + hybrid
SrO	0.792	0.873	0.869	0.881
TiO_2	0.869	1.016	1.029	1.012

Table 5.2. (a) MIP of bulk truncations of (100) STO calculated with different functionals and experiment. (b) Product of the MIP and equilibrium volume. Experimental values are taken from Ref. [**205**].

with experiment and different MgO (111) reconstructions. The calculated MIP of 13.4 V for the MgO (100) surface is similar to the MIP of 13.01 V measured with electron holography [**175**]. Unlike STO, the difference between the calculated and experimental MIP for MgO is fully accounted for from the difference between the DFT optimized and experimental lattice parameters: $\overline{V}_{LDA} \cdot \Omega_{LDA}$=0.969 V nm^3 and $\overline{V}_{exp} \cdot \Omega_{exp}$=0.972 V nm^3 [**175, 179**].

For unhydroxylated polar MgO (111) surfaces, we start with (2×2) octapolar reconstructions which are canonical, low energy structure [**197**]. Surface chemistry affects polar surface MIPs in a similar manner to how it affects non-polar surface MIPs: Table 5.3 shows the Mg-terminated and O-terminated octapolar structures have a 2.5 V MIP difference which is comparable to the difference between the SrO and TiO_2 bulk truncations of (100) STO. This indicates there is nothing special about polar surface MIPs other than polar surfaces must resolve their polarity through reconstruction or other means to exist [**183**].

Note, the MgO (100) bulk truncation MIP is approximately the average of the MIP of the octapolar structures. This follows from the difference in electron affinity of Mg and O.

The (2×2)-α structures are similar to the (2×2) octapolar surfaces [**200, 198**]. There are three variants of the unhydroxylated (2×2)-α structure which possess identical surface chemistries and minor structural differences: the generic (2×2)-α shown in Figure 5.6 has three oxygen surface sites and the three variants have two out of three surface sites occupied. The (2×2)-α-O1 and (2×2)-α-O2 structures have nearly identical MIPs with values of 18.5 V and 18.8 V, respectively, the (2×2)-α-O3 structure has a MIP of 17.1 V. This result is surprising given the structural similarities between the three variants, and is attributed to the relative stability of these three structures: the (2×2)-α-O3 is ∼0.5 eV per (1×1) unit cell lower in energy than the other two structures [**198**]. These results further indicate structural and chemical differences have a comparable impact on the MIP.

Next, we examine the MIP of hydroxylated MgO (111) surface reconstructions [**198**] to study the role of adsorbates. Table 5.3 indicates that the introduction of hydrogen tends to reduce the MIP from 16.5 V (averaged over all unhydroxylated) to 14.1 V (averaged over all hydroxylated structures). A clear example of this trend is in the three (2x2)-α structures: the MIP of the (2×2)-α-OH1, (2×2)-α-OH2, and (2×2)-α-OH3 are decreased by 3.4 V, 3.9 V, and 1.4 V relative to (2×2)-α-O1, (2×2)-α-O2, and (2×2)-α-O3, respectively. The difference in the MIP reductions upon hydroxylation further emphasizes the importance of surface structure. Finally, we find the O-rich variant of the hydroxylated Rt3 structures has a higher MIP than the Mg-rich variant. This behavior is similar to that

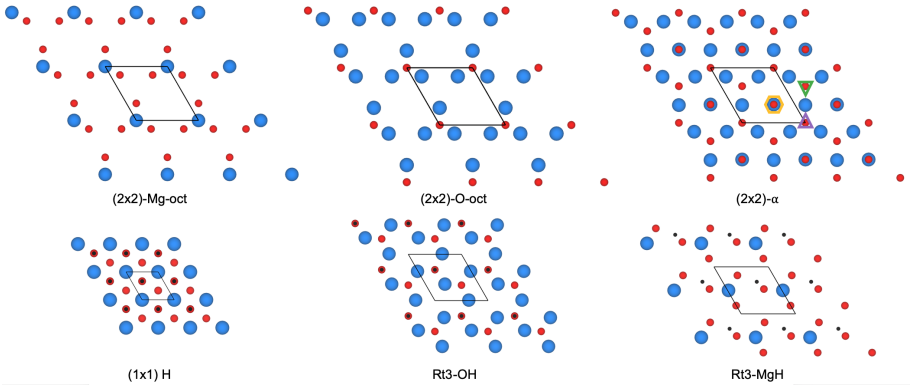

Figure 5.6. DFT relaxed (111) MgO surface structures studied in this work. In all structures, Mg, O, and H atoms are blue, red, and black, respectively, and reconstructed unit cells are outlined in black. The generic (2×2)-α structure is shown with the three distinct O sites indicated by an orange hexagon, green triangle, and purple triangle. The (2×2)-α-O1, -O2, and -O3 structures have O at the orange hexagon and purple triangle, orange hexagon and green triangle, and purple triangle and green triangle occupied, respectively. The (2×2)-α-OH1, -OH2, and -OH3 structures have all three sites occupied by O as well as H atop the orange hexagon and purple triangle, orange hexagon and green triangle, and purple triangle and green triangle, respectively.

of the (2×2)-octapolar structures, consistent with the difference in the electron affinity of Mg and O, and indicates that the underlying surface chemistry still plays a large role in determining the MIP in hydroxylated surfaces.

We are not aware of any MIP measurements for (111) MgO surfaces, so we cannot make a direct comparison with experiment. We note that test calculations with different DFT functionals changed the MIP and optimized lattice parameter so that $\overline{V} \cdot \Omega$ was constant for a given surface, independent of the functional used. This is similar to the effect of functionals on the MIP of STO surface.

Surface	$\overline{V}$ (V)	ϕ (V)	δ (V)	Δ (V)	$\overline{V}_{exp}$ (V)
Bulk (100)	13.4	5.5	0.1	7.8	13.01
Mg-oct	12.7	4.3	0.5	7.9	
O-oct	15.2	6.6	0.8	7.8	
(2×2)-α-O1	18.5	7.9	2.7	7.9	
(2×2)-α-O2	18.8	8.1	2.9	7.8	
(2×2)-α-O3	17.1	7.2	2.0	7.9	
(2×2)-α-OH1	15.1	5.3	1.9	7.9	
(2×2)-α-OH2	14.9	5.5	1.4	7.9	
(2×2)-α-OH3	15.7	5.2	2.6	7.9	
(1x1)H	11.7	3.8	0.0	7.9	
Rt3-MgH	11.7	3.5	0.3	7.9	
Rt3-OH	15.2	6.1	1.2	7.9	

Table 5.3. DFT calculated MIP for each MgO surface. Values are defined in Figure 5.4. All surfaces have the same Δ values (within the uncertainty of these calculations), whereas the work function and surface valence band offsets vary significantly, leading to a large MIP spread for nominally similar surfaces. The experimental value is taken from Ref. [**175**].

5.3.5. (100) Si Surfaces

The two Si (100) surfaces studied were the (1×1) bulk truncation and asymmetric dimerized (2×1) reconstruction which are shown in Figure 5.7 [**201**]. These surfaces have identical chemistry, minor structural differences, and, as shown in Table 5.4, a difference of 0.5 V between their MIPs. This MIP difference is smaller, but comparable to the differences in the MIP of the chemically identical but structurally distinct STO and MgO surfaces discussed in Section 5.3.3 and 5.3.4. We cannot make a quantitative comparison with experiment because we could not find MIP measurements for (100) Si surfaces and there is a sizable spread in the available experimental values of the MIP for other Si surfaces [**176, 177, 175**]. However, our calculated MIP values are similar to some measured MIPs for Si [**176, 177, 175**].

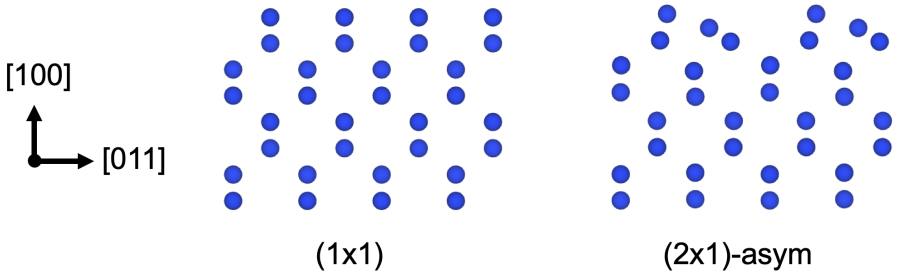

Figure 5.7. DFT relaxed (100) Si surface structures studied in this work with Si atoms in blue.

Surface	$\overline{V}$ (V)	ϕ (V)	δ (V)	Δ (V)
(1×1)	13.0	5.3	0.2	7.5
(2×1)-asym	12.5	5.1	0.0	7.4

Table 5.4. DFT calculated MIP for each Si surface. Values are defined in Figure 5.4. All surfaces have the same Δ values (within the uncertainty of these calculations), whereas the work function and surface valence band offsets vary.

5.3.6. Ibers Approximation to the Mean-Inner Potential

The calculations in Sections 5.3.3, 5.3.4, and 5.3.5 demonstrate the MIP is sensitive to surface structure, chemistry, and adsorbates leading to a large spread in MIP values for nominally similar surfaces. Unfortunately, such calculations require a known surface structure to determine the MIP, which is frequently not the case in experiment. When the surface structure is not known, it is possible to approximate the MIP using knowledge of the bulk structure, electron scattering factors, and experimental lattice parameters according to the Ibers approximation [**164**] introduced in Section 5.2. We now evaluate the accuracy of this approximation.

Figure 5.8 compares the MIP predicted by electron scattering factors using Eq. 5.7 to those calculated with DFT for the surfaces analyzed in Sections 5.3.3, 5.3.4, and 5.3.5.

We find predicted MIPs of 18.4 V (12.6 V), 15.1 V (22.3 V), and 13.8 V for MgO, STO, and Si, respectively, using the appropriate atomic (ionic) electron scattering factors values from Ref. [**166**]. The atomic and ionic electron scattering factors do a comparable job with mean absolute errors (MAE) of 3.0 V for atomic electron scattering factors and 3.3 V for ionic electron scattering factors across all surfaces. Most MIP values computed were ∼15 V, so the MAE indicates the Ibers approximation is good to ∼20%. For individual materials, there are minor differences with the use of ionic and atomic electron scattering factors. MgO is better captured by ionic electron scattering factors (MAE = 2.7 V) than atomic scattering factors (MAE = 3.5 V), whereas atomic scattering factors (MAE = 3.0 V) are more appropriate for STO than ionic scattering factors (MAE = 3.3 V). Si has no ionic scattering factors, but the performance of atomic scattering factors is comparable to the other materials mentioned (MAE = 3.0 V).

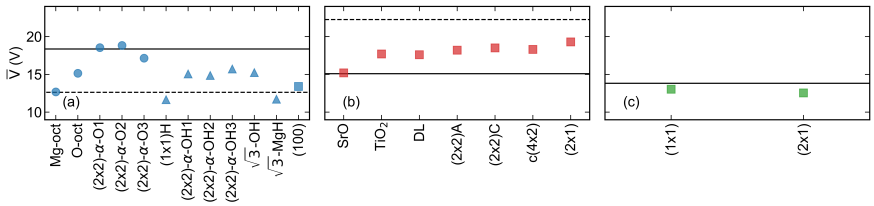

Figure 5.8. Comparison between the MIP calculated with DFT and with atomic (solid) and ionic (dashed) electron scattering factors for (a) MgO, (b) STO, and (c) Si surfaces. The MAE across all surfaces is 3.0 V and 3.3 V for atomic and ionic electron scattering factors, respectively.

5.4. Calculations of f_{MIP}

The results from Section 5.3 clearly demonstrate the MIP is sensitive to the details of the surface including its structure, chemistry, and adsorbates. We now explore the

sensitivity of f_{MIP} to these factors using the same STO, MgO, and Si surfaces shown in Figures 5.5, 5.6, and 5.7.

5.4.1. Methods

A core-level approach analogous to Eq. 5.11 was used to calculate the f_{MIP} for each surface using the same DFT parameters described in Section 5.3.2.

(5.12)
$$f_{MIP} = \frac{d\overline{V}}{d\epsilon} = \frac{d\left(V_{avg} - E_{vac}\right)}{d\epsilon} = \left(\frac{d\left(V_{avg} - E_{core}\right)}{d\epsilon}\right)_{bulk} + \left(\frac{d\left(E_{core} - E_{vac}\right)}{d\epsilon}\right)_{surf}.$$

The quantity $\left(\frac{d(E_{core}-E_{vac})}{d\epsilon}\right)_{surf}$ corresponds to the strain derivative of the difference between E_{vac} and E_{core} from the innermost atomic plane of the slab. The strains used here are a modified form of the clamped plate bending strain [**74**] introduced in Chapter 3.

(5.13)
$$\epsilon_{clamped} = \epsilon \begin{pmatrix} 1 & 0 & 0 \\ 0 & 1 & 0 \\ 0 & 0 & -2\nu \end{pmatrix}$$

The x_3 axis in Eq. 5.13 is normal to the surface, $\nu = \frac{c_{12}}{c_{11}}$ for (100) cubic surfaces, and $\nu = \frac{c_1 1+2(c_1 2-c_4 4)}{c_1 1+2(c_1 2+2c_4 4)}$ for (111) cubic surfaces (these follow from the analysis in Chapter 3 and Ref. [**53**]). Experimental elastic constants were used for STO [**161**], MgO [**207**], and Si [**208**]. The quantity $\left(\frac{d(V_{avg}-E_{core})}{d\epsilon}\right)_{bulk}$ is the strain derivative of the difference between V_{avg} and E_{core}. It is calculated from a set of bulk calculations performed under uniform strains and corresponds to the hydrostatic deformation potential of E_{core} [**132**] scaled by the trace of Eq. 5.13.

At least 5 strains were used to determine all slopes and the procedure was repeated for multiple core eigenvalues to ensure consistency. Figure 5.9 demonstrates the quality of the linear fits using the Mg1s eigenvalue as E_{core}. After calculating f_{MIP} from Eq. 5.12 it was separated into f_{MIP}^{bulk} and f_{MIP}^{surf} using the energies of the surface and bulk VBM according to Eq. 5.10. We found the parameters and methods outlined above yielded an uncertainty in f_{MIP} ~0.2 V.

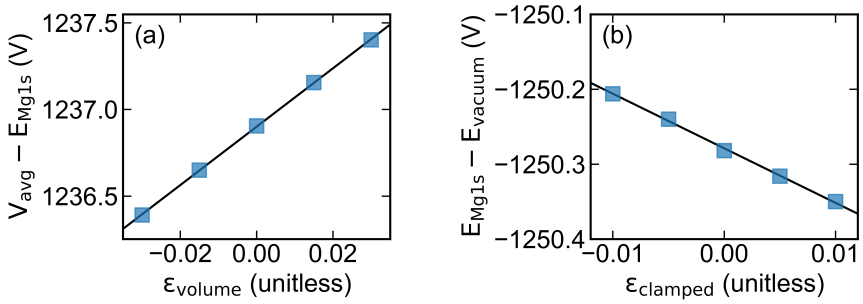

Figure 5.9. A representative example of the data (blue squares) and linear fits (black lines) used to calculate the strain derivative of the MIP. (a) Difference between the average Coulomb potential and Mg1s eigenvalue in bulk MgO as a function of hydrostatic strain. (b) Difference between the vacuum energy and Mg1s eigenvalue in the innermost layer of a MgO (100) slab as a function of clamped plate bending strain.

The clamped plate bending in Eq. 5.13 was computationally advantageous since many of the investigated surfaces have tetragonal symmetry, but flexoelectric responses are often reported in the $\phi = 0$ beam bending limit [**52**]. To facilitate comparison with the literature, all reported f_{MIP} values throughout the chapter have been converted to pure beam bending values using the relation

$$f_{MIP}^{beam} = \frac{1}{1+\nu} f_{MIP}^{clamped} \tag{5.14}$$

which follows from the framework developed in Chapter 3.

5.4.2. Calculations for Specific Surfaces

Table 5.5 includes the DFT calculated values of the MIP contributions to the total flexoelectric response (f_{MIP}), and the bulk (f_{MIP}^{bulk}) and surface (f_{MIP}^{surf}) components of f_{MIP} defined by Eq. 5.10 for each of the investigated surfaces.

We begin with an analysis of the (100) STO surfaces. Starting with the (1x1) SrO and TiO_2 SL structures, Table 5.5 shows that surface dependent contributions modify f_{MIP} by upwards of 30% and change the sign of f_{MIP}^{surf}. These results directly demonstrate f_{MIP}^{surf} is sizable and underscore the integral role of surface chemistry in determining the MIP contributions to the total flexoelectric response. My calculations also agree with Ref. [**74**], which found f_{MIP} of 6.6 V and 9.4 V for SrO and TiO_2 SL structures, respectively.

Next we isolate the effects of surface structure on f_{MIP} in STO by studying the (1×1), (2×2)A, (2×2)C, (2×1), and c(4×2) DL reconstructions which have identical stoichiometry. Table 5.5 indicates an average f_{MIP} of 9.0 V and range of 1.6 V for the DL reconstructions which is smaller, but comparable to, the difference in f_{MIP} between SrO and TiO_2 terminations. This shows the f_{MIP} has a sensitivity to the detailed surface structure, as was the case for the MIP. However, the relationship between Ti-O polyhedra coordination, excess TiO_2 coverage, and the MIP is not reflected in the f_{MIP} values in Table 5.5. Instead, we find all TiO_2-rich terminations possess qualitatively similar surface contributions with $f_{MIP}^{surf} \geq 0$ V, which is in stark contrast to $f_{MIP}^{surf} < 0$ V for the SrO termination.

Collectively, this work shows that surface structure is important in dictating the magnitude of the f_{MIP}^{surf}, but is a secondary consideration to surface chemistry which controls the sign. The cleanest demonstration of this point is in the f_{MIP} of the (1×1) and (2×1) surfaces of Si. Table 5.5 shows that these two surfaces, which have identical surface chemistry and very minor structural differences compared to the structural differences in the STO DL reconstruction, have identical f_{MIP} within the uncertainty of these calculations.

Now we focus on MgO surfaces to further explore the relative importance of surface chemistry and structure, and ascertain the impact of polar surfaces and adsorbates. The f_{MIP} of the (100) and (111) MgO surfaces in Table 5.5 demonstrate substantial surface-dependent modifications. Like the STO surfaces, surface chemistry dictates the sign of f_{MIP}^{surf} (e.g. f_{MIP}^{surf} in the Mg-terminated and O-terminated (2×2) octapolar structures differ in sign and by 2.5 V, similar to the change in magnitude and sign of f_{MIP}^{surf} between the (1×1) bulk SL terminations of (100) STO). In general, Table 5 indicates Mg-rich MgO surfaces have $f_{MIP}^{surf} \leq 0$ V, O-rich MgO surfaces have $f_{MIP}^{surf} \geq 0$ V, and mixed termination surfaces (e.g. the (100) bulk-terminated MgO surface) have $f_{MIP}^{surf} \approx 0$ V.

Surface structure is also an important consideration in f_{MIP} for MgO, particularly when the surface chemistry is the same. For example, the (2×2)-α-O1 and (2×2)-α-O2 structures have f_{MIP}^{surf} which are approximately half that of the (2×2)-α-O3 structure despite these structures having identical stoichiometries and only small differences in surface site occupancy. Similarly, the large differences in the hydroxylated (2×2)-α structures f_{MIP}^{surf} highlights the important role of surface structure.

On the topic of polar surfaces, my calculations show the magnitudes of f_{MIP} and f_{MIP}^{surf} are similar for both polar and non-polar surfaces. This suggests that while polar

surfaces can possess a wider range of f_{MIP} values owing to their need to stabilize through reconstruction, metallization, or adsorption, their flexoelectric response is not inherently different than that of non-polar surfaces. On the other hand, adsorbates have a significant effect on f_{MIP}. On average, hydroxylation reduces f_{MIP} from 10.7 V (averaged over all unhydroxylated surfaces) to 9.4 V (averaged over all hydroxylated surfaces). This behavior is most clearly shown by comparing the (2×2)-α structures, where f_{MIP} is reduced by 1.4 V, 0.9 V, and 5.0 V upon hydroxylation of (2×2)-α-O1, (2×2)-α-O2, and (2×2)-α-O3, respectively.

5.4.3. Ibers Approximation

As previously noted, DFT calculations require knowledge of the surface structure at a level that is often experimentally inaccessible for typical flexoelectric experiments. In such cases it is possible to estimate f_{MIP} using knowledge of the bulk structure and electron scattering factors according to the Ibers approximation. Combining Eq. 5.7 and 5.9 in the limit of small strains yields an expression for the Ibers approximation [**164**] to f_{MIP}:

$$f_{MIP}^{Ibers} \approx \overline{V}_{Ibers} \frac{\Delta\Omega}{\Omega_0} \tag{5.15}$$

where $\overline{V}_{Ibers}$ is the MIP at the equilibrium volume Ω_0 calculated from electron scattering factors and $\frac{\Delta\Omega}{\Omega_0}$ is volumetric strain (calculated from elastic constants, e.g. the trace of Eq. 5.13).

Figure 5.10 contains a comparison of f_{MIP}^{Ibers} calculated using atomic and ionic electron scattering factors with f_{MIP} calculated using DFT for the STO, MgO, and Si surfaces considered in this chapter. Even though both scattering factors performed comparably in

Materials	Surface	f_{MIP}^{bulk} (V)	f_{MIP}^{surf} (V)	f_{MIP} (V)
$SrTiO_3$ (100)	SrO	8.1	-1.9	6.2
	TiO_2	8.1	1.8	9.9
	(1×1) DL	8.2	1.4	9.6
	(2×2)A	8.2	0.4	8.6
	(2×2)C	8.1	1.6	9.7
	c(4×2)	8.1	0	8.1
	(2×1)	8.2	0.7	8.9
MgO (100)	Bulk	6.1	-0.4	5.7
MgO (111)	Mg-oct	8.9	-2	6.9
	O-oct	8.9	0.5	9.4
	(2×2)-α-O1	8.8	2.9	11.7
	(2×2)-α-O2	8.9	2.4	11.3
	(2×2)-α-O3	8.8	5.2	14.0
	(2×2)-α-OH1	8.8	1.5	10.3
	(2×2)-α-OH2	8.9	1.5	10.4
	(2×2)-α-OH3	8.8	0.2	9.0
	(1×1)H	8.8	-0.3	8.5
	Rt3-MgH	8.8	-2.7	6.1
	Rt3-OH	8.9	3.2	12.1
Si (100)	(1×1)	5.5	0	5.5
	(2×1)-asym	5.5	-0.1	5.4

Table 5.5. DFT-calculated flexocoupling voltages for each of the surfaces explored in this work. The MIP contribution (f_{MIP}) is the sum of the bulk (f_{MIP}^{bulk}) and surface (f_{MIP}^{surf}) components defined in Eq. 5.10. All values correspond to $\phi = 0$ pure beam bending (Chapter 3).

Section 5.3.6 for approximating the MIP, the atomic electron scattering factors outperform the ionic scattering factors for approximating f_{MIP}: across all surfaces we find MAE of 1.7 V and 3.3 V using atomic and ionic electron scattering factors, respectively. This is also the case for each individual material system where we find MAE of 2.0 (3.4) V for MgO, 1.3 (2.9) V for STO, and 1.0 V for Si using atomic (ionic) electron scattering factors. Since the value of f_{MIP} across all surfaces was ∼10 V, utilizing the Ibers approximation

with atomic electron scattering factors to estimate MIP contributions to flexoelectricity is good to ∼20%.

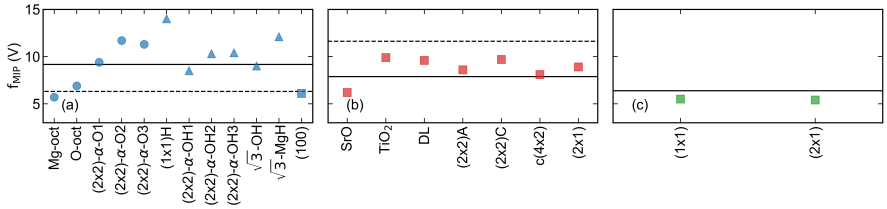

Figure 5.10. Comparison between the strain derivative of the MIP calculated with DFT and with atomic (solid) and ionic (dashed) electron scattering factors for (a) MgO, (b) STO, and (c) Si surfaces. The MAE across all surfaces is 1.7 V and 3.3 V for atomic and ionic electron scattering factors, respectively.

5.4.4. Trends

Table 5.5 indicates there are sizable variations in f_{MIP} across materials systems, even for nominally similar surfaces. Despite this, inspired by Eq. 5.15, we find $\overline{V}_0 \frac{\Delta\Omega}{\Omega_0}$ is a good predictor for f_{MIP} (r=0.87) where $\overline{V}_0$ is the DFT value for the MIP of the equilibrium structure and $\frac{\Delta\Omega}{\Omega_0}$ is the volumetric strain arising from bending. The slope in Figure 5.11(a) is also very close to 1 (0.96), indicating the volume change associated with bending is the dominant contribution to strain-induced MIP changes.

Similarly, Eq. 5.10 indicates the ionization potential could serve as a good predictor for f_{MIP}^{surf}, which is confirmed by the strong correlation (r=0.79) in Figure 5.11(b). Figure 5.11(b) suggests materials with either high or low ionization potentials have strong surface-dependent contributions to flexoelectricity, with high ionization potentials leading to large, positive f_{MIP}^{surf} values and low ionization potentials leading to large, negative f_{MIP}^{surf} values. Empirically, I ≈5.7 V is the cross-over from negative to positive f_{MIP}^{surf} values. This

indicates the change in sign between the SrO and TiO_2 bulk truncations of a STO beam with {100} faces [**74**] could be replicable in other systems.

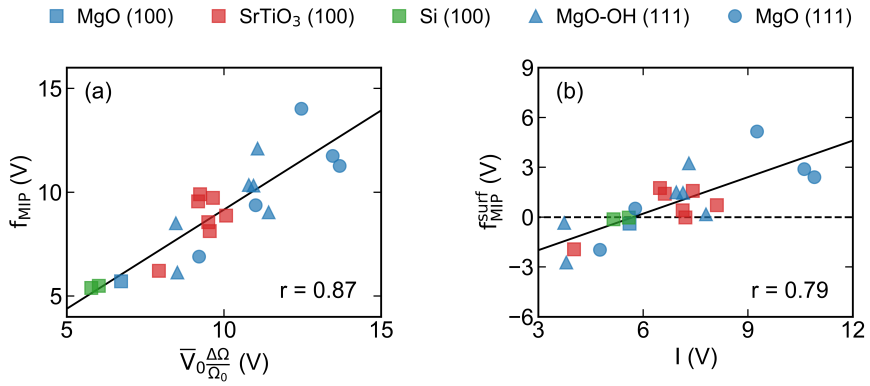

Figure 5.11. (a) Strain derivative of the MIP (f_{MIP}) as a function of the product of the DFT value for the MIP of the equilibrium structure ($\overline{V}_0$) and volumetric bending strain ($\frac{\Delta\Omega}{\Omega_0}$). (b) Surface contributions to the strain derivative of the MIP (f^{surf}_{MIP}) as a function of ionization potential (I).

5.5. Implications for the Total Flexoelectric Response

5.5.1. Total Flexoelectric Response for Specific $SrTiO_3$, MgO, and Si Surfaces

From Eq. 5.8, the total flexoelectric response is the sum of f_{MIP} included in Table 5.5 for each surface and the bulk flexocoupling voltage. Combining the first principles bulk flexocoupling voltage components for STO, MgO, and Si (from Ref. [**58**]) with the expressions for the effective flexocoupling voltage of cubic beams with {100} faces (Chapter 3, ϕ=0 beam bending limit) yields f_{bulk} values of -7.7 V for (100) STO, -2.4 V for (100) MgO, -4.7 V for (111) MgO, and 0.8 V for (100) Si. The sum of f_{bulk} and f_{MIP} for each of the surfaces studied in this work is provided in Table 5.6. It is clear from these calculations that there is a large variation in the magnitude of the total flexoelectric response owing to

surface-sensitive MIP contributions. For example, the total flexocoupling voltage of the MgO (111) surfaces investigated here has a 7.9 V range. These results could explain the variation in the sign and magnitude of experimentally measured flexoelectric coefficients [**10**], though there may be additional interfacial effects from electrodes and/or adsorbed hydrocarbons in flexoelectric experiments.

Materials	Surface	f_{bulk} (V)	f_{MIP} (V)	f_{total} (V)
$SrTiO_3$ (100)	SrO	-7.7	6.2	-1.5
	TiO2	-7.7	9.9	2.2
	(1×1) DL	-7.7	9.6	1.9
	(2×2)A	-7.7	8.6	0.9
	(2×2)C	-7.7	9.7	2.0
	c(4×2)	-7.7	8.1	0.4
	(2×1)	-7.7	8.9	1.2
MgO (100)	Bulk	-2.4	5.7	3.3
MgO (111)	Mg-oct	-4.7	6.9	2.2
	O-oct	-4.7	9.4	4.7
	(2×2)-α-O1	-4.7	11.7	7.0
	(2×2)-α-O2	-4.7	11.3	6.6
	(2×2)-α-O3	-4.7	14	9.3
	(2×2)-α-OH1	-4.7	10.3	5.6
	(2×2)-α-OH2	-4.7	10.4	5.7
	(2×2)-α-OH3	-4.7	9	4.3
	(1×1)H	-4.7	8.5	3.8
	Rt3-MgH	-4.7	6.1	1.4
	Rt3-OH	-4.7	12.1	7.4
Si (100)	(1×1)	0.8	5.5	6.3
	(2×1)-asym	0.8	5.4	6.2

Table 5.6. The total flexoelectric response (f_{total}) is the sum of f_{MIP} and the effective bulk flexocoupling voltage [**58**]

5.5.2. Experimental Comparison with Measurements in Chapter 3

Now we revisit the bulk flexoelectric coefficients calculated in Chapter 4 and account for f_{MIP} to obtain the total flexocoupling voltage that is comparable to the measurements in Chapter 3. We use the Ibers approximation [**164**] for the f_{MIP} (Eq. 5.15) with atomic electron scattering factors from Ref. [**166**] and experimental elastic constants from Ref. [**161, 207, 208**]. The results of this process are summarized in Table 5.7 for samples in the beam and plate bending limits with {100} faces. After accounting for f_{MIP}, we find good agreement between the predicted and measured effective flexocoupling voltages for STO and KTO and poor agreement with LAO and GSO. The agreement with STO and KTO is encouraging because the treatment of the bulk flexocoupling voltage using the DFT approach in Chapter 4 should be robust for true cubic perovskites. The latter disagreement is anticipated based upon the discussion in Chapter 4: LAO and GSO in our calculations were approximated as cubic perovskites. While this approximation is better for LAO, in both cases lattice-quadrupole contributions to the bulk flexoelectric coefficient are neglected, which are likely sizable terms.

	Bulk		Bulk + Ibers		Exp.
	Beam (ϕ=0)	Plate (ϕ=1)	Beam (ϕ=0)	Plate (ϕ=1)	
$SrTiO_3$	-8.18	-10.74	3.46	4.54	4.5 ±0.2
$KTaO_3$	-12.15	-14.50	2.39	2.82	2.1 ± 0.2
$LaAlO_3$	-8.28	-11.40	3.48	4.80	14.5 ± 1.4
$GdScO_3$	-8.44	-11.97	1.33	1.88	-47.2 ± 2.3 (DSO)

Table 5.7. Effective flexocoupling voltages for cubic samples with ⟨100⟩ edges computed from the tensor components in Chapter 4, Table 4.9 for the beam and plate bending limits compared with experimental values from Chapter 3. Columns 2 and 3 only include f_{bulk}, and columns 4 and 5 include f_{bulk} and f_{MIP} within the Ibers approximation using atomic electron scattering factors. All values are in V.

5.5.3. Prediction of Flexoelectric Response in Other Cubic Materials

It is also possible to the predict total flexoelectric responses in a wider range of materials by combining Eq. 5.15 with the flexocoupling voltages of all the cubic materials whose bulk flexocoupling voltage tensor components were calculated in Ref [**58**]. Table 5.8 includes the predicted total flexocoupling voltages for samples with {100}-type faces in the beam-bending (ϕ=0) limit. As mentioned in the previous section, we find good agreement with the experimental STO flexocoupling voltages, which we have measured as 4.5 V and others have measured as 2.2 V [**52**]. There is poor agreement with the experimental BTO flexocoupling voltage of 22 V [**53**], which likely stems from the presence of precursor ferroelectric domains in experiments [**53, 209, 210**] and does not necessarily invalidate the Ibers approximation in this context. A more complete comparison to experimental measurements is not possible because of a deficiency in the number of experimental flexoelectric investigations on single crystals.

5.6. Revisiting the Finite Bulk Flexoelectric Coefficient of Al

In Chapter 4 I demonstrated FCC Al has finite octupole moments which manifest in non-zero bulk flexocoupling voltages. For example, I showed that f_{1111} = -13.80 V. This result was troubling because an elemental metal like Al should not support a polarization. The resolution to this issue is in the MIP contribution we have described in this chapter: the total flexocoupling voltage is the sum of the bulk flexocoupling voltage and the MIP contribution, and a potential difference will develop across a bent slab only if the total flexocoupling voltage is non-zero.

	f_{bulk} (V)	f_{MIP}^{Ibers} (V)	f_{total} (V)
C	-5.0	16.4	11.4
Si	0.0	6.4	6.4
MgO	-3.9	9.2	5.3
NaCl	-7.4	6.3	-1.1
CsCl	0.0	10.1	10.1
$BaZrO_3$	-11.3	13.8	2.5
$BaTiO_3$	-12.2	11.2	-0.9
$PbTiO_3$	-10.5	9.7	-0.7
$SrTiO_3$	-7.8	11.6	3.8

Table 5.8. Bulk and MIP contributions to the total flexocoupling voltage of bent beams with {100}-type faces for a range of cubic materials. Bulk contributions are calculated from flexocoupling tensor components reported in Ref. [**58**]. MIP contributions are estimated with the Ibers approximation with atomic scattering factors from Ref. [**166**] and Poisson ratios from Ref. [**161, 207, 208**].

The above suggests that the MIP contribution to the total flexocoupling voltage, for any given strain gradient configuration, must be equal and opposite to the effective bulk flexocoupling voltage. As a test, I calculated f_{MIP} from a surface slab of FCC aluminum subjected to longitudinal strains as shown in Figure 5.12 using the approach described in Section 5.4 where the clamped plate bending strains were replaced with a longitudinal strain of

$$\epsilon_{long} = \epsilon \begin{pmatrix} 1 & 0 & 0 \\ 0 & 0 & 0 \\ 0 & 0 & 0 \end{pmatrix}. \tag{5.16}$$

With this strain profile, f_{bulk}=f_{1111}. Therefore, if the arguments presented in this chapter are correct we should find $f_{MIP} = -f_{1111}$.

We performed these calculations with WIEN2k parameters that matched those used in the calculations presented in Section 4.9. The results of the surface slab calculations and the bulk calculation used to obtain f_{MIP} are shown in Figure 5.12(b)-(c). We find $\frac{d(V_{avg}-E_{Al1s})}{d\epsilon_{vol}}$=14.61 V and $\frac{d(E_{Al1s}-E_{vac})}{d\epsilon_{11}}$= -0.85 V. The sum of these two quantities gives f_{MIP}=13.76 V, which, within the uncertainty of these calculations, demonstrates

$$f_{total} = f_{1111} + f_{MIP} = 0V \tag{5.17}$$

for elemental Al. This result makes very clear that only by including the MIP contributions to the total flexoelectric response does one obtain a physically consistent description of flexoelectricity.

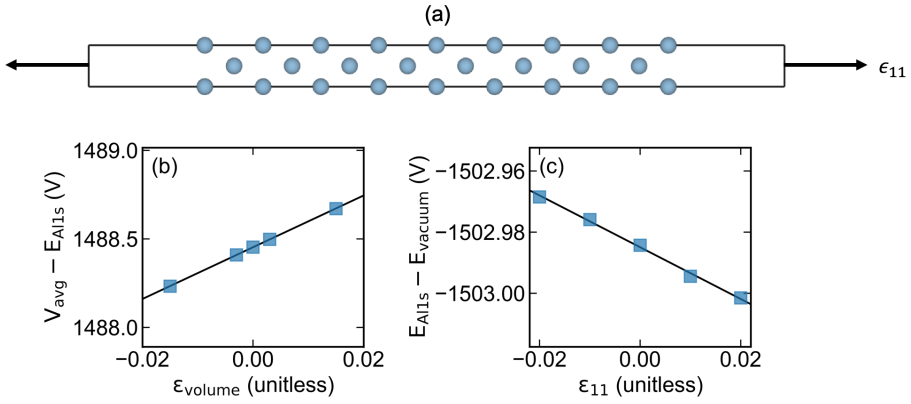

Figure 5.12. (a) Al surface slab used in the simulation subjected to a longitudinal strain ϵ_{11}. (b) Difference between the average Coulomb potential and Al1s eigenvalue in bulk Al as a function of hydrostatic strain. (c) Difference between the vacuum energy and Al1s eigenvalue in the innermost layer of a Al (100) slab as a function of longitudinal strain. Data from each calculation are blue squares and linear fits are black.

CHAPTER 6

Extrinsic Contributions to Flexoelectricity

6.1. Introduction

One of the primary tenants of materials science is understanding and manipulating defects to engineer materials properties. Though the field of flexoelectricity is still nascent, there have been many demonstrations that extrinsic contributions to flexoelectricity (i.e. terms related to microstructure, point defects, etc.) are as, if not more, important than intrinsic contributions (i.e. terms which depend on bulk crystallography and chemistry). For example, experiments have shown free carriers in semiconductors [**114**], polar nanoregions in relaxor ferroelectrics [**209, 211**], and polar selvedge regions in ferroelectric ceramics [**212**] significantly modify the overall flexoelectric response of a sample. Similarly, large flexoelectric polarization has been observed around dislocation cores [**30**] and crack tips [**31**], and we have investigated the importance of surfaces in Chapter 5. Experimentally isolating extrinsic and intrinsic contributions to flexoelectricity is an important step toward improving our fundamental understanding of flexoelectricity, closing the sizable divide between the experimental and theoretical states of the field [**10, 11**], and substantiating the viability of flexoelectricity for practical applications.

After providing an overview of the experimental methods used for the work described in this chapter, I explore extrinsic contributions to flexoelectricity in three cases. First, in

Section 6.3 I explore the implications of TB polarization and microstructure on the flexoelectric response of twinned LAO, showing TBs have flexoelectric coefficients substantially higher than the surrounding bulk [**75**]. This work also demonstrates how oxides with ferroelastic phase transitions, such as LAO, offer a rich platform for controlled studies of flexoelectricity which bridge the gap between single crystals and polycrystalline ceramics. Next, in Section 6.4 I explore the flexoelectric response of Nb-doped STO single crystals. These measurements indicate doping yields a $\sim 10^3$ increase in the effective flexoelectric coefficient over undoped STO single crystals, providing further indication of the generality of the observations reported by Ref. [**114**]. In Section 6.5 I describe the observation of anomalously large flexoelectric responses in MgO crystals and discuss some possible origins of this phenomenon. Experiments meant to further explore the results presented in Section 6.4 and 6.5 were hindered by the onset of the COVID-19 pandemic, so future research directions on these topics are presented in Chapter 9. I performed all analyzes, simulations, and measurements, and Binghao (Evan) Guo also assisted with some of the flexoelectric sample preparation and TPB measurements. The measurements on LAO are described in Ref. [**75**]. All work benefitted from discussions with the LDM group members, especially Professor Laurence D. Marks.

6.2. Methods

6.2.1. Flexoelectric and Mechanial Characterization with Dynamic Mechanical Analysis

Flexoelectric and mechanical characterization were performed using TPB as described in Chapters 2 and 4. Here we only provide specific details which differ from the procedures described there.

A TA Instruments RSA-III DMA was used to bend samples at 33 Hz while a Signal Recovery 7265 Dual Phase DSP LIA measured the short-circuit current generated due to the flexoelectric effect. Unless otherwise stated, a constant static force of ∼1.5 N was used to hold the sample in place while an oscillatory force was applied. Temperature was controlled for temperature-dependent experiments using a forced-air convection oven on the DMA. It was changed in small increments (<5 °C) and the sample was allowed to equilibrate for ∼5 minutes before flexoelectric characterization. Each data point shown in the temperature-dependent data corresponds to the slope of a line made from measurements of at least 5 strain gradient values.

6.2.2. Polarized Optical Microscopy

A polarized optical microscope operates under the same principles as a traditional optical microscope except it possesses polarizing plates before and after the sample [**213**]. The polarizing plate before the sample (known as the polarizer) polarizes the white light from the source and the polarizing plate after the sample (known as the analyzer) polarizes the light leaving the sample. Most commonly, the polarizer and analyzer are aligned in the crossed position so no transmitted light reaches the detector without a sample present. In

this configuration, contrast is generated from spatial variations in the refractive properties of the sample, making this imaging mode sensitive to the grain and domain orientation. As such, this technique is commonly used in the mineral science and ferroic communities to characterize microstructure [**213**].

In this work, reflection and transmission mode images were acquired on an Olympus PMG 3 and a Nikon SMZ 1500, respectively. A Nomarski prism was used to enhance contrast in the reflection geometry. There were no qualitative differences between the transmission and reflection images for the samples used for flexoelectric characterization.

6.2.3. Impedance Spectroscopy

Impedance spectroscopy refers to a set of characterization techniques commonly used in the dielectric and electrochemical communities which measure the frequency response of impedance [**214**]. Impedance is the ratio of an applied AC voltage

$$V_{applied} = |V|e^{i(\omega t+\delta)} \tag{6.1}$$

to the induced current

$$I_{measured} = |I|e^{i(\omega t+\phi)} \tag{6.2}$$

and is given by

$$Z = \frac{|V|e^{i(\omega t+\delta)}}{|I|e^{i(\omega t+\phi)}} \tag{6.3}$$

where Z is impedance, $|V|$ and $|I|$ are the amplitudes of the voltage and current, δ and ϕ are phase shifts, and ω is frequency. Impedance contains information on the resistance, capacitance, and inductance of a sample.

Since the samples used for flexoelectric characterization are essentially parallel-plate capacitors, the dielectric constant can be extracted by fitting the measured impedance of the flexoelectric samples to the equation for the impedance of a capacitor

$$Z = \frac{1}{i\omega C} \tag{6.4}$$

where C is capacitance. The capacitance obtained from Eq. 6.4 is related to the dielectric constant via the expression for the capacitance of a parallel-plate capacitor

$$C = \frac{A}{d}\varepsilon_0\varepsilon_r \tag{6.5}$$

where A is the electrode area, d is the sample thickness, ε_0 is the permittivity of free space, and ε_r is the relative permittivity of the sample. The measurements reported here utilized a Solartron 1260 Impedance Spectrometer. The frequency of the AC voltage was swept from 1 kHz to 1 MHz and the AC voltage was kept at 100 mV.

6.2.4. X-ray Diffraction

x-ray diffraction (XRD) is one of the primary materials characterization tools. Instead of providing an overview of XRD techniques, which can be found in numerous texts such as Ref. [**215**], I will briefly describe the XRD technique utilized in this work to investigate MgO crystals: $\omega - \phi$ maps [**216**]. $\omega - \phi$ maps are a series of ω rocking curves acquired as function of rotation about the surface normal. This measurement allows one to discern the

number of, and angular relationship between, grains/domains in a polycrystalline sample. The convention used to define angles here is illustrated in Figure 6.1.

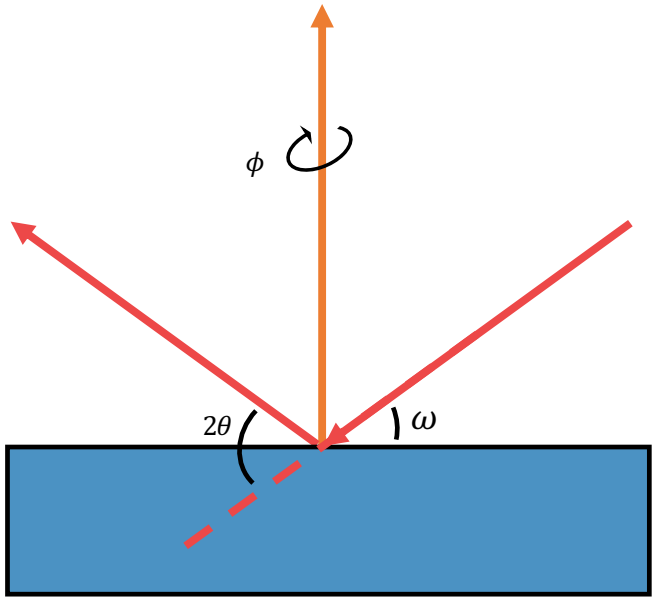

Figure 6.1. Illustration of a typical XRD geometry. ω is the angle between the sample surface and incident beam, 2θ is the angle between the incident beam and the detector, and ϕ is the rotation angle about the surface normal of the sample.

All diffraction patterns were acquired on a Rigaku Smartlab with a 9 kW rotating Cu source, Ge (220) 2 bounce monochromator, 1 mm incident slit, 2 mm receiving slits (RS1 and RS2), and 5 mm length limiting slit. $\omega - \phi$ maps were acquired at $0 \leq \phi \leq 360°$ with a step size of 5° and $\omega = 42.908° \pm 0.48°$ with a step size of 0.0004° and speed of 0.48°/min. The detector was fixed at 2θ=42.908° for the $\omega - \phi$ maps.

6.3. Twin Boundary Mediated Flexoelectricity in $LaAlO_3$

6.3.1. Twinning in $LaAlO_3$

LAO is a rhombohedral 332 perovskite with space group $R\bar{3}c$ at room temperature and atmospheric pressure [**96**] that is commonly used as a substrate and film in epitaxial thin-film growth [**217, 218**]. It undergoes an improper ferroelastic phase transition at 550 °C from a high temperature cubic phase to a low temperature rhombohedral phase characterized primarily by octahedral rotations about the cubic [111] directions [**97**]. Since there are four axes about which the octahedral rotations can occur, the phase transition yields four rhombohedral twin domains [**102, 103**] each of which is separated by a TB. These twins can be paired in 12 different strain-free configurations [**105, 106**] leading to a rich array of TB microstructures as shown in Figure 6.2.

The crystallography of the TBs [**102, 103, 216, 105, 106**] as well as their mechanical response to dynamic mechanical stimuli has been extensively studied [**97, 66, 104, 219, 220, 221, 222**] making LAO a great candidate to examine TB effects on flexoelectricity. While experiments on twinned STO have indicated the existence of TB contributions to flexoelectricity [**52**], there has been no quantitative analysis of TB flexoelectric contributions such as determining the flexoelectric coefficient of a TB. Moreover, although simulations have suggested ferroelastic microstructure is important in other electromechanical contexts [**223, 224, 225**], the role of TB microstructure in flexoelectricity has not been addressed.

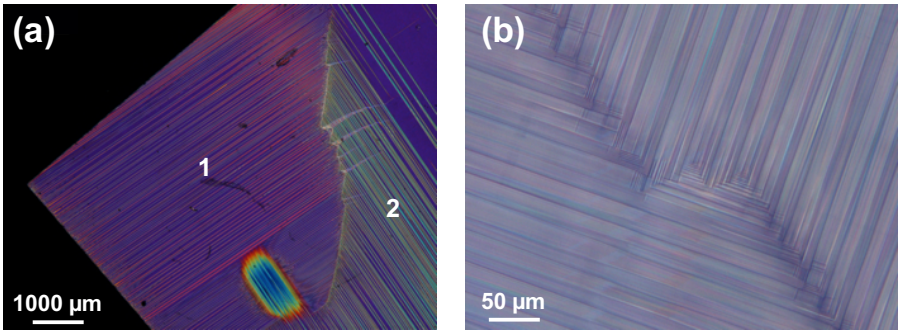

Figure 6.2. Polarized optical micrographs of the $(001)_{pc}$ surface of a LAO crystal acquired in the cross-polarized position. (a) Positions 1 and 2 indicate one of the more common twin microstructures seen in these samples: lamellar twins oriented along the $\langle 001 \rangle_{pc}$ directions. (b) Polarized optical micrograph showing how lamellar twins can meet in complex ways.

6.3.2. Twin Boundary Dynamics with Dynamic Mechanical Analysis

The low-frequency mechanical response of twinned materials is dominated by the dynamics of TBs and well suited for characterization with dynamic mechanical analysis, especially with TPB [**60, 66, 226**]. Extensive investigations of the mechanical properties of LAO with TPB have shown they depend sensitively on the frequency and amplitude of the oscillatory force, magnitude of the static force, temperature, and TB microstructure [**97, 66, 104, 219, 220, 221, 222**]. For the purposes of this work, the relevant findings are summarized in the phase diagram shown in Figure 6.3.

At high temperatures ($T > T_c$) LAO is in its paraelastic phase [**66**]. There are no TBs and the mechanical response is that of a single crystal. As the temperature is lowered below T_c LAO twins as described in Section 6.3.1. The mechanical properties of twinned LAO for $T^* < T < T_c$ are dominated by TB motion which causes ferroelastic LAO to be significantly softer than paraelastic LAO [**66**]. The mechanical response in this regime is also time-dependent and is often referred to as anelasticity. TBs in LAO remain mobile

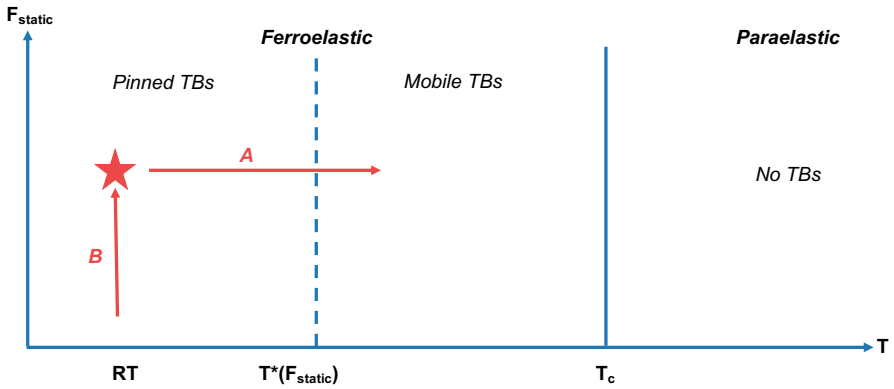

Figure 6.3. TPB "phase diagram" of LAO at fixed frequency (∼10-100 Hz) and dynamical force. Above T_c, LAO is cubic and twin-free. When the temperature drops below T_c, LAO undergoes a cubic to rhombohedral phase transition and twins. For $T^*<T<T_c$, the mechanical properties of twinned LAO are dictated by TB motion. When $T<T^*$ long-range TB motion is not possible and mechanical properties are controlled by TB deformation. A and B denote the experiments in Section 6.3.3, respectively. The star indicates the location of the experiments in Section 6.3.4.

until the temperature, static force, and frequency combination drop below a critical value (T^*) at which point the TBs are immobilized by pinning. This is not a sharp transition [**66, 222**] and is dependent on microstructure and defect distribution (represented as a dashed line in Figure 6.3). When $T < T^*$ long-range TB motion does not occur and the mechanical response is controlled by TB deformation. Samples at low static forces appear softer in this regime than samples at high static forces because the extent to which TBs deform in response to the dynamic force is sensitive to the static force [**227**].

We leverage the known impact of TBs on the mechanical properties of LAO described above to isolate TB contributions to flexoelectricity. First, in Section 6.3.3.1 we measure the effective flexoelectric coefficient as a function of temperature across the pinned-to-mobile TB transition (Path A in Figure 6.3). By connecting the temperature dependence of the flexoelectric coefficient to that of TB mobility, we demonstrate the existence of

TB contributions to flexoelectricity. Next, in Section 6.3.3.2 we measure the flexoelectric response at room temperature as a function of static force (Path B in Figure 6.3). This experiment demonstrates TB flexoelectric properties without contributions from TB motion or dynamic deformation are accessible at high static forces at room temperature. These intrinsic TB flexoelectric properties are characterized in Section 6.3.4 and explained in terms of a catenary cable model in Section 6.3.5. Estimates of TB flexoelectric coefficients are provided in Section 6.3.6.

6.3.3. Dynamic Twin Boundary Contributions

6.3.3.1. Flexoelectric Response as Function of Temperature. At room temperature TBs are pinned defects which deform under external forces, but there is no long-range motion because of pinning site interactions. It is established that TBs become mobile when temperature is increased as this provides thermal energy for TBs to escape pinning sites [**97, 66, 104, 219, 220, 221, 222**]. At first, increasing temperature locally enhances TB deformations, but after a sample-dependent threshold (typically ∼100 °C), large-scale TB motion and annihilation become possible. When TBs become mobile, their elastic properties exhibit a dramatic softening and increased attenuation (measured as $\tan(\delta)$, the ratio of the real and imaginary components of the dynamic modulus, see Chapter 2).

These behaviors are reflected in the temperature dependence of the flexoelectric response and attenuation of a twinned LAO sample shown in Figure 6.4. Namely, μ_{eff} increases between ∼30-100 °C as TBs become more deformable and decreases once TB motion becomes possible, with a maximum corresponding to the onset of motion. The mechanical response of the sample as a function of temperature is consistent with the TB

mobility explanation for the temperature-dependent flexoelectric characterization: there is a maximum in internal friction at ∼80 °C which coincides with the maximum in the flexoelectric response. Additionally, imaging of the sample before and after the measurement confirms TB motion because there are microstructural changes in the sample after the temperature dependent experiments.

The flexoelectric response of twinned materials when TB motion is possible is not solely a function of the individual TB properties, but will be sensitive to TB microstructure, distribution of pinning sites, etc. Therefore, while Figure 6.4 clearly demonstrates an enhanced flexoelectric response in twinned samples originating from TBs, it is difficult to use such experiments to discern the flexoelectric properties of the TBs themselves. For this we use room temperature measurements in which TB motion contributions to the flexoelectric response are suppressed.

6.3.3.2. Flexoelectric Response as a Function of Static Force. At room temperature TBs are immobile owing to pinning [**66**]. At low static forces the mechanical response of twinned materials is dominated by dynamic TB deformations which have a softening effect [**227**]. At high static forces, these dynamic TB deformations are suppressed [**227**]. This behavior is in sharp contrast to single crystal samples where the mechanical properties measured in TPB are insensitive to static force. As a consequence, unlike the flexoelectric characterization shown in Chapters 2 and 3 where the flexoelectric response of single crystals was proportional to dynamic force and insensitive to static force, the flexoelectric response of twinned LAO should depend on static force.

Figure 6.5 shows the characterization of a sample with a mixture of TBs at a constant dynamic force while varying the static force holding the sample in place during TPB.

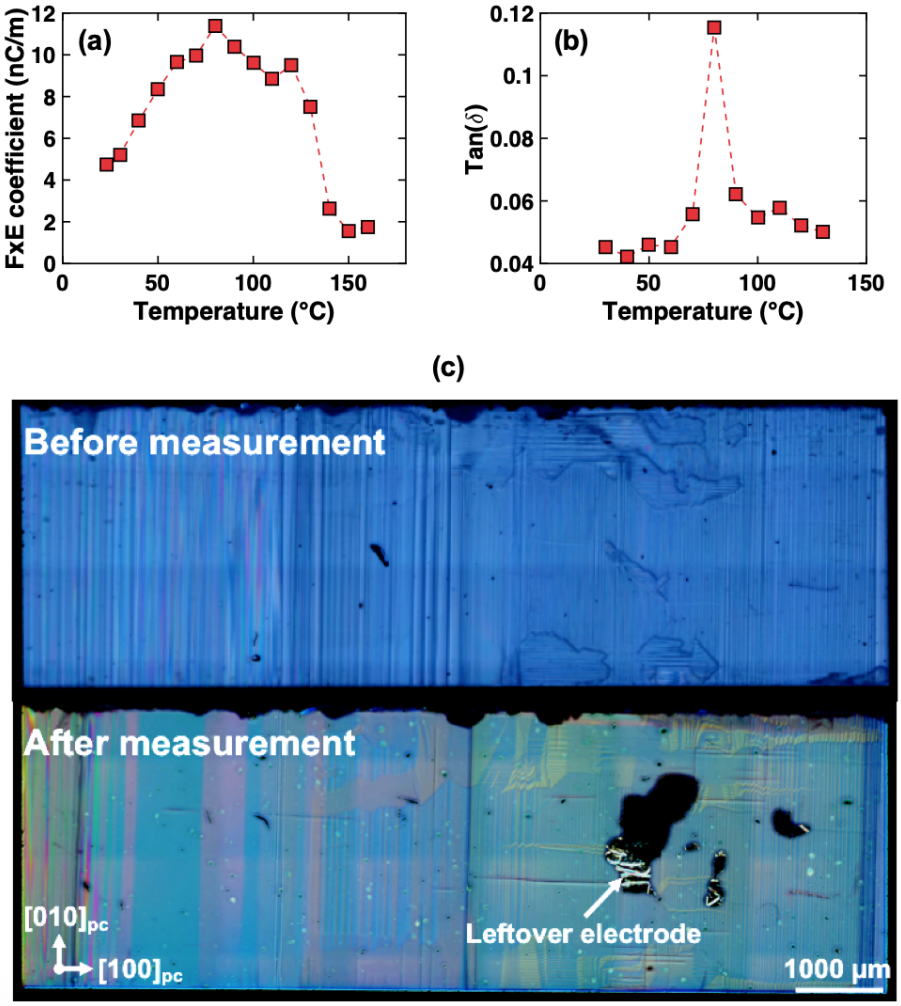

Figure 6.4. Characterization of LAO crystal with a mixture of TB orientations as a function of temperature at fixed static force. The temperature dependence of (a) the effective flexoelectric coefficient and (b) elastic attenuation correlates with the known temperature dependence of TB motion, with the peak corresponding to the onset of TB motion. Lines are visual guides. (c) Imaging of the sample before and after temperature-dependent flexoelectric characterization confirms changes to the microstructure.

As established in Section 6.3.2, at low static forces dynamic TB deformation is relatively unhindered, whereas at high static forces dynamic TB deformations are largely suppressed.

This behavior is confirmed by the storage modulus and attenuation measurements shown in Figure 6.5.

In addition to these changes in the mechanical properties, Figure 6.5 indicates an increase in the flexoelectric polarization as the static force is decreased. We attribute this enhancement to dynamic TB deformations. Like the temperature dependent flexoelectric enhancements, these flexoelectric contributions are sensitive to microstructure and defects. At high static forces, the dynamic TB deformations are suppressed and the flexoelectric response approaches a constant behavior. Since there are minimal dynamic TB deformations in this high static force regime, any differences between the flexoelectric responses of twinned crystals are a consequence of the intrinsic flexoelectric properties of the TBs. Measurements in this regime are used in Section 6.3.4 to quantify the flexoelectric properties of TBs.

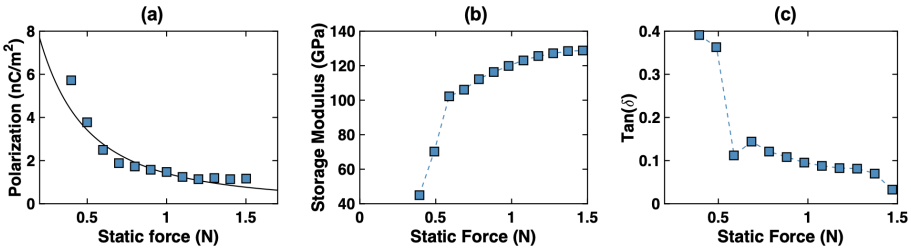

Figure 6.5. Characterization of LAO crystal with a mixture of TB orientations as a function of static force at room temperature and fixed dynamic force. (a) Flexoelectric polarization decreases with increasing static force because of dynamic TB deformations. Solid line is a fit using a catenary cable model (Section 6.3.5). (b) Storage modulus and tan(δ) for sample with mixture of Type I and II orientations as a function of static force. The sample is softer and has increased elastic attenuation at lower static forces owing to dynamic TB deformations.

6.3.4. Intrinsic Twin Boundary Flexoelectricity

Having determined that the intrinsic flexoelectric properties of TBs can be probed at room temperature with high static forces, we now seek to minimize the complexities associated with TB microstructures (e.g. see images in Figures 6.2 and 6.4) and separate TB and crystallographic effects. To accomplish this, in Section 6.3.4.1 we investigate the flexoelectric response of LAO samples with uniform TB microstructures cut to have identical sample geometries (10 mm × 3 mm × 0.5 mm beams) and crystallographic orientation (all surfaces are $\{100\}_{pc}$ planes). The TBs in each of these samples have TB normals perpendicular or parallel to the long axis of the sample (Figure 6.6). The former case will be referred to as Type I TBs, and the latter as Type II TBs. After characterizing the flexoelectric responses of samples with pure Type I and II TBs in Section 6.3.4.1, we then investigate the flexoelectric response of a sample with a mixture of Type I and II TBs in Section 6.3.4.2.

6.3.4.1. Pure Twin Boundary Samples. The flexoelectric responses of both the pure Type I and II samples are shown in Figure 6.6. The initial flexoelectric response of the Type I sample was linear with μ_{eff} = 3.6±0.2 nC/m. I found the flexoelectric response remained linear after continuously increasing and decreasing the strain gradient (a process which we will refer to as strain gradient cycling), but μ_{eff} increased, eventually reaching a steady-state value of 4.8±0.3 nC/m. The Type II sample exhibited qualitatively similar behavior in that the flexoelectric response of the sample was linear, but μ_{eff} increased from 3.1±0.3 nC/m to a steady-state value of 3.5±0.2 nC/m after strain gradient cycling.

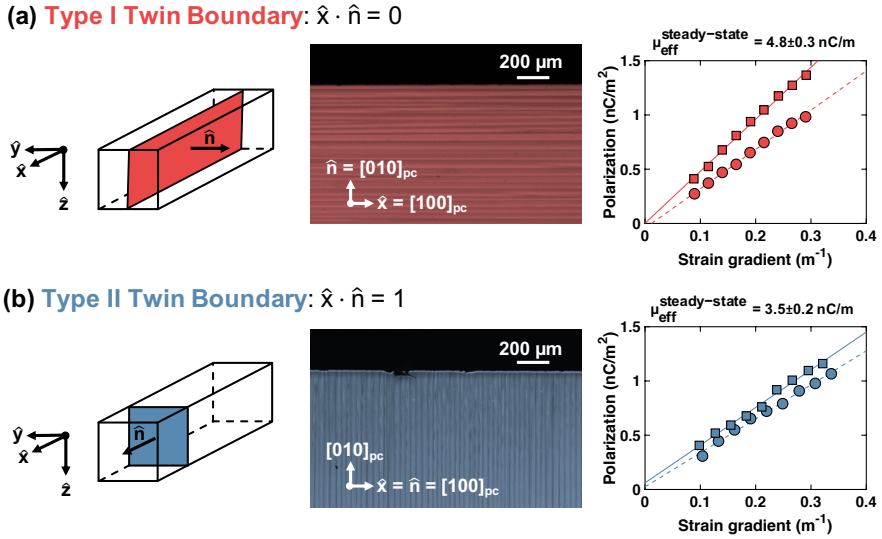

Figure 6.6. Flexoelectric characterization of LAO crystals with uniform, lamellar TB microstructures. (a) Type I boundaries have normals ($\hat{n}$) perpendicular to the long axis of the sample ($\hat{x}$) as shown by reflection polarized optical microscopy. The flexoelectric response of the Type I sample was linear and increased to an effective steady-state flexoelectric coefficient of 4.8±0.3 nC/m after strain gradient cycling. (b) Type II boundaries have normals parallel to the long axis of the sample as shown by reflection polarized optical microscopy. The flexoelectric response of the Type II sample was linear and increased to an effective steady-state flexoelectric coefficient of 3.5±0.2 nC/m after strain gradient cycling. Circles and dashed lines correspond to the initial measurements and linear fit, respectively. Similarly, squares and solid lines correspond to the steady-state measurements after gradient cycling and linear fit, respectively. Uncertainties correspond to the 95% confidence interval of the fit. Images are false-colored for clarity.

The flexoelectric response of twinned LAO shown in Figure 6.6 differs from the flexoelectric response of twin-free LAO in two important ways. First, the flexoelectric response of samples with TB is larger than that of twin-free samples. Recall from Chapter 3 that twin-free LAO had an effective flexoelectric coefficient of $\mu_{eff} = 3.2\pm0.3$ nC/m. Comparing these values to the steady-state flexoelectric responses of the twinned samples shown in Figure 6.6 suggests that twin boundaries are mechanically polarized by strain gradients

with flexoelectric contributions that are distinct from the bulk. We find TB polarization can increase the effective flexoelectric coefficient by upwards of 50% over twin-free samples; this is similar to the difference between the effective flexoelectric coefficients of single crystals with different crystallographic orientation (e.g. see measurements of the flexoelectric coefficients of STO crystals with (100) and (110) surfaces in Chapter 3).

Second, the flexoelectric response of LAO with twins differs from the measurements performed on twin-free LAO, and all other single crystals analyzed in Chapter 3, because of the time-dependent nature of the flexoelectric response. To investigate the time-dependent response, I performed additional flexoelectric measurements on subsequent days (Figure 6.7). We found that the enhancements were partially reversible, with the effective flexoelectric coefficients returning to the same steady-state value after strain gradient cycling. Additionally, as shown in Figure 6.8, imaging the Type I and II samples after flexoelectric characterization reveals no evidence for microstructure changes, which confirms the elastic nature of the time-dependent flexoelectric enhancements and indicates they are associated with TB deformation, not TB motion.

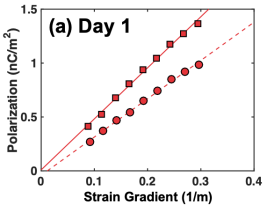

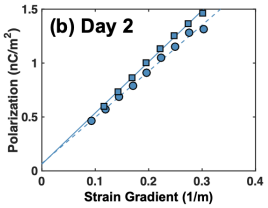

(c) Flexoelectric Coefficient (nC/m)

	Initial	Steady-State
Day 1	3.6±0.2	4.8±0.3
Day 2	4.3±0.3	4.8±0.3

Figure 6.7. Measurements performed on subsequent days on the Type I sample. In both (a) and (b) circles and dashed lines correspond to the initial measurement data and linear fit, respectively. Similarly, squares and solid lines correspond to the steady-state measurement data and linear fit, respectively. (c) The values of the effective flexoelectric coefficients with uncertainties corresponding to the 95% confidence interval of the linear fits.

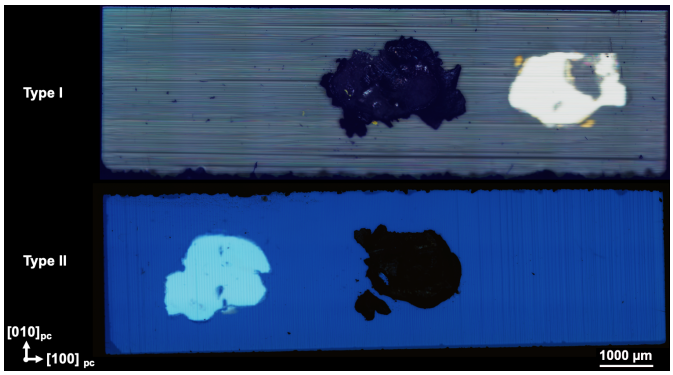

Figure 6.8. Imaging of Type I and II samples after flexoelectric characterization using reflection polarized optical microscopy confirms no permanent changes to the microstructure. Both samples still have uniform lamellar TB microstructures. The splotches correspond to left-over electrode.

We attribute the reversible, time-dependent flexoelectric behavior shown in Figures 6.6 and 6.7 to residual dynamic TB deformation [**66, 227**]. Even at the high static forces used here, some dynamic deformations can occur because of the statistical distribution of pinning sites and TB-pinning site interactions. This is reflected in the elastic response data shown in Figure 6.9 where the pure Type I and II samples are softer and exhibit more internal friction than the twin-free sample, but are significantly stiffer than situations in which dynamic TB deformations occur freely (Figure 6.5).

6.3.4.2. Mixed Twin Boundary Samples. Next, the flexoelectric response of sample with a mixture of Type I and II TBs at fixed static force was measured under the same conditions as the measurements in Figure 6.6. As shown in Figure 6.10, μ_{eff} increased from an initial value of 3.6±0.1 nC/m to a steady-state value of 4.0±0.2 nC/m (as determined from the first 5 data points in each data set) after strain gradient cycling. This time-dependence is similar to those of the pure Type I and II samples and the steady-state μ_{eff} is between those of the pure Type I and Type II samples, consistent with the mixture

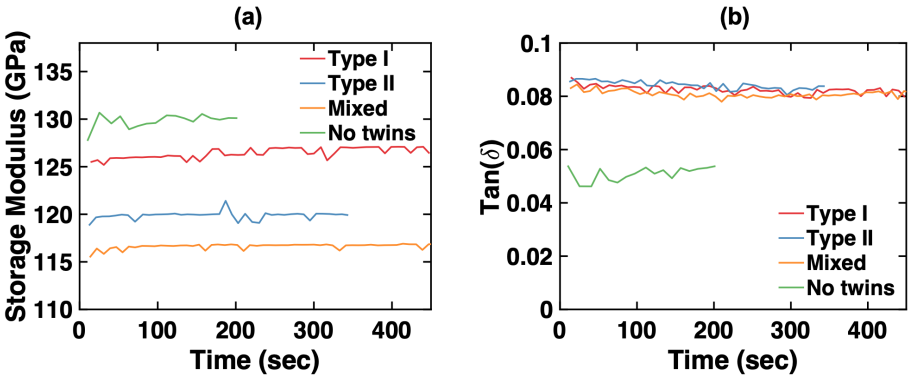

Figure 6.9. Storage modulus and tan(δ) for a twin-free sample and samples with Type I, Type II, and a mixture of Type I and II orientations. The data was acquired at a constant frequency (33 Hz), static force (1.5 N) and dynamic force (0.6 N).

of Type I and II TBs present in the sample. Additionally, these measurements indicate a non-linear flexoelectric response when the strain gradient exceeds $\sim$0.25 m^{-1}. This starkly contrasts with the flexoelectric responses of the other twinned samples and single crystals investigated in Chapter 3, which remained linear for all strain gradients used. The non-linearity became more pronounced in steady-state, but a linear flexoelectric response was always recovered by decreasing the strain gradient below $\sim$0.25 m^{-1}. Given the return to linear flexoelectricity below a certain strain gradient, and that post-experiment imaging confirmed no permanent changes to TB microstructure (Figure 6.10), the non-linearity is attributed to TB-pinning site interactions. This behavior is consistent with the catenary cable model described in Section 6.3.5.

6.3.5. Catenary Cable Model

To understand the flexoelectric properties of TBs, it is useful to analyze a simple model for a pinned defect: the one-dimensional catenary cable [**56**]. Consider a one-dimensional

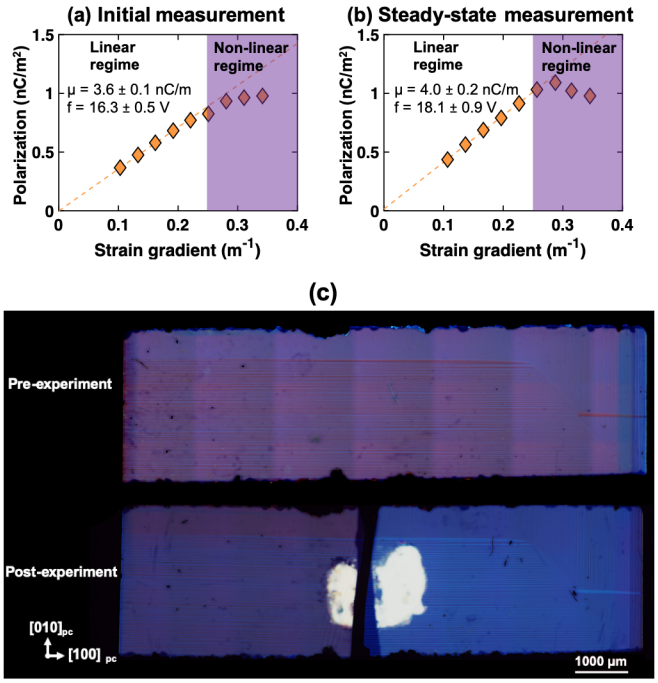

Figure 6.10. Flexoelectric characterization of a LAO crystal with a mixture of Type I and II TB orientations. (a) The initial flexoelectric response is linear at low strain gradients with an effective flexoelectric coefficient of 3.6±0.1 nC/m, and non-linear above a strain gradient of ∼0.25 m^{-1}. (b) The steady-state flexoelectric response after strain gradient cycling remains linear at low strain gradients with an increased effective flexoelectric coefficient of 4.0±0.2 nC/m. There is pronounced non-linear behavior above ∼0.25 m^{-1}. (c) Imaging the sample with a mixture of Type I and II TBs before and after flexoelectric characterization using reflection polarized optical microscopy confirms no permanent changes to the microstructure. The vertical lines in the pre-experiment image are imaging artifacts. The central bright region in the post-experiment image is left-over electrode. There is a black portion in the middle of the sample in the post-experiment image because the sample fractured into two pieces after the experiment was performed.

representation of the flexoelectric effect

$$\frac{dP}{dt} = \mu \frac{d\kappa}{dt} \tag{6.6}$$

where t is time and μ is the flexoelectric coefficient linearly relating the change in polarization ($\frac{dP}{dt}$) to the change in strain gradient ($\frac{d\kappa}{dt}$). For TPB, it is useful to expand $\frac{d\kappa}{dt}$ in Eq. 6.6 as a function of static force (f_S) and dynamic force (f_D)

$$\frac{dP}{dt} = \mu \left(\frac{\partial \kappa}{\partial f_S} \frac{df_S}{dt} + \frac{\partial \kappa}{\partial f_D} \frac{df_D}{dt} \right) \tag{6.7}$$

which reduces to

$$\frac{dP}{dt} = \mu \frac{\partial \kappa}{\partial f_D} \frac{df_D}{dt} \tag{6.8}$$

because f_S is constant in TPB experiments.

Next, we recognize that the strain gradient in a bent feature is proportional to its central displacement (e.g. see Chapter 4)

$$\kappa = Cu \tag{6.9}$$

where C is a geometric/elastic constant. Using Eq. 6.9 to express Eq. 6.8 in terms of u yields

$$\frac{dP}{dt} = C\mu \frac{\partial u}{\partial f_D} \frac{df_D}{dt}. \tag{6.10}$$

Eq. 6.10 indicates that a non-linear elastic material (i.e. a material exhibiting a non-linear response between u and f) can yield a non-linear flexoelectric response with only linear flexoelectric couplings.

Now it is necessary to specify $\frac{\partial u}{\partial f_D}$ for a pinned defect. We approximate the deformation of a pinned defect as a catenary cable.

$$u(x) = \frac{T}{f_S + f_D} \cosh\left(\frac{f_S + f_D}{T} x\right) \tag{6.11}$$

where x is the position along a defect subjected to a force $f = f_S + f_D$. T is a constant related to line tension. Figure 6.11 shows catenary cable solutions [**56**] for different values of T/f.

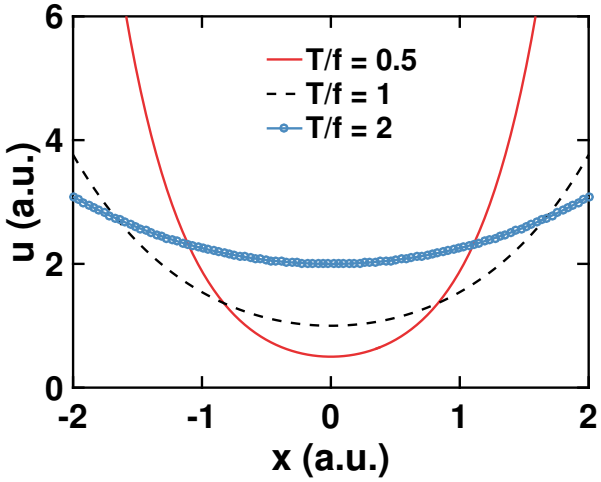

Figure 6.11. Catenary cable solutions for different values of T/f.

For simplicity, we work with the average displacement u_{avg} between two pinning sites spaced L apart.

$$u_{avg} = \frac{1}{L}\int_{-L/2}^{L/2} u(x)dx = 2\frac{T^2}{(f_S + f_D)^2 L} \sinh\left(\frac{(f_S + f_D)\, L}{2T}\right) \tag{6.12}$$

Substituting Eq. 6.12 into Eq. 6.10, we find

(6.13)
$$\frac{dP}{dt} = C\mu \left(\frac{T}{\left(f_S + f_D\right)^2} \cosh\left(\frac{\left(f_S + f_D\right) L}{2T} \right) - 4 \frac{T^2}{\left(f_S + f_D\right)^3 L} \sinh\left(\frac{\left(f_S + f_D\right) L}{2T} \right) \right) \frac{df_D}{dt}$$

With the approximation $\frac{df_D}{dt} \approx \omega f_D$ where ω is the oscillatory frequency of the experiment, Eq. 6.13 can be written as

(6.14)
$$\frac{dP}{dt} = C\mu \left(\frac{T}{\left(f_S + f_D\right)^2} \cosh\left(\frac{\left(f_S + f_D\right) L}{2T} \right) - 4 \frac{T^2}{\left(f_S + f_D\right)^3 L} \sinh\left(\frac{\left(f_S + f_D\right) L}{2T} \right) \right) .\omega f_D$$

This model captures much of the essential physics behind the effects of pinned TBs on flexoelectricity. As an example, consider the experiments shown in Figure 6.5 and 6.10. In the former case, $\frac{dP}{dt}$ was measured as a function of f_S for a fixed f_D and in the latter $\frac{dP}{dt}$ was measured as a function of f_D for a fixed f_S. Setting $C = \mu = T = L = \omega = 1$, these two experiments would yield polarization responses shown in Figure 6.12, which are in excellent agreement with the flexoelectric characterization shown in Figure 6.5 and 6.10.

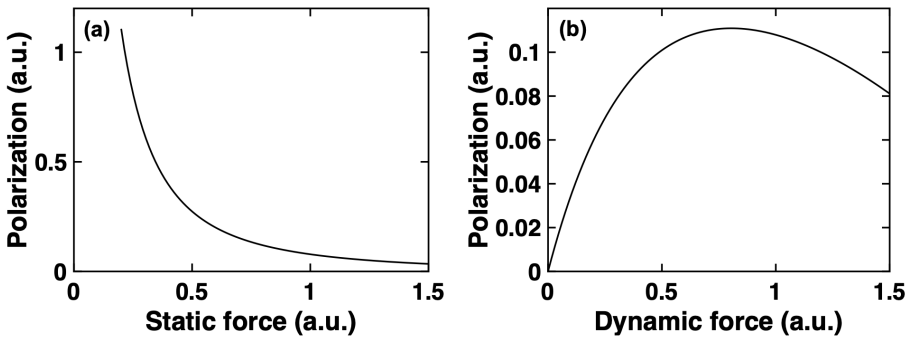

Figure 6.12. Flexoelectric polarization of a pinned defect modeled as a catenary cable as (a) a function of static force for a fixed dynamic force and (b) a function of dynamic force for a fixed static force.

6.3.6. Estimating Twin Boundary Flexoelectric Coefficients

Together, the measurements shown in Section 6.3.3 and 6.3.4 and the model in Section 6.3.5 indicate that TBs in LAO are mechanically polarized by strain gradients with flexoelectric contributions that are distinct from, but comparable in magnitude to, the bulk. Now we attempt to use the measurements in Figure 6.6 to estimate the TB flexoelectric coefficients responsible for the flexoelectric enhancements in twinned LAO.

The crudest estimate is to ignore the effects of TB orientation and use the average measurement of μ_{eff} for the Type I and II samples and the TB-free sample to isolate the contributions stemming from TBs. To do this, we utilize an approach based upon the rule of mixtures sketched in Figure 6.13.

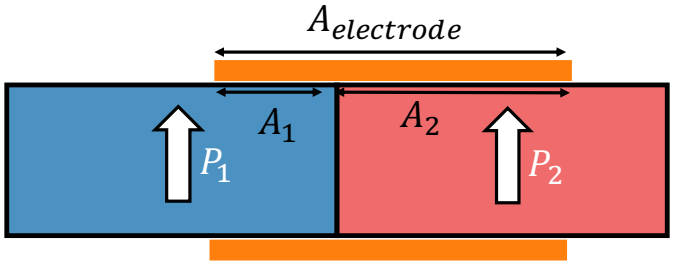

Figure 6.13. Rule of mixture approach to the polarization material with two polarizable regions, 1 and 2. The polarization measured by the electrode will be given by the product of the polarization in each region and the areal fraction of the region covered by the electrode.

In short, because both the bulk and TBs can develop a polarization in response to the beam bending strain gradients, the total polarization of a twinned sample measured in the x_1 direction (P_1) is the sum of two contributions

$$P_1 = (1-f)P_1^{bulk} + fP_1^{TB} \tag{6.15}$$

where P_1^{bulk} is the contribution arising from the sample bulk, P_1^{TB} is the contribution arising from TBs, and f is the fraction of the electrode area consisting of TBs. Since each polarization in Eq. 6.15 arises from same applied strain gradient, Eq. 6.15 can be rewritten as

$$P_1 = \mu_{eff}^{twinned} \bar{\epsilon}_{33,1} \tag{6.16}$$

where $\mu_{eff}^{twinned}$ is the effective flexoelectric coefficient of a sample with twins.

$$\mu_{eff}^{twinned} = (1-f)\mu_{eff}^{bulk} + f\mu_{eff}^{TB} \tag{6.17}$$

For lamellar TB microstructures, $f \approx \rho w$ where ρ is the linear TB density and w is the TB width. The TB density can be extracted from images of the samples (approximately 50 mm^{-1} from Figure 6.6 and TB widths have been measured using XRD ($w \approx$2 nm [**228**]). Together this gives $f \approx 10^{-4}$which when combined with $\mu_{eff}^{twinned}$=4.8 nC/m (Type I value) and μ_{eff}^{bulk}=3.2 nC/m indicates $\mu_{eff}^{TB} \sim$10 μC/m. This value is comparable to flexoelectric coefficients of bulk polar materials [**53**] which supports the interpretation that like TBs in STO [**229**] and $CaTiO_3$ [**230**], LAO TBs are polar [**107, 108, 109**].

Instead of working with the average flexoelectric coefficient of the Type I and II samples, we account for the differences in crystallographic orientation to obtain a better approximation for the TB flexoelectric coefficients. To begin, we derive expressions for μ_{eff}^{I} and μ_{eff}^{II} which are the effective flexoelectric coefficients of the samples solely containing Type I and II TBs, and replace μ_{eff}^{TB} in Eq. 6.17 with them.

Type I TBs are parallel to the x_1-x_3 plane, so contributions to the polarization from Type I TBs, $P_1^{TB,I}$, can only couple to $\overline{\epsilon}_{33,1}$ and $\overline{\epsilon}_{11,1}$.

$$P_1^{TB,I} = \mu_{1133}^{TB}\overline{\epsilon}_{33,1} + \mu_{1111}^{TB}\overline{\epsilon}_{11,1} \tag{6.18}$$

Similarly, Type II TBs are parallel to the x_1-x_2 plane, so contributions to the polarization from Type II TBs, $P_1^{TB,II}$, can only couple to $\overline{\epsilon}_{22,1}$ and $\overline{\epsilon}_{11,1}$. Therefore,

$$P_1^{TB,II} = \mu_{1122}^{TB}\overline{\epsilon}_{22,1} + \mu_{1111}^{TB}\overline{\epsilon}_{11,1}. \tag{6.19}$$

In the pure beam bending limit and assuming (1) TBs with different orientations have the same flexoelectric coefficient tensor, and (2) bulk Poissons ratio applies to TBs, Eqs. 6.18 and 6.19 become

$$P_1^{TB,I} = \left(\mu_{1133}^{TB} - \nu\mu_{1111}^{TB}\right)\overline{\epsilon}_{33,1} \tag{6.20}$$

$$P_1^{TB,II} = -\nu\left(\mu_{1133}^{TB} + \mu_{1111}^{TB}\right)\overline{\epsilon}_{33,1}. \tag{6.21}$$

Therefore

$$\mu_{eff}^{I} = \mu_{1133}^{TB} - \nu\mu_{1111}^{TB} \tag{6.22}$$

$$\mu_{eff}^{II} = -\nu\left(\mu_{1133}^{TB} + \mu_{1111}^{TB}\right) \tag{6.23}$$

After reintroducing the bulk contributions, we have an expression for the total polarization in the Type I and II samples analogous to Eq. 6.17

$$P_1^I = (1-\rho_I w)\, P_1^{bulk} + \rho_I w P_1^{TB,I} = \left((1-\rho_I w)\, \mu_{eff}^{bulk} + \rho_I w \left(\mu_{1133}^{TB} - \nu \mu_{1111}^{TB}\right)\right) \overline{\epsilon}_{33,1} \tag{6.24}$$

$$P_1^{II} = (1-\rho_{II} w)\, P_1^{bulk} + \rho_{II} w P_1^{TB,I} = \left((1-\rho_{II} w)\, \mu_{eff}^{bulk} - \rho_{II} w \nu \left(\mu_{1133}^{TB} + \mu_{1111}^{TB}\right)\right) \overline{\epsilon}_{33,1} \tag{6.25}$$

yielding the following expressions for μ_{eff}^{I} and μ_{eff}^{II}.

$$\mu_{eff}^{I} = (1-\rho_I w)\, \mu_{eff}^{bulk} + \rho_I w \left(\mu_{1133}^{TB} - \nu \mu_{1111}^{TB}\right) \tag{6.26}$$

$$\mu_{eff}^{II} = (1-\rho_{II} w)\, \mu_{eff}^{bulk} - \rho_{II} w \nu \left(\mu_{1133}^{TB} + \mu_{1111}^{TB}\right). \tag{6.27}$$

From Eq. 6.26 and 6.27, measurements on the TB-free, Type I, and Type II samples, and the literature Poissons ratio [**168**] and TB width [**228**], $\mu_{1133}^{TB} \approx 11 \pm 3.0$ μC/m and $\mu_{1111}^{TB} \approx$ -18.0$\pm$4.0 μC/m. These values are comparable to flexoelectric coefficients to the order of magnitude estimate from Eq. 6.17 and are consistent with LAO TBs being polar. Note, as described in Chapter 4, beam-bending experiments of bulk materials alone cannot be used to determine individual flexoelctric tensor coefficient components because the effective flexoelectric coefficients measured in beam-bending for different directions are not linearly independent expressions [**52**]. However, this is not the case for TBs, as shown above, because TBs are essentially 2D objects.

6.4. Barrier Layer Enhancements in Nb-doped $SrTiO_3$

6.4.1. Background on Barrier-Layer Mechanism

Ref. [**114**] demonstrated that oxygen-vacancy doped BTO and Nb doped TiO_2 single crystals exhibited effective flexoelectric coefficients $\sim 10^3$ times larger than their undoped counterparts. They attributed this to the barrier-layer mechanism: the flexoelectric polarization is screened in the conducting bulk, leaving only contributions from the nominally insulating surfaces [**231**]. These near-surface regions have very large polarizations owing to the thickness dependence of the capacitance of a parallel plate capacitor (Eq. 6.5). Barrier-layer or Maxwell-Wagner capacitors leverage this inverse scaling of capacitance with dielectric thickness to dramatically increase capacitor storage density. The fundamental principle of a barrier layer capacitor is illustrated in Figure 6.14. Commercially, barrier-layer capacitors consist of reduced ceramics which have been partially re-oxidized at grain boundaries and/or surfaces creating thin insulating regions surrounded by conducting regions [**231**].

Putting the observations of Ref. [**114**] on firmer theoretical ground, Tagantsev and Yurkov [**172**] showed that in 1D, the polarization (P) arising from a near-surface piezoelectric layer in the presence of a strain gradient ($\frac{d\epsilon}{dx}$) under short-circuit boundary conditions ($E = 0$) is

$$P = e^{*E}_{surf} \lambda \frac{d\epsilon}{dx} \tag{6.28}$$

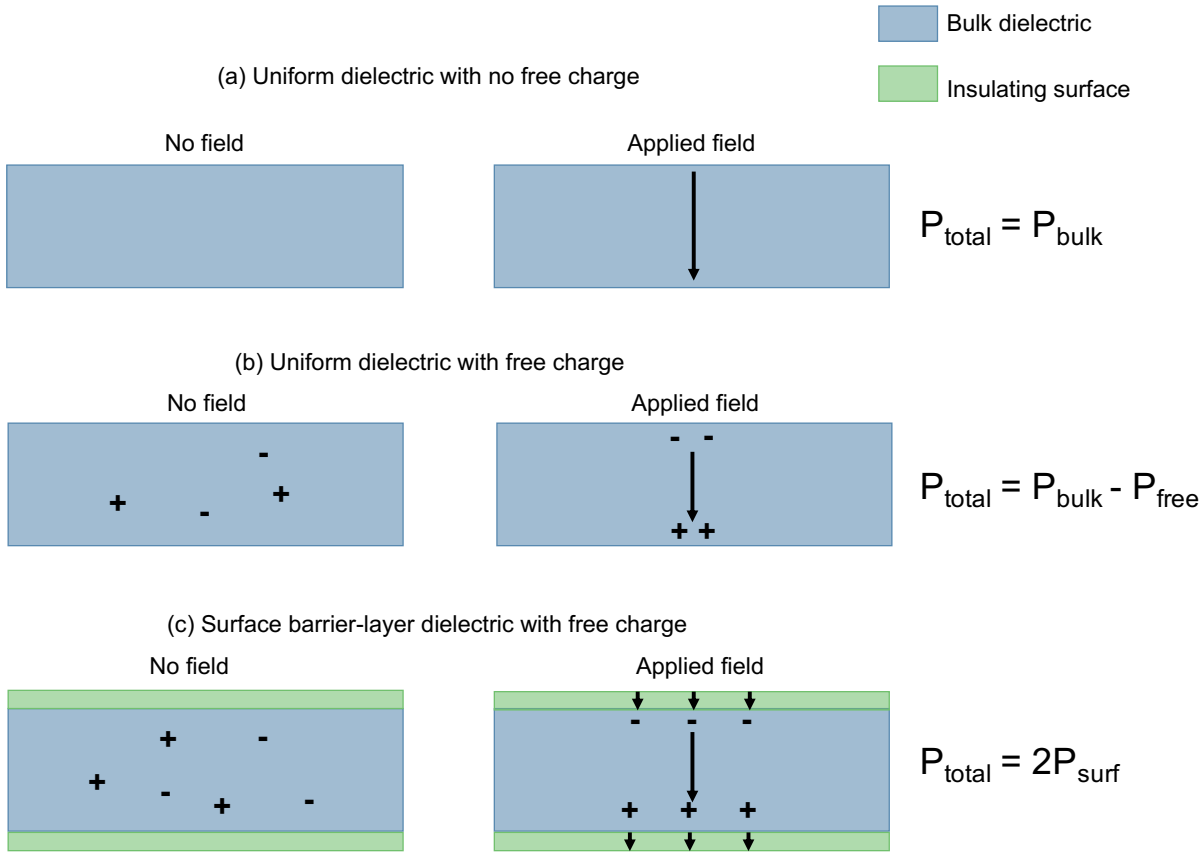

Figure 6.14. (a) A dielectric under an applied field will polarize. (b) Free charge in the dielectric will screen the polarization. (c) If the bulk dielectric has an insulating surface layer and enough free charge to completely screen the bulk polarization, only the polarization of the insulating surface will contribute to the total polarization.

where

$$e^{*E}_{surf} = e^{E}_{surf} \frac{h\varepsilon_{bulk}}{2\lambda\varepsilon_{bulk} + h\varepsilon_{surf}}. \tag{6.29}$$

In Eqs. 6.28 and 6.29, e^E_{surf} is the short-circuit surface piezoelectric coefficient, h is the thickness of the bulk region of the sample, λ is the thickness of the piezoelectric near-surface region, ε_{bulk} is the dielectric constant of the bulk material and ε_{surf} is the dielectric constant of the surface.

In their analysis Tagantsev and Yurkov [**172**] neglected the bulk flexoelectric effect which is effectively the situation for bent barrier-layer dielectrics where the free charge in the bulk acts to screen the bulk flexoelectric field [**114**]. If we are to assume that this screening is perfect, i.e. $\varepsilon_{bulk} \to \infty$, then

$$e^{*E}_{surf} = e^E_{surf}\frac{h}{2\lambda} \tag{6.30}$$

by L'Hospital's Rule. From Eq. 6.28 and Eq. 6.30 it follows that

$$P = e^E_{surf}\frac{h}{2}\frac{d\epsilon}{dx}. \tag{6.31}$$

Therefore, if one uses the conventional definition for the short-circuit effective flexoelectric coefficient measured in a bending experiment

$$\mu^E_{eff} = \left(\frac{dP}{d\left(\frac{d\epsilon}{dx}\right)}\right)_E \tag{6.32}$$

for a barrier-layer sample in which Eq. 6.31 applies, then μ^E_{eff} is given by

$$\mu^E_{eff} = e^E_{surf}\frac{h}{2}. \tag{6.33}$$

The measurements reported by Ref. [**114**] suggest a thickness dependence to the effective flexoelectric coefficients measured in doped semiconductors, however the linearity of this relationship is an open question.

6.4.2. Flexoelectricity in Nb-Doped $SrTiO_3$

While measurements investigating the barrier-layer mechanism have been performed on doped BTO and TiO_2, STO is one of the best characterized flexoelectric materials, so it is natural to explore the barrier-layer phenomenon in this materials system. Moreover, doped STO is commonly used as a substrate/thin film [**217, 218**] where these effects will likely be more relevant, owing to the size dependency of strain gradients, and there is evidence indicating the near-surface region of Nb-doped STO is insulating [**232, 233, 234**]; this is a pre-requisite for the barrier-layer mechanism [**231, 114**].

The results of the flexoelectric characterization of two STO single crystals doped with 1.4 at% Nb are shown in Figure 6.15. These samples had {100}-type faces and exhibited highly linear responses with an average effective flexoelectric coefficient ∼20 μC/m. Similar to the measurements on doped BTO and TiO_2, the effective flexoelectric response of doped STO single crystals is $\sim 10^3$ larger than that of undoped STO single crystals (Chapter 3).

Using Eq. 6.33 in conjunction with the measured value of the effective flexoelectric coefficient ($\mu_{eff} = 20$ μC/m) and known thickness ($h = 0.5$ mm) yields $e^E_{surf} \approx 0.08$ C/m^2. Piezoelectric coefficients are commonly reported as charge constants [**114, 3**] defined as

$$d^E_{surf} = e^E_{surf} s_{11}. \tag{6.34}$$

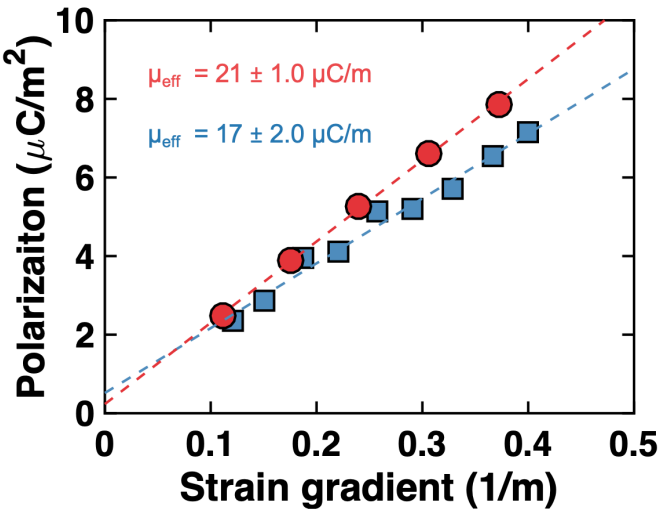

Figure 6.15. Flexoelectric characterization of Nb-doped STO single crystals with {100}-type faces. The flexoelectric response is highly linear (r^2 >0.98 with RMSE < 0.03) with an average effective flexoelectric coefficient of 20 μC/m.

Using the elastic compliance of STO yields d^E_{surf}=0.3 pC/N=0.3 pm/V. For comparison, the charge constant piezoelectric coefficient of quartz is ∼2pm/V [**114, 3**], which indicates the surface piezoelectric coefficient of STO is smaller than, but comparable to, some common bulk piezoelectrics. Note, particularly rigorous sample treatments (besides a bake to burn off hydrocarbons before electrode deposition) and surface characterization were not employed in the experiment shown in Figure 6.15, so it is possible the true surface piezoelectric coefficient is different.

The measurement of this surface piezoelectric coefficient can be directly compared to the MIP contributions to the flexoelectric response (Chapter 5). The short-circuit surface piezoelectric coefficient is the change in the surface polarization (P_λ) with strain (ϵ).

$$e^E_{surf} = \left(\frac{dP_\lambda}{d\epsilon}\right)_E . \tag{6.35}$$

Recall the definition of the MIP contribution to the flexoelectric response

$$f_{MIP} = \frac{d\overline{V}}{d\epsilon}. \tag{6.36}$$

If we assume the variation in the MIP is characterized by a constant electric field E over a piezoelectric surface region with thickness λ then Eq. 6.36 can be rewritten as

$$f_{MIP} = -\lambda \frac{dE}{d\epsilon}. \tag{6.37}$$

Since the flexocoupling voltage is an open-circuit quantity, the electric field in Eq. 6.37 can be replaced with the polarization using

$$P = -\varepsilon_0 E \tag{6.38}$$

which yields

$$f_{MIP} = \frac{\lambda}{\varepsilon_0}\left(\frac{dP}{d\epsilon}\right)_D = \frac{\lambda}{\varepsilon_0} e^D_{surf} \tag{6.39}$$

where e^D_{surf} is the open-circuit surface piezoelectric coefficient. The last step needed to compare the measured surface piezoelectric coefficient to the MIP contribution is to change the constant condition on the surface piezoelectric coefficient.

$$\left(\frac{dP}{d\epsilon}\right)_D = \left(\frac{dP}{d\epsilon}\right)_E + \left(\frac{dP}{dE}\right)_\epsilon \left(\frac{dE}{d\epsilon}\right)_D \tag{6.40}$$

Substituting the definitions $\left(\frac{dP}{d\epsilon}\right)_D = e^D_{surf}$, $\left(\frac{dP}{d\epsilon}\right)_E = e^E_{surf}$, $\left(\frac{dP}{dE}\right)_\epsilon = \chi\varepsilon_0$, and $E = \frac{1}{\varepsilon_0}(D - P)$ gives

$$e^D_{surf} = \frac{1}{1+\chi} e^E_{surf} \tag{6.41}$$

which can be combined with Eq. 6.39 to yield

$$f_{MIP} = \frac{\lambda}{\varepsilon_0 \varepsilon_r} e^E_{surf}. \tag{6.42}$$

Eq. 6.42 relates the measured value of e^E_{surf}=0.08 C/m^2 to the (nominally) known f_{MIP} through the unknown thickness of piezoelectric surface region and surface dielectric constant. It would be desirable to use Eq. 6.42 to predict the thickness of the piezoelectric surface region, however the thickness depends sensitively upon the surface dielectric constant. Assuming the Ibers approximation for f_{MIP} (11.6 V for STO, see Chapter 5), in the limit that ε_r=1 Eq. 6.42 predicts λ=1.3 nm, which is reasonable and close to the predicted thickness of the surface piezoelectric region [**235**]. However, while the surface dielectric constant is smaller than the bulk dielectric constant, it is more commonly taken to be ε_r=10 for materials with large dielectric constants like STO [**172**]. Using this surface dielectric constant gives λ=40 nm, which is too large and points to some discrepancy in the above analysis. It is unclear at the present time if this is because (1) ε_r=10 is a poor approximation and the surface dielectric constant in the surface piezoelectric region is substantially smaller than the surrounding bulk, (2) it is improper to interpret the enhanced flexoelectric response of doped STO as a surface piezoelectric effect, or (3) the disagreement is a consequence of sample preparation (e.g. adsorbates on the surface).

At any rate, these measurements clearly demonstrate large flexoelectric enhancements in doped STO and warrant future research.

6.5. Flexoelectricity in MgO

6.5.1. Background

MgO possesses a rock salt structure with space group $Fm\bar{3}m$ at room temperature and atmospheric pressure. It is an archetypal ionic material with a large band gap and simple electronic structure that lacks d or f electrons. This simplicity makes it ideal to test flexoelectric theories and calculations. Theoretical predictions in the literature suggest bulk flexoelectric coefficient values between 10 pC/m and 100 pC/m [**58, 236**]. There are no reported experimental attempts to measure the flexoelectric response of MgO, presumably because theory predicted the effect to be so small in this material. In Section 6.5.2 I provide the first measurements of flexoelectricity in MgO crystals. We find the flexoelectric response to be large compared to the first principles calculations presented in Section 6.5.3, even when the MIP contribution is accounted for. The measured dielectric response is found to be in agreement with single crystal literature values, but XRD indicates the nominally single crystalline MgO samples are actually polycrystalline (Section 6.5.4). Future research directions to understand this behavior are given in Chapter 9.

6.5.2. Flexoelectric characterization of MgO crystals

Figure 6.16 shows the flexoelectric characterization of crystals of MgO with two different crystallographic orientations. The relationship between the measured polarization and applied strain gradient is found to be highly linear with flexoelectric coefficients of 2.1 ± 0.3

nC/m for the sample with the (100) surface and 5.4±0.6 nC/m for the sample with the (111) surface. Using the dielectric constant of 9.8 for MgO [**237**] yields flexocoupling voltages of 62±7 V and 24±3V for the (100) and (111) samples, respectively.

According to the framework developed in Chapter 3, the effective flexoelectric coefficient different samples are expressed in terms of the underlying flexoelectric tensor components (in the beam bending limit) by

$$\mu_{eff}^{(100)} = \frac{s_{1122}}{s_{1111}}\mu_{1111} + \frac{s_{1111}+s_{1122}}{s_{1111}}\mu_{1122} \tag{6.43}$$

for the sample with the (100) surface (x_1'=[100], x_2'=[010], and x_3'=[001]) and

$$\mu_{eff}^{(111)} = \frac{2(s_{1111}+2s_{1122})}{3(s_{1111}+s_{1122}+2s_{1212})}\mu_{1111} + \frac{4(s_{1111}+2s_{1122})}{3(s_{1111}+s_{1122}+2s_{1212})}\mu_{1122} - \frac{8(s_{1111}+2s_{1122})}{s_{1111}+s_{1122}+2s_{1212}}\mu_{11212} \tag{6.44}$$

for the sample with the (111) surface (x_1'=[111], x_2'=[1$\bar{2}$1], and x_3'=[$\bar{1}$01]).

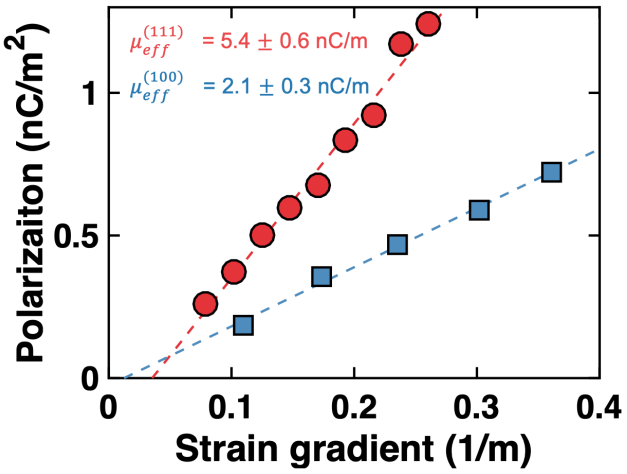

Figure 6.16. Flexoelectric characterization of MgO crystals. The flexoelectric response is highly linear (r^2 >0.97 with RMSE < 0.03) with effective flexoelectric coefficients of 5.4 nC/m and 2.1 nC/m for the samples with the (111) and (100) surfaces, respectively.

6.5.3. First principles calculations of flexoelectricity in MgO

First principles calculations of the flexoelectric coefficient tensor for MgO found in the literature indicate short-circuit values of μ_{1111}=-1.1 nC/m, μ_{1122}=-0.6 nC/m, and μ_{1212}=-0.3 nC/m [**58**]. Using these values with the elastic constants of MgO of s_{1111}= 4.4 $\times$ 10^{-12} Pa^{-1}, s_{1122} = -1.1$\times$ 10^{-12} Pa^{-1}, and s_{1212}= 7.1 $\times$ 10^{-12} Pa^{-1} and Eqs. 6.43 and 6.44 yield the predicted effective flexoelectric coefficients and flexocoupling voltages in Table 6.1 for the beam (ϕ=0) and plate (ϕ=1) bending limits. While accounting for the MIP contributions to the effective flexoelectric response through the Ibers approximation (Chapter 5) addresses the sign issue, the flexoelectric responses measured in Figure 6.16 are significantly larger than those predicted from first principles, even in the plate bending limit.

	Bulk		Bulk + Ibers		Exp.
	Beam (ϕ=0)	Plate (ϕ=1)	Beam (ϕ=0)	Plate (ϕ=1)	
$\mu_{eff}^{(100)}$ (nC/m)	-0.18	-0.22	0.55	0.73	5.4 $\pm$0.6
$f_{eff}^{(100)}$ (V)	-2.25	-2.81	6.95	9.49	24 $\pm$ 3
$\mu_{eff}^{(111)}$ (nC/m)	-0.32	-0.36	0.41	0.61	2.1 $\pm$ 0.3
$f_{eff}^{(111)}$ (V)	-4.05	-4.63	5.15	7.67	62 $\pm$ 7

Table 6.1. Effective flexoelectric coefficients and flexocoupling voltages for the (100) and (111) MgO samples using flexoelectric tensor components from Ref. [**58**] and elastic constants from Ref. [**207**] for the beam and plate bending limits compared with experimental values. Columns 2 and 3 only include bulk flexoelectric contributions, and columns 4 and 5 include bulk and MIP contributions within the Ibers approximation using atomic electron scattering factors [**164, 166**].

As there are known issues with computing flexoelectric coefficients from first principles with DFT implementations relying on pseudopotentials, I computed the flexoelectric coefficients of MgO with the all-electron code WIEN2k [**145**] to investigate if this could

be the origin of the discrepancy. The same approach described in Chapter 4 is used where the bulk flexoelectric coefficients are obtained from moments of the changes in charge density and forces induced by symmetrically inequivalent sub-lattice displacements [**58**].

Table 6.2 summarizes the results of the DFT-calculated flexoelectric tensor components using the LDA [**148**] and PBEsol [**152**] functionals. Because MgO has such a simple structure, it does not support some of the potential sources of enhanced flexoelectricity seen in other single crystals in Chapter 4: there are no lattice-quadrupole terms and MgO has no anomalous Born charges. Overall, the values in Table 6.2 computed with LDA are in good agreement with the literature, and the short-circuit flexoelectric coefficients are within ± 0.1 nC/m of those in Ref. [**58**]. We find the different functionals yield very similar Q and T tensor components with minimal net effect on the flexoelectric tensor components. The largest difference between the LDA and PBEsol computed values are the flexocoupling voltages; this originates from a difference in the static dielectric constant predicted by each functional (PBEsol gives 10.19 whereas LDA gives 9.51).

Regardless, neither functional resolves the large discrepancy with the experimental measurements, even after including MIP contributions (Table 6.3). As a final check, I investigated the variation in the flexoelectric coefficients as a function of volume to rule out any issue originating from differences between the DFT optimized lattice parameter and the experimental lattice parameter. Figure 6.17 shows that the short-circuit flexoelectric tensor components are relatively insensitive to volumetric strain.

Since the first principles calculations shown above yielded similar values to the literature values, the predictions appear to be largely invariant to the functional, and volumetric

(a) Q and T Tensor Components

	$Q^{(1),E}$ (e)	$Q^{(1),D}$ (e)	$Q^{(3),D}_{L1}$ (e bohr^2)	$Q^{(3),D}_{L2}$ (e bohr^2)	T^{D}_{L1} (eV)	T^{D}_{L2} (eV)	T^{E}_{1122} (eV)
Mg	1.97	0.62	-14.07	-21.77	17.84	29.22	7.63
	1.98	0.61	-14.19	-22.25	16.77	28.89	7.44
O	-1.97	-0.62	-12.89	-13.77	19.56	10.74	9.71
	-1.98	-0.61	-12.79	-13.63	18.66	10.42	9.50

(b) Bulk Flexoelectric Tensor Coefficients

	μ_{1111}	μ_{1212}	μ_{1122}
Fixed D (pC/m)	-113.62	-19.47	-80.98
	-110.93	-18.31	-78.24
Fixed E (nC/m)	-1.08	-0.19	-0.77
	-1.13	-0.19	-0.80
Flexocoupling (V)	-14.35	-2.46	-10.23
	-13.90	-2.29	-9.80

Table 6.2. Summary of MgO flexoelectric first principles calculations. The top and bottom entries in each row corresponds to calculations using LDA and PBEsol, respectively. (a) Moments of the change in charge density and forces owing to Mg and O displacements. (b) Bulk flexoelectric tensor components.

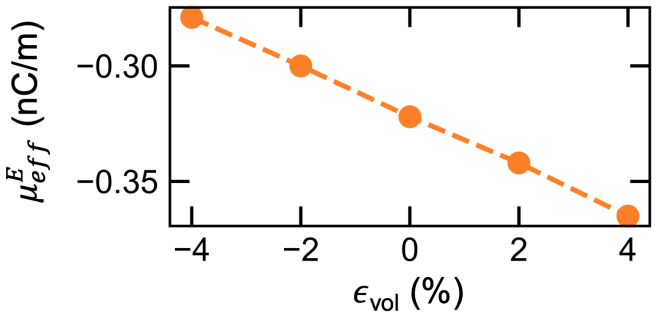

Figure 6.17. Variation in the effective short-circuit flexoelectric coefficient for a (100) MgO sample in the beam bending limit (ϕ=0) calculated with the LDA functional as a function of volumetric strain.

	Bulk		Bulk + Ibers		Exp.
	Beam (ϕ=0)	Plate (ϕ=1)	Beam (ϕ=0)	Plate (ϕ=1)	
$\mu_{eff}^{(100)}$ (nC/m)	-0.33	-0.41	0.40	0.54	5.4 ±0.6
$f_{eff}^{(100)}$ (V)	-4.17	-5.22	5.03	7.08	24 ± 3
$\mu_{eff}^{(111)}$ (nC/m)	-0.49	-0.57	0.24	0.40	2.1 ± 0.3
$f_{eff}^{(111)}$ (V)	-6.34	-7.26	2.86	5.04	62 ± 7

Table 6.3. Effective flexoelectric coefficients and flexocoupling voltages for the (100) and (111) MgO samples using flexoelectric tensor components in Table 6.2 and elastic constants from Ref. [**207**] for the beam and plate bending limits compared with experimental values. Columns 2 and 3 only include bulk flexoelectric contributions, and columns 4 and 5 include bulk and MIP contributions within the Ibers approximation using atomic electron scattering factors [**164, 166**].

effects on the bulk flexoelectric tensor components seem to be small, there must be some additional contribution to the flexoelectric response of MgO beyond bulk and mean-inner potential contributions. To quantify the issue, I define the excess flexoelectric coefficient for each sample according to

$$\mu_{excess} = \mu_{measured} - \left(\mu_{DFT}^{bulk} + \mu_{Ibers}\right). \tag{6.45}$$

Using the values from Figure 6.16 and Table 6.3, $\mu_{excess}^{(100)}$= 1.6 nC/m and $\mu_{excess}^{(111)}$=5.0 nC/m.

6.5.4. Dielectric and Structural Characterization

Short of the first principles theory of flexoelectricity missing some important physics (which seems unlikely for a simple material like MgO), the excess flexoelectric coefficients must stem from extrinsic contributions. The first experiment to deduce the origin of these extrinsic contributions was to measure the dielectric properties of the sample using

impedance spectroscopy. Since the electrode configuration used for flexoelectric characterization is essentially a parallel-plate capacitor geometry, it was possible to perform dielectric characterization on the same samples whose flexoelectric properties were shown in Figure 6.16. Impedance spectroscopy measurements on these crystals (Figure 6.18) yielded dielectric constants in good agreement with the literature values for MgO single crystals [**237**]. This suggests that whatever is responsible for the flexoelectric enhancement does not manifest in changes in the dielectric response.

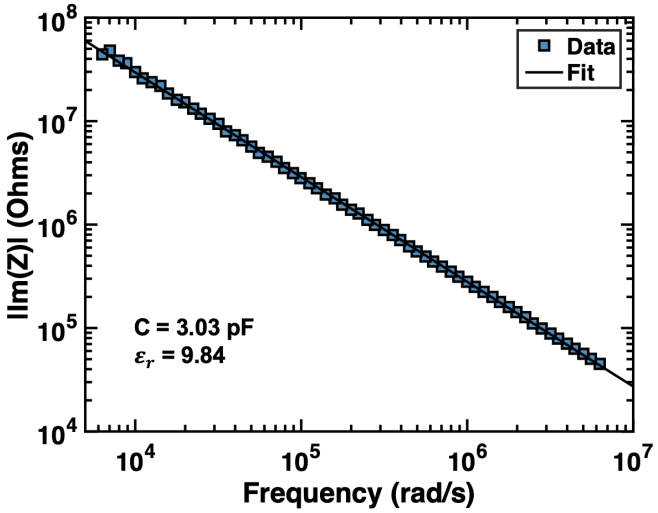

Figure 6.18. Dielectric characterization of MgO crystals. The imaginary component of the impedance is inversely proportional to the frequency, with a corresponding capacitance of 3.03 pF. Using the sample thickness (0.5 mm), electrode area ($1.74 \times 10^{-5)}$ m^2), and this capacitance with the capacitance of a parallel-plate capacitor yields a dielectric constant of 9.84.

Next, structural characterization of the MgO crystals was performed with XRD because MgO single crystals purchased from vendors are notoriously polycrystalline [**238**]. If the MgO crystals were polycrystalline with a similar grain boundary density to the TB density in LAO [**75**], then a possible explanation for the large flexoelectric response of MgO is grain boundary contributions.

$\omega - \phi$ maps to detect the presence of multiple grains were measured on MgO crystals from the same batch of crystals from which the samples measured in Figure 6.16 were made. The width of a $\omega - \phi$ map is twice the miscut and grains appear as multiple curves [**216, 238**]. The results of this experiment are shown in Figure 6.19(a). From this map the maximum miscut is found to be 0.18°, and there are clear indications of multiple grains.

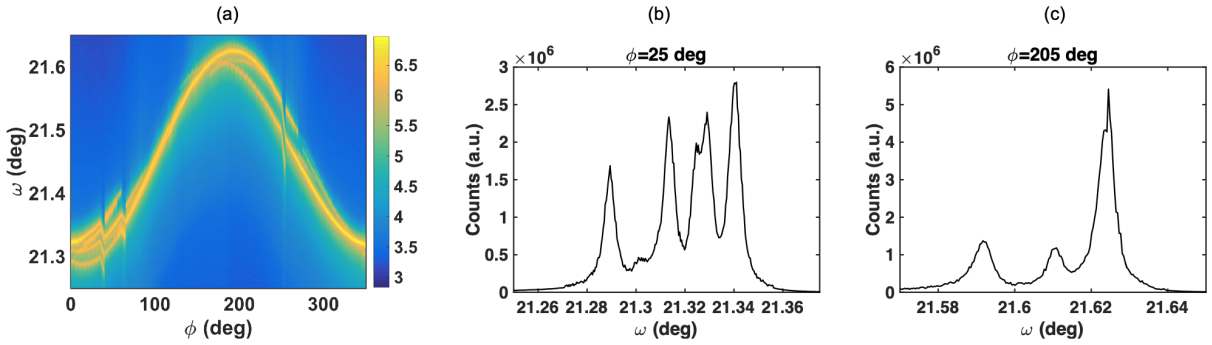

Figure 6.19. (a) $\omega - \phi$ map from a (100) MgO crystal around the (200) diffraction condition. Intensity is plotted on a log scale. (b)-(c) Rocking curves about the (200) diffraction condition for different values of ϕ.

In order to analyze the crystallinity in each grain and more readily count the number of grains, Figure 6.19(b)-(c) shows representative cross-sections of the $\omega - \phi$ map in Figure 6.19(a) at fixed ϕ values. These diffraction patterns are traditional rocking curves. They clearly show there are ∼5 misoriented domains that each have high crystallinity (FWHM of rocking curve ∼20 arcsec/0.006°). Since the x-ray optics in this experiment were adjusted so the beam illuminated ∼50% of the surface of the 10 mm × 10 mm sample and the attenuation length of MgO at the experimental conditions is ∼70 m, these measurements indicate there are ∼20 grains in a typical flexoelectric sample with dimensions 10 mm × 3 mm × 0.5 mm [**215**]. The number of grain boundaries is likely

too few to account for the excess flexoelectric coefficients (e.g. compared to the number of TBs in LAO).

Future research into the role of adsorbed water, built-in strain, and point defect contributions are suggested in Chapter 9.

CHAPTER 7

The Interplay Between Electronic Structure, Surface Structure, and Flexoelectricity in Lanthanide Scandates

7.1. Introduction

Lanthanide scandates are distorted orthorhombic perovskites (space group *Pbnm* at room temperature and atmospheric pressure [**118**]) which are most commonly of interest for use as substrates for thin film growth [**127**] and as catalytic supports [**239, 240**]. However, many aspects of lanthanide scandates relevant to these applications are poorly understood including the nature of their 4f electrons [**162**] and the atomic and electronic structure of their surfaces [**241**]. This chapter includes a summary of the work I have performed on lanthanide scandates, much of which has been performed in collaboration. I begin with the utilization of x-ray photoelectron spectroscopy (XPS), ultraviolet photoelectron spectroscopy (UPS), and DFT to characterize the bulk electronic structure of DSO, GSO, and $TbScO_3$ (TSO) in Section 7.3 (I performed and analyzed the XPS/UPS measurements and simulated XPS spectra from DFT calculations performed by Professor Laurence D. Marks [**162**]). Then in Section 7.4 I discuss solving the (110) surface of DSO (I acquired and analyzed the AFM and XPS data and performed the pDOS analysis, Dr. Pratik Koirala was responsible for the transmission electron diffraction (TED), Zachary R. Mansley developed the XPS model, and Professor Laurence D. Marks performed the DFT calculations [**241**]). In Section 7.5 I discuss the observation of large

charging [**162, 27, 242**] in lanthanide scandates (I acquired and analyzed the XPS and UPS data. Dr. Ahmet Gulec obtained the electron-energy loss spectroscopy (EELS) data and I performed the analysis with Dr. Pratik Koirala. Dr. Pratik Koirala performed the reflection electron-energy loss spectroscopy (REELS) measurement and Tiffany Ly obtained the secondary electron (SE) image. Dr. Ryan Paull supplied the GSO nanoparticles [**239, 240**] and Tiffany Ly supplied the KTO nanoparticles [**243**]). Lastly, in Section 7.6 I explain how the scandates' propensity for charging and large flexoelectric coefficients (Chapter 3) lead to large, reversible bending in electron microscopes (Dr. Pratik Koirala made the initial observation and performed all transmission electron microscopy (TEM), and I performed the flexoelectric characterization. The analysis was the result of much discussion between Professor Laurence D. Marks, Dr. Pratik Koirala, and myself. [**27**]).

7.2. Methods

7.2.1. X-ray and Ultraviolet Photoelectron Spectroscopy

Photoelectron spectroscopies are surface-sensitive probes of electronic structure which operate on the photoelectric effect: a sample subjected to sufficiently high energy electromagnetic radiation will eject electrons with a kinetic energy equal to the difference between the energy of the incident radiation and the binding energy of the electron in the sample [**244, 245**]. Information about the underlying electronic structure of the sample is determined from the binding energies, intensities, and angular distribution of ejected photoelectrons. Two common forms of photoelectron spectroscopy use an X-ray source (i.e. XPS) or an ultraviolet source (i.e. UPS). Comprehensive reviews of these techniques

and more detailed accounts of the operating principles can be found in Ref. [**244**] and [**245**].

In the experiments reported in this chapter, XPS measurements were performed on an ESCALAB 250Xi equipped with a monochromated, micro-focused Al K-Alpha (1486.6 eV) x-ray source. A 180° double focusing hemispherical analyzer with a dual detector system was used in constant analyzer energy mode [**162**]. First, general survey spectra were used to check for impurities and then higher resolution XPS spectra to study particular peaks were acquired with a pass energy of 20 eV, step size of 0.1 eV, spot size of 650 μm, and averaged over 10-20 scans. UPS measurements were performed on the same instrument using a He II (40.8 eV) UV source with a photon flux of $\sim$1.5 $\times$ 10^{12} photons/second, pass energy of 2 eV, step size of 0.05 eV, spot size of $\sim$1.5 mm, and averaged over 20 scans. The ESCALAB 250Xi was also used for the REELS experiments described in Section 7.5. These measurements were taken using a 1 keV incident energy with an emission current of 5 μA, 150 μm aperture, dwell time of 50 ms, and pass energy of 10 eV with a 0.1 eV step.

XPS spectra were collected with an argon flood gun operated at a beam voltage of 2 V, emission current of 50 μA, focus voltage of 20 V, and extractor bias of 30 V to minimize charging. The chamber pressure was $\sim 10^{-7}$ mbar when the flood gun was used. Some residual charging persisted even with a flood gun, so spectra were shifted using the adventitious C1s peak centered at 285 eV (if this peak was sufficiently intense) or the Sc3p peak at 30.8 eV.

UPS charge compensation using the flood gun was not possible because artifacts from its use masked the relatively low photoelectron intensity. Other charge compensation

methods were also not possible: the UPS incident photon energy is too low to induce C1s photoemission, and secondary electron emission masked the Sc3p. Therefore, only relative UPS binding energies are meaningful in the data reported in Section 7.3.4.

7.2.2. Transmission Electron Microscopy

TEMs utilize high energy electron beams to characterize the structure and chemical composition of materials. Interested readers are directed to one of numerous textbooks (e.g. Ref. [**246**]) for overviews of TEM, its operating principles, and a review of some of the more common operating modes. Egertons book on EELS [**247**] is particularly relevant for the work described in Section 7.4.5 and 7.5.2. The TEM results shown in Section 7.4 and 7.6 utilized a Hitachi H8100 operated at 200 kV with a nominal exposure time of 0.1 seconds and electron flux in the range of 1- 100 electrons/nm^{2}s. The bending experiments were done starting with a spread beam which was gradually converging. SE imaging of the nanoparticles included in Figure 7.12(d) was performed on a Hitachi HD-2300 STEM operated at 200 kV. The EELS data reported in Sections 7.4.5 and 7.5.2 were acquired on a JEOL ARM200CF equipped with a cold field emission source and a CEOS probe spherical-aberration corrector operated at 200 kV with a semi-convergence angle of 27 mrad. A dispersion of 0.05 eV/channel, collection angle of 22 mrad, and acquisition time of 1 μs (although in practice this is closer to 0.1 ms due to detector limitations) were used on a Gatan Enfina EELS spectrometer. The data in Section 7.5.2 consisted of 100 individual spectra acquired at these conditions under constant illumination.

7.2.3. Atomic Force Microscopy

AFM is a versatile materials characterization tool with many modes of operation. Detailed explanations of this method and its capabilities and limitations can be found in reviews such as Ref. [**248**]. In Section 7.4.3 tapping mode AFM imaging was used to measure topography with a Bruker Dimension FastScan AFM operated in air.

7.2.4. Density Functional Theory Calculations

DFT calculations were performed with the all-electron augmented plane wave + local orbitals WIEN2k code [**145**]. For the bulk calculations described in Section 7.3, muffin tin radii of 1.68, 1.82, and 2.02 were used for O, Sc, and Dy, respectively. These radii minimized the O2p tails within the metal muffin tins which can perturb the calculation of the exact-exchange corrections. The plane-wave expansion parameter RKMAX was 9.0 and the k-mesh was 8x6x8. An on-site hybrid approach [**153, 154**] with the PBEsol function [**152**] was used to approximate the exchange and correlation term. On-site hybrid fractions of 0.38, 0.50, and 0.80 for the Dy4f, Dy5d, and Sc3d orbitals, respectively, were used; how these were selected is described in Section 7.3.5 [**162**]. Section 7.3.5 also explains how a generalized gradient approximation (GGA) approach using the PBEsol functional was used in conjunction with the on-site hybrid calculations to simulate XPS spectra [**162**]. The (110) surface of DSO described in Section 7.4.4 was simulated with a 70.000×7.926×7.936 $\AA$ cell containing 260 atoms (92 unique) with P121/m1 symmetry and approximately 14 $\AA$ of vacuum [**241**]. An RKMAX was of 7.0 was used with a 6×6×1 mesh. The surface calculations used the on-site hybrid approach with the same on-site

hybrid fractions given above. All calculations used ferromagnetic ordering, and spin-orbit couplings were not considered.

7.3. Bulk Electronic Structure of (Gd,Tb,Dy)ScO_3

7.3.1. Motivation

Understanding the electronic, magnetic, and catalytic properties of lanthanide scandates requires thorough characterization of their electronic structures, especially their valence band (VB)s. The prevailing interpretation is that the valence band is comprised of lanthanide 4f (Ln4f), scandium 3d (Sc3d), and oxygen 2p (O2p) states [**120, 249, 250, 251, 252**], although there is some ambiguity regarding the positions of these states stemming from the inherent difficulty of treating 4f states in DFT: mean-field approaches often poorly model correlated electrons. More often than not, Ln4f are treated as atomic-like states far from the VBM, which is taken to be dominated by O2p contributions [**120**].

Here we use a combination of photoelectron spectroscopies and first principles calculations to characterize the electronic structure of lanthanide scandates (GSO, TSO, and DSO). XPS and UPS are used to experimentally measure the valence bands of these three lanthanide scandates and then a method is developed to simulate their photoelectron spectra. The consistency between simulated and experimental spectra points toward substantial contributions from Ln4f states in the VB [**162**].

7.3.2. Sample Preparation

10 mm × 10 mm × 0.5 mm single crystalline substrates of [110] oriented GSO, TSO, and DSO (Pbnm convention) were purchased from MTI Corp. Samples were annealed at

1050°C for 10 hours in air to promote surface ordering. Additionally, samples were baked at 600°C for 6 hours in air immediately prior to XPS and UPS measurements to minimize surface contamination, and then placed in the high vacuum chamber of the XPS system to degas overnight. The color of the DSO changed from yellow to brown after the 1050°C anneal, whereas GSO and TSO remained white. This color change may indicate small concentrations of point defects (e.g. Dy and O vacancies [**253, 254**]). No color changes were observed after the 600°C bake.

7.3.3. Valence Band XPS Measurements

XPS spectra of GSO, TSO, and DSO acquired following the methods described in Section 7.2 are shown in Figure 7.1. Under the experimental conditions, the 95% probe depth of photoelectrons contributing to these spectra, estimated as 3× the inelastic mean free path, is ∼10 nm [**255**].

First, we focus on the near-valence region with binding energies greater than 15 eV. In this region, all three scandates exhibit a peak at 30.8 eV originating from Sc3p states, Ln5p doublet peaks near 20 and 28 eV, and an O2s peak at 23 eV. The Sc3p peak at 30.8 eV is invariant for the three different lanthanide scandates investigated here, reflecting the similar Sc bonding environment in these three materials. On the contrary, the Ln5p and O2s peaks differ in the scandates, increasing in binding energy with the atomic number of the lanthanide species: this increase is attributed to the increase in nuclear charge of the Ln species in $LnScO_3$ as Ln changes from Gd to Tb to Dy [**244, 245**]. These peak assignments are consistent with existing literature [**249, 250, 251**].

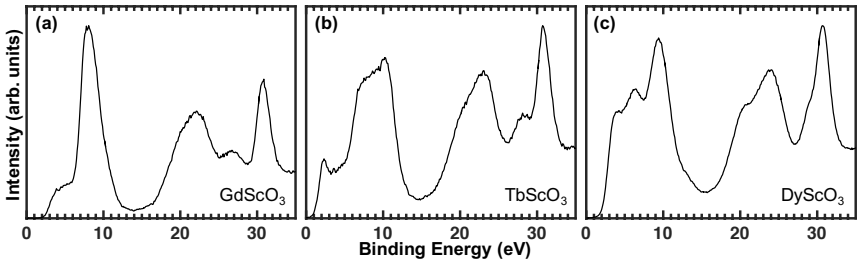

Figure 7.1. Experimental XPS spectra acquired with 1486.6 eV incident x-rays for (a) GSO, (b) TSO, and (c) DSO after origin correction.

Next we focus on the VBs which in all three spectra span 15 eV. Unlike the near-valence region, the valence band XPS spectra qualitatively differ between the three scandates. The GSO VB spectrum has two major peaks at 4 eV and 8 eV, the TSO VB spectrum has a sharp peak at 2 eV and a wide feature centered at 9 eV, and the DSO VB spectrum consists of three peaks at 4 eV, 6 eV, and 9 eV. At the incident x-ray energy of 1486.6 eV used in these experiments, the Ln4f cross-sections are orders of magnitude larger than the O and Sc states contributions to the VB, indicating these differences originate from Ln4f states [**256**].

7.3.4. Valence Band UPS Measurements

To confirm that Ln4f states are responsible for the differences in the VB spectra measured with XPS, VB UPS spectra were acquired because O2p cross-sections are ∼2-5 times larger than Ln4f cross-sections at the UPS incident photon energy [**256**]. Figure 7.2 shows UPS VB spectra for the three scandates. This technique is more surface-sensitive than XPS: the 95% probe depth of photoelectrons is ∼1.2 nm at the experimental conditions [**255**]. Whereas the VB XPS spectra in Figure 7.1 were qualitatively different for GSO, TSO,

and DSO, the UPS spectra are nearly identical, consisting of two major peaks separated by 4-5 eV.

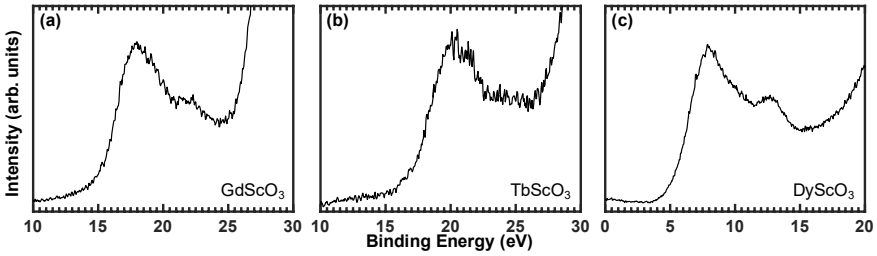

Figure 7.2. Experimental UPS spectra acquired with 40.8 eV photons for (a) GSO, (b) TSO, and (c) DSO. Because of charging, only relative binding energies have meaning in these spectra. The spectrum for each lanthanide scandate is qualitatively similar, consisting of two peaks separated by 4-5 eV. Secondary electron emission begins to occur at (a) ∼25 eV, (b) ∼27 eV, and (c) ∼20 eV, masking higher binding energy features of the VB spectra.

Together, the experimental spectra in Figures 7.1 and 7.2 and the literature cross-sections indicate the VB in all three scandates consists mainly of Ln4f contribution (XPS) and O2p contributions (UPS). However, owing to the experimental resolution limits there is some ambiguity regarding the location of these states, their distribution, and the role of Sc3d states (Sc3d cross-sections are much smaller than the Ln4f and O2p cross-sections at the incident energies used for these experiments). We turn to DFT to simulate the XPS spectra and address these questions.

7.3.5. X-ray Photoelectron Spectroscopy Simulations

XPS spectra were simulated using a four-step method.

7.3.5.1. Ground State Electronic Structure. First, it is necessary to obtain an accurate ground state electronic structure. We found conventional LDA+U and GGA+U methods, independent of the functional, resulted in highly-localized, essentially atomic

4f occupied states, which disagrees with the spectra in Figure 7.1. The on-site hybrid method, which uses an exact-exchange hybrid correction within the muffin tins, was found to give an improved description of the electronic structure. After the atomic positions and bulk optimized lattice constants were calculated using the on-site hybrid method with the PBEsol functional, the optimal hybrid fractions were found by varying the hybrid fractions to minimize the forces on the atoms using the known bulk positions. Optimized on-site hybrid fractions were found to be 0.80 for Sc3d, 0.50 for Dy5d, and 0.375 for Dy4f states, within an uncertainty of approximately 0.05. The same values were used for the Ln and Sc species in TSO and GSO.

The pDOS from the on-site hybrid calculations are shown in Figure 7.3. The VBM in each plot is set to 0 eV and negative energies indicate occupied states. We found only O2p, Sc3d, and Ln4f states made significant contributions to the VB, so all other states are excluded from this analysis. The O2p and Sc3d VB contributions are similar in all three scandates (O2p states are delocalized and have the largest contributions, while the Sc3d states have minor contributions throughout the valence band), whereas the Ln4f contributions are noticeably different. Gd has one 4f peak since Gd3+ has no minority 4f electrons. The presence of minority 4f electrons causes a minority 4f state close to or at the VBM and splits the majority 4f state, as seen for TSO and DSO.

The pDOS in Figure 7.3 indicate band gaps of 5.2 eV, 4.9 eV, and 5.3 eV for GSO, TSO, and DSO, respectively, which are similar to reported band gaps [**252, 242, 27**]. The Sc3d and O2p contributions to the conduction band are similar in all three materials, being dominated by Sc3d, and the unoccupied Ln4f states are all minority spin. The placement of unoccupied Gd4f states in the band gap is likely a consequence of the system-dependent

nature [**153**] of the hybrid fraction (the optimized values were acquired on DSO), but ultimately does not impact the XPS simulations, which only use occupied states.

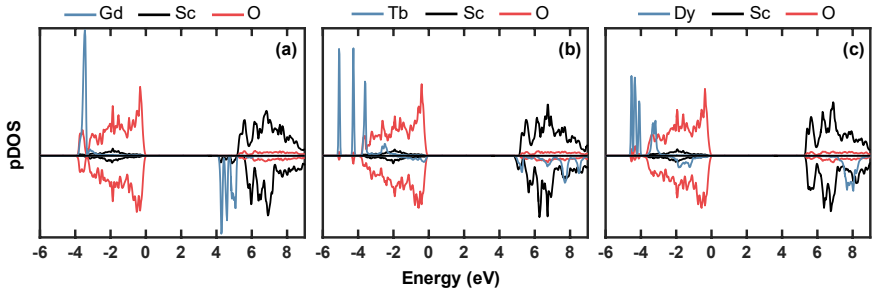

Figure 7.3. pDOS of (a) GSO, (b) TSO, and (c) DSO from on-site hybrid DFT calculations. The upper and lower panels correspond to the spin up and spin down pDOS, respectively. Blue lines indicate Ln4f, black lines correspond to Sc3d, and red lines show O2p pDOS. Negative energies are taken to be occupied states and the VBM has been set to 0 eV. For visual clarity, in this figure the O2p and Sc3d pDOS have been scaled by a factor of 10.

7.3.5.2. Relaxation Effect. Having established a means to model the ground state electronic structure in the lanthanide scandates, we now turn to relaxation effects. The removal of a photoelectron in photoelectron spectroscopies modifies the occupancy of a given state and causes an energy level shift [**244, 245**]. To model this effect, we adopt a Slater-Janak transition state method [**257, 258, 259, 260**]: since the Hubbard U is defined as the correction that makes the energy of a particular state independent of occupancy [**261**], calculating the Hubbard U for a particular state is equivalent to correcting for a hole in that state. Performing this procedure for the 4f states by placing the 4f electrons into the core and varying their occupancy yielded $U = 8.2$ eV, $J = 0$ eV which when used with GGA+U with PBEsol calculations led to 4f energies with better agreement to the XPS in Figure 7.1.

The energies of the 4f states from the GGA+U with PBEsol calculations account for the loss of a photoelectron during the XPS process, so these energies were used to linearly scale the on-site hybrid energies, which provide a better representation of the ground state electronic structure. This process effectively placed the on-site hybrid 4f positions at the same energy as the GGA+U 4f positions. Gd was used to determine the scaling factor since it had the simplest 4f structure (scaling factor = 1.7). The same scaling factor was used for TSO and DSO.

7.3.5.3. Photoionization Cross-sections and Peak Broadening. To quantitatively compare the pDOS in Figure 7.3 with the spectra in Figure 7.1, the differences in the photoionization cross-sections of different states must be accounted for. Literature photoionization cross-sections are often not accurate for valence bands [**262**] because they are calculated for isolated atoms [**256**], which neglect the effects of reconfiguration [**244, 245**] and dielectric screening [**263**]. Using the literature values led to simulated spectra overly weighted by Ln4f contributions when compared to the spectra in Figure 7.1. As an alternative, I utilized the literature cross-sections as starting points and varied the cross-sections to find the best agreement with the data in Figure 7.1. GSO was used for this process because the states close to the VBM can only come from O2p contributions since Gd has no minority 4f electrons. We found the simulated and experimental intensities matched if the O2p cross-section was increased by a factor of 10 compared to the literature value and the Gd4f and Sc3d cross-sections were left unchanged. The O2p cross-sections in the TSO and DSO pDOS were also scaled by this factor of 10.

Lastly, Gaussian broadening was used to address the combined effects of instrument resolution, thermal broadening, and state lifetime which are present in experiment [**244,**

245]. Gaussian broadening values of 0.57 eV (Gd4f), 0.30 eV (Tb4f), 0.41 eV (Dy4f), and 0.30 eV (O2p, determined from GSO) were found to reproduce the experimental peak widths.

7.3.5.4. XPS Simulations. Combining the steps outlined in Section 7.3.5.1- 7.3.5.3 yielded the XPS simulations for GSO, TSO, and DSO shown in Figure 7.4. In each plot, the VBM is 0 eV and each spectrum has been normalized by its maximum intensity. There are differences ∼0.5-1 eV between the experimental and simulated peak positions. These simulations provide a reasonable match with the experimental spectra: the GSO simulation reproduces a two-peak structure, the TSO simulation exhibits a sharp peak at the VBM and a wide peak spanning ∼5 eV, and the DSO simulation possesses a three-peak structure.

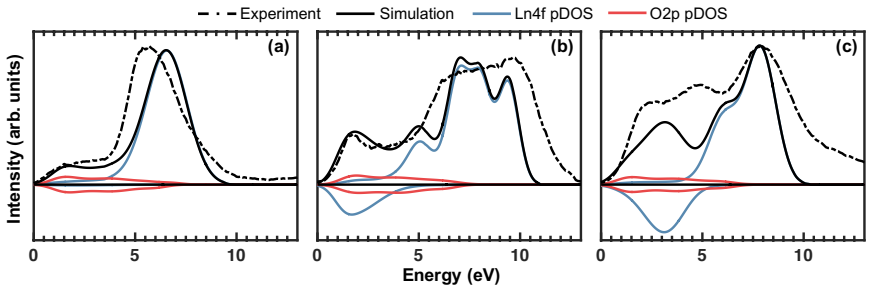

Figure 7.4. Comparison between experimental XPS spectra (dashed lines) and simulated XPS spectra (solid lines, black) for (a) GSO, (b) TSO, and (c) DSO. The upper and lower panels correspond to the spin up and spin down pDOS, respectively. The simulations correspond to the sum of the O2p pDOS (solid lines, red), Sc3d pDOS (not shown), and Ln4f pDOS (solid lines, blue). Each spectrum has been normalized by its maximum VB intensity and each VBM has been set to 0 eV.

The simulated spectra in Figure 7.4 match the experimental XPS spectra well. Together, these results support the generally accepted interpretation that O2p states are delocalized throughout the VB in lanthanide scandates [**120, 249, 250, 251, 252**]. The

Sc3d cross-sections were too low to probe Sc3d states directly with XPS or UPS, but the simulations in Figure 7.4 (which accurately capture the 4f peak structure and O2p delocalization) indicate Sc3d states have a very small, delocalized contribution throughout the VB in all the scandates. This is also consistent with existing literature.

The Ln4f VB contributions are more complex than the O2p or Sc3d contributions. It is common to treat Ln4f states as highly localized, essentially atomic states which exist at energies well below the VBM and have little consequence for properties. The results shown above indicate that the minority Ln4f and O2p states are at comparable energies to the VBM, which suggests minority Ln4f electrons may have a more significant impact on lanthanide scandate properties. It is worth noting the addition of minority 4f electrons lead to worse agreement between our simulations and experiment, which may stem from the existence of different spin configurations.

7.4. Surface Atomic and Electronic Structure of (110) $DyScO_3$

7.4.1. Motivation

As mentioned in Section 7.1, much interest in lanthanide scandates is related to their use as thin film substrates [**127**] and catalytic supports [**239, 240**]. Oxide surfaces are known to deviate from their bulk atomic and electronic structure in a bid to stabilize, and a detailed understanding of the exact surface structure is critical to both applications [**183**]. Bulk truncations in 332 perovskites along {100} pseudo-cubic planes (which includes the (110) surface of DSO) are not valence neutral; they must, for example, reconstruct, adsorb a foreign species, or metallize to exist [**183**].

There has been some work to understand the pseudo-cubic surfaces of lanthanide scandates. For example, the review by Biswas et al. [**264**] indicates the existence of both A and B site terminations, but no exact surface structures or chemistries have been reported [**265, 266, 267**]. In this section, I describe the work to solve a Sc rich double layer with a Sc_3O_4 termination on the (110) surface of DSO using a combination of XPS, AFM, TED, and DFT [**241**]. Then I discuss the experimental evidence for a surface state associated with this surface reconstruction [**242**].

7.4.2. Sample Preparation

10 mm × 10 mm × 0.5 mm single crystalline substrates of [110] oriented DSO (purchased from MTI Corp) were cut into 3 mm discs with an ultrasonic cutter, mechanically thinned to ∼100 μm thick using silicon carbide sandpaper, and dimpled with a Gatan 656 Dimple Grinder and 0.5 μm diamond slurry until the center thickness was ∼15 μm. A Gatan Precision Ion Polishing System (PIPS-I) was used to Ar^+ ion mill the samples to electron transparency. An initial energy of 5 keV and milling angle of 10° were used, which were gradually reduced to 3 keV and 4° respectively for final polishing and surface cleaning. Afterwards, the samples were annealed in a tube furnace for 10 hours at 1050 °C in air.

7.4.3. Stepped, Sc-rich Surfaces with (1×1) Periodicity

AFM and TED were used to characterize surface topography and structure. Following the sample treatment in Section 7.4.2, AFM images (in tapping mode) were acquired with the experimental conditions described in Section 7.2. An image of a 2 μm × 2 μm area of a [110]-oriented, self-supported DSO TEM sample is shown in Figure 7.5(a). This image

indicates that the annealing conditions yielded a terraced, atomically stepped surface, similar to what has been found for other oxides [**264, 268**]. TED (also performed under the conditions described in Section 7.2) on the same samples resulted in the diffraction pattern shown in Figure 7.5(b). This pattern exhibits no evidence of additional reflections and minimal diffuse scattering, indicating a well-ordered 1×1 surface with no surface reconstructions or additional phases, and few bulk defects [**241**].

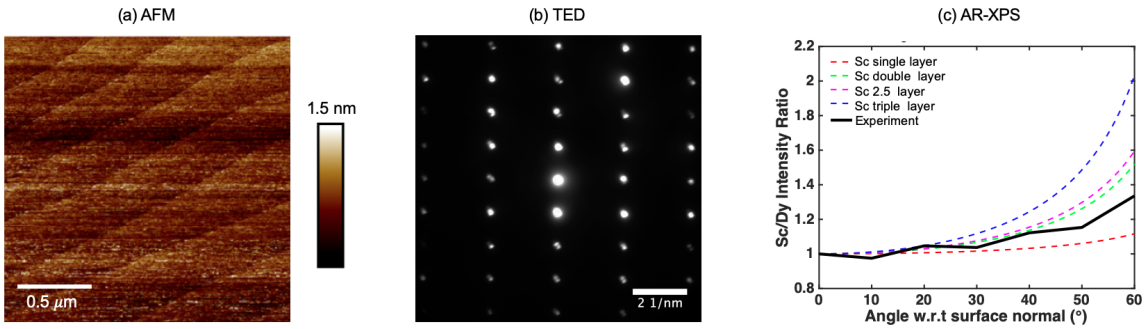

Figure 7.5. Characterization of (110) DSO surface. (a) AFM indicates atomically terraced surfaces. (b) TED along the [110] zone axis demonstrates a lack of extra surface diffraction spots and minimal diffuse scattering. (c) angle-resolved x-ray photoelectron spectroscopy (AR-XPS) intensity ratios of the integrated Sc2p and the Dy3d signals compared to modeled signals with different Sc-rich surfaces.

Surface chemistry was examined using AR-XPS (experimental conditions described in Section 7.2). Figure 7.5(c) depicts the ratio of the Sc2p intensity to the Dy3d intensity as a function of angle. Normal incidence is defined to be zero degrees according to convention, so surface contributions become more prominent as the angle increases. As such, the increase in the ratio of Sc2p and Dy3d intensities with angle shown in Figure 7.5(c) indicates the DSO surface is Sc rich. To quantify the amount of Sc at the surface, the intensity ratio was modelled with a layer model [**269, 270, 271**], taking the relative

photoionization cross-sections, inelastic mean free paths, and relative atomic densities of the different species into account. As shown in Ref. [**241**], the intensity ratio from a ScO_2^- terminated slab is given by

$$\frac{I_{Sc2p}}{I_{Dy3d}} = \frac{\alpha_{Sc2p}\rho_{Sc}}{\alpha_{Dy3d}\rho_{Dy}} \frac{1}{D_{Sc2p}^2 - 1} \frac{D_{Dy3d}^2 - 1}{D_{Dy3d}} \tag{7.1}$$

where α_i is the photoionization cross section of the indicated orbital, ρ_i is the areal number density of the atom, and $D_i = exp(-\frac{t}{cos(\theta)\lambda_i})$ is an exponential damping function which is a function of the layer thickness t, inelastic mean free path of the electron λ_i, and angle towards the detector θ. The intensities from samples with different surface chemistries can be included by modifying Eq. 7.1 with additional layers. The results of this modeling for a number of different Sc surface layers are shown in Figure 7.5(c). Although there is a large uncertainty associated with these measurements (from surface contamination, photoelectron channeling, etc.), the experimental data indicates a scandium oxide double layer with some stoichiometry Sc_xO_y.

7.4.4. Surface Atomic and Electronic Structure from Density Functional Theory

The XPS data and modeling shown in Figure 7.5(c) are consistent with a scandium oxide double layer, but the experiments were too coarse to determine the exact chemistry. Since oxide surfaces adhere to chemical constraints, such as valence neutrality and Paulings Rules [**183**], it is possible to generate chemically sensible scandium oxide double layer structures (which, for example, are valence neutral, maximize symmetry, and maintain reasonable coordination) with bulk periodicity (Figure 7.5(b)) and compare the energetic

stability of the structures using DFT calculations to identify the lowest energy structure [**241**].

The combination of the experimental and chemical constraints yields (110) surfaces with Sc_3O_4 surface chemistry, corresponding to six occupied Sc polyhedral sites for the outermost layer out of the eight available sites. DFT calculations were performed (using the parameters and approach described in Section 7.2) on all unique permutations and the lowest energy minimized structure is shown in Figure 7.6 [**241**]. This structure is a Sc rich double-layer dominated by $ScO_{5\square}$ octahedra with a vacant site. It is like the STO (001) double-layer reconstructions, which follows from the similarity between the 1×1 (110) surface of GSO (an orthorhombic perovskite) and 2×2 (001) surface of STO.

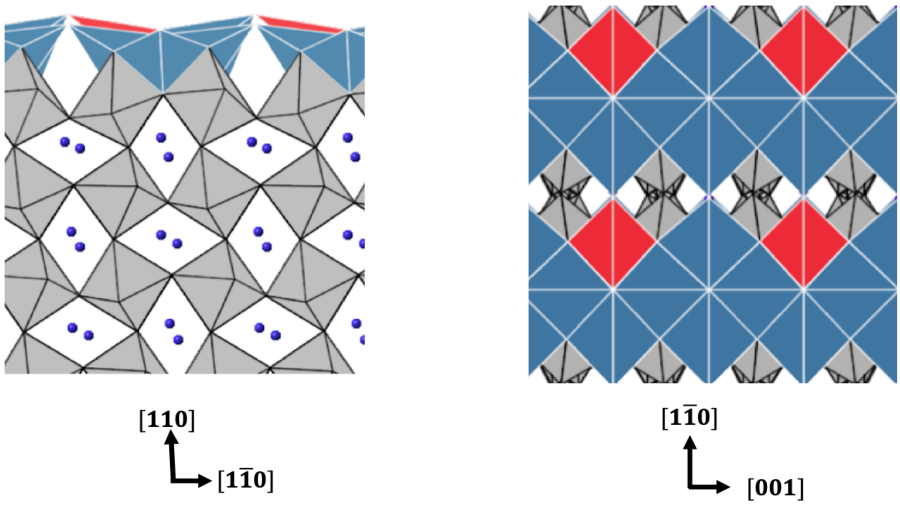

Figure 7.6. Lowest energy, DFT relaxed structure for (110) DSO. Directions are given with respect to the *Pbnm* convention. Bulk ScO_6 octahedra are grey, surface $ScO_{5\square}$ octahedra are blue, and surface ScO_4 tetrahedra are red. Dy atoms are pictured as blue spheres.

Having determined the atomic structure of the (110) DSO reconstruction, we now analyze deviations from the bulk electronic structure arising from the Sc rich surfaces

using DFT. We focus on differences in the VB and in-gap surface states because both are important for electronic applications. Figure 7.7 compares the Dy4f, Sc3d, and O2p pDOS associated with the surface shown in Figure 7.6 [**241**]. The VB is dominated by filled O 2p and Dy4f states, and the conduction band (CB) by unoccupied Sc3d states, as was found in Section 7.3 for the bulk. The Dy4f states are essentially bulk-like throughout the slab and their VB contributions match those discussed in Section 7.3. The Sc3d and O2p pDOS differ near the surface depending on the Sc-O coordination environment. Figure 7.7 shows the pDOS associated with ScO_6 octahedra, $ScO_{5\square}$ surface octahedra with a missing oxygen, and ScO_4 surface tetrahedra in the DSO slab. The ScO_6 octahedra pDOS taken from the central-most slab layer are nearly indistinguishable from independent bulk calculations, indicating sufficiently large slabs were used in the simulations. The Sc3d and O2p states in the surface double layer show sizable differences from the bulk pDOS: ScO_4 and $ScO_{5\square}$ states are concentrated near the VB maximum and minimum, respectively. There are in-gap surface states with mostly Sc3d character located 4-5 eV above the VBM. These are primarily associated with the surface ScO_4 tetrahedra.

7.4.5. Experimental Observation of Surface States with Electron Energy Loss Spectroscopy

EELS measurements on the DSO samples analyzed above provide experimental evidence for the surface states indicated in Figure 7.7. These measurements were acquired under the conditions described in Section 7.2 and have been charge corrected according to the procedure in Section 7.5.2 [**242**]. Figure 7.8(a) shows the low-loss EELS region for the [110]-oriented DSO sample and Figure 7.8(b) shows the region surrounding the zero loss

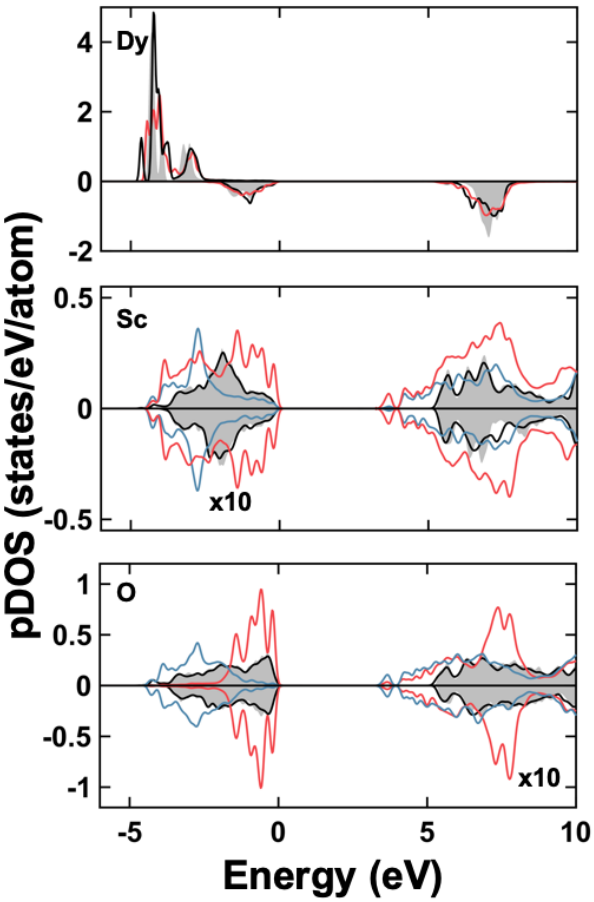

Figure 7.7. pDOS associated with Dy4f, Sc3d, and O2p states in a DSO slab with the surface shown in Figure 7.6. Positive and negative pDOS values are spin up and down, respectively. Negative and positive energies are occupied and unoccupied states, respectively, and zero is the bulk VBM. In each panel, states from the central-most layer of the surface slabs (black, solid lines) are compared to states from separate bulk calculations (black, shaded). The red in the Dy4f panel are pDOS from the Dy in the second subsurface layer. The blue and red in the Sc and O panels show pDOS associated with $ScO_{5[]}$ and ScO_4, respectively. The occupied Sc and unoccupied O states are scaled by 10 for clarity.

peak (ZLP). Figure 7.8(b) indicates the presence of a feature at 3.8 eV. The location of this peak is attributed to the surface acceptor states with primarily Sc3d character at ∼3.7 eV above the VBM shown in Figure 7.7. Besides the agreement with the peak location, the

peak intensity is consistent with that of a surface state: estimating the sample thickness as 50 nm and the total surface thickness as 1.5 nm (2 surfaces), one would expect surface energy loss features to be 6% of the intensity of bulk energy loss features [**247**]. This is reasonably close to our findings.

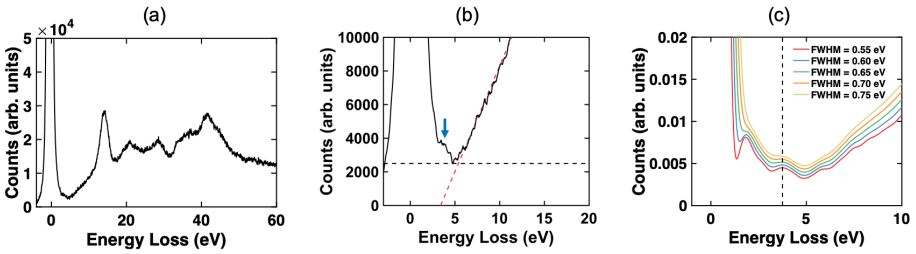

Figure 7.8. (a) Charging-corrected EELS spectrum using the cross-correlation procedure described in Section 7.5.2. (b) The spectrum indicates an in-gap feature at approximately 3.8 eV (blue arrows). (c) Example of Fourier-ratio deconvolution analysis, demonstrating the 3.8 eV feature (black dashed line) is present independent of the full-width-half-maximum of the Gaussian deconvolution function when modeling the ZLP as a Pearson VII function. Similar results were found using other ZLP models.

It is important to address the possibility that the peak in 3.8 eV is an artifact, which is confounded by the typical difficulties associated with treating the ZLP and its long tail [**247, 272**]. We adopt a Fourier-ratio deconvolution method [**247, 272, 273, 274**] using a Gaussian deconvolution function to investigate this possibility. Since an experimental instrument response function was unavailable, the instrument response function was modelled with several functions (simple truncations, power law, Gaussians, Gaussian-Lorentzian mixtures, Pearson VII) fit to the experimental ZLP. An example of the Fourier-ratio deconvolution is shown in Figure 7.8(c). The persistence of the 3.8 eV feature for every ZLP model used and for a wide range of Gaussian deconvolution full-width-half-maximum values indicates the 3.8 eV feature is not an artifact.

Although not an artifact, it is possible that the 3.8 eV feature is a result of a Cerenkov process [**275**], since DSO has a moderately high dielectric constant [**125**] and is firmly in the Cerenkov regime under the experimental conditions used here. However, the good agreement between the experimental peak location and the independent DFT calculations of the surface, which was consistent with XPS and TED, and the agreement between the peak intensity and the intensity of a surface state imply that this feature is not a Cerenkov loss.

7.4.6. Applicability to Other Lanthanide Scandate Surfaces

As shown in Ref. [**241**], the surface structure described above for the (110) surface of DSO is found to occur on (110) GSO surfaces and there is evidence for it on (110) TSO surfaces. Since it exists independent of the A-site cation, it is possible the same reconstruction could be found on other (110) lanthanide scandate surfaces, beyond DSO, GSO, and TSO. Furthermore, since the {100} pseudocubic surfaces of 332 perovskites have the same valence and structural units, this double layer reconstruction may lie on the convex hull for other {100} pseudocubic surfaces.

7.5. Large Charging in Lanthanide Scandates

7.5.1. Motivation

Most insulators subjected to sufficiently high energy illumination will charge [**276, 277**]. The charging can be net positive or negative depending on the material, sample, and experimental conditions, and the magnitude and spatial extent of charging will also depend upon these factors. Over the course of working with the lanthanide scandates, we have

observed that they charge far more than most materials. For the purposes of the work described in Section 7.3 and 7.4, the charging was undesirable: charging complicates XPS and electron microscopy experiments so samples with a propensity for charging will frequently be processed (e.g. depositing carbon passivating films) to avoid charging effects. Here we use XPS and EELS to show the presence of large charging in the lanthanide scandates, some of its effects, and methods to overcome it (when this is desirable). We also use UPS, REELS, and SE imaging to explain the origin of the charging, laying the groundwork for Section 7.6 where we show "charging ain't all bad" [**242**] and can be a source of new science [**27**].

7.5.2. Charging in XPS

Sample holders in XPS are usually made of metal and grounded to mitigate charging effects [**244, 245**]. Even with the grounding, charging is generally a problem for thick insulators: their negligible conductivity means they cannot compensate for the ejected photoelectrons [**277**]. This form of charging in XPS leaves the sample positive, reducing the kinetic energy of the ejected photoelectron which manifests as a binding energy shift to higher energies. Commonly, this is corrected by aligning the XPS spectrum to some standard (either a $Au4f_{7/2}$ or adventitious C1s peak) and/or using an argon flood gun to provide a source of charge compensation [**244, 245**]. An example of an XPS spectrum for an insulator exhibiting typical charging is the STO spectrum shown in Figure 7.9. This spectrum was acquired for a STO (100) sample which was processed under similar conditions to the DSO sample preparation conditions described in Section 7.2 with no

charge compensation mechanisms. There is ∼10 eV binding energy shift, indicative of charging, but the peak structure is still very well defined.

In more extreme charging cases, the energies of the photoelectrons are shifted and the peak structure is heavily affected. An example of this behavior is shown with the DSO spectrum in Figure 7.9. This sample was processed as described in Section 7.2. There is ∼700 eV binding energy shift and no discernable peak structure. Depositing a thin layer of carbon onto the sample does little to change the binding energy shift, but does lead to the presence of some peaks indicating some charge compensation.

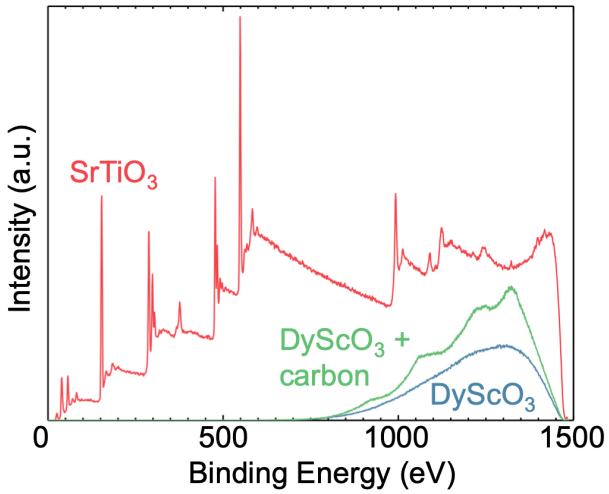

Figure 7.9. XPS spectra acquired from the (100) surface of a STO single crystal (red) and the (110) surface of a DSO single crystal (blue) with no charge compensation. The lack of peak structure and sizable binding energy shift in the DSO spectrum compared to the STO spectrum indicates large charging. Common charge passivation techniques such as carbon coating (green) have little effect.

7.5.3. Charging in EELS: Rapid Spectra Acquisition and Cross-Correlation

A low-loss EELS spectrum for a charged DSO sample with a standard acquisition time (in practice, this spectrum is the sum of 100 individual spectra, each of which has a shorter acquisition time, see Section 7.2) is shown in Figure 7.10(a) [**242**]. Although some peak locations are discernible, charging-related instabilities reduce the signal-to-noise ratio (SNR), making quantitative analysis nearly impossible. By analyzing the individual spectra (e.g. Figure 7.10(b)) which sum to the spectrum in Figure 7.10(a), it is apparent that the low SNR originates from interactions between the electron beam and charge on the sample, which induce energy loss shifts. This shift was quantified by tracking the ZLP position in each individual spectrum (an example of which is included in Figure 7.10(b)). As shown in Figure 7.10(c), the ZLP position varies by $\sim$2 eV throughout the experiment, with the average position of the ZLP tending to a steady-state, positive value under continued beam exposure. We interpret this steady-state as a saturation of charging and the positive average ZLP shift as positive charging (in agreement with the XPS data in Figure 7.9). Even though the average ZLP position tended to a steady-state value, the spread was consistently $\sim$0.5 eV. This suggests that charging saturated on average, but local fluctuations in the charge distribution were present as the sample interacted with the beam.

To mitigate the charging effects, the origin in each individual spectrum contributing to the spectrum in Figure 7.10(a) was shifted using cross-correlation before performing the sum [**242**]. Figure 7.11(a) demonstrates significant improvements in the SNR from correcting for charging shifts from cross-correlating the ZLP position, and Figure 7.11(b) indicates a 0.5 eV reduction in the full-width-half-max of the ZLP. The higher SNR

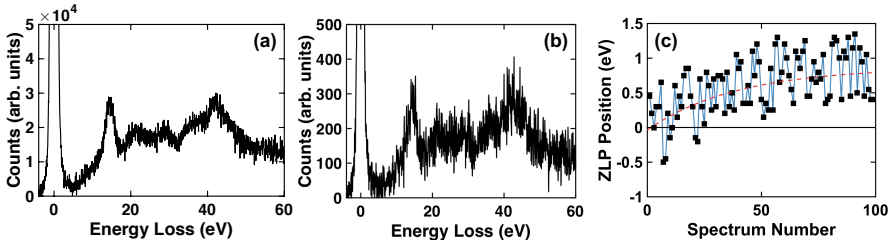

Figure 7.10. (a) EELS spectrum of charged DSO obtained by summing 100 spectra, each with an effective acquisition time of 0.1 ms and no charge correction. (b) A single spectrum included in the sum shown in (a). (c) ZLP position of each spectrum shows energy loss shifts due to charging effects. The average ZLP position (red dashed line) tends to saturate, but the spread about the average indicates local fluctuations in the charge distribution persist.

spectrum in Figure 7.11(a) enables a quantitative analysis of the low-loss region. As has already been described in Section 7.4.5, there is evidence for an energy loss associated with a surface state in Figure 7.11(c). Additionally, it is possible to extract the band gap from the charge-corrected spectrum. Since DSO is a large band gap insulator, a linear-fit method was used to find the band gap. The linear-fit method consists of finding the intersection between a line fit to the onset of the loss spectrum and a horizontal line at the background level [**278**]. Data was smoothed using a moving average of 5 data points prior to linear fitting. As shown in Figure 7.11(c), this process yielded a minimum energy loss of ∼5.4 eV, which is similar to literature values [**252**] and the measurements in Section 7.6.

7.5.4. Origin of Charging

Section 7.5.2 and 7.5.3 provide two examples of large charging in lanthanide scandates, and some ways to overcome the charging, but do not explain the origin of the charging. Excessive charging in the lanthanide scandates occurs because their band gaps and work

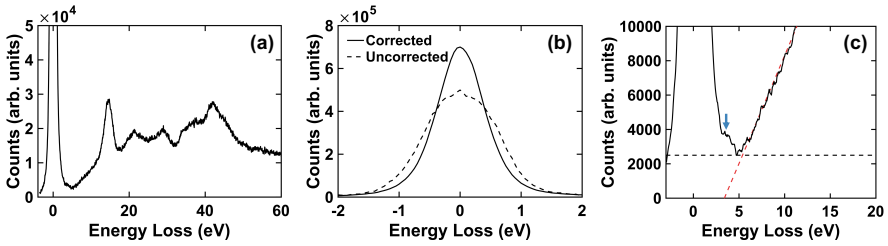

Figure 7.11. (a) EELS shown in Figure 7.10(a) after an origin correction using cross-correlation. (b) The ZLP full-width-half-maximum was reduced by 0.5 eV after charge correction. (c) The band gap of DSO was determined to be 5.4 eV using a linear-fit method with the spectrum in (a). The linear fit marking the onset of the loss spectrum is a red dashed line and the background level is a black dashed line. The arrow indicates the in-gap feature at ∼3.8 eV.

functions are approximately equal [**27**]. Consequently, if there are few trap states (e.g. from defects), excited electrons which normally could reside in unoccupied states exit the material and leave the sample positively charged [**27, 242**].

To confirm this interpretation, the band gap and work function were measured on a DSO sample prepared according to Section 7.2. Figure 7.12(a) shows a UPS spectrum used to extract the work function, which corresponds to the lowest measured photoelectron kinetic energy. A value of 5.8 eV is obtained from a linear extrapolation to the region shown in the inset of Figure 7.12(a) [**27**]. Note, the low kinetic energy tail consists of secondary electrons which have suffered inelastic collisions, so the signal does not provide information on occupied DSO states. Figure 7.12(b) includes a REELS measurement which shows DSO possesses a band gap of 5.7 eV [**27**]. Both the work function and band gap values are in agreement with the literature, and similar to the EELS measurement in Section 7.5.3. The band diagram in Figure 7.12(c) summarizes the origin of charging in the scandates.

The SE image in Figure 7.12(d) is a way to visualize, and confirm, the understanding summarized in Figure 7.12(c). The SE image contains GSO [**239, 240**] and KTO nanoparticles [**243**], supplied by Dr. Ryan Paull and Tiffany Ly, respectively. The GSO nanoparticles have lower signal and less topographic contrast than the KTO nanoparticles, except near the conducting carbon support or KTO nanoparticles. The lower signal is because the GSO nanoparticles are charged significantly more positively than the KTO nanoparticles. The lack of topographic contrast indicates a long electron mean free path [**27**].

7.6. Flexoelectric Bending of Lanthanide Scandates

7.6.1. Background

In 1968, Bursian and Zaikovskii [**13**] noticed BTO films tended to bend when subjected to electric fields. They found that a potential of 20 V applied to a 2.5 μm BTO thick film yielded curvatures $\sim$150 m^{-1}. In a subsequent paper, Bursian and Trunov [**279**] derived an expression for the curvature (κ) that developed in terms of the applied potential difference (V), the flexural rigidity of the sample (D), and the flexoelectric coefficient (μ).

$$\kappa = \frac{\mu V}{D} \tag{7.2}$$

For an isotropic plate-like sample (Chapter 3), the flexural rigidity is

$$D = \frac{12\,(1-\nu^2)}{Y d^3} \tag{7.3}$$

where Y is the Youngs modulus, ν is the Poisson ratio, and d is the elastic thickness [**54, 56**]. Combining Eq. 7.2 and 7.3 yields an expression for the curvature in terms of

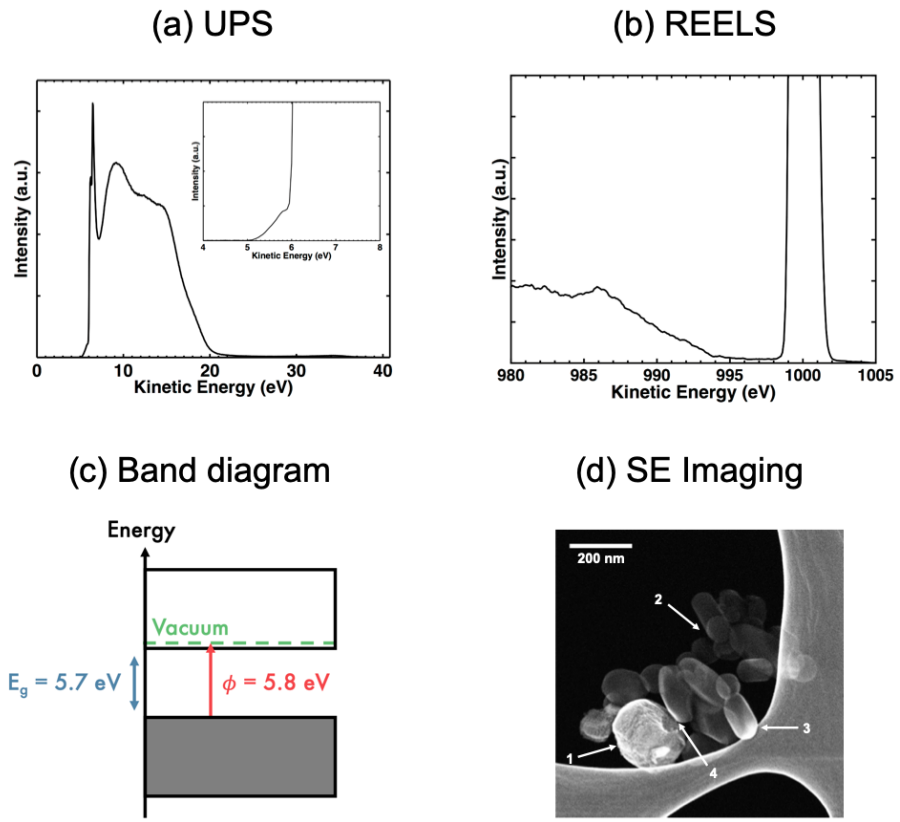

Figure 7.12. (a) UPS spectrum of DSO sample with an embedded subpanel showing the fine details of the edge. A linear fit yields a work function of 5.8 eV. (b) REELS spectrum with an incident energy of 1 keV. A linear fit yields a band gap of 5.7 eV. (c) A band diagram summary for the scandates where the shaded band is occupied and the unshaded band is unoccupied. (d) SE image of GSO and KTO nanoparticles (imaging conditions given in Section 7.2). Typically, SE images show strong topographic contrast, e.g. the KTO nanoparticle at 1. GSO nanoparticles have significantly less signal and topographic contrast, such as at 2, but exhibit enhanced signal where local charge compensation is possible, such as near the carbon support at 3 or the KTO nanoparticles at 4.

sample dimensions, elastic constants, the strength of the flexoelectric coupling, and the applied potential difference.

$$\kappa = \mu V \frac{12\,(1-\nu^2)}{Y d^3} \tag{7.4}$$

Under the conditions used in Bursian and Zaikovskii's [**13**] experiment, Eq. 7.4 predicts the measured curvature. In addition, Eq. 7.4 indicates $\kappa \sim 10^6$-10^{10} m^{-1} for nm thick films because the flexural rigidity of a plate scales as the cube of the elastic thickness [**27**].

In the subsequent sections we describe the direct observation of large flexoelectric bending at the nanoscale in lanthanide scandates. This bending is found to be intimately tied to the charging introduced in Section 7.5 and a consequence of the flexoelectric response measured in Chapter 3. These measurements demonstrate that the large nanoscale curvatures predicted by Eq. 7.4 are physically realistic and not merely extrapolations [**27**].

7.6.2. Bending Observation in the TEM

Samples used in this study were prepared according to the procedure outlined in Section 7.2 and TEM was performed as described in Section 7.2. Figure 7.13 includes a sequence of frames in which the illumination of a TEM electron beam caused bending in a thin DSO sample [**27**]. The bending increased and decreased as the electron flux was increased and decreased, and the sample bent away from the beam if the beam was not centered on the sample. If the bending was too severe, the sample would fracture, but the bending was generally reversible.

The bending occurred along the length and width of the sample such that the sample approach a spherical shape as the electron flux was increased. A depiction of the bending is included in Figure 7.14(a). The curvature along the length and width of the sample as a function of flux shown in Figure 7.14(b) was extracted from the images in Figure 7.13

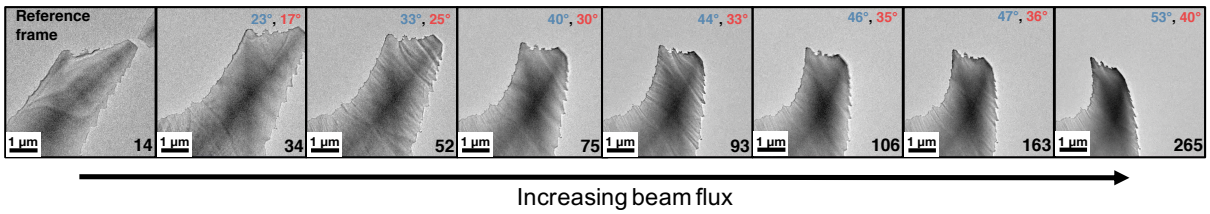

Figure 7.13. Downward bending of a [110] oriented DSO sample under the electron beam. Eight frames from a video indicate the bending increases as the flux increases. In each frame, the number in the bottom right corner is the approximate electron flux (electrons/nm^{2}s) and the bending angles (with respect to the reference frame) along the length (blue) and width (red) of the feature are given at the top right corner.

and is empirically described by

$$\kappa = A\left(1 - \exp\left(-\frac{J}{B}\right)\right) + \kappa_0 \tag{7.5}$$

where κ is the curvature, J is the flux, A and B are constants, and κ_0 is the (unmeasured) curvature of the reference frame. Eq. 7.5 indicates the curvature saturates as a function of flux, suggesting a link to the saturation of charging described in Section 7.5.

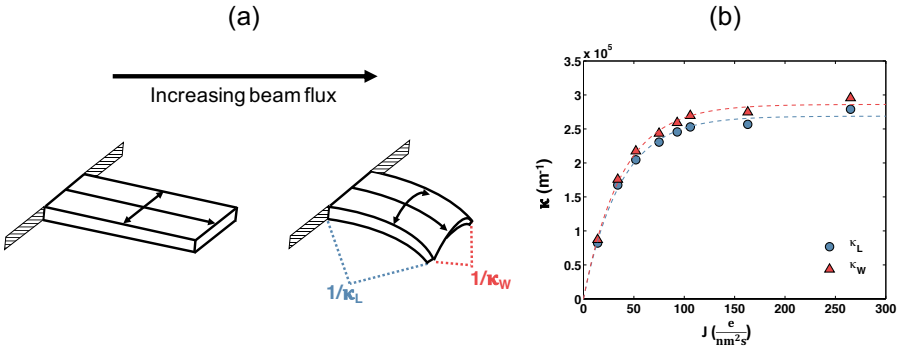

Figure 7.14. (a) Bent samples, drawn as black cantilevers, exhibited curvatures along the length (κ_L) and width (κ_W). (b) Curvature (κ) along the length and width of the feature in Figure 7.13 as a function of beam flux (J). Dashed lines are fits to Eq. 7.5.

The bending described in Figures 7.13 and 7.14 occurred for ∼50 different features from 20 different samples, including DSO, TSO, GSO samples. Similar charging and bending were not found to occur in STO, KTO, $NdGaO_3$ (NGO), or LAO (NGO and LAO charged a little, but significantly less than the scandates and with minimal bending).

7.6.3. Connection to Charging

It was established in Section 7.5 that lanthanide scandate samples dramatically charge, and that this charging is related to their electronic structure [**27**]. As was the case in XPS and EELS experiments, there was considerable sample charging in these exerpiments even though the electron fluxes used were significantly lower than electron fluxes typically used for high resolution imaging or chemical analysis (e.g. in Figure 7.13 the electron fluxes were ∼1-100 electrons/nm^2s whereas typical fluxes are ∼10^4-10^6 electrons/nm^2s). The charging was linked to the bending because when a sample was coated with a carbon coating, charging was non-existent and minimal bending was observed. This suggests the bending occurs because of charging and that charge saturation with flux is responsible for the behavior shown in Figure 7.14(b).

High energy electrons in typical electron microscope act as a white source for inelastic scattering. At low accelerating voltages (e.g. those used in a typical scanning electron microscope), a net accumulation of electrons in the sample is possible, but beyond a material and sample specific energy threshold there will be a net loss of SEs in the sample, causing the sample to be net positive [**276**]. The charging will tend to increase with electron flux and one would anticipate the top surface of the sample to charge positive with respect to the bottom surface owing to the nature of SE emission [**27, 276**]. Accompanying

this inhomogeneous charge distribution is a potential difference across the sample which has a maximum value of the band gap in the limit of a thin insulator: once the potential is sufficiently large, any additional charging is mitigated by Zener tunneling [**280**]. Thus, for a sufficiently high incident flux the charging and potential should saturate, as is observed. A qualitative depiction of the charging is shown in Figure 7.15.

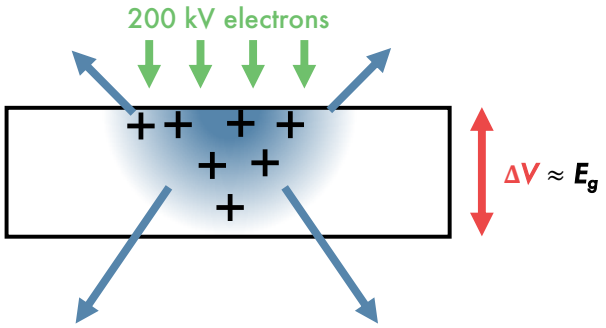

Figure 7.15. Schematic illustrating electron beam-induced charging. Electron beam-sample interactions cause asymmetric SE emission, yielding an inhomogeneous charge distribution in the sample (blue). For a thin, insulating sample, the maximum potential difference accompanying this inhomogeneous charge distribution is limited by Zener tunneling and will be approximately equal to the band gap.

7.6.4. Link to Flexoelectricity

Eq. 7.4 provides a means to quantitatively connect the flexoelectric measurements on DSO in Chapter 3 with in-situ TEM observations described above. Recall, in Chapter 3 we found μ^{eff}=-8.1 nC/m for a DSO sample with the same crystallographic orientation as the samples bent in the TEM. If we use the literature Poissons ratio of 0.25 [**281**], a Voigt-Reuss-Hill average [**282, 281**] for the Youngs modulus of 183 GPa (the sample is a single crystal, but it is ambiguous what elastic tensor components should be used), and

approximate the potential difference as the band gap (Section 7.6.3), the last quantity we need to use Eq. 7.4 is the thickness. Based upon EELS measurements, the samples were ∼50 nm thick at the base of the bending features and ∼5 nm or less at the edges, corresponding to an average thickness of 22.5 nm. Using these values in Eq. 7.4, we obtain a curvature of 2.5×10^5 m^{-1}, which is in semi-quantitative agreement with the saturated curvatures $\sim3\times10^5$ m^{-1} shown in Figure 7.14(b). In passing, we will also note that using a low energy ion-beam mill to disorder the DSO sample surface led to less severe charging and near-complete reduction in bending. This indicates the surface plays a large role in the observed charging and bending, which is consistent with attributing these observations to flexoelectricity (Chapter 5).

CHAPTER 8

How Flexoelectricity Drives Triboelectricity

8.1. Background

Charge transfer associated with rubbing or contacting two materials is known as triboelectricity or the triboelectric effect [**283, 284, 285**]. It is a very familiar phenomenon, as anyone who has touched a doorknob on a cold winter's day will surely attest, with a long history dating to at least 600 BC. These first observations of triboelectricity are often attributed to a Greek philosopher named Thales of Miletus who, as the story goes, observed that fur attracted dust after it had been rubbed by amber [**284**]. Not only are these observations consequential for triboelectricity, but they are also important for the history of materials science: the word electron comes from lektron, the Greek word for amber [**284**].

The first modern scientific studies of triboelectricity occurred in the early 1900s when Shaw quantified triboelectric charge transfer and created the (now defunct) triboelectric series [**286**]. In the ensuing decades there has been much progress (see, e.g., Ref. [**283**], [**284**], and [**285**] for summaries) in understanding triboelectric charge transfer arising from metal-on-metal contact in terms of contact potential differences (i.e. work function differences between different metals drive electron transfer [**287**]), but the thermodynamic driver for charge transfer in metal-on-insulator and insulator-on-insulator contact is unresolved [**285**]. There is experimental evidence for the exchange of electrons

[**288, 289, 290**], ions [**291, 292**], or charged molecular fragments [**293**] during contact in different cases, and almost as many models as there are experiments. Some of the more common mechanisms that are invoked to explain triboelectricity in insulators include temperature differences [**294**] and trapped charge [**295, 296, 297**].

Triboelectricity is thought to play a significant role in many physical processes, ranging from planetary formation [**298**] to dust storms [**299**], so furthering the fundamental physics of triboelectricity could have important implications for many academic areas beyond the triboelectric effect. In addition, triboelectricity has consequences in industries such as pharmaceuticals manufacturing [**300**] and xerography [**301**], and can lead to electrostatic discharges which can cause fires with devastating consequences.

Before Bowden and Tabor [**302**] developed a nanoscale understanding of friction and wear in terms of asperity contact, adhesion, and deformation, Volta and Helmholtz suggested rubbing was important in the context of triboelectricity because it increases the number of contact points between two contacting bodies [**303, 304, 305**]. To date, little attention has been given to the role of microscopic deformations at asperity contacts in triboelectricity [**40**], although there is much evidence that macroscopic deformations play an important role [**306, 307, 308, 309, 310**].

In this chapter, I analyze the electrical changes arising from elastic deformations during contact using flexoelectricity. In Section 8.2 I show that elastic strain fields during typical asperity contact generate potential differences via the flexoelectric effect which are sufficiently large to cause charge transfer [**40**]. I generalize and expand the model in Section 8.3 to incorporate band structure and treat contact-induced band bending effects

[**311**]. After exploring some general consequences of this framework in Section 8.4, specific band bending profiles are computed using first principles and FEA simulations for contact between dissimilar materials (Si sphere on STO flat) and similar materials (STO sphere on STO flat) in Section 8.5. In Section 8.6 I explain how the contact-induced band bending profiles computed in Section 8.5 relate to charge transfer mechanisms involving trap states and ion transfer. Lastly, I connect the flexoelectric model for triboelectricity to a number of experimental observations in Section 8.7. The initial idea for the work described in Section 8.2 was conceived by Professor Laurence D. Marks and the analysis was conducted in collaboration with Dr. Alex (Yu-Wei) Lin [**40**]. I performed all simulations and analyses in Sections 8.3 - 8.7 and benefitted from discussions with Professor Laurence D. Marks [**311**].

8.2. Flexoelectric Couplings During Contact and Pull-Off

8.2.1. Overview

The goal of this section is to estimate the size of the electric fields (and ultimately the change in the electrostatic potential) arising from contact deformations through flexoelectricity [**40**]. This is simplest beginning with the definition of the flexocoupling voltage introduced in Chapter 2,

$$E_i = -f_{ijkl}\epsilon_{kl,j} \tag{8.1}$$

where E_i is the electric field arising from the strain gradient $\epsilon_{kl,j}$ which is mediated by the flexocoupling voltage f_{ijkl} [**10, 11**]. For simplicity, we consider an isotropic material characterized by a single flexocoupling voltage such that the flexocoupling voltage tensor

has the form

$$f_{ijkl} = f\left(\delta_{ij}\delta_{kl} + \delta_{ik}\delta_{jl} + \delta_{il}\delta_{jk}\right) \tag{8.2}$$

and only consider the component of the electric field that will be normal to the contact interface (see Section 8.2.2 for a discussion of the contact geometry). Taking z to be this direction and combining Eq. 8.1 and 8.2 gives

$$E_i = -f \left.\frac{d\epsilon}{dz}\right|_{eff} \tag{8.3}$$

where

$$\left.\frac{d\epsilon}{dz}\right|_{eff} = 3\epsilon_{zz,z} + \epsilon_{xx,z} + \epsilon_{yy,z} + \epsilon_{zx,x} + \epsilon_{xz,x} + \epsilon_{zy,y} + \epsilon_{yz,y} \tag{8.4}$$

Now we use analytic theories of contact to acquire expressions for the strain gradients in Eq. 8.4 for indentation and pull-off.

8.2.2. Contact Strain Gradients

8.2.2.1. Indentation. The venerated Hertzian contact model is used to describe indentation [**312**]. We focus on the simple case of a flat, elastic half-space (commonly referred to as the flat in contact mechanics literature) indented by a rigid sphere. Taking both materials to be homogeneous and isotropic, the stresses in the deformed flat in cylindrical

coordinates [**313**] are given by

$$\frac{\sigma_{rr}}{P} = \frac{1-2\nu}{3}\frac{a^2}{r^2}\left(1-\left(\frac{z}{u^{1/2}}\right)^3\right)+\left(\frac{z}{u^{1/2}}\right)^3\frac{a^2u}{u^2+a^2z^2}+ \frac{z}{u^{1/2}}\left(u\frac{1-\nu}{a^2+u}+(1+\nu)\frac{u^{1/2}}{a}\tan^{-1}\left(\frac{a}{u^{1/2}}\right)-2\right) \tag{8.5}$$

(8.6)

$$\frac{\sigma_{\theta\theta}}{P} = -\frac{1-2\nu}{3}\frac{a^2}{r^2}\left(1-\left(\frac{z}{u^{1/2}}\right)^3\right)+\frac{z}{u^{1/2}}\left(2\nu+u\frac{1-\nu}{a^2+u}+(1+\nu)\frac{u^{1/2}}{a}\tan^{-1}\left(\frac{a}{u^{1/2}}\right)\right)$$

$$\frac{\sigma_{zz}}{P} = -\left(\frac{z}{u^{1/2}}\right)^3\frac{a^2u}{u^2+a^2z^2} \tag{8.7}$$

$$\frac{\sigma_{rz}}{P} = -\frac{rz^2}{u^2+a^2z^2}\frac{a^2u^{1/2}}{a^2+u} \tag{8.8}$$

where

$$u = \frac{1}{2}\left\{(r^2+z^2-a^2)+\left((r^2+z^2-a^2)^2+4a^2z^2\right)^{1/2}\right\} \tag{8.9}$$

$$P = \frac{3F}{2\pi a^2} \tag{8.10}$$

$$a = \left(\frac{3FR}{4Y}(1-\nu^2)\right)^{1/3} \tag{8.11}$$

In these expressions, P is the contact pressure, F is the applied force, a is the deformation radius, Y is the Youngs modulus, ν is the Poissons ratio, and r and z are cylindrical coordinates.

The strains in cylindrical coordinates are obtained from Eq. 8.5- 8.8 using Hookes law

$$\epsilon_{rr} = \frac{1}{Y}\left(\sigma_{rr}-\nu(\sigma_{\theta\theta}+\sigma_{zz})\right) \tag{8.12}$$

$$\epsilon_{\theta\theta} = \frac{1}{Y}\left(\sigma_{\theta\theta} - \nu(\sigma_{rr} + \sigma_{zz})\right) \tag{8.13}$$

$$\epsilon_{zz} = \frac{1}{Y}\left(\sigma_{zz} - \nu(\sigma_{\theta\theta} + \sigma_{rr})\right) \tag{8.14}$$

$$\epsilon_{rz} = \frac{2(1+\nu)}{Y}\sigma_{rz} \tag{8.15}$$

An appropriate transformation can then be applied to Eq. 8.12- 8.15 to get Cartesian strains which can be differentiated to determine the strain gradient components entering into Eq. 8.4.

Because of the axial symmetry of the sphere-on-flat case, only five strain gradient components in Eq. 8.4 are symmetrically inequivalent ($\epsilon_{yz,y} = \epsilon_{zy,y}$ and $\epsilon_{xz,x} = \epsilon_{zx,x}$. They are depicted in Figure 8.1(a)-(e) as contour plots. The spatial distributions of each strain gradient component depend on external parameters (applied force, indenter size) and materials properties (Youngs modulus, Poissons ratio). To develop some intuition about the magnitude of the strain gradients, we calculate the average of $\frac{d\epsilon}{dz}\big|_{eff}$ within the indentation volume (approximated as a^3). The average effective strain gradient is negative and scales inversely with indenter radius because the indented material develops a curvature opposite to the direction of the applied force with a magnitude dictated by the indenter size. Figure 8.1(f) demonstrates the magnitude of the average effective strain gradient associated with Hertzian indentation is $\sim 10^8$ m^{-1} in all materials at the nanoscale, suggesting large flexoelectric responses are possible.

8.2.2.2. Pull-Off. Pull-off is modelled using JKR theory [**314**], a simple modification of Hertzian contact which treats adhesion. The JKR pull-off force, i.e. the tensile force

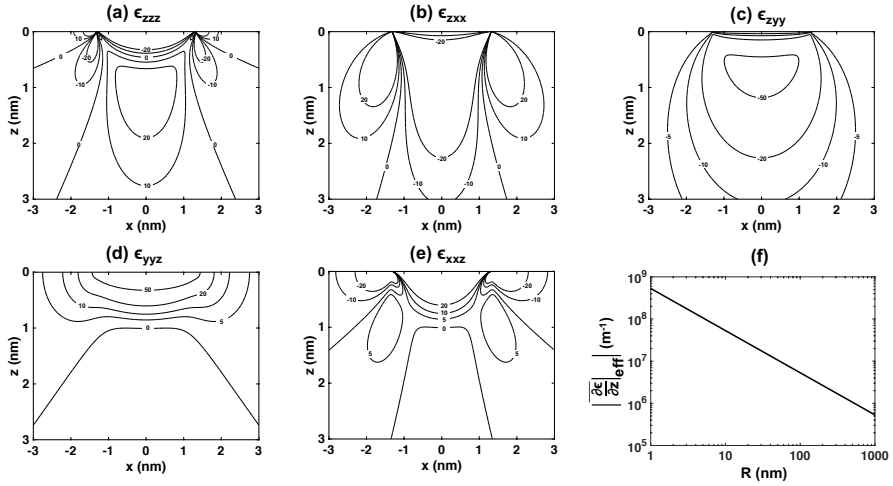

Figure 8.1. (a) (e) Symmetrically inequivalent strain gradients arising from Hertzian indentation of an elastic half-space entering Eq. 8.3. Lines indicate constant strain gradient contours in units of 10^6 m^{-1}, z is the direction normal to the surface with positive values going into the bulk, x is an in-plane direction, and the origin is the central point of contact. Data corresponds to 1 nN of force applied to an elastic half-space with a Youngs modulus of 3 GPa and a Poissons ratio of 0.3 (typical polymer) by a 10 nm rigid indenter. (f) The magnitude of the average effective strain gradient ($|\left.\frac{d\epsilon}{dz}\right|_{eff}|$) as a function of indenter radius (R).

required to separate an indenter from the surface, is

$$F_{adh} = -\frac{3}{2}\pi\Delta\gamma R \tag{8.16}$$

where $\Delta\gamma$ is the adhesive energy per unit area and R is the radius of the indenter. Replacing the applied force in the Hertzian indentation strain gradient expressions developed in Section 8.2.1 with Eq. 8.16 provides pull-off strain gradients immediately before contact is broken. These strain gradient distributions are qualitatively similar to those shown in Figure 8.1 and the average effective strain gradient within the pull-off volume is also $\sim 10^8$ m^{-1} in all materials at the nanoscale. The major difference between indentation

and pull-off is a change in sign of the strain gradients (the force is applied in the opposite direction).

8.2.3. (Flexo) Electric Fields During Contact

We now substitute the strain gradient components shown in Figure 8.1 for indentation and pull-off into Eq. 8.3. The electric field component in Eq. 8.3 arising in the indentation case is shown in Figure 8.2, assuming a positive flexocoupling voltage (the signs of the electric field are reversed for the pull-off case, but the result is otherwise similar). Because the electric field induced by the flexoelectric effect is the effective strain gradient scaled by the flexocoupling voltage, its magnitude is linearly proportional to the flexocoupling voltage and inversely proportional to the indenter size. This leads to average electric fields in the indentation/pull-off volume $\sim 10^8$-10^9 V/m for all materials at the nanoscale [**40**].

8.2.4. Surface Potential

The electric fields induced by the flexoelectric effect in the deformed body will generate a potential difference on its surface relative to the potential in the undeformed portions of the deformed body. The flexoelectric surface potential difference can be estimated from the normal component of the electric field via

$$V(x,y) = -\int E_z(x,y,z)dz \tag{8.17}$$

Note, this is not a proper electrostatic potential since we have only considered a component of the electric field, but is indicative of the magnitude of the potential difference

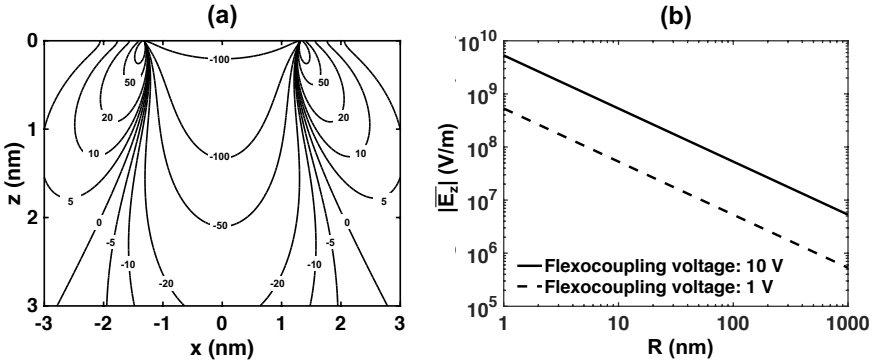

Figure 8.2. (a) Normal component of the electric field given by Eq. 8.3 induced by Hertzian indentation via a flexoelectric coupling. Lines indicate constant electric field contours in units of MV/m, z is the direction normal to the surface with positive values going into the bulk, x is an in-plane direction, and the origin is the central point of contact. Data corresponds to 1 nN of force applied to an elastic half-space with a Youngs modulus of 3 GPa and a Poissons ratio of 0.3 (typical polymer) by a 10 nm indenter. A flexocoupling voltage of 1 V is assumed. (b) Magnitude of the average electric field ($|\overline{E}_z|$) in the indentation/pull-off volumes as a function of indenter radius (R) assuming a flexocoupling voltage of 1 V (dashed) and 10 V (solid).

at the surface induced by the contact deformations. Figure 8.3 shows the surface potential difference calculated from Eq. 8.17 along the deformed surface of a typical polymer (Youngs modulus of 3 GPa, Poissons ratio of 0.3, and adhesion energy of 0.06 N/m) with a flexocoupling voltage of 10 V. The pull-off surface potential difference is larger in magnitude and spatial extent than the indentation surface potential difference, and both are sensitive to the applied force, indenter size, and materials properties of the deformed body (Youngs modulus, Poissons ratio, adhesion energy, flexocoupling voltage).

To understand how the indentation and pull-off surface potential differences scale with the applied force, indenter size, and materials properties, we calculated the indentation and pull-off surface potential differences while varying one property/parameter with all

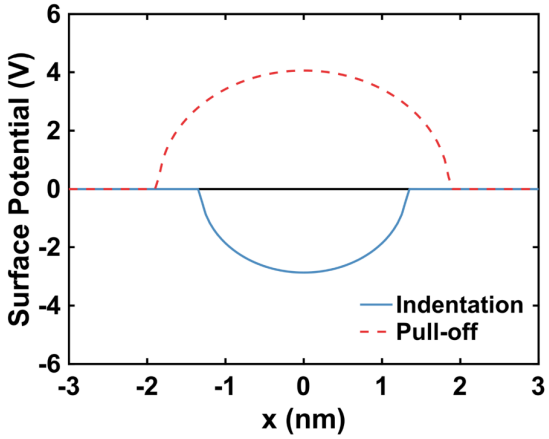

Figure 8.3. Surface potential along the surface of the deformed body for indentation (solid) and pull-off (dashed). x is an in-plane direction and the origin is the central point of contact. Data corresponds to 1 nN of force applied to an elastic half-space with a Youngs modulus of 3 GPa, a Poissons ratio of 0.3, adhesion energy of 0.06 N/m (typical polymer), and flexocoupling voltage of 10 V by a 10 nm indenter.

other terms held constant. Then, power-law fits to the minimum surface potential difference during indentation and maximum surface potential difference during pull-off were used to determine the scaling behavior in Figures 8.4 and 8.5. The end results are summarized in the expressions

$$V_{indentation,min} \propto -f\left(\frac{F}{R^2Y}\right)^{1/3} \tag{8.18}$$

$$V_{pull-off,min} \propto f\left(\frac{\Delta\gamma}{RY}\right)^{1/3} \tag{8.19}$$

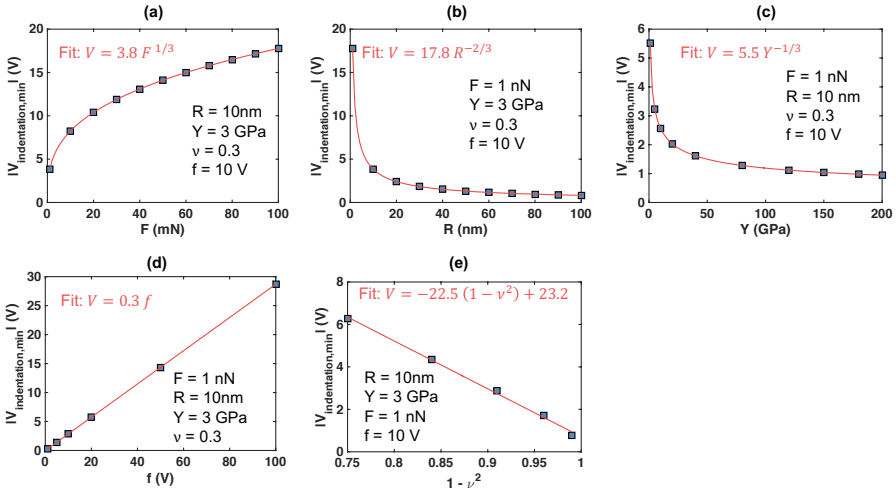

Figure 8.4. Scaling of the minimum surface potential difference during indentation with applied force (F), indenter radius (R), Youngs modulus (Y), flexocoupling voltage (f), and Poisson ratio (ν). Surface potential differences are calculated numerically (blue squares) by varying one quantity while keeping all other parameters constant (constant values are black text in each plot). Red lines show fits to the calculated values and the equation of fit is in red text.

8.2.5. Connections to Experiment

The above model demonstrates the existence of large electric fields and potential differences during contact and has many features which can explain numerous triboelectric observations. First, stick-slip tribocurrents exhibit bipolar characteristics which is consistent, with the change in the sign of the surface potential difference for indentation and pull-off predicted by our model [**315**]. Second, tribocurrents scale with indentation force to the 1/3 power, which is the same force scaling of the indentation surface potential difference in our model [**316**]. Thirdly, non-uniform tribocharge patterns [**317, 318, 319, 320**] can be explained because local variations in surface topography will dictate which contacting body locally acts as the indenter and, consequently, the charge transfer direction

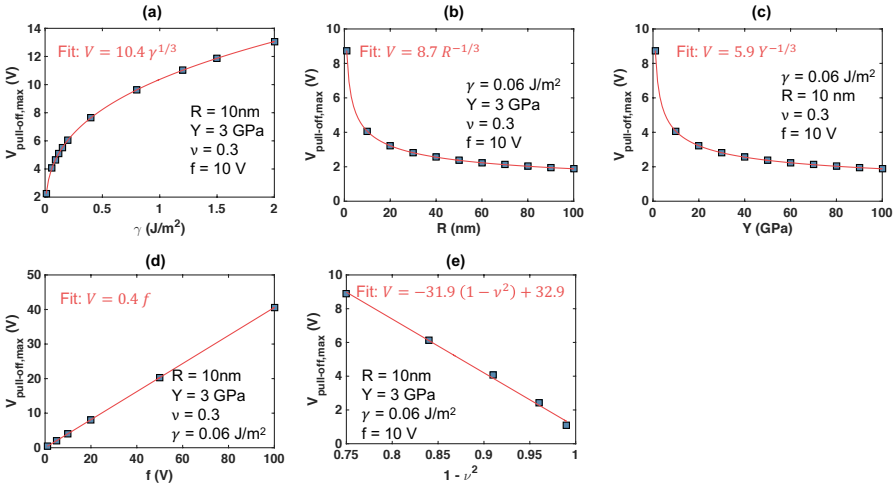

Figure 8.5. Scaling of the maximum surface potential difference during pull-off with adhesion energy ($\Delta\gamma$), indenter radius (R), Youngs modulus (Y), flexocoupling voltage (f), and Poisson ratio (ν). Surface potential differences are calculated numerically (blue squares) by varying one quantity while keeping all other parameters constant (constant values are black text in each plot). Red lines show fits to the calculated values and the equation of fit is in red text.

[**321**]. Finally, it is known that macroscopic curvature biases tribocharging with convex and concave samples tending to charge negative and positive, respectively [**306, 322**]. This change in charge transfer with curvature is a natural consequence of the flexoelectric model developed above.

8.3. Contact-Induced Band Bending: The Framework

8.3.1. Overview

Section 8.2 demonstrated the presence of large potential differences between two materials in contact owing to flexoelectricity. Even under some simplifications, the flexoelectric model for triboelectricity in Section 8.2 was able to qualitatively connect with many experimental observations [**40**]. In this section we solidify the theoretical basis of the

arguments in Section 8.2 by formally incorporating band structure and developing connections to ab initio theory [**311**]. The underlying premise of this formalism is shown in Figure 8.6: rather than thinking purely about the contact-induced potential difference (as was done in Section 8.2), it is necessary to consider the band bending induced by the elastic deformations associated with contact. In the Schottky-Mott limit of no charge transfer [**323, 324**], this amounts to analyzing the spatial variation of the CB and VB edges of two bodies in contact arising from elastic deformations. Developing a framework for this analysis is the goal of this section.

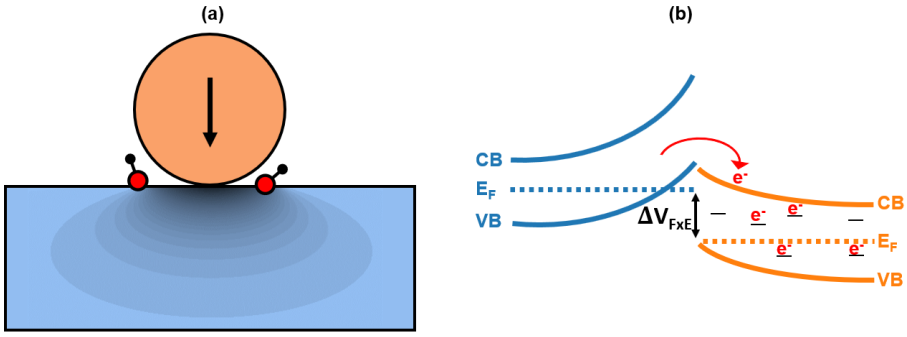

Figure 8.6. (a) Schematic of contact between a sphere and flat showing the contact induced deformation fields in the flat and adsorbed species on the surface. (b) Contact-induced band bending arises from flexoelectricity, which can cause the occupation of trap states, bulk charge transfer, or the adsorption of charged species depending on the materials, geometry, and extent of deformation.

8.3.2. A Flexoelectric Contact Model

Inhomogeneous strain in a centrosymmetric insulator will change the energy of a band feature E_i referenced to vacuum E_{vac} according to

$$\Delta\left(E_i(\mathbf{r}) - E_{vac}(\mathbf{r})\right) = \Delta\overline{V}_{FxE}(\mathbf{r}) + \left(\varphi + D_i\right)\epsilon(\mathbf{r}) \tag{8.20}$$

The first term $\Delta\overline{V}_{FxE}(\mathbf{r})$ describes the bulk flexoelectric effect (Chapter 4), i.e. the change in the average Coulomb potential from strain gradients [**58**]. The second term φ gives the shift in the MIP induced by strain ϵ (Chapter 5). The third term D_i is the relative deformation potential, i.e. the strain-induced local change in the energy of a band feature relative to the average Coulomb potential [**325, 326**]. For two materials (A and B) in contact, Eq. 8.20 applied to the VBM must be combined with their work function difference ($\Delta\phi$) to describe the relative offset between the materials.

$$\Delta\left(E^{A}_{VBM}(\mathbf{r}) - E^{A}_{vac}(\mathbf{r})\right) = \Delta\left(E^{B}_{VBM}(\mathbf{r}) - E^{B}_{vac}(\mathbf{r})\right) + \Delta\phi \tag{8.21}$$

Eq. 8.20 and 8.21 represent a general description of the band structure changes in centrosymmetric insulators arising from flexoelectricity [**311**]. We focus on flexoelectricity because it is important at the small length scales relevant to asperity contact due to the intrinsic size-dependence of strain gradients, and it is a coupling that occurs in all insulators [**10, 11**]. Piezoelectricity is neglected because explanations for triboelectricity using piezoelectricity are known to be inadequate [**283**], and unlike flexoelectricity, piezoelectricity occurs only as a bulk property in a sub-set of materials [**6, 3**].

To explore these expressions for specific cases we must make some simplifications. First, we limit ourselves to elastic contact and axially symmetric contact geometries. Second, we consider cubic materials, reducing the number of non-trivial bulk flexoelectric coefficients (Chapter 3). Third, we only treat volumetric strain effects on φ and D_i as the dominant shear strain effect is to split, not shift, energy levels [**132**]. Now we develop expressions for $\Delta\overline{V}_{FxE}(\mathbf{r})$, φ, and D_i with these simplifications.

8.3.3. The Bulk Flexoelectric Term

As described in Chapter 2 and 3, the polarization P_i in a centroysmmetric insulator with dielectric and flexoelectric couplings is

$$P_i = \varepsilon_0 \chi_{ij} E_j + P_i^{FxE} \tag{8.22}$$

where ε_0 is the permittivity of free space, χ_{ij} is the dielectric susceptibility, E_j is the electric field, and P_i^{FxE} is the flexoelectric polarization given by

$$P_i^{FxE} = \mu_{ijkl} \epsilon_{kl,j} \tag{8.23}$$

where μ_{ijkl} is the short-circuit flexoelectric coefficient tensor and $\epsilon_{kl,j}$is the symmetrized strain gradient [**10, 11, 150**].

From electrostatics [**73**], the electric field and charge density are related via

$$\nabla \cdot \mathbf{E} = \frac{\rho_b + \rho_f}{\varepsilon_0} \tag{8.24}$$

where the total charge density is expressed as the sum of the bound charge (ρ_b) and free charge (ρ_f). These charges are related to the polarization and dielectric displacement through

$$\nabla \cdot \mathbf{P} = -\rho_b \tag{8.25}$$

and

$$\nabla \cdot \mathbf{D} = \rho_f \tag{8.26}$$

Assuming a perfect insulator ($\rho_f = 0$) with cubic symmetry ($\chi_{ij} = \chi\delta_{ij}$), Eq. 8.22- 8.26 indicate the electrostatic potential and flexoelectric polarization are related by

$$\nabla^2 V = \frac{1}{\varepsilon_0(1+\chi)} \nabla \cdot \mathbf{P}_{FxE} \tag{8.27}$$

where we have used $\mathbf{E} = -\nabla V$. Eq. 8.27 is a Poisson equation with a flexoelectric charge density

$$\rho_{FxE} = -\frac{1}{1+\chi} \nabla \cdot \mathbf{P}_{FxE} \tag{8.28}$$

Recasting Eq. 8.27 in integral form (assuming there is an appropriate reference, see next paragraph)

$$V(\mathbf{r}) = \frac{1}{4\pi\varepsilon_0(1+\chi)} \int_\Omega \frac{\mathbf{P}_{FxE}(\mathbf{r}') \cdot (\mathbf{r} - \mathbf{r}')}{|\mathbf{r} - \mathbf{r}'|^3} d\Omega' \tag{8.29}$$

which reduces to Eq. 8.30 for axially symmetric cases.

$$V(\mathbf{r}) = \frac{1}{\varepsilon_0(1+\chi)} \int_\Omega \frac{\mathbf{P}_{FxE}(\mathbf{r}') \cdot (\mathbf{r} - \mathbf{r}')}{|\mathbf{r} - \mathbf{r}'|^3} \rho d\rho dz \tag{8.30}$$

In Eq. 8.30 ρ is the radial coordinate and z is the axial coordinate.

As shown in Ref. [**58**] and Chapter 4 and 5, bulk flexoelectric coefficients describe the gradient of the average Coulomb potential arising from strain gradients, so the potential in Eq. 8.30 implicitly references the undeformed average Coulomb potential. If the crystal is large enough and the deformations sufficiently localized, then the average Coulomb potential V_{avg} is recovered far from the contact point and is a suitable reference potential.

Explicitly including this reference yields

$$\Delta\overline{V}_{FxE}(\mathbf{r}) = V(\mathbf{r}) - V_{avg} = \frac{1}{\varepsilon_0(1+\chi)}\int_{\Omega}\frac{\mathbf{P}_{FxE}(\mathbf{r}')\cdot(\mathbf{r}-\mathbf{r}')}{|\mathbf{r}-\mathbf{r}'|^3}\rho d\rho dz \tag{8.31}$$

Lastly, to use Eq. 8.31 we must know $\mathbf{P}_{FxE}$. Since we are assuming cubic materials symmetry, there will only be three independent flexoelectric coefficients: the longitudinal (μ_L), transverse (μ_T), and shear (μ_S) coefficients (Chapter 3). Taking these coefficients to be known quantities (in practice we use the DFT calculated coefficients, Chapter 4), the components of $\mathbf{P}_{FxE}$ in cylindrical coordinates assuming axial symmetry are

$$\begin{aligned} P_r &= \mu_L\epsilon_{rr,r} + \mu_T\left(\epsilon_{\theta\theta,r} + \epsilon_{zz,r}\right) + 2\mu_S\epsilon_{rz,z} \\ P_z &= \mu_L\epsilon_{zz,z} + \mu_T\left(\epsilon_{\theta\theta,z} + \epsilon_{rr,z}\right) + 2\mu_S\epsilon_{rz,r} \\ P_\theta &= 0 \end{aligned} \tag{8.32}$$

8.3.4. The Mean-Inner Potential Term

As described in Chapter 5, the potential change given by Eq. 8.31 is incomplete: the average Coulomb potential must be referenced to vacuum which requires knowing the change in the difference between the vacuum energy and average Coulomb potential (i.e. the MIP) with strain.

$$\varphi = \frac{d\left(V_{avg} - E_{vac}\right)}{d\epsilon} = \frac{d\overline{V}}{d\epsilon} \tag{8.33}$$

Values for φ in Eq. 8.33 are approximated from electron scattering factors (Chapter 5).

8.3.5. The Deformation Potential Term

The last term in Eq. 8.20 is the relative deformation potential of the CB and VB edges. The relative deformation potential is the change in the energy of band feature E_i with respect to the average Coulomb potential as a function of strain ϵ.

$$D_i = \frac{d\left(E_i - V_{avg}\right)}{d\epsilon} \tag{8.34}$$

Since we are neglecting shear effects, hydrostatic deformation potentials can be calculated using finite differences from DFT calculations on bulk structures with uniform volume expansions/compressions about the optimized lattice constant. Specifically, the hydrostatic deformation potential D_i, where i is some band feature such as the CB minimum, is given by

$$D_i \approx \frac{\left(E_i - V_{avg}\right)^+ - \left(E_i - V_{avg}\right)^-}{3\left(\epsilon^+ - \epsilon^-\right)} \tag{8.35}$$

E_i refers to the band feature and V_{avg} refers to the average Coulomb potential in the expanded $(+)$ and compressed $(-)$ strained structures. Examples of these calculations are reported in Table 8.1 where hydrostatic strains of $\pm 0.1\%$ have been used. DFT calculations were performed using WIEN2k [**145**] with the parameters given in Chapter 5.

	D_{VB} (eV)	D_{CB} (eV)
$SrTiO_3$	-15.6	-17.2
Si	-11.9	-10.2

Table 8.1. Hydrostatic deformation potentials for the CB minimum and VB maximum in STO and Si calculated with DFT. Values are given in eV.

8.3.6. Finite Element Contact Simulations

In Section 7.2 we used Hertz theory [**312**] to investigate flexoelectric effects during sphere-on-flat contact. In this section, we again focus on sphere-on-flat contact but use FEA calculations to determine deformation fields. FEA simulations are not only a more general approach than Hertz theory (which only provides strain fields for specific geometries), but also allow one to move past the Hertz theory approximations. For example, one of the fundamental assumptions of Hertz theory is that both contacting bodies can be treated as elastic half-spaces. From this assumption it follows that normal contact between two chemically identical bodies with different curvatures (e.g. a sphere contacting a flat made of the same material) will have identical strain fields, which is incorrect [**327**]. A detailed discussion of the parameters used in the finite element analysis of sphere-on-flat contact can be found in Appendix A. For our purposes, it is sufficient to understand that the strains and strain gradients entering Eq. 8.20 and 8.31 are readily computed from FEA simulations.

8.3.7. Summary

Quantitatively determining contact-induced band bending amounts to evaluating Eq. 8.20 for the specific contacting bodies. This involves computing three contributions:

(1) The change in the average Coulomb potential from bulk flexoelectric effect given by Eq. 8.31. Evaluating this expression requires materials parameters (i.e. flexoelectric coefficient and dielectric properties, which can be calculated from first principles [**58**], see Chapter 4) and strain fields (calculated with FEA, see Appendix A).

(2) The MIP contribution expressed as Eq. 8.33. This expression requires knowing f_{MIP} (estimated from electron scattering factors [**164**], see Chapter 5) and strain fields (calculated with FEA, see Appendix A).

(3) The deformation potential contribution shown in Eq. 8.34. This is approximated as the hydrostatic deformation potential of the VB and CB edge (calculated from first principles, see Section 8.3.5) and strain fields (calculated with FEA, see Appendix A).

8.4. Contact-Induced Band Bending: General Findings

8.4.1. Relative Strengths of the Flexoelectric, Mean-Inner Potential, and Deformation Potential Terms

To get a sense of the relative strengths of the three terms in Eq. 8.20, we explicitly consider them for the CB minimum in a flat STO sample deformed by a sphere with a contact pressure of 8 GPa. Figure 8.7 shows the flexoelectric term is largest near the contact radius and rapidly decays with distance. The MIP and deformation potential terms decay less rapidly with distance and are largest near the contact point; these properties follow from their dependence on strain and not strain gradient. For the pressures and geometry considered here, the MIP and deformation potential terms also largely cancel, although the extent of this cancellation is system dependent. The net effect of Eq. 8.20 is inhomogeneous band bending $\sim \pm 1$ V in the contact region, even for soft contact involving materials with modest flexoelectric properties such as STO.

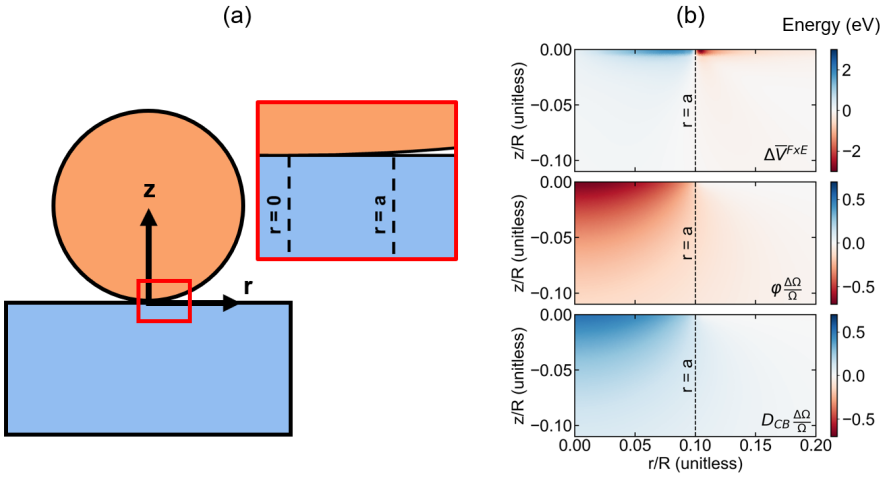

Figure 8.7. (a) Sphere-on-flat contact with coordinate system definition. (b) Change in the average Coulomb potential owing to flexoelectricity ($\Delta\overline{V}_{FxE}$), the MIP ($\varphi\frac{\Delta\Omega}{\Omega}$), and the CB minimum relative to the average Coulomb potential ($D_{CB}\frac{\Delta\Omega}{\Omega}$) in flat STO contacted by a sphere with a contact pressure of 8 GPa. Distances are normalized by the indenter radius R.

8.4.2. Pressure Dependence

In Section 8.2.4 it was shown that the electrostatic potential difference induced by Hertzian contact scaled as

$$V \sim f\left(\frac{F}{R^2 Y}\right)^{1/3} \tag{8.36}$$

where V is the electrostatic potential, f is the effective flexocoupling voltage, F is the applied force, R is the effective indenter radius, and Y is the effective modulus [**40**]. While Eq. 8.36 is useful for a specific experiment (e.g. applying a force using an indenter with a known radius), it is useful to generalize this expression in terms of contact pressure.

Substituting Eq. 8.10 and 8.11 into Eq. 8.36 yields

$$V \sim f\frac{a}{R} \sim f\frac{P}{Y} \tag{8.37}$$

This analysis maps the effects of different combinations of forces and indenter radii for a particular material onto a single curve.

Figure 8.8 depicts the change in the average Coulomb potential from bulk flexoelectricity at the surface of a STO flat contacted by a sphere as functions of a/R and P. While Eq. 8.37 is not exactly followed throughout the contact region (it strictly only applies for Hertzian contact), this data shows large, inhomogeneous band bending ($\sim \pm$ V) can be expected near the contact area and that the magnitude of band bending monotonically increases with contact pressure. The direction of band bending depends on the flexoelectric properties, but the bands tend to bend in opposite directions inside and outside the contact radius. Importantly, the band bending implied by Figure 8.8 is not limited to nanoscale features; it is possible in macroscopic features provided proportionately larger forces are applied.

8.4.3. Variations with Flexoelectric Coefficient

Now we isolate the effects of the relative size of the flexoelectric coefficients by calculating the bulk flexoelectric term in Eq. 8.31 for three fictitious materials which have two out of three flexoelectric coefficients set to zero and the remaining coefficient set to -10 nC/m. Figure 8.9 shows the results of this analysis for a flat contacted by a sphere with a contact pressure of 8 GPa. This analysis suggests that shear and transverse contributions dominate if the flexoelectric coefficients are of comparable magnitude.

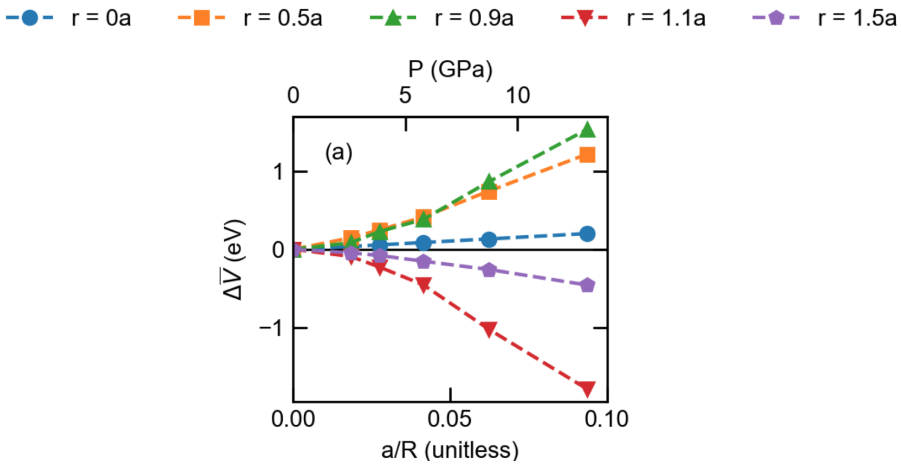

Figure 8.8. Change in the average Coulomb potential from flexoelectricity at the surface of a STO flat contacted by a sphere as a function of the ratio of the contact radius to indenter radius (a/R) and contact pressure (P). Colors/symbols correspond to different radial distances from the contact point.

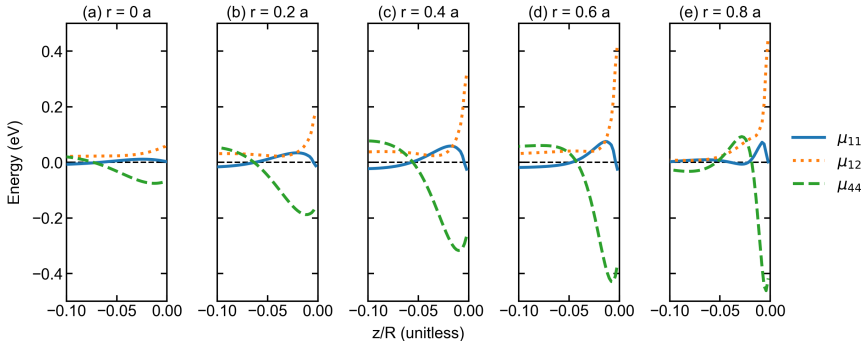

Figure 8.9. (a)-(e) Change in the average Coulomb potential owing to the bulk flexoelectric effect of a STO flat contacted by a sphere with a contact pressure of 6 GPa as a function of depth (normalized by the indenter radius R) at different radial distances (in units of the contact radius a) from the contact point. The three cases have μ_L=-10 nC/m,μ_T=μ_S=0 (blue, solid), μ_T=-10 nC/m,μ_L=μ_S=0 (orange, dotted), and μ_S=-10 nC/m,μ_L=μ_T=0 (green, dashed).

8.5. Contact-Induced Band Bending: Specific Examples

8.5.1. Dissimilar Materials: Contact Between a Si sphere and a $SrTiO_3$ Flat

We now utilize the framework developed above to explore contact-induced band bending for specific cases. First, we analyze contact between dissimilar materials using a Si sphere and STO flat as an example. Figure 8.10 shows the band bending at different radial distances from the contact point at a constant pressure of 6 GPa. Figure 8.11 shows the band bending at different contact pressures and a fixed radial distance. In both cases, spatially inhomogeneous band bending occurs in both the sphere and the flat. The band bending has the largest magnitude within the vicinity of the contact radius. Note, there are qualitative differences in the band bending profiles for the two materials because Si has larger shear contributions than STO (Section 8.4.3). This highlights how sensitive the spatial evolution of contact-induced band bending is to the flexoelectric coefficients.

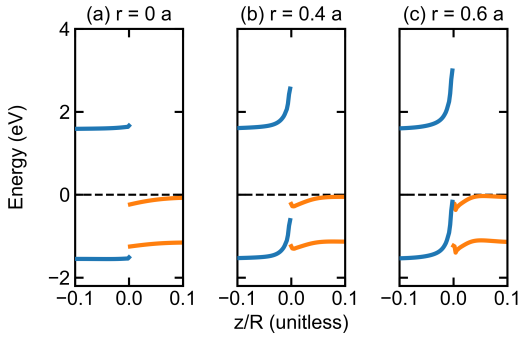

Figure 8.10. Contact band diagram for a Si sphere (orange) and STO flat (blue) with a contact pressure of 6 GPa. (a)-(c) show the CB minimum and VB maximum as a function of depth (normalized by the indenter radius R) at different radial distances (in units of the contact radius a) from the contact point as defined in Figure 8.7(a). The unstrained Fermi level of each material is assumed to be at its band gap center and zero energy is taken to be the unstrained STO Fermi level.

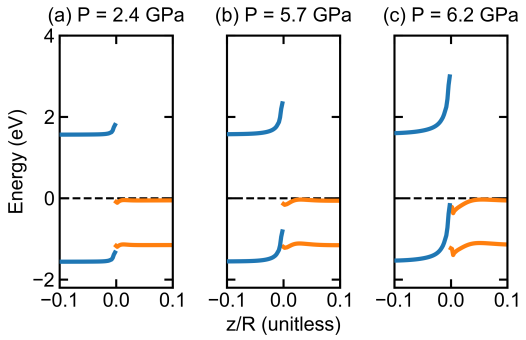

Figure 8.11. Contact band diagram for a Si sphere (orange) and STO flat (blue) at a fixed radial distance of $0.6a$ from the contact point as defined in Figure 8.7(a). (a)-(c) show the CB minimum and VB maximum as a function of depth (normalized by the indenter radius R) at different contact pressures for a fixed radial distance of 0.6a from the contact point as defined n Figure 8.7(a). The unstrained Fermi level of each material is assumed to be at its band gap center and zero energy is taken to be the unstrained STO Fermi level.

8.5.2. Similar Materials: Contact Between a $SrTiO_3$ sphere and a $SrTiO_3$ Flat

Next we consider the sphere-on-flat contact between two STO bodies. Although in the Hertzian limit there is no driving force for contact-deformation-driven charge transfer because contact between two chemically identical bodies is symmetric for all combinations of curvature [**312**], beyond Hertz theory there are differences between two bodies with different curvatures [**327**]. Contact between two chemically identical materials with different geometries is fundamentally important because it represents the minimal asymmetry between two bodies in which tribocharging should be possible [**283, 328**].

Figure 8.12 indicates the presence of asymmetric band bending across the contact interface between the two STO bodies. As was the case for contact between dissimilar

materials (e.g. Figure 8.10), the largest differences in band bending occur along the edge of the contact region. Under these simulation conditions, there would be some transfer of electrons from the sphere to the flat, assuming states were available.

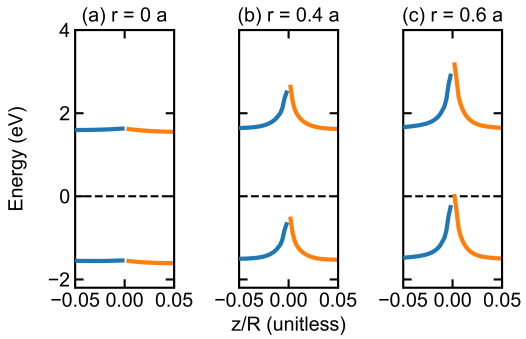

Figure 8.12. Contact band diagram for a STO sphere (orange) and STO flat (blue) with a contact pressure of 8 GPa. (a)-(c) show the CB minimum and VB maximum as a function of depth (normalized by the indenter radius R) at different radial distances (in units of the contact radius a) from the contact point as defined in Figure 8.7(a). The unstrained Fermi level of each material is assumed to be at its band gap center and taken to be zero energy.

8.6. Contact-Induced Band Bending: Implications for Charge Transfer

8.6.1. The Role of Trap States in Electron and Hole Transfer

Tribocharging between two metals is well understood by contact potential theory: the difference in work functions drives charge transfer until the Fermi level is the same everywhere [**287**]. It is generally accepted that contact potential theory cannot explain tribocharging in insulators because band gaps present too large an energy barrier for charge transfer [**285, 303, 329**]. The framework described above also indicates that work function differences alone are insufficient to explain charge transfer in insulators, but

shows how, through flexoelectricity, contact deformations sufficiently lower the energy barrier to enable charge transfer. In this sense, the flexoelectric model described above is a generalization of contact potential theory.

In the limit of no in-gap states our model predicts zero charge transfer below a contract pressure threshold (e.g. Figure 8.11(a)). Then as the pressure is increased some transfer will occur assuming states are available (e.g. hole transfer from the STO VB to the Si CB in Figure 8.11(b)). Once the contact pressure is sufficiently large, there will be direct transfer between bulk states on different bodies via Zener-tunneling (e.g. electrons will tunnel from the VB of STO into the CB of Si around the edge of the contact in Figure 8.11(c)). This indicates the sign of the charge transfer will change with contact pressure, which has been a well-known but unexplained experimental observation [**305, 293**]. Our model indicates this is a natural consequence of Zener-tunneling [**280**].

This type of band bending-driven charge transfer is reversible in an adiabatic limit, but in practice there will always be in-gap states which trap charge. Charge within trap states remains once the contacting bodies have returned to their original configurations, leaving the materials charged. Triboluminescence experiments directly confirm the relationship between trapped charges and triboelectricity [**330, 331**], and charge in trap states is known to have a long decay time [**332**]. Previous triboelectric models have also invoked the idea of non-equilibrium charge distributions in localized trap states during contact [**296, 297**], but the origin of the non-equilibrium distributions in these models has not been addressed. Our model indicates non-equilibrium charge distributions are a natural consequence of contact. Interestingly, the contact deformations may significantly increase the trapped charge densities beyond intrinsic amounts [**333**]: this can be thought of

as a mechanical analogue to the increase in trapped charge densities at semiconductor interfaces driven by applied electric potentials [**334**].

8.6.2. Band Bending Effects on Ion Transfer

There is also a large amount of experimental evidence that triboelectricity in insulators is linked to ion transfer [**283, 284**], often OH^- or H^+ [**335, 336, 292**]. These observations are readily incorporated into our framework since it is known that band bending at surfaces can drive adsorption [**337, 338**], although the relevant band banding for this charge transfer mechanism would be outside the contact radius. Figure 8.13 shows the band bending profiles associated with a Si sphere contacting a STO flat for radii larger than the contact radius. Figure 8.14 contains the analogous band bending profiles for contact between a STO sphere and STO flat. As with the band bending occurring within the contact radius, there are more significant band bending differences between dissimilar materials than similar materials. However, in both cases the band bending is substantial enough to drive ion transfer. Unlike the electron/hole charge transfer mechanisms described in Section 8.6.1, this charge transfer mechanisms would be largely irreversible on the time scale of contact because ionic motion is slow [**303**].

8.7. Contact-Induced Band Bending: Connections to Experiment

In Sections 8.2.5 we discussed a few qualitative connections to experiment, and in Section 8.6 we connected our model to some experimental observations such as the importance of trap states, the work function difference, and ion transfer. In this section we

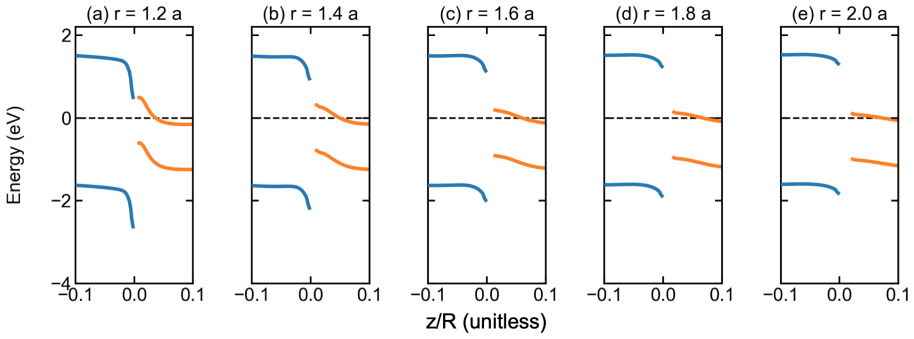

Figure 8.13. Contact band diagram for a Si sphere (orange) and STO flat (blue) with a contact pressure of 6 GPa. (a)-(e) show the CB minimum and VB maximum as a function of depth (normalized by the indenter radius R) at different radial distances (in units of the contact radius a) from the contact point as defined in Figure 8.7(a). The unstrained Fermi level of each material is assumed to be at its band gap center and zero energy is taken to be the unstrained STO Fermi level.

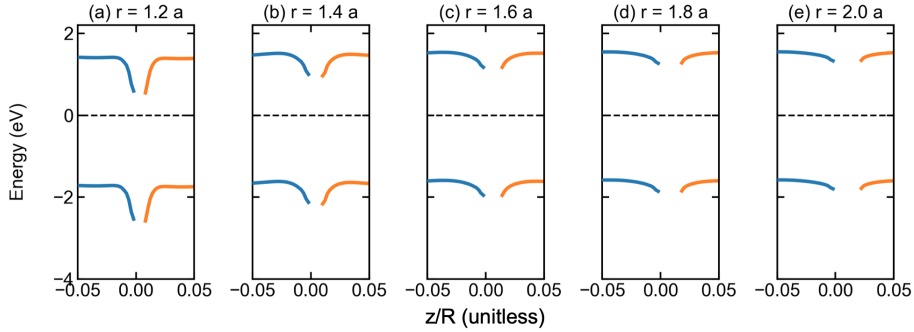

Figure 8.14. Contact band diagram for a STO sphere (orange) and STO flat (blue) with a contact pressure of 8 GPa. (a)-(e) show the CB minimum and VB maximum as a function of depth (normalized by the indenter radius R) at different radial distances (in units of the contact radius a) from the contact point as defined in Figure 8.7(a). The unstrained Fermi level of each material is assumed to be at its band gap center and taken to be zero energy.

explain how a wider set of experimental observations are consistent with the flexoelectric model for triboelectricity.

Charging between similar materials. One of the most mysterious aspects of triboelectricity has been charging between identical materials: chemically identical particles of different sizes tend to charge one another, with the relative size of the particles dictating the sign of the accumulated charge [**339, 340, 341, 333**]. This is explained by our model owing to the curvature-dependence of contact strain fields. Our model predicts the sign of charge accumulation on two chemically identical materials of different sizes is dictated by their relative size [**333**] and their flexoelectric properties.

Pressure dependence. The sign and magnitude of charge transfer is known to change with contact pressure [**305, 293**]. This is explained by our model through the pressure-dependent onset of Zener-tunneling, e.g. Figure 8.11, and our results suggest the pressure threshold for a sign change will depend on numerous properties of the two materials in contact (e.g. flexoelectric coefficients, band gap, surface treatments, etc.).

Temperature dependence. It has been observed that as temperature increases, triboelectric charging decreases and exhibits an exponential decay at high temperatures [**342, 343**]. The statistical occupation of states (i.e. the Fermi-Dirac distribution) accounts for these temperature dependences. It also possible to expand our model to include other temperature-related band structure effects, like Thomson/Seebeck effects [**283, 342**], which may contribute during rubbing.

Dielectric constant. Some experiments indicate the amount of charge transferred during triboelectric processes is proportional to the dielectric constant, whereas others suggest the dielectric constant has no influence [**344, 345, 290**]. This discrepancy in the literature can be attributed to the surface sensitivity of the flexoelectric coefficient (Chapter 5): there is a dielectric constant dependence in Eq. 8.31, but the detailed band bending will

depend on the flexoelectric coefficient which is surface-sensitive. Related to the role of dielectric constants in triboelectricity, it has been observed that dielectric breakdown strength is reduced by contact pressure [**346**]. This is explained with our model through pressure-dependent band bending.

Velocity dependence. Measurements of triboelectricity in particles typically focus on the velocity-dependence of impact charge (the amount of charge transferred from impact for an initially uncharged sample). This velocity dependence is attributed to changes in contact area [**300**], which is included in our model through its description of how band bending, the charge transfer driver, varies with contact area.

Triboluminescence, fractoluminescence, and fractoelectrification. It has been observed that light can be emitted when two materials are rubbed together and that fracture can be accompanied by light emission or charging [**330, 331, 347**]. Large flexoelectric fields are known to be associated with fracture [**47, 31**]. These fields can induce charge transfer and/or light emission associated with recombination of charge trapped in in-gap states through the band bending mechanisms described in this chapter.

CHAPTER 9

Summary and Future Directions

9.1. Summary

This dissertation has explored the flexoelectric effect and its implications using a combined experimental and theoretical approach. After introducing flexoelectricity and the basic features of flexoelectric characterization in Chapters 1 and 2, I provide a method to generate expressions for the effective flexoelectric coefficient measured in TPB for crystals of arbitrary symmetry and orientation in terms of independent flexoelectric tensor components, elastic constants, and geometric factors. In doing so, I also treat the partial suppression of anticlastic bending in TPB and quantify the accuracy of utilizing Euler-Bernoulli beam theory in these contexts. Using this flexoelectric characterization framework, I measure and interpret the flexoelectric response of a range of commercially available single crystal oxides in Chapter 3. These measurements not only significantly increase the number of materials in which the flexoelectric effect has been experimentally studied, but also raise new questions for the community related to the observation that low dielectric constant materials tend to have large flexocoupling voltages which exceed nominal expectations.

First principles calculations offer a means to elucidate the structural origins of flexoelectric coefficients, including those I measured in Chapter 3, and progress towards flexoelectric design rules. In Chapter 4 I summarize the first principles theory of bulk flexoelectricity and describe how I utilize this theory to perform ab initio calculations of bulk flexoelectric coefficients using WIEN2k. As an example, I calculate the bulk flexoelectric coefficients of STO and examine the impact of the exchange and correlation functional on these coefficients. These are the first complete calculations of bulk flexoelectric coefficients using an all-electron code and the first investigation of the impact of the exchange and correlation functional on bulk flexoelectric coefficients, making these calculations a benchmark for future work. I also calculate the flexoelectric coefficients in the (pseudo) cubic oxides measured in Chapter 3 to explore the importance of materials chemistry and compare the flexoelectric coefficients predicted by first principles theory with measurements. These calculations reproduce the well-known disparity between predicted and measured flexoelectric coefficients.

To address this disparity, I investigate the role of surfaces in flexoelectricity. Among the many subtleties associated with the flexoelectric effect, the seemingly disproportionate impact of surfaces is perhaps the most counter-intuitive. I demonstrate in Chapter 5 that the surface sensitivity of flexoelectricity follows naturally from considering the strain derivative of the MIP. Reframing the problem in the language of the MIP also leads to a method to estimate this contribution to the total flexoelectric response using electron scattering factors. The efficacy of using electron scattering factors in this context is assessed through DFT calculations I perform on a range of low energy surfaces from archetypal ionic, covalent, and mixed ionic-covalent systems. This also demonstrates the

total flexoelectric response of a finite sample is surface sensitive owing to the impact of surface chemistry, structure, and adsorbates on the strain derivative of the MIP. I show there are sizable differences in the total flexoelectric response of samples with nominally similar surfaces. Including this contribution to the total flexoelectric response with the bulk flexoelectric coefficients calculated in Chapter 4 leads to good agreement with STO and KTO measurements I presented in Chapter 3.

Although experiments and calculations on single crystals are important for furthering the fundamental science of flexoelectricity, flexoelectric applications will likely utilize engineering materials which are often defective. Therefore, it is important to move beyond flexoelectricity in single crystals and ascertain extrinsic contributions to flexoelectricity originating from defects. I present three case studies in Chapter 6 which indicate the total flexoelectric response is substantially modified by defects. First, I demonstrate flexoelectricity in LAO is mediated by TBs which have flexoelectric coefficients $\sim$10 C/m and are likely polar. Then, I show that doping STO with Nb leads to a 10^3 times enhancement in the flexoelectric response over undoped STO. Lastly, I find the flexoelectric response of MgO greatly surpasses ab initio flexoelectric coefficients even with the MIP contribution. Together, these experiments demonstrate that extrinsic contributions can overshadow intrinsic contributions to flexoelectric responses and emphasize the need to combine flexoelectric characterization with other materials characterization techniques to interpret measured flexoelectric coefficients.

Chapter 7 includes my work on the bulk electronic structure, atomic and electronic surface structure, charging, and flexoelectric bending in the lanthanide scandates, and demonstrates these materials are a rich playground owing to their complex atomic and

electronic structure. First, I address the role of the 4f states in the bulk VB of GSO, DSO, and TSO through a combination of experimental XPS and UPS VB characterization with ab initio calculations. Then, I discuss solving the (110) surface of DSO and provide experimental evidence for the atomic and electronic structure of the lowest energy surface predicted by DFT calculations. Lastly, I explain how large charging occurs in the lanthanide scandates, why it is unavoidable, and how it leads to large flexoelectric bending.

Chapeter 8 includes my work investigating the connection between flexoelectricity and triboelectricity. I put forward the argument that triboelectric charge transfer is thermodynamically driven by electric fields induced through the flexoelectric effect by the large strain gradients present at asperities during contact. First, I develop a simplified flexoelectric model for triboelectricity based upon Hertzian contact which captures much of the underlying physics and I demonstrate predictions from this model are in qualitative agreement with many experimental observations. After I generalize the model to incorporate band structure and treat contact-induced band bending effects for two arbitrary materials in contact, I explore the implications of this framework for some specific contact cases and explain how contact-induced band bending relates to well-known charge transfer mechanisms and experimental triboelectric observations which have historically escaped explanation.

9.2. Future Directions

Now I discuss some possible future directions based upon the work described in this dissertation.

9.2.1. Experimental Flexoelectric Characterization

A TPB approach was used for flexoelectric characterization throughout this dissertation, but to characterize flexoelectricity in smaller samples and improve the accuracy and precision of flexoelectric coefficient measurements, it will be useful to modify this approach. Characterizing flexoelectricity in smaller samples requires moving past bending geometries. One possibility is to use conducting AFM to extract flexoelectric coefficients from the changes in transport properties caused by AFM tip-sample contact (see Section 9.2.5 below), but it is also possible to perform DMA-based flexoelectric measurements on smaller samples using alternative sample geometries like truncated pyramid compression. Although truncated pyramid compression measurements has been used to characterize flexoelectricity in some polymers and ferroelectric ceramic systems [**10, 11, 43**], it will be important to demonstrate that the flexoelectric coefficients measured with different methods on the same material (e.g. the flexoelectric response of STO single crystals from TPB and truncated pyramid compression) are consistent before the truncated pyramid compression method can be adopted to investigate new materials.

To improve the accuracy and precision of flexoelectric characterization, it would be advantageous to implement a four-point bending approach to flexoelectric characterization. Although a four-point bending geometry is more technically challenging than TPB, it has the benefit of providing a constant strain gradient between the two knife edges at the sample center [**56**]. This means it would not be necessary to average the linear strain gradient profile in TPB to compute the effective flexoelectric coefficient, which will improve the accuracy of flexoelectric measurements. Additionally, combining four-point bending with patterned electrodes over the region which has a nominally constant strain

gradient would provide a way to easily check for variations in the flexoelectric coefficient, investigate the importance of surface treatments on different portions of the sample, and assess the importance of the electrode-sample contact on a single sample. It would also be an interesting experiment to use patterned electrodes with TPB to measure local variations in the flexoelectric polarization which are suggested by the TPB strains shown, for example, in Figure 3.7. Experiments with patterned electrodes should first be attempted on materials with large flexoelectric coefficients (e.g. ferroelectric single crystals like BTO which have μ ~1-10 μC/m [**53**]) since the reduction in electrode area will decrease the magnitude of the short-circuit current.

9.2.2. First Principles Calculations of Flexoelectric Coefficients

The calculations presented in Chapters 4 and 5 indicated good agreement between the predicted and measured flexoelectric responses of cubic perovskites once the mean-inner potential term was accounted for, but there was still poor agreement for non-cubic perovskites. This discrepancy was attributed to neglecting lattice-quadrupole contributions which may be sizable. It is computationally taxing to calculate lattice-quadrupole terms using the supercell approach adopted in Chapter 4, but these terms can be readily calculated with the DFPT approach which has been recently implemented in ABINIT [**140, 139**]. After comparing the flexoelectric coefficients predicted by the DFPT approach in ABINIT and the supercell approach in WIEN2k using a standard material like STO, it would be interesting to use ABINIT to compute the complete flexoelectric response for R$\bar{3}$c LAO, Pnma DSO, and Pnma YAO to determine if the lattice-quadrupole

contributions are responsible for the large flexocoupling voltages. I suspect the lattice-quadrupole terms will be large, particularly in the Pnma perovskites since they will contain contributions from the anti-polar A-site displacements [**117**].

Another future direction regarding the first principles calculations of flexoelectric coefficients concerns computing electronic contributions to flexoelectric coefficients from the ground state charge density. As indicated in Chapter 4, dynamic octupolar moments are equivalent to static quadrupolar moments [**137**], which suggests electronic contributions to flexoelectric coefficients can be obtained from bulk unit cells alone without the need for the supercell approach. This would be immensely more efficient than the approach used in Chapter 4 and should be assessed in simple crystals (e.g. MgO and STO). It is also possible that the other dynamical moments contributing to the lattice-dipole and lattice-quadrupole terms could be obtained in a similar fashion.

9.2.3. The Role of Surfaces in Piezoelectricity

The treatment of the MIP contribution in Chapter 5 is theoretically sound and has indirect experimental support (e.g. comparison with the STO and KTO measurements), but requires direct experimental confirmation. Kelvin probe microscopy (KPM) would be an ideal method to experimentally measure the MIP contribution to flexoelectricity. KPM measures the local work function using a scanning probe tip [**348**] and, according to Chapter 5, the surface-specific component of the MIP contribution to the flexoelectric response is essentially the strain derivative of the work function. Therefore, by constructing (or purchasing) a sample holder capable of subjecting a sample to uniform strain and measuring the change in work function with KPM, it should be possible to directly

measure this flexoelectric contribution. This quantity (measured for suitable sample orientations and types of strain) can be combined with the effective flexoelectric coefficient measured with TPB (for a sample with a sufficiently similar surface) to isolate the bulk flexoelectric coefficient. The difference between these measurements should be directly comparable to the sum of the ab initio-calculated bulk flexoelectric coefficient [**58**] and f_{MIP}^{bulk} defined in Chapter 5). After establishing the efficacy of this approach for simple materials and surfaces, it would be ideal to work with thin film growers to perform this experiment on samples with well-defined surface chemistries and determine the extent to which the flexoelectric response can be tuned by surface treatments.

9.2.4. Extrinsic Contributions to Flexoelectricity

The experiments reported in Chapter 6 on Nb-doped STO and MgO indicate extrinsic contributions to flexoelectricity are substantial, but experiments meant to deduce the origin of these observations were unable to be performed owing to the COVID-19 pandemic. Regarding MgO, structural characterization with XRD indicated samples possessed large, high crystallinity grains. Although it is unlikely that the number of grain boundaries alone is sufficient to account for the enhanced flexoelectric response, it is possible that there is residual strain in the sample (e.g. from sample processing at the manufacturer) which could be affecting the flexoelectric response. The existence of strain should be checked with additional XRD (e.g. reciprocal space maps). Chemical characterization (e.g. with XPS and inductively coupled plasma spectroscopy) should also be performed to make sure point defect concentrations are not substantial. Although the large flexoelectric response

in MgO could stem from the grain boundaries or point defects, I suspect it will be important to investigate the role of adsorbed water. It is well documented that MgO has a proclivity for water adsorption (e.g., [**349**])and if one takes the experimentally measured MIP [**350**] and dielectric constant of water and assumes that a water monolayer acts as a thin film that will strain with the underlying substrate, then according to the framework in Chapter 5, a water monolayer can yield a substantial effective flexoelectric coefficient through the MIP term. It would be an interesting experiment to compare the flexoelectric response across a series of hydrated MgO samples in which the amount of adsorbed water is known (e.g. with XPS) and sample topography is characterized (e.g. with AFM).

Regarding the enhanced flexoelectric response in doped STO, a primary goal of future experiments should be to demonstrate the relationship between μ_{eff} and sample thickness predicted by Eq. 6.33 [**172, 114**]. This would provide the clearest evidence for the barrier-layer mechanism, although care should be taken to make sure the samples have comparable surfaces (chemistry, roughness, etc.) if polishing is used to thin samples. After this has been established, the surface piezoelectric coefficient from these measurements and the strain derivative of the work function measured with KPM (Section 9.2.3) should be used to determine the thickness of the near-surface region responsible for the barrier-layer enhancement through Eq. 6.42. It would also be interesting to measure the flexoelectric response as a function of doping concentration to determine the critical doping density at which there are insufficient carriers to screen the bulk flexoelectric effect and the barrier-layer mechanism is no longer effective. This would provide operating guidelines for those wishing to utilize barrier-layer flexoelectrics for applications.

9.2.5. Flexoelectricity and Triboelectricity

The band bending induced by contact deformations described in Chapter 8 are most readily probed using conductive AFM experiments. In this type of experiment, IV curves are measured by a conductive AFM tip as a function of tip force. Changes in the IV curves at different tip forces provide a direct, local measure of the deformation-induced band bending established in Chapter 8 and should allow for the extraction of flexoelectric coefficients. Preliminary results from experiments on Nb-doped STO conducted by Karl Olson clearly indicate the presence of contact-deformation induced band bending with $F^{1/3}$ scaling, but it has not yet been possible to extract flexoelectric coefficients. Once established, this method will enable the measurement of flexoelectric coefficients in smaller samples (e.g. crystals grown by researchers which are not commercially available) and also unconventional flexoelectric samples such as powders.

9.3. Closing Comments

The flexoelectric effect is a pervasive phenomenon which imbues insulators of any symmetry with electromechanical functionality. Though it is tempting to treat flexoelectricity as a simple extension of piezoelectricity, it has become increasingly apparent that this approach glosses over important subtleties which make the flexoelectric effect distinct from both fundamental science and applications perspectives. Using a combined experimental and theoretical approach in this dissertation, I show how to measure flexoelectric coefficients and interpret them in terms of first principles quantities. In doing so, I also demonstrate the total flexoelectric response of a finite sample is particularly sensitive to surfaces (through the strain derivative of the mean-inner potential) and defects (such as

twin boundaries). This offers enticing, new opportunities to tune flexoelectric properties through defect and surface engineering. The latter is particularly intriguing, as it suggests the applicability of surface science (such as my work on the lanthanide scandates) beyond traditional research domains like thin film growth and catalysis. Lastly, I establish the existence of large inhomogeneous band bending during contact owing to flexoelectric couplings, which I argue serves as the thermodynamic driver for triboelectric charge transfer. By suggesting triboelectricity and flexoelectricity are intimately linked, this work makes significant strides towards a priori predictions of triboelectric charge transfer between insulators and a first principles theory of triboelectricity.

References

[1] J. Curie and P. Curie, Bulletin de la Société minéralogique de France **3**, 90 (1880).

[2] J. Curie and P. Curie, Journal de Physique Théorique et Appliquée **1**, 245 (1882).

[3] S. Trolier-Mckinstry, S. Zhang, A. J. Bell, and X. Tan, Annual Review of Materials Research **48**, 191 (2018).

[4] R. M. Martin, Physical Review B **5**, 1607 (1972).

[5] D. Vanderbilt, Journal of Physics and Chemistry of Solids **61**, 147 (2000).

[6] P. S. Halasyamani and K. R. Poeppelmeier, Chemistry of Materials **10**, 2753 (1998).

[7] M. D. Maeder, D. Damjanovic, and N. Setter, Journal of Electroceramics **13**, 385 (2004).

[8] J. Nye, *Physical Properties of Crystals*, Oxford University Press, Oxford, 1985.

[9] R. E. Newnham, *Properties of Materials: Anistropy, Symmetry, Structure*, Oxford University Press, Oxford, 2005.

[10] P. Zubko, G. Catalan, and A. K. Tagantsev, Annual Review of Materials Research **43**, 387 (2013).

[11] P. V. Yudin and A. K. Tagantsev, Nanotechnology **24**, 432001 (2013).

[12] V. Mashkevich and K. Tolpygo, Journal of Experimental and Theoretical Physics **5**, 435 (1957).

[13] E. V. Bursian and O. I. Zaikovskii, Soviet Physics - Solid State **10**, 1121 (1968).

[14] W. Ma and L. E. Cross, Applied Physics Letters **78**, 2920 (2001).

[15] W. Ma and L. E. Cross, Applied Physics Letters **81**, 3440 (2002).

[16] W. Ma and L. E. Cross, Applied Physics Letters **82**, 3293 (2003).

[17] W. Ma and L. E. Cross, Applied Physics Letters **86**, 072905 (2005).

[18] W. Ma and L. E. Cross, Applied Physics Letters **88**, 232902 (2006).

[19] M. Gharbi, Z. H. Sun, P. Sharma, and K. White, Applied Physics Letters **95**, 142901 (2009).

[20] C. R. Robinson, K. W. White, and P. Sharma, Applied Physics Letters **101**, 122901 (2012).

[21] G. Catalan, L. J. Sinnamon, and J. M. Gregg, Journal of Physics: Condensed Matter **16**, 2253 (2004).

[22] M. S. Majdoub, R. Maranganti, and P. Sharma, Physical Review B **79**, 115412 (2009).

[23] D. Lee et al., Advanced Materials **26**, 5005 (2014).

[24] F. Vasquez-Sancho, A. Abdollahi, D. Damjanovic, and G. Catalan, Advanced Materials **30**, 1705316 (2018).

[25] R. Núñez-Toldrà, F. Vasquez-Sancho, N. Barroca, and G. Catalan, Scientific Reports **10**, 254 (2020).

[26] T. D. Nguyen et al., Advanced Materials **25**, 946 (2013).

[27] P. Koirala, C. A. Mizzi, and L. D. Marks, Nano Letters **18**, 3850 (2018).

[28] G. Catalan et al., Nature Materials **10**, 963 (2011).

[29] D. Lee et al., Physical Review Letters **107**, 057602 (2011).

[30] P. Gao et al., Physical Review Letters **120**, 267601 (2018).

[31] H. Wang et al., Nano Letters **20**, 88 (2020).

[32] J. Očenášek et al., Physical Review B **92**, 35417 (2015).

[33] H. Lu et al., Science **336**, 59 (2012).

[34] Q. Deng, M. Kammoun, A. Erturk, and P. Sharma, International Journal of Solids and Structures **51**, 3218 (2014).

[35] X. N. Jiang, W. B. Huang, and S. J. Zhang, Nano Energy **2**, 1079 (2013).

[36] W. B. Huang, S. R. Yang, N. Y. Zhang, F. G. Yuan, and X. N. Jiang, Experimental Mechanics **55**, 313 (2015).

[37] U. K. Bhaskar et al., Nature Nanotechnology **11**, 263 (2016).

[38] K. D. Breneman, W. E. Brownell, and R. D. Rabbitt, PLoS ONE **4** (2009).

[39] A. G. Petrov, Analytica Chimica Acta **568**, 70 (2006).

[40] C. A. Mizzi, A. Y. W. Lin, and L. D. Marks, Physical Review Letters **123**, 116103 (2019).

[41] S. M. Kogan, Soviet Physics - Solid State **5**, 2069 (1964).

[42] T. D. Nguyen, S. Mao, Y. W. Yeh, P. K. Purohit, and M. C. McAlpine, Advanced Materials **25**, 946 (2013).

[43] B. Wang, Y. Gu, S. Zhang, and L. Q. Chen, Progress in Materials Science **106**, 100570 (2019).

[44] R. E. Newnham, V. Sundar, R. Yimnirun, J. Su, and Q. M. Zhang, Journal of Physical Chemistry B **101**, 10141 (1997).

[45] M. Stengel, N. A. Spaldin, and D. Vanderbilt, Nature Physics **5**, 304 (2009).

[46] X. Wu, D. Vanderbilt, and D. R. Hamann, Physical Review B **72**, 035105 (2005).

[47] A. Abdollahi et al., Physical Review B **92**, 094101 (2015).

[48] K. Cordero-Edwards, H. Kianirad, C. Canalias, J. Sort, and G. Catalan, Physical Review Letters **122**, 135502 (2019).

[49] A. Abdollahi, F. Vásquez-Sancho, and G. Catalan, Physical Review Letters **121**, 205502 (2018).

[50] A. Abdollahi, N. Domingo, I. Arias, and G. Catalan, Nature Communications **10**, 1266 (2019).

[51] N. A. Pertsev, A. K. Tagantsev, and N. Setter, Physical Review B **61**, R825(R) (2000).

[52] P. Zubko, G. Catalan, A. Buckley, P. R. L. Welche, and J. F. Scott, Physical Review Letters **99**, 167601 (2007).

[53] J. Narvaez, S. Saremi, J. Hong, M. Stengel, and G. Catalan, Physical Review Letters **115**, 037601 (2015).

[54] L. Landau and E. Lifshitz, *Theory of Elasticity*, Pergamon Press, Elmsford, New York, 1986.

[55] A. Love, *A Treatise on the Mathematical Theory of Elasticity*, Dover Publications, New York, 1944.

[56] S. Timoshenko and J. Goodier, *Theory of Elasticity*, McGraw-Hill, New York, 1970.

[57] P. W. Voorhees and W. C. Johnson, Solid State Physics **59**, 1 (2004).

[58] J. Hong and D. Vanderbilt, Physical Review B **88**, 174107 (2013).

[59] M. Stengel, Physical Review B **88**, 174106 (2013).

[60] W. Schranz, Phase Transitions **64**, 103 (1997).

[61] E. K. H. Salje and W. Schranz, Zeitschrift fur Kristallographie **226**, 1 (2011).

[62] F. F. Balakirev, S. M. Ennaceur, R. J. Migliori, B. Maiorov, and A. Migliori, Review of Scientific Instruments **90**, 121401 (2019).

[63] A. Zevalkink et al., Applied Physics Reviews **5**, 021303 (2018).

[64] J. G. Dil, Reports on Progress in Physics **45**, 285 (1982).

[65] K. P. Menard and N. R. Menard, Dynamic Mechanical Analysis in the Analysis of Polymers and Rubbers, in *Encyclopedia of Polymer Science and Technology*, number 9, pages 1–33, Wiley, 2015.

[66] R. J. Harrison and S. A. Redfern, Physics of the Earth and Planetary Interiors **134**, 253 (2002).

[67] R. Resta, Journal of Physics: Condensed Matter **22**, 123201 (2010).

[68] N. A. Spaldin, Journal of Solid State Chemistry **195**, 2 (2012).

[69] R. D. King-Smith and D. Vanderbilt, Physical Review B **47**, 1651(R) (1993).

[70] R. Resta, Europhysics Letters **22**, 133 (1993).

[71] D. Vanderbilt and R. D. King-Smith, Physical Review B **48**, 4442 (1993).

[72] M. Meade, *Lock-in Amplifiers: Principles and Applications*, Peregrinus, London, 1983.

[73] D. J. Griffiths, *Introduction to Electrodynamics*, Cambridge University Press, Cambridge, 2017.

[74] M. Stengel, Physical Review B **90**, 201112 (2014).

[75] C. A. Mizzi, B. Guo, and L. D. Marks, Physical Review Materials **In Review**, arXiv:1911.02634 (2021).

[76] L. Shu, X. Wei, T. Pang, X. Yao, and C. Wang, Journal of Applied Physics **110**, 104106 (2011).

[77] H. Le Quang and Q.-C. He, Proceedings of the Royal Society A: Mathematical, Physical and Engineering Sciences **467**, 2369 (2011).

[78] G. Searle, *Experimental Elasticity*, Cambridge University Press, Cambridge, 1933.

[79] S. K. Kaldor and I. C. Noyan, Applied Physics Letters **80**, 2284 (2002).

[80] S. K. Kaldor and I. C. Noyan, Materials Science and Engineering A **399**, 64 (2005).

[81] K. W. Wojciechowski, Computational Methods in Science and Technology **11**, 73 (2005).

[82] B. Szabo and I. Babuska, *Introduction to Finite Element Analysis: Formulation, Verification and Validation*, Wiley, Hoboken, 2011.

[83] D. G. Ashwell, The Journal of the Royal Aeronautical Society **54**, 708 (1950).

[84] R. J. Pomeroy, International Journal of Solids and Structures **6**, 277 (1970).

[85] Y. A. Abramov, V. G. Tsirelson, V. E. Zavodnik, S. A. Ivanov, and I. D. Brown, Acta Crystallographica Section B **51**, 942 (1995).

[86] E. A. Zhurova, Y. Ivanov, V. Zavodnik, and V. Tsirelson, Acta Crystallographica Section B **56**, 594 (2000).

[87] A. M. Glazer, Acta Crystallographica Section B **28**, 3384 (1972).

[88] K. Van Benthem, C. Elsässer, and R. H. French, Journal of Applied Physics **90**, 6156 (2001).

[89] G. E. Jellison, I. Paulauskas, L. A. Boatner, and D. J. Singh, Physical Review B **74**, 155130 (2006).

[90] H. E. Weaver, Journal of Physics and Chemistry of Solids **11**, 274 (1959).

[91] D. Kahng and S. H. Wemple, Journal of Applied Physics **36**, 2925 (1965).

[92] S. E. Rowley et al., Nature Physics **10**, 367 (2014).

[93] J. F. Schooley, W. R. Hosler, and M. L. Cohen, Physical Review Letters **12**, 474 (1964).

[94] K. Ahadi et al., Science Advances **5**, 1 (2019).

[95] C. Liu et al., Science **371**, 716 (2021).

[96] H. D. Megaw and C. N. W. Darlington, Acta Crystallographica Section A **31**, 161 (1975).

[97] S. A. Hayward et al., Physical Review B **72**, 054110 (2005).

[98] J. M. Phillips, Journal of Applied Physics **79**, 1829 (1996).

[99] A. Ohtomo and H. Y. Hwang, Nature **427**, 423 (2004).

[100] B. E. Park and H. Ishiwara, Applied Physics Letters **79**, 806 (2001).

[101] P. Delugas, V. Fiorentini, and A. Filippetti, Physical Review B **71**, 134302 (2005).

[102] S. Bueble, K. Knorr, E. Brecht, and W. W. Schmahl, Surface Science **400**, 345 (1998).

[103] S. Bueble and W. W. Schmahl, Materials Structure **6**, 140 (1999).

[104] R. J. Harrison, S. A. T. Redfern, and E. K. H. Salje, Physical Review B **69**, 144101 (2004).

[105] K. Aizu, Physical Review B **2**, 754 (1970).

[106] J. Sapriel, Physical Review B **12**, 5128 (1975).

[107] E. K. Salje et al., Scientific Reports **6**, 27193 (2016).

[108] H. Yokota, S. Matsumoto, E. K. Salje, and Y. Uesu, Physical Review B **98**, 104105 (2018).

[109] H. Yokota et al., Physical Review B **102**, 104117 (2020).

[110] F. Zhang et al., Physical Review Letters **122**, 257601 (2019).

[111] S. D. Mo and W. Y. Ching, Physical Review B **51**, 13023 (1995).

[112] R. A. Parker, Physical Review **124**, 1719 (1961).

[113] A. L. Linsebigler, G. Lu, and J. T. Yates, Chemical Reviews **95**, 735 (1995).

[114] J. Narvaez, F. Vasquez-Sancho, and G. Catalan, Nature **538**, 219 (2016).

[115] F. J. Maier et al., Acta Materialia **190**, 124 (2020).

[116] M. W. Lufaso and P. M. Woodward, Acta Crystallographica Section B **57**, 725 (2001).

[117] N. A. Benedek and C. J. Fennie, Journal of Physical Chemistry C **117**, 13339 (2013).

[118] M. Schmidbauer, A. Kwasniewski, and J. Schwarzkopf, Acta Crystallographica Section B **68**, 8 (2012).

[119] S. Geller and E. A. Wood, Acta Crystallographica **9**, 563 (1956).

[120] M. Raekers et al., Physical Review B **79**, 125114 (2009).

[121] X. Ke et al., Applied Physics Letters **94**, 152503 (2009).

[122] S. Kamba et al., Phase Transitions **86**, 206 (2013).

[123] R. Diehl and G. Brandt, Materials Research Bulletin **10**, 85 (1975).

[124] V. V. Afanas'ev et al., Applied Physics Letters **85**, 5917 (2004).

[125] S. Coh et al., Physical Review B **82**, 064101 (2010).

[126] S.-Y. Cho, I.-T. Kim, and K. S. Hong, Journal of Materials Research **14**, 114 (1999).

[127] J. H. Haeni et al., Nature **430**, 758 (2004).

[128] A. K. Tagantsev, Physical Review B **34**, 5883 (1986).

[129] P. V. Yudin, R. Ahluwalia, and A. K. Tagantsev, Applied Physics Letters **104**, 082913 (2014).

[130] A. Askar, P. C. Lee, and A. S. Cakmak, Physical Review B **1**, 3525 (1970).

[131] P. Lawaetz, Physical Review **183**, 730 (1969).

[132] C. G. Van De Walle and R. M. Martin, Physical Review Letters **62**, 2028 (1989).

[133] R. Resta, L. Colombo, and S. Baroni, Physical Review B **41**, 12358 (1990).

[134] R. Resta, Physical Review B **44**, 11035 (1991).

[135] R. Resta, Physical Review Letters **105**, 127601 (2010).

[136] J. Hong and D. Vanderbilt, Physical Review B **84**, 180101 (2011).

[137] M. Stengel, Nature Communications **4**, 2693 (2013).

[138] C. E. Dreyer, M. Stengel, and D. Vanderbilt, Physical Review B **98**, 075153 (2018).

[139] A. H. Romero et al., Journal of Chemical Physics **152**, 124102 (2020).

[140] M. Royo and M. Stengel, Physical Review X **9**, 21050 (2019).

[141] M. Springolo, M. Royo, and M. Stengel, arXiv , 2010.08470 (2020).

[142] P. Ghosez, J.-P. Michenaud, and X. Gonze, Physical Review B **58**, 6224 (1998).

[143] H. B. Callen, Physical Review **76**, 1394 (1949).

[144] M. Born and K. Huang, *Dynamical Theory of Crystal Lattices*, University Press, Oxford, 1968.

[145] P. Blaha et al., Journal of Chemical Physics **152**, 074101 (2020).

[146] D. J. Singh and L. Nordstrom, *Planewaves, Pseudopotentials and the LAPW Method*, Springer US, 2006.

[147] S. Cottenier, *Density Functional Theory and the Family of (L)APW-methods: a step-by-step introduction*, 2 edition, 2013.

[148] J. P. Perdew and Y. Wang, Physical Review B **45**, 13244 (1992).

[149] S. J. Ahmed et al., Computer Physics Communications **184**, 647 (2013).

[150] A. K. Tagantsev and P. V. Yudin, *Flexoelectricity in Solids*, World Scientific, 2016.

[151] J. P. Perdew, K. Burke, and M. Ernzerhof, Physical Review Letters **77**, 3865 (1996).

[152] J. P. Perdew et al., Physical Review Letters **100**, 136406 (2008).

[153] P. Novak, J. Kunes, L. Chaput, and W. E. Pickett, physica status solidi (b) **243**, 563 (2006).

[154] F. Tran, P. Blaha, K. Schwarz, and P. Novák, Physical Review B **74**, 155108 (2006).

[155] U. Aschauer and N. A. Spaldin, Journal of Physics: Condensed Matter **26**, 122203 (2014).

[156] P. Ghosez, X. Gonze, P. Lambin, and J. P. Michenaud, Physical Review B **51**, 6765 (1995).

[157] F. Labat, P. Baranek, C. Domain, C. Minot, and C. Adamo, Journal of Chemical Physics **126** (2007).

[158] S. Piskunov, E. Heifets, R. I. Eglitis, and G. Borstel, Computational Materials Science **29**, 165 (2004).

[159] A. R. Benrekia et al., Physica B: Condensed Matter **407**, 2632 (2012).

[160] M. De Jong et al., Scientific Data **2**, 150009 (2015).

[161] R. O. Bell and G. Rupprecht, Physical Review **129**, 90 (1963).

[162] C. A. Mizzi, P. Koirala, and L. D. Marks, Physical Review Materials **2**, 025001 (2018).

[163] M. O'Keeffe and J. C. Spence, Acta Crystallographica Section A **50**, 33 (1994).

[164] J. A. Ibers, Acta Crystallographica **11**, 178 (1958).

[165] P. Becker and P. Coppens, Acta Crystallographica Section A **46**, 254 (1990).

[166] D. Rez, P. Rez, and I. Grant, Acta Crystallographica Section A **50**, 481 (1994).

[167] S. Cabuk, physica status solidi (B) **247**, 93 (2010).

[168] X. Luo and B. Wang, Journal of Applied Physics **104** (2008).

[169] M. A. Islam, J. M. Rondinelli, and J. E. Spanier, Journal of Physics: Condensed Matter **25** (2013).

[170] I. Sokolović et al., arXiv , 2012.08831 (2020).

[171] D. K. Saldin and J. C. Spence, Ultramicroscopy **55**, 397 (1994).

[172] A. K. Tagantsev and A. S. Yurkov, Journal of Applied Physics **112**, 044103 (2012).

[173] A. S. Yurkov and A. K. Tagantsev, Applied Physics Letters **108**, 022904 (2016).

[174] J. C. Spence, Acta Crystallographica Section A **49**, 231 (1993).

[175] M. Gajdardziska-Josifovska et al., Ultramicroscopy **50**, 285 (1993).

[176] R. S. Pennington, C. B. Boothroyd, and R. E. Dunin-Borkowski, Ultramicroscopy **159**, 34 (2015).

[177] P. Kruse, M. Schowalter, D. Lamoen, A. Rosenauer, and D. Gerthsen, Ultramicroscopy **106**, 105 (2006).

[178] M. Y. Kim, J. M. Zuo, and J. Spence, physica status solidi (a) **166**, 445 (1998).

[179] M. Schowalter, D. Lamoen, A. Rosenauer, P. Kruse, and D. Gerthsen, Applied Physics Letters **85**, 4938 (2004).

[180] M. Schowalter, A. Rosenauer, D. Lamoen, P. Kruse, and D. Gerthsen, Applied Physics Letters **88**, 86 (2006).

[181] L. Kleinman, Physical Review B **24**, 7412 (1981).

[182] A. Kahn, Materials Horizons **3**, 7 (2016).

[183] T. K. Andersen, D. D. Fong, and L. D. Marks, Surface Science Reports **73**, 213 (2018).

[184] M. R. Castell, Surface Science **516**, 33 (2002).

[185] M. R. Castell, Surface Science **505**, 1 (2002).

[186] N. Erdman et al., Journal of the American Chemical Society **125**, 10050 (2003).

[187] B. Cord and R. Courths, Surface Science **162**, 34 (1985).

[188] J. E. T. Andersen and P. J. Møller, Applied Physics Letters **56**, 1847 (1990).

[189] Q. D. Jiang and J. Zegenhagen, Surface Science **338**, L882 (1995).

[190] P. J. Møller, S. A. Komolov, and E. F. Lazneva, Surface Science **425**, 15 (1999).

[191] T. Kubo and H. Nozoye, Surface Science **542**, 177 (2003).

[192] Y. Lin et al., Surface Science **605**, L51 (2011).

[193] O. Warschkow et al., Surface Science **573**, 446 (2004).

[194] N. Erdman et al., Nature **419**, 55 (2002).

[195] D. Tang and H. E. Elsayed-Ali, Physical Review B **50**, 18674 (1994).

[196] D. Jiang and J. Zegenhagen, Surface Science **425**, 343 (1999).

[197] D. Wolf, Physical Review Letters **68**, 3315 (1992).

[198] J. Ciston, A. Subramanian, and L. D. Marks, Physical Review B **79**, 085421 (2009).

[199] R. Plass et al., Physical Review Letters **81**, 4891 (1998).

[200] F. Finocchi, A. Barbier, J. Jupille, and C. Noguera, Physical Review Letters **92**, 136101 (2004).

[201] A. Ramstad, G. Brocks, and P. J. Kelly, Physical Review B **51**, 14504 (1995).

[202] L. D. Marks, Journal of Chemical Theory and Computation **9**, 2786 (2013).

[203] S. Massidda, B. I. Min, and A. J. Freeman, Physical Review B **35**, 9871 (1987).

[204] A. Franceschetti, S.-h. Wei, and A. Zunger, Physical Review B **50**, 17797 (1994).

[205] H. Y. Sun et al., Nature Communications **9** (2018).

[206] M. Mrovec, J. M. Albina, B. Meyer, and C. Elsässer, Physical Review B **79**, 245121 (2009).

[207] K. Marklund and S. A. Mahmoud, Physica Scripta **3**, 75 (1971).

[208] H. J. McSkimin and P. Andreatch, Journal of Applied Physics **35**, 2161 (1964).

[209] L. M. Garten and S. Trolier-McKinstry, Journal of Applied Physics **117**, 094102 (2015).

[210] I. B. Bersuker, Applied Physics Letters **106**, 022903 (2015).

[211] J. Narvaez and G. Catalan, Applied Physics Letters **104**, 162903 (2014).

[212] X. Zhang et al., Physical Review Letters **121**, 57602 (2018).

[213] A. K. Tagantsev, L. E. Cross, and J. Fousek, *Domains in Ferroic Crystals and Thin Films*, Springer New York, New York, NY, 2010.

[214] J. R. Macdonald, Annals of Biomedical Engineering **20**, 289 (1992).

[215] B. Cullity, Elements of X-ray diffraction, Pearson, New York, 1956.

[216] X. Wang, U. Helmersson, J. Birch, and W.-X. Ni, Journal of Crystal Growth **171**, 401 (1997).

[217] D. G. Schlom et al., Annual Review of Materials Research **37**, 589 (2007).

[218] D. G. Schlom et al., MRS Bulletin **39**, 118 (2014).

[219] R. J. Harrison, S. A. Redfern, A. Buckley, and E. K. Salje, Journal of Applied Physics **95**, 1706 (2004).

[220] E. K. Salje and M. A. Carpenter, Applied Physics Letters **99**, 051907 (2011).

[221] S. Kustov, I. Liubimova, and E. K. Salje, Applied Physics Letters **112**, 042902 (2018).

[222] S. Puchberger, V. Soprunyuk, W. Schranz, and M. A. Carpenter, Physical Review Materials **2**, 013603 (2018).

[223] G. Lu, S. Li, X. Ding, J. Sun, and E. K. H. Salje, Physical Review Materials **3**, 114405 (2019).

[224] G. Lu, S. Li, X. Ding, and E. K. Salje, Applied Physics Letters **114**, 202901 (2019).

[225] G. Lu, S. Li, X. Ding, J. Sun, and E. K. Salje, Scientific Reports **9**, 1 (2019).

[226] E. K. Salje, Annual Review of Materials Research **42**, 265 (2012).

[227] A. V. Kityk et al., Physical Review B **61**, 946 (2000).

[228] J. Chrosch and E. K. Salje, Journal of Applied Physics **85**, 722 (1999).

[229] E. K. Salje, O. Aktas, M. A. Carpenter, V. V. Laguta, and J. F. Scott, Physical Review Letters **111**, 1 (2013).

[230] S. Van Aert et al., Advanced Materials **24**, 523 (2012).

[231] R. Glaister, Proceedings of the IEE - Part B: Electronic and Communication Engineering **109**, 423 (1962).

[232] L. Q. Han et al., Solid State Ionics **175**, 431 (2004).

[233] C. Rodenbücher et al., New Journal of Physics **15**, 103017 (2013).

[234] C. Rodenbücher et al., Scientific Reports **6**, 32250 (2016).

[235] E. Meirzadeh et al., Advanced Materials **31**, 1904733 (2019).

[236] A. Chatzopoulos, P. Beck, J. Roth, and H. R. Trebin, Physical Review B **93**, 024105 (2016).

[237] J. Fontanella, C. Andeen, and D. Schuele, Journal of Applied Physics **45**, 2852 (1974).

[238] J. L. Schroeder, A. S. Ingason, J. Rosén, and J. Birch, Journal of Crystal Growth **420**, 22 (2015).

[239] R. J. Paull, Z. R. Mansley, T. Ly, L. D. Marks, and K. R. Poeppelmeier, Inorganic Chemistry **57**, 4104 (2018).

[240] R. J. Paull, T. Ly, Z. R. Mansley, K. R. Poeppelmeier, and L. D. Marks, Crystals **9**, 218 (2019).

[241] Z. R. Mansley, C. A. Mizzi, P. Koirala, J. Wen, and L. D. Marks, Physical Review Materials **4**, 045003 (2020).

[242] C. A. Mizzi, P. Koirala, A. Gulec, and L. D. Marks, Ultramicroscopy **203**, 119 (2019).

[243] T. Ly, J. Wen, and L. D. Marks, Nano Letters **18**, 5186 (2018).

[244] D. Briggs and M. Seah, *Practical Surface Analysis*, Wiley, Chichester, 1996.

[245] S. Hufner, *Photoelectron Spectroscopy: Principles and Applications*, Springer, Berlin, 2003.

[246] D. B. Williams and C. B. Carter, *Transmission Electron Microscopy*, Springer US, Boston, MA, 2009.

[247] R. Egerton, *Electron Energy-Loss Spectroscopy in the Electron Microscope*, Springer US, Boston, MA, 2011.

[248] F. J. Giessibl, Reviews of Modern Physics **75**, 949 (2003).

[249] R. T. Haasch, L. W. Martin, and E. Breckenfeld, Surface Science Spectra **21**, 165 (2014).

[250] R. T. Haasch, L. W. Martin, and E. Breckenfeld, Surface Science Spectra **21**, 149 (2014).

[251] R. T. Haasch, L. W. Martin, and E. Breckenfeld, Surface Science Spectra **21**, 157 (2014).

[252] C. Derks et al., Physical Review B **86**, 155124 (2012).

[253] R. Uecker et al., Journal of Crystal Growth **310**, 2649 (2008).

[254] B. Veličkov, V. Kahlenberg, R. Bertram, and M. Bernhagen, Zeitschrift fur Kristallographie **222**, 466 (2007).

[255] C. J. Powell, A. Jablonski, and F. Salvat, Surface and Interface Analysis **37**, 1068 (2005).

[256] J. Yeh and I. Lindau, Atomic Data and Nuclear Data Tables **32**, 1 (1985).

[257] J. F. Janak, Physical Review B **18**, 7165 (1978).

[258] C. Goransson, W. Olovsson, and I. A. Abrikosov, Physical Review B **72**, 134203 (2005).

[259] S. Sanna, T. Frauenheim, and U. Gerstmann, Physical Review B **78**, 085201 (2008).

[260] J. Slater, *The Self-Consistent Field for Molecules and Solids*, McGraw-Hill, New York, 1974.

[261] V. I. Anisimov, J. Zaanen, and O. K. Andersen, Physical Review B **44**, 943 (1991).

[262] A. Walsh et al., Physical Review B **73**, 235104 (2006).

[263] C. Hogan, M. Palummo, and R. Del Sole, Comptes Rendus Physique **10**, 560 (2009).

[264] A. Biswas, C.-H. Yang, R. Ramesh, and Y. H. Jeong, Progress in Surface Science **92**, 117 (2017).

[265] R. Dirsyte et al., Surface Science **604**, L55 (2010).

[266] J. E. Kleibeuker et al., Advanced Functional Materials **20**, 3490 (2010).

[267] J. E. Kleibeuker et al., Physical Review B - Condensed Matter and Materials Physics **85**, 1 (2012).

[268] M. Kawasaki et al., Science **266**, 1540 (1994).

[269] T. A. Carlson and G. E. McGuire, Journal of Electron Spectroscopy and Related Phenomena **1**, 161 (1972).

[270] C. S. Fadley, R. J. Baird, W. Siekhaus, T. Novakov, and S. Å. L. Bergström, Journal of Electron Spectroscopy and Related Phenomena **4**, 93 (1974).

[271] E. McCafferty and J. P. Wightman, Applied Surface Science **143**, 92 (1999).

[272] B. Rafferty, S. J. Pennycook, and L. M. Brown, Journal of Electron Microscopy **49**, 517 (2000).

[273] J. A. Aguiar, B. W. Reed, Q. M. Ramasse, R. Erni, and N. D. Browning, Ultramicroscopy **124**, 130 (2013).

[274] F. Wang, R. Egerton, and M. Malac, Ultramicroscopy **109**, 1245 (2009).

[275] M. Stöger-Pollach et al., Micron **37**, 396 (2006).

[276] J. Cazaux, Journal of Applied Physics **59**, 1418 (1986).

[277] J. Cazaux, Journal of Electron Spectroscopy and Related Phenomena **105**, 155 (1999).

[278] J. Park et al., Ultramicroscopy **109**, 1183 (2009).

[279] E. Bursian and N. Trunov, Soviet Physics - Solid State **16**, 760 (1974).

[280] C. Zener, Proceedings of the Royal Society A: Mathematical, Physical and Engineering Sciences **145**, 523 (1934).

[281] M. Janovska et al., Journal of Physics: Condensed Matter **24**, 385404 (2012).

[282] D.-H. Chung, Philosophical Magazine **8**, 833 (1963).

[283] W. R. Harper, *Contact and Frictional Electrification*, Oxford University Press, Oxford, 1967.

[284] D. J. Lacks and R. Mohan Sankaran, Journal of Physics D: Applied Physics **44**, 453001 (2011).

[285] D. J. Lacks and T. Shinbrot, Nature Reviews Chemistry **3**, 465 (2019).

[286] P. Shaw, Proceedings of the Royal Society of London. Series A. Mathematical and Physical Sciences. **94**, 16 (1917).

[287] W. Harper, Proceedings of the Royal Society of London. Series A. Mathematical and Physical Sciences. **205**, 83 (1951).

[288] C. Liu and A. J. Bard, Nature Materials **7**, 505 (2008).

[289] J. Lowell and A. Rose-Innes, Advances in Physics **29**, 947 (1980).

[290] D. K. Davies, Journal of Physics D: Applied Physics **2**, 1533 (1969).

[291] A. F. Diaz and D. Fenzel-Alexander, Langmuir **9**, 1009 (1993).

[292] L. S. McCarty and G. M. Whitesides, Angewandte Chemie - International Edition **47**, 2188 (2008).

[293] H. T. Baytekin, B. Baytekin, J. T. Incorvati, and B. A. Grzybowski, Angewandte Chemie - International Edition **51**, 4843 (2012).

[294] S. Lin et al., Advanced Materials **31**, 1808197 (2019).

[295] J. F. Kok and D. J. Lacks, Physical Review E **79**, 051304 (2009).

[296] D. J. Lacks, N. Duff, and S. K. Kumar, Physical Review Letters **100**, 188305 (2008).

[297] J. Lowell and W. S. Truscott, Journal of Physics D: Applied Physics **19**, 1281 (1986).

[298] J. Blum and G. Wurm, Annual Review of Astronomy and Astrophysics **46**, 21 (2008).

[299] J. F. Kok and N. O. Renno, Physical Review Letters **100**, 014501 (2008).

[300] H. Watanabe et al., International Journal of Pharmaceutics **334**, 149 (2007).

[301] C. B. Duke, J. Noolandi, and T. Thieret, Surface Science **500**, 1005 (2002).

[302] F. Bowden and D. Tabor, *The Friction and Lubrication of Solids*, Clarendon Press, 1958.

[303] W. R. Harper, Contemporary Physics **2**, 345 (1961).

[304] H. Helmholtz, Annalen der Physik und Chemie **243**, 337 (1879).

[305] E. Perucca, Zeitschrift fr Physik **51**, 268 (1928).

[306] W. Jamieson, Nature **83**, 189 (1910).

[307] P. Shaw and R. Hanstock, Proceedings of the Royal Society of London. Series A. Mathematical and Physical Sciences. **128**, 474 (1930).

[308] J. Lowell and W. S. Truscott, Journal of Physics D: Applied Physics **19**, 1273 (1986).

[309] M. Sow, D. J. Lacks, and R. Mohan Sankaran, Journal of Applied Physics **112**, 084909 (2012).

[310] M. Sow et al., Angewandte Chemie **124**, 2749 (2012).

[311] C. A. Mizzi and L. D. Marks, arXiv , 2010.12963 (2020).

[312] H. Hertz, Journal für die reine und angewandte Mathematik **1882**, 156 (1882).

[313] K. Johnson, *Contact Mechanics*, Cambridge University Press, Cambridge, England, 1985.

[314] K. Johnson, J. Kendall, and A. Roberts, Proceedings of the Royal Society of London. A. Mathematical and Physical Sciences **324**, 301 (1971).

[315] T. A. L. Burgo and A. Erdemir, Angewandte Chemie **126**, 12297 (2014).

[316] J. V. Escobar, A. Chakravarty, and S. J. Putterman, Diamond and Related Materials **36**, 8 (2013).

[317] H. T. Baytekin et al., Science **333**, 308 (2011).

[318] T. A. Burgo et al., Langmuir **28**, 7407 (2012).

[319] U. G. Musa, S. D. Cezan, B. Baytekin, and H. T. Baytekin, Scientific Reports **8**, 2472 (2018).

[320] B. D. Terris, J. E. Stern, D. Rugar, and H. J. Mamin, Physical Review Letters **63**, 2669 (1989).

[321] B. N. Persson, Europhysics Letters **129**, 10006 (2020).

[322] C. Xu et al., ACS Nano **13**, 2034 (2019).

[323] W. Schottky, Zeitschrift fr Physik **113**, 367 (1939).

[324] N. F. Mott, Proceedings of the Royal Society of London. Series A. Mathematical and Physical Sciences. **1**, 153 (1939).

[325] J. Bardeen and W. Shockley, Physical Review **80**, 72 (1950).

[326] W. Shockley and J. Bardeen, Physical Review **77**, 407 (1950).

[327] C. W. Shih, W. S. Schlein, and J. C. Li, Journal of Materials Research **7**, 1011 (1992).

[328] P. S. Henry, British Journal of Applied Physics **4**, S6 (1953).

[329] W. R. Harper, British Journal of Applied Physics **11**, 324 (1960).

[330] A. J. Walton, Advances in Physics **26**, 887 (1977).

[331] J. I. Zink, Accounts of Chemical Research **11**, 289 (1978).

[332] J. Randall and M. Wilkins, Proceedings of the Royal Society of London. Series A, Mathematical and Physical Sciences **184**, 365 (1945).

[333] S. R. Waitukaitis, V. Lee, J. M. Pierson, S. L. Forman, and H. M. Jaeger, Physical Review Letters **112**, 218001 (2014).

[334] E. Mikheev, B. D. Hoskins, D. B. Strukov, and S. Stemmer, Nature Communications **5**, 3990 (2014).

[335] I. A. Harris, M. X. Lim, and H. M. Jaeger, Physical Review Materials **3**, 085603 (2019).

[336] V. Lee, N. M. James, S. R. Waitukaitis, and H. M. Jaeger, Physical Review Materials **2**, 35602 (2018).

[337] Z. Zhang and J. T. Yates, Chemical Reviews **112**, 5520 (2012).

[338] S. Ma, M. E. Reish, Z. Zhang, I. Harrison, and J. T. Yates, Journal of Physical Chemistry C **121**, 1263 (2017).

[339] K. M. Forward, D. J. Lacks, and R. M. Sankaran, Physical Review Letters **102**, 028001 (2009).

[340] R. Pham, R. C. Virnelson, R. M. Sankaran, and D. J. Lacks, Journal of Electrostatics **69**, 456 (2011).

[341] T. Shinbrot, T. S. Komatsu, and Q. Zhao, Europhysics Letters **83**, 24004 (2008).

[342] P. S. Henry, British Journal of Applied Physics **4**, S31 (1953).

[343] C. Xu et al., Advanced Materials **30**, 1706790 (2018).

[344] G. S. Rose and S. G. Ward, British Journal of Applied Physics **8**, 121 (1957).

[345] H. Zou et al., Nature Communications **11**, 2093 (2020).

[346] S. Jeffery, C. J. Sofield, and J. B. Pethica, Applied Physics Letters **73**, 172 (1998).

[347] B. P. Chandra et al., Journal of Luminescence **132**, 2012 (2012).

[348] M. Nonnenmacher, M. P. O'Boyle, and H. K. Wickramasinghe, Applied Physics Letters **58**, 2921 (1991).

[349] D. K. Aswal et al., Journal of Crystal Growth **236**, 661 (2002).

[350] M. N. Yesibolati et al., Physical Review Letters **124**, 18 (2020).

[351] G. E. Fasshauer, *Meshfree Approximation Methods with Matlab*, volume 6 of *Interdisciplinary Mathematical Sciences*, World Scientific, 2007.

APPENDIX A

Finite Element Contact Simulations

A.1. Simulation Parameters

FEA simulations were performed with Abaqus using CAX4R mesh elements with reduced integration. Frictionless, hard-contact with surface-to-surface discretization were used in the simulations with YSYMM mechanical boundary conditions on the bottom-most surface (i.e. no Z-displacement or rotation about the R or Z axes were allowed) and Z-displacements on the top surface. $\sim 10^6$ elements were used in the flat and $\sim 10^5$ elements in the sphere. A typical mesh is shown in Figure A.1. Tests were performed with different mesh densities and meshing elements to ensure all quantities were adequately converged. For calculations on STO and Si, literature values for the Young's modulus and Poisson's ratio were used (270 GPa, 0.24 for STO [**161**], and 160 GPa, 0.27 for Si [**208**]) and materials were assumed to be isotropic.

A.2. Radial Basis Function Interpolation

Once strain fields were obtained from Abaqus, it was necessary to interpolate them to perform the differentiation and integration needed to evaluate Eq. 8.20. The interpolation method was a radial basis function (RBF) implemented in Python with third-order polyharmonic splines [**351**] and a shape parameter of 10^{-5}. Multiple basis functions and shape parameter combinations were tested and the interpolated mesh density was varied

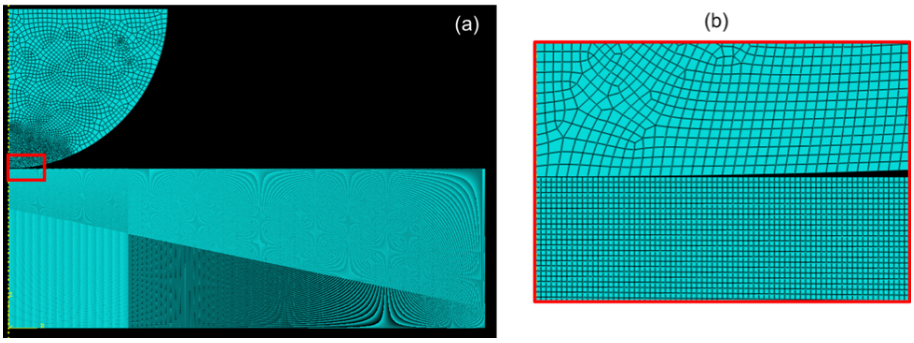

Figure A.1. (a) A typical mesh used for Abaqus simulations. (b) A magnified view of the contact point. The contact interface at the maximum contact deformation consisted of $\sim 10^2$ mesh elements.

to minimize numerical errors. Figure A.2 compares an Abaqus strain output and a radial basis function interpolation to demonstrate the quality of the interpolation.

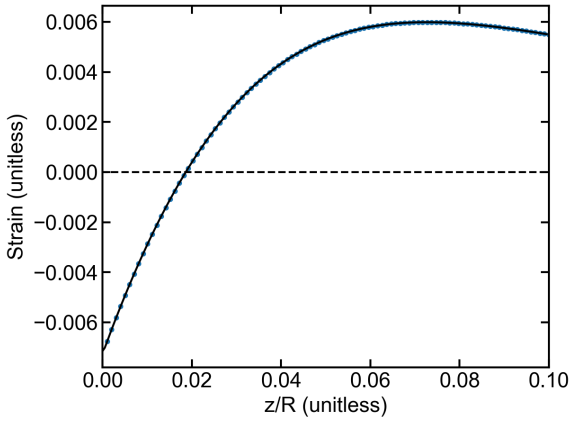

Figure A.2. Comparison between FEA output (blue points) and RBF interpolation (black line) of ϵ_{rr} strain at the contact point as a function of depth (z) normalized by the sphere radius (R). The strains are in a STO flat in contact with a STO sphere with a contact pressure of 8 GPa.

A.3. Deviations from Hertz Theory

First, we demonstrate that the FEA simulations properly capture that two bodies made of the same material, but with different geometries, have different strain fields in

contact. Figure A.3 shows the ϵ_{rr} strain component for sphere-on-flat contact between two STO bodies with a contact pressure of 8 GPa. This data indicates the flat has strain fields which generally match those predicted by Hertz theory [**312**], whereas the sphere has larger strains in the contact area ($z < 0.1\ R$, where R is the indenter radius) which deviate from Hertz theory. In both cases, strain fields predicted by Hertz theory [**312**] are recovered sufficiently far from the contact point. Generally, we find bodies with smaller radii of curvature, i.e. those which are more poorly approximated as an elastic half-space, exhibit greater deviations from Hertz theory within the contact area.

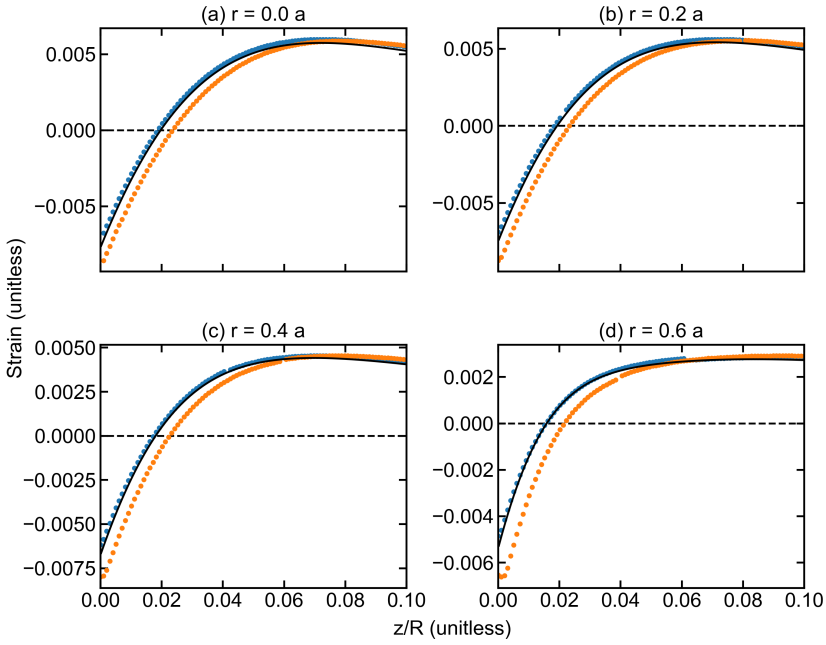

Figure A.3. ϵ_{rr} strain component for normal contact between a STO sphere (orange) and flat (blue) with a contact pressure of 8 GPa calculated with FEA compared to the Hertz theory solution (black). Radial distances (r) are given in terms of the contact radius (a) and axial distance from the point of contact (z) is normalized by the sphere radius (R).

The differences between the individual strain components for two chemically identical, geometrically distinct bodies in contact manifest in differences in the volumetric strain $\epsilon_{vol} = \epsilon_{rr} + \epsilon_{\theta\theta} + \epsilon_{zz}$. This term is necessary to quantify the MIP and deformation potential effects. Figure A.4 depicts the differences in volumetric strain between a STO sphere and flat in contact with a contact pressure of 8 GPa.

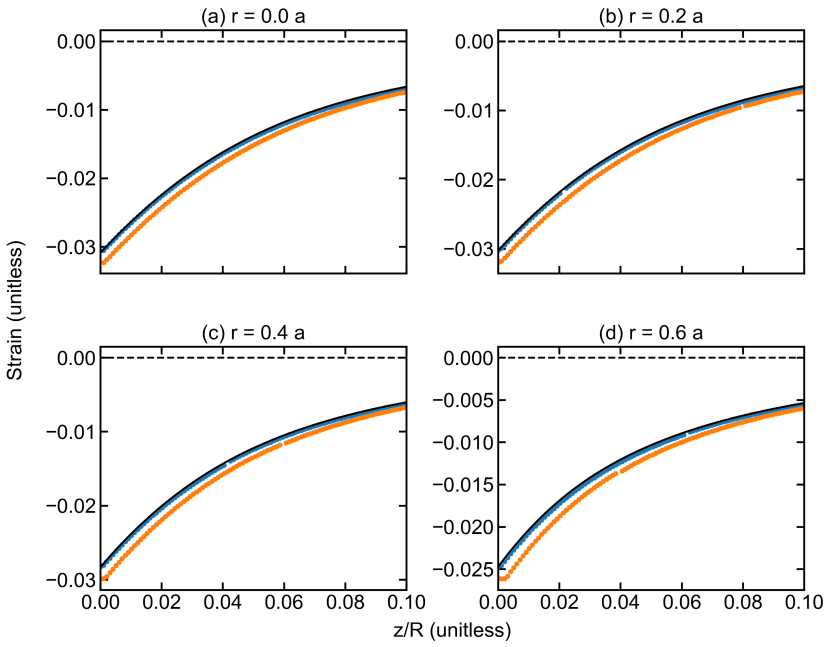

Figure A.4. Volumetric strain for normal contact between a STO sphere (orange) and flat (blue) with a contact pressure of 8 GPa calculated with FEA compared to Hertz theory solution (black). Volumetric strains are given as a function of depth (normalized by the indenter radius R) at different radial distances (in units of the contact radius a) from the contact point.

A.4. Strain Gradients, Flexoelectric Polarization, and $\Delta\overline{V}^{FxE}$

Now we use the interpolated strain fields to determine the non-trivial strain gradients used to calculate the flexoelectric polarization. Examples of the non-trivial strain gradients which can couple to the radial (axial) components of polarization in a STO flat contacted by a STO sphere are shown in Figure A.5 (A.6). The polarization components are shown in Figure A.7, assuming the first principles values of the bulk flexoelectric coefficients (Chapter 4).

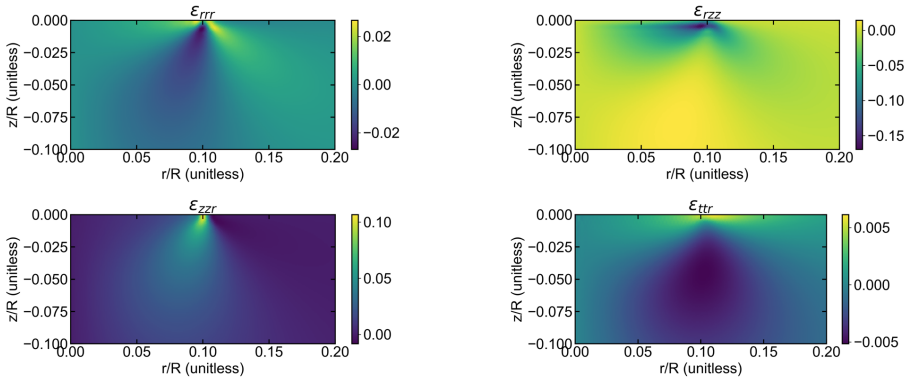

Figure A.5. Strain gradients which couple to radial polarization in a STO flat contacted by a STO sphere with a contact pressure of 8 GPa. Values are given in units of 1/mm.

From the polarization components shown in Figure A.7, it is possible to calculate the change in the average Coulomb potential according to Eq. 8.31. An example of this process is included in Figure A.8 for contact between a STO flat and STO sphere with a contact pressure of 8 GPa. This figure demonstrates the difference between the change in the average Coulomb potential in two bodies which are chemically identical, but have different curvatures.

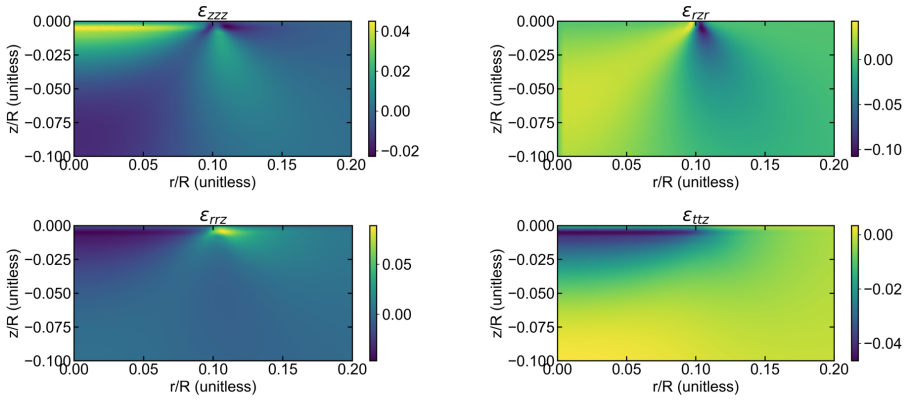

Figure A.6. Strain gradients which couple to axial polarization in a STO flat contacted by a STO sphere with a contact pressure of 8 GPa. Values are given in units of 1/mm.

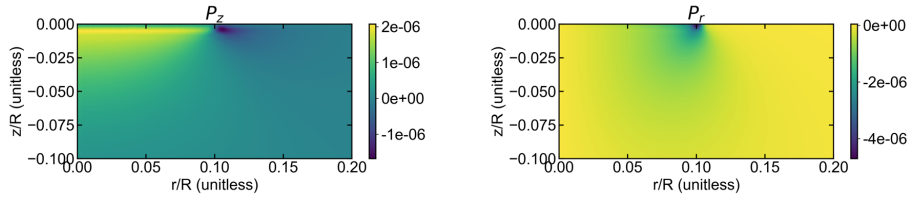

Figure A.7. (a) Axial and (b) radial polarization in a STO flat contacted by a STO sphere with a contact pressure of 8 GPa. Values are given in units of C/m^2.

Additionally, the framework described above allows us to confirm the reference potential defined in Eq. 8.31 is appropriate. Figure A.9 demonstrates the variation in the average Coulomb potential owing to the bulk flexoelectric effect quickly returns to zero as a function of depth from the point of contact, validating the choice of reference potential. This example uses contact between a Si sphere and STO flat with a contact pressure of 6 GPa.

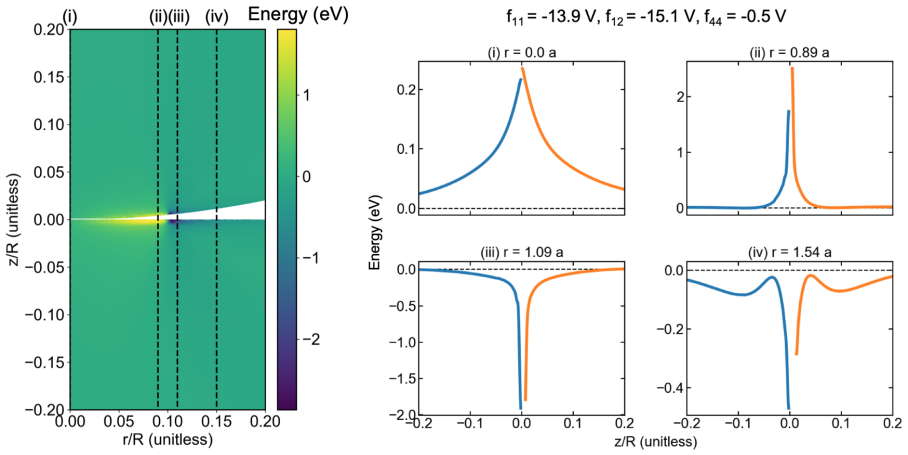

Figure A.8. (a) Change in the average Coulomb potential for a STO sphere contacting a STO flat with a contact pressure of 8GPa. (b) Change in the average Coulomb potential as a function of depth (normalized by the indenter radius R) at different radial distances (in units of the contact radius a) from the contact point as defined in (a).

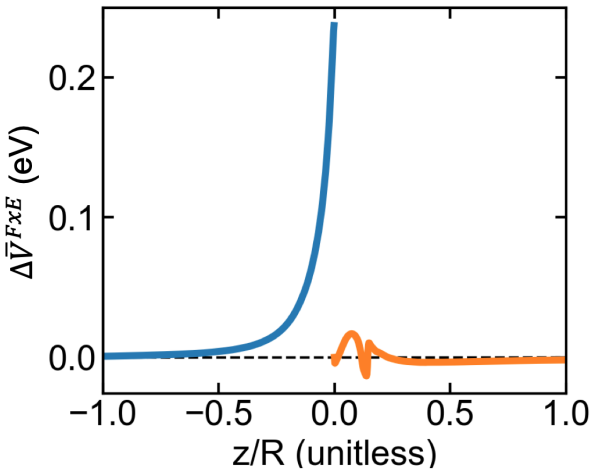

Figure A.9. Change in the average Coulomb potential from the bulk flexoelectric effect (Eq. 8.31) at the point of contact ($r = 0$) as a function of depth (z) normalized by the sphere radius (R) in a STO flat (blue) contacted by a Si sphere (orange) with a contact pressure of 6 GPa. Both potentials rapidly drop to zero. The differences in the shape of the two potential profiles originates from the relative size of the different flexoelectric coefficients in STO and Si (Section 8.4.3).